Average Wave Propagation and Scattering in Random Particulate Media: a broad frequency range

Paulo Sergio Piva

School of Mechanical, Aerospace and Civil Engineering

University of Sheffield

Supervisors: Dr Artur L. Gower and Dr Carl R. Tipton

A Thesis submitted for the degree of
Doctor of Philosophy
in the University of Sheffield

Sheffield
March 17, 2026

Declaration

I, Paulo Sergio Piva, confirm that this is my own work. I am aware of the University's Guidance on the Use of Unfair Means. This work has not been previously presented for an award at this, or any other, university.

Acknowledgements

A PhD is much more than just an academic degree, and my own journey proved that to be true. It all began with a leap into the unknown: moving abroad during the pandemic, my first time leaving the American continent. I arrived in Sheffield with little idea of what awaited me. The very next day, I met Artur Gower, who quickly became not just my supervisor but also a close friend. I'm deeply thankful for his guidance, encouragement, and support in helping me settle into life in the UK. Some of my best memories are from the times we cooked, played board games, shared morning coffees, and worked together, especially on trains.

On my very first day in the office, I met Aristeidis Karnezis, my first collaborator and someone who made me feel instantly welcome. Aris showed me around the University, helped me settle in, and stood by me throughout the PhD. I'll always remember our time together, whether in the office, traveling for conferences, looking out for one another, or enjoying unforgettable days at his family home in Greece.

Not long after, I met Kevish Napal, who joined as a postdoc. Working with him directly shaped one of the chapters in this thesis, but also gave me countless memories, from hikes in the Peak District to unexpected adventures. Kevish even gave me a Hindi name, Nitish, which I'll always hold dear.

Over time, I became part of the Dynamics Research Group, a community that gave me not just colleagues but true friends. With them, I shared lively discussions, inspiring seminars, and plenty of laughter, which made the PhD feel lighter and far more enjoyable.

Living far from Brazil wasn't easy, and "saudade" often kept me company. I missed my family and childhood friends deeply, especially my parents and brother. But I was lucky. Halfway through my PhD, my wife, Julia Niro, joined me in Sheffield. Her presence and support made all the difference. Visits from my parents, relatives, and friends also brought much-needed warmth and familiarity to my life abroad.

I also want to thank the colleagues and friends I met along the way, including Carl Tipton, Jess Kent, David Abrahams, Richard Vincent, Marco Bolognini, and Costela, who later joined Sheffield for his own PhD in Sheffield after we had already shared our undergraduate years at Unicamp.

Finally, I'm grateful to the University of Sheffield for providing the space and facilities that supported my research, and to both Johnson Matthey and the Engineering and Physical Sciences Research Council for their generous funding.

Abstract

This thesis presents theoretical results in the study of ensemble averaging of acoustic waves in random particulate media, which consists of a collection of randomly placed particles in a homogeneous background medium. The main advance in theory is the generalisation of a closure assumption known as the Quasi-Crystalline Approximation (QCA), which enables accounting for multiple scattering of waves between particles and walls. We perform numerical simulations of average reflection and transmission coefficients for layers of particulate media, which reproduce recent experimental findings such as Fabry-Pérot resonances. These numerical simulations contribute to the modelling of non-invasive and non-intrusive ultrasound characterisation setups for determining statistical particle properties. On another front, we deduce simple formulae for frequency dependent effective-properties for a mixture of randomly placed sub-wavelength resonators. We explain how to use these formulae to design broadband multiple tunable band gaps, leading to novel acoustic disordered metamaterials. The effective-properties are validated against high-fidelity Monte Carlo simulations of wave transmission for moderately long wavelengths compared to the diameter of each resonator.

Contents

List of Symbols

Symbol/Acronym	Description
RQ	Research Question
QCA	Quasi-Crystalline Approximation
X-QCA	eXtended Quasi-Crystalline Approximation
EW method	Effective Waves method
ECAH theory	Epstein-Carhart-Allegra-Hampton theory
MC	Monte Carlo
u_{in}	Incident wave (or field)
u_{scat}	Scattered wave (or field)
u_{tot}	Total wave (or field)
u_{exc}	Exciting wave (or field)
u_{reg}	Regular wave (or field)
c	Speed of sound in the exterior medium
c_0	Speed of sound in the matrix (Chapters 2 and 3)
ϱ	Density of the exterior medium
ϱ_0	Density of the matrix (Chapters 2 and 3)
β	Bulk modulus of the exterior medium
Z	Impedance of the exterior medium
ω	Angular frequency
k	Wavenumber of the exterior medium
k_0	Wavenumber of the matrix (Chapters 2 and 3)

Symbol	Description
$k_\star$	Effective wavenumber
$c_\star$	Effective wave speed
$\varrho_\star$	Effective density
$\beta_\star$	Effective bulk modulus
$Z_\star$	Effective impedance
a	Radius of the particles (or inner radius of resonators in Chapter 4)
b	Outer radius of resonators
$\mathfrak{n}$	Number of particles per unit volume (number density)
ϕ	Volume fraction of a type of particle or resonator
φ	Total volume fraction of particles or resonators
$g_n, g_{\boldsymbol{n}}$	Bessel coefficients of the incident wave (2D,3D)
f_n	Outgoing Hankel coefficients of the scattered wave (in Chapter 4)
$f_n^i, f_{\boldsymbol{n}}^i$	Scattering coefficients of the i-th particle or resonator (2D,3D)
V_n	Regular Bessel wave mode (2D)
U_n	Outgoing Hankel wave mode (2D)
$\mathrm{v}_{\boldsymbol{n}}$	Regular Bessel wave mode (3D)
$\mathrm{u}_{\boldsymbol{n}}$	Outgoing Hankel wave mode (3D)
$\mathcal{V}_{\boldsymbol{n}}$	Regular addition translation matrix (3D)
$\mathcal{U}_{\boldsymbol{n}}$	Outgoing addition translation matrix (3D)
$\mathrm{Y}_{\boldsymbol{n}}$	Spherical harmonic function
$T_n, T_{\boldsymbol{n}}$	T-matrix (2D,3D)
$\boldsymbol{r}$	Position vector
$\boldsymbol{\lambda}$	Particle properties array (non-dimentional in Chapter 4)
$\boldsymbol{q}$	Particle configuration vector
$\boldsymbol{k}$	Wavevector of the exterior medium
$\boldsymbol{k}_0$	Wavevector of the matrix
$\boldsymbol{k}_\star$	Effective wavevector

Symbol	Description
$\mathcal{R}$	Region of space occupied by the particulate (matrix and particles)
$\mathcal{P}$	Region of space occupied by particles
$\mathcal{S}$	Set of all possible particle (or resonator) properties
$p(\circ)$	Probability distribution of $\circ$
$\langle\circ\rangle$	Ensemble average of $\circ$
$\mathbb{T}_\sigma$	Backscattering operator
G	Amplitude of the incident wave
$R_\star$	Effective reflection coefficient
$T_\star$	Effective transmission coefficient
$\langle R\rangle$	Average amplitude of the reflected wave
$\langle T\rangle$	Average amplitude of the transmitted wave
$\langle\Sigma_{\text{sc}}\rangle$	Average scattering cross-section
$\mathcal{F}_n$	Material scattering coefficients
$z(\boldsymbol{\lambda})$	Resonance factor of a resonator with properties $\boldsymbol{\lambda}$

List of Figures

Chapter 1

Introduction

This PhD thesis is a collection of three articles, written in the format of journal papers, which follow the guidelines for *publication format thesis* of the University of Sheffield. All of these articles share the objective of advancing the theoretical understanding of acoustic wave scattering by *particulate media*, that we define here as a collection of small separated particles embedded in a homogeneous background medium. The theoretical contributions of these three papers provide useful insights on two main applications: non-invasive and non-intrusive sensing of statistical properties of particulates, and designing materials for wave control applications.

The first article (Chapter 2) [1] was published in a peer-reviewed academic journal, the second article (Chapter 3) will be submitted after the completion of the PhD degree, and the third article (Chapter 4) [2] was also published in a peer-reviewed academic journal. For the purpose of this thesis, the content of these articles has been adapted for readability and coherence. The PhD candidate is the first author on each of these papers, and is classified as the *primary contributor*, as required by the guidelines of the University of Sheffield.

In addition to the work presented in this thesis, the PhD candidate contributed significantly to two other peer-reviewed journal articles on the same subject [3, 4]. These publications are acknowledged here as part of the broader scientific output that the author has contributed. However, they are not included as thesis chapters because their scope falls outside the theme selected for this work.

A complete list of all scientific output of the PhD candidate, including journal articles, scientific reports and conference papers, follow bellow:

- Report from study group with PepsiCo, ESGI 171: C. J. Budd OBE, P. S. Piva, M. D. Shirley, and R. J. Whittaker (2023). *Microwave cooking of thin potato discs. Mathematics in industry reports*. DOI: 10.33774/miir-2023-mxttp.

- Conference paper: P. S. Piva, et al (2023). *Mathematical Model for Layered Acoustic Materials with Random Particulate Microstructure.* Phononics.
- Journal paper: K. K. Napal, P. S. Piva, and Art L. Gower (2024). *Effective T-matrix of a cylinder filled with a random two-dimensional particulate.* Proc. R. Soc. A 48020230660. DOI: 10.1098/rspa.2023.0660.
- Journal paper: A. Karnezis, P. S. Piva, and Art L. Gower (2024). *The average transmitted wave in random particulate materials.* New J. Phys. 26 063002. DOI: 10.1088/1367-2630/ad49c2.
- Journal paper: P. S. Piva, K. K. Napal, and Art L. Gower (2024). *Acoustic waves in a halfspace material filled with random particulate.* New J. Phys. 26 123033. DOI: 10.1088/1367-2630/ad9ed0.
- Conference paper: P. S. Piva and Art L. Gower (2025). *Acoustic waves in layered material filled with random particulate: Applications and Theoretical Advancements.* Bremen Workshop on Light Scattering.
- Journal paper: P. S. Piva, A. L. Gower, & I. D. Abrahams (2026). *Designing band gaps with randomly distributed sub-wavelength Helmholtz resonators.* npj Acoustics, 2, 10. DOI: 10.1038/s44384-026-00045-w.

1.1 Background

Acoustic phenomena have been used as a diagnostic tool in many areas of science, industry, defense, and engineering throughout the recent history of modern society [5]. A few well known applications of sound waves for sensing are medical ultrasound, seismology, material characterisation, structure health monitoring, sonar technologies and oceanography. Although these applications differ in their sensing devices and strategies, they all share the same underlying principle: a known source generates waves that propagate through the region of interest, where they are measured to infer information about the probed medium. One key step to extract information through this method is the quantitative description of how acoustic waves propagate through complex media, and their scattering at areas with contrasting acoustic properties, which constitutes the main object of investigation in this thesis.

One common type of obstacle for waves is small compact inhomogeneities, which are found in real-world materials as solid fragments, bubbles, defects, or inclusions. We call these inhomogeneities *particles*, which together with their embedding continuous medium, the *matrix*, form a complex multiphase medium named *particulate*. For many practical purposes, mainly at long wavelengths compared to particle sizes, these particles can be

treated as impurities in the matrix, which translates into effective corrections in propagation models. Taking as an example underwater acoustics, every 1PSU increase in salinity of ocean water translates into 1.3m/s increase in the speed of sound [6], or the wavespeed in bubbly water can drop more than 90% with only 1% of volume of gas in the mixture [7].

Although low-frequency effects are already noticeable, and even strong for void-like inclusions (bubbles in [7]), some applications require broad frequency measurements to be informative, such as particle size distribution estimation [8, 9]. Once the acoustic wavelength in the matrix drops to sizes comparable to interparticle distances and particle diameter, the interaction between waves and particles becomes dependent on the specific configuration of each phase in the particulate, and the description of propagation via homogeneous effective-properties (speed of sound, attenuation and mass density) is no longer accurate. In short, the contribution to wave scattering from the particles for higher frequencies can become *incoherent*, which we define here as a lack of stable phase relationship between scattered waves from different configurations of particles. Consider bubbles in the ocean disturbing sonar readings, low resolution of medical ultrasound images due to inhomogeneities in the tissue, or apparent noise in measurements of light in granular media; in each of these examples, incoherent scattering plays an important role.

Particulates are often classified as *disordered materials*, which are defined by the lack of control of their microstructure. In such materials, predictions of incoherent scattering are highly dependent on the limited amount of knowledge about particle configuration, and a statistical approach is required, introducing extra assumptions or measurements about the likelihood of each configuration. In this thesis, we focus on the case of numerous small particles, for which control or measurement of particle positioning is not attainable in practice. Then, we model the particulate as a collection of *randomly placed* particles in the matrix. Even though each configuration has a complex response to an incoming wave, the *average response* of the whole particulate can be calculated [10].

Equipped with the definitions and concepts above, we can state the main open question that guides the investigations conducted in this thesis:

> "How to model the average acoustic wave response for a broad frequency range in random particulate media?"

Here we emphasize that this open question has been addressed in the literature through various frameworks, several of which we discuss next. However, to answer any open question, one must first establish narrowing assumptions. In this thesis, we focus on acoustic (pressure) waves in the frequency domain. The background medium is modeled as a linear, isotropic, homogeneous, non-absorbing material with vanishing shear modulus. Particles

are treated as penetrable homogeneous spheres in three dimension space in Chapters 2 and 3 (applying continuity of pressure and normal velocity boundary conditions); or rigid circular scatterers in two dimensions in (2D) Chapter 4 (with non-penetrable Neumann boundary conditions). These assumptions allow us to isolate the effects of multiple scattering for wavelenghts ranging from much shorter, to much longer than particle diameter, without the added complexity of elastic waves, or absorption.

1.2 Methodological landscape

Wave scattering from randomly placed particles is a problem that dates back to the late 19th and early 20th centuries, with particular emphasis on two studies on electromagnetic waves: the explanation of why the sky is blue, by Rayleigh [11]; and the description of the optical response of colloidal metal solutions, by Mie [12]. Even though both studies concern light scattering by particulate media, the approach taken in each of them is notably distinct. Rayleigh scattering is valid only for particles which are significantly smaller than the incident wavelength, while Mie theory assumes dilute media, where rescattering between particles is negligible.

Several decades later, still within this context, Foldy proposed a different framework based on first principle calculations from statistical mechanics to model the average response of acoustic waves in random particulate media [10]. Foldy's approach accommodated multiple scattering effects over a wide frequency range and, for the first time, bridged the regimes traditionally described by Rayleigh and Mie. However, Foldy's calculations involved a series of hierarchical integral equations, which only achieved closed-form analytic solutions for the dilute media limit, as in Mie theory. The description of multiple wave scattering in densely packed particulate media was advanced by Lax, who introduced the quasi-crystalline approximation to Foldy's approach [13]. Subsequent significant contributions were made by Waterman, who incorporated his T-matrix formalism into the framework [14–17]. Within the low frequency and low density regimes, the statistical mechanics formalism provided higher order corrections [18–20], thus extending the classical approaches from Rayleigh and Mie to more general scenarios.

Beyond Foldy's statistical framework, the theory of asymptotic homogenisation was introduced to calculate analytical solutions of partial differential equations in composite media [21–25]. While this approach broadly addresses various physical phenomena, its application relies on the existence of small parameters, typically ratios between a microstructural length scale and a macroscopic one. In wave propagation, for instance, this is usually defined as the ratio of particle size (or interparticle distance) to wavelength. Exam-

ples of applications of homogenization techniques to waves range from vibration of elastic structures with small inclusions [26–29], to flexural waves in composite beams [30, 31], or even acoustic propagation in media with periodic arrays of wave scatterers [32, 33].

As computing power became more accessible, the strategies for calculating wave scattering by random and periodic particulates for a broad frequency range underwent a major shift. The use of *semi-analytical methods* became popular [34, 35] by integrating numerical computations into underlying theoretical models. These hybrid strategies extend the applicability of classical theories to more complex scenarios. A prominent example to describe wave phenomena is the use of *meso-scale approximations* [34, 36–38], a technique that explicitly links micro- and macro-scale wave field descriptions. Unlike standard homogenisation, meso-scale approximations remain accurate for large clusters of particles even when their size is not vanishingly small relative to the wavelength [31], extending applicability of standard homogenisation techniques. Alternatively to semi-analytical methods, *full numerical simulations* have also been employed to compute wave scattering by random particulates, usually in a Monte-Carlo fashion [3, 39, 40].

To investigate random particulates in this thesis, we make use of two methods: 1) the *Effective Waves method* introduced by Gower and Kristensson [3, 4, 41], which is a semi-analytical solution of the integral equations from Foldy-Lax-Waterman formalism; and 2) Monte-Carlo simulations, which employ direct calculation of the wave equation via modal decomposition for several particle configurations [3, 39, 40, 42]. The main advantage of approach 1 over approach 2 lies in its lower computational cost. However, the main drawback of approach 1 is that it cancels out all contributions from incoherent scattering in the acoustic response calculations, whereas approach 2 produces data for each configuration, which can then be averaged *a posteriori*. As both methods rely on first-principles multiple scattering, they remain valid across diverse densities, material properties and frequency ranges, provided the single-particle scattering physics is fully described. Throughout Chapters 2 to 4, we compare the results from the Effective Waves method against both effective medium theory (low and broad frequency regimes), and high fidelity Monte-Carlo simulations.

Alternatively, on top of the strategies discussed above, there are several models in the literature to calculate wave response for specific frequency bands, density regimes and material properties. Some examples are ECAH theory for suspensions [43–45], Biot theory for fluid-saturated porous solids [46, 47], and small inclusion models [35, 48–51].

1.3 Research questions and knowledge gaps

Among the applications of wave scattering in particulate media, two in particular require an accurate description over a broad frequency range: particle property characterisation and material design for wave propagation control. Although these two applications may seem unrelated at first glance, both can be classified as distinct inverse problems with a similar forward problem setup [52]. For example, to measure particle size distribution of a powder using ultrasound, one must first characterise the range of all possible acoustic responses for different particle size combinations, and then determine whether a given measured response corresponds to one specific size distribution, or even a range of compatible size combinations. Similarly, to determine which particles to add to a region to block specific bands of frequency from propagating through a material, the first step is to calculate a range of wave propagation properties for different combinations of particles.

In this thesis, we present theoretical advances in the forward problem setting for both applications, which we divide into two parts: modelling wave response in particle sensing setups, discussed in Chapters 2 and 3, and computation of wave propagation properties in disordered materials, presented in Chapter 4.

1.3.1 Non-invasive and non-intrusive sensing

Ultrasound inspection is a widely used technique for material characterisation, primarily because it is energy-efficient and non-invasive across a range of setups [53], allowing waves to be introduced into the material and propagate through it, without the insertion of any device or probe into the material being measured. On top of that, ultrasound inspection can often be performed non-intrusively, which means the measurement device does not affect wave propagation within the material being measured. In the context of ultrasound in particulate media, a non-intrusive process requires no probes being in direct contact with the material. The measurement is commonly made non-intrusive by inserting a layer of the same material as the matrix (*i.e.*, background medium where particles are embedded) between the probe and the particulate [54]. See Figure 1.1 for a comparison between a non-intrusive and an intrusive setup.

This strategy to separate the material and the probe is important to avoid the boundary effects of waves being rescattered multiple times between the particles and the interface, represented by the green and red arrows in Figure 1.1a between the solid and dashed black lines. If the layer is sufficiently thick (*i.e.*, δ is much larger than the wavelength), these multiple scattering boundary effects can be neglected, or accounted experimentally

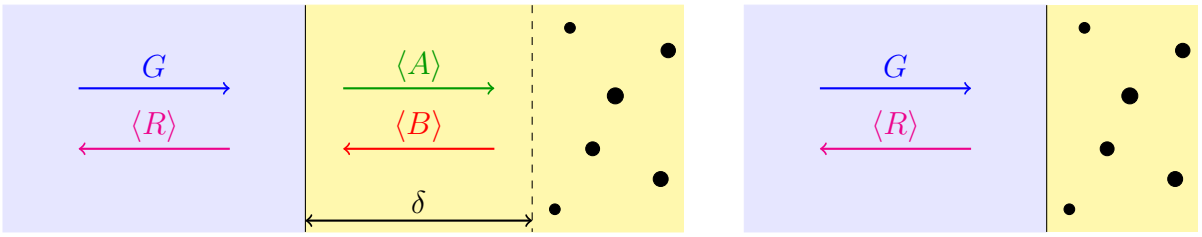

(a) Case $\delta > 0$ (b) Case $\delta \to 0$

Figure 1.1: An illustration of a non-intrusive measurement setup on the left (a), in contrast with an intrusive setup on the right (b). The blue region on the left represents the tip of the probe, from where the source (G) originates from, and the reflected wave ($\langle R \rangle$) heads into. The region on the right of both (a) and (b) is a homogeneous matrix with embedded particles. The middle region in (a) is a layer with thickness δ, which is homogeneous, and has the same properties as the background matrix of the halfspace filled with particles. Figure taken from [1].

as separated time signals from several reflections (echos) of an incident ultrasound pulse. Then, the material response $\langle B \rangle$ is well approximated by the material response when no probe touches the particulate media. However, to separate the particulate medium and the surface of the probe, as illustrated in Figure 1.1, is mostly convenient for controlled laboratory experiments, and it may not be feasible in many real-world applications to insert a layer of material similar to the matrix between the probe and the particulate. Consider a suspension of solid particles in a fluid; if more fluid is added between the particulate and the probe, the particles may leak into the layer of added fluid, altering both particle concentration in the particulate, and also pushing the boundary of the particulate back to the tip of the probe, as represented in the limit $\delta \to 0$ in Figure 1.1b.

Another strategy to make the ultrasound inspection non-intrusive is to add an extra layer of a material different to the acoustic medium of the matrix. This strategy not only helps in the case of a fluid matrix, but also allows mathematical models to account for the vessel containing the particulate media in the model, and the sensors can be placed outside this vessel. For example, to sense particle size distribution of solid particles suspended in water flowing through a pipe, one can make the measurement non-intrusive by attaching the probe to the external walls of the pipe. See Figure 1.2 below for an illustration.

Adding a vessel to the measurement setup is more general than the strategy presented in Figure 1.1, and the vessel can be designed so that its thickness is much larger than the wavelength, which solves the problem of multiple scattering boundary effects between the probe and the vessel. However, we still need to consider the multiple scattering on the boundary between the particulate media and the internal walls of the vessel. This problem of multiple scattering boundary effects seems to be unavoidable in practical measurement

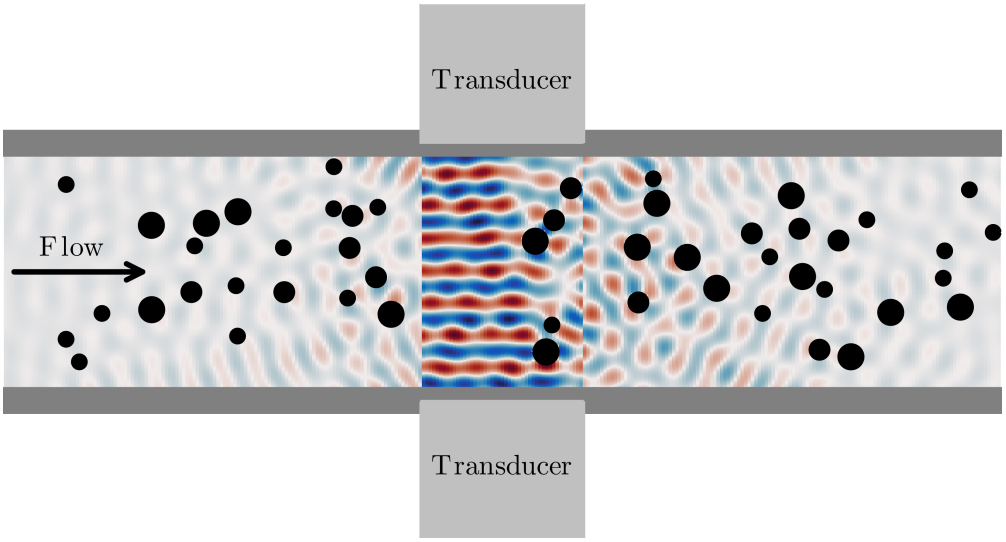

Figure 1.2: Shows the cross-section of a pipe, with a fluid flowing in the direction of the black arrow. Particles are suspended in the fluid, represented by black circles. A pair of transducers (acoustic sensors) are attached to the pipe walls. Figure taken from [1].

setups, and that is what motivates one of the two main research questions of this thesis:

(RQ1) "How to quantify rescattering between particles and the interface of a vessel, or probe, in random particulate media in an acoustic sensing setup?"

Answering (RQ1) is surprisingly challenging, despite the extensive literature on multiple scattering and ensemble averaging in random particulate media. This difficulty arises from the fact that the Quasi-Crystalline Approximation (QCA), introduced by Lax in [13], only accounts for multiple scattering of waves between particles, and the problem of boundaries in the particulate is not addressed. Recent progress on the problem was made by Kristensson and Wellander [55], which reaches Foldy-like integral equations for electromagnetic wave response of a collection of scatterers inside a dielectric slab. Kristensson and Wellander adopt a similar approach to the one pursued in this thesis; however, their formulation leads to integral equations that need to be specialised to either the low-frequency or dilute regimes to obtain tractable numerical solutions.

Beyond simply addressing (RQ1) theoretically, Chapters 2 and 3 aim to establish a framework capable of reaching efficient numerical calculations for the average acoustic response of particulate media across a broad frequency range and particle concentration regime, while accounting for multiple scattering of waves between particles and interfaces. These results are obtained by first examining the set of physical and statistical assumptions underlying Lax's QCA [13], and then employing the same assumptions to derive an

extended version of QCA, that also accounts for waves rescattered between particles and the walls of the vessel containing the particulate.

All that said, in Chapter 3 we also employ our models as a theoretical basis for recent experimental observations of ultrasound in particulate materials by Valier-Brasier et al. [56–58]. The key findings consist of: 1) an effective material density which is agnostic to particle properties across broad frequency ranges [56, 57], and 2) Fabry-Perot resonances in particulate layers [58]. While the experiments involved linear elastic waves (longitudinal and shear), we theoretically reproduce these phenomena for acoustic pressure waves within our model's constraints.

1.3.2 Disordered materials for wave control

Sound waves can be generated whenever a vibrating structure or object comes into contact with a fluid, which makes it difficult to control sound emission in practice. The lack of control on sound emission in large cities has motivated substantial efforts toward developing both active and passive soundproofing strategies [59, 60]. While active sound cancellation has proven effective for reducing noise through windows in residential settings [59], passive soundproofing remains the predominant approach for walls, and one reason for this is the development of lightweight, compact materials, specifically engineered for sound propagation control, referred to as *acoustic metamaterials* [60].

The design process of a metamaterial for wave control begins with its microstructure, which is typically chosen as a periodically repeating pattern [60]. The characteristic length scales of these spatial repetitions interact with sound waves in such a way that certain wavelengths are prevented from propagating through the material. The range of specific wavelengths that cannot propagate is called a *band gap*, a term borrowed from the terminology of electrical conductivity and insulation [61]. In addition to creating band gaps, some substance containing sound absorbing properties can be incorporated within this structure to attenuate the amplitude of the waves that are still able to propagate.

Although the design of periodic microstructure for metamaterials is well established in the literature, two main challenges exist for producing these materials for sound insulation applications: 1) to achieve wider band gaps, and possibly disconnected ones, several length scales of spatial periodicity are required, which may not be attainable due to fabrication constrains; and 2) for such materials to function as designed, they may depend on careful positioning of these repeating structures, necessitating sophisticated manufacturing techniques to ensure the required accuracy [62]. One strategy to overcome these challenges is to consider *disordered* microstructure to design metamaterials, which is the

approach we adopt in this thesis.

The class of disordered metamaterials we investigate is the one with its microstructure given by random particulate media. Because the acoustic response of particulates has contributions both from particles and the matrix, for simplicity, we focus solely on the effect of (homogeneously) randomly placed particles on the acoustic wave response, without considering different background media or interface effects. We also disregard any attenuation from absorbing materials to simplify the analysis. Even after all these assumptions, there is still room for valuable insights on the design of disordered metamaterials without any of the fabrication disadvantages of periodic microstructures. However, disordered materials based on particulate media do not contain any intrinsic length scale other than the size of their particles, which may pose a restriction to the range of blocked wavelengths.

To introduce another length scale to the metamaterial microstructure, one common strategy is to perform an average over particle configurations [41]. From this perspective, we can use Foldy-Lax-Waterman [10, 13, 14] statistical formalism to compute the average wave scattered from these randomly placed particles. Then, the average interparticle distance, and its higher statistical moments, introduce new length scales to the material, which contribute to band gaps. However, a band gap for the average acoustic wave in disordered media is different from the usual definition for periodic media that we provided in the second paragraph of this section. Controlling the propagation of the average wave through the metamaterial corresponds to blocking only the coherent component of scattering, while incoherent scattering (defined in Section 1.1) in any individual configuration can still occur, producing a speckle pattern of waves that leak through the material. Although this is a major disadvantage of disordered media compared to periodic structures, some applications may still be attainable via disordered microstructures, mainly at lower frequencies, as shown in Chapter 4. We also provide the physical interpretation of the resulting band gaps in Chapter 4 by comparing the intensity of the coherent field (average amplitude), and the average intensity of the scattered wave, which accounts for incoherent scattering.

One alternative strategy to achieve band gaps at longer wavelengths, larger than the size of the individual particles, is to use Helmholtz resonators as particles. One example in two dimensions is a split ring resonator [63], which consists in a neck-cavity system that has a resonance frequency at wavelengths that are larger than any of its characteristic lengths. See an illustration in Figure 1.3 below, which shows a typical split-ring resonator together with its scattering cross-section. The resonance is clearly sub-wavelength, occurring at $kb < 1$, where k is the wavenumber of the background medium and b the outer radius of the split-ring. This strategy can also be applied to periodic media [64, 65];

however, mixtures of different types of resonators face the same fabrication challenges discussed in the third paragraph of this section.

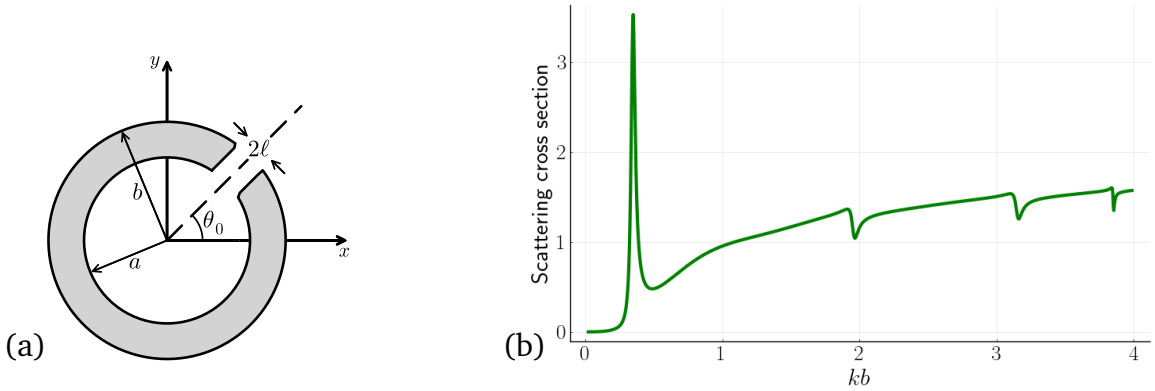

Figure 1.3: The left figure (a) shows an illustration of a typical split-ring resonator with outer radius b. The right figure (b) shows the scattering cross section of a sound-hard 2D split-ring resonator with an aperture size of $2\ell = 0.1b$, and k is the wavenumber of the background medium. Figure taken from [2]

By combining both strategies listed above, averaging over configurations and replacing particles by sub-wavelength resonators, it is possible to engineer disordered metamaterials with tunable sound propagation properties via designing multiple wide band gaps for targeted frequency bands [2]. However, beyond the drawbacks already discussed, there is an additional challenge to consider: calculating the average response of a generic mixture of different types of resonators within a microstructure can be computationally expensive. Even when the effective waves method is employed, generating phase diagrams can be time-consuming if several variables are considered in the search for viable microstructures for targeted applications [3]. This final challenge is the leading motivation for the second main research question of this thesis:

(RQ2) "How to quantify the average acoustic response of randomly placed sub-wavelength resonators efficiently, to allow for optimal band gap design?"

In the literature, the main strategy to achieve simple formulae for effective-properties of composite media is via the long wavelength limit [41, 66]. Although these formulae provide an efficient way to calculate acoustic response, they are not frequency dependent, and higher-order contributions to the asymptotic analysis are needed to capture the frequency dependence of the resonators in the particulate [67].

Chapter 4 addresses this question from a top-down perspective, where we begin with the effective waves method [41] to obtain a dispersion equation for the full average wave propagation properties of the metamaterial. Then, we take the limit of long wavelengths

compared to particle sizes, while still accounting for the frequency dependence of the sub-wavelength resonators. As a result, we reach a frequency dependent effective bulk modulus formula for the average wave propagation, together with an extension of the well known quasi-static limit for mass density [66] for Neumann particles. For simplicity, we restrict ourselves to 2D particles.

1.4 Outline of the thesis

In Chapter 2, we solve the problem of multiple scattering between particles and interfaces for a halfspace filled with randomly placed identical particles. The framework is deduced from first principles calculations, starting with the equations for one single configuration of particles, and then performing the ensemble average over particle configurations. The eXtended Quasi-Crystalline Approximation (X-QCA) is deduced and introduced in the multiple scattering governing equations, which results in a simpler version of the ensemble average equations in the presence of boundaries. Then, we perform numerical simulations of the average reflection of acoustic waves by particulate media for a broad range of frequencies, and with different matrix and particle properties. The numerical results are compared against both low and high frequency limits.

In Chapter 3, the results for reflection from a halfspace in Chapter 2 are extended to average reflection and transmission of acoustic waves by a layer filled with particulate media. Furthermore, we derive X-QCA for a polydisperse particulate, when the particles can differ from each other in size or materials. Then, we calculate average reflection and transmission by a layer filled with particles numerically, focusing on the case of a fluid matrix containing metallic powder, bubbles, or a mixture of both types of particles. These results are compared with effective medium theory, and certain recent experimental findings for linear elastic waves (pressure and shear) are reproduced, within the limits of possibility, for our model containing only acoustic (pressure) waves.

In Chapter 4, we reach simple frequency dependent effective-properties for a random configuration of 2D sub-wavelength resonators. The formulae for these effective-properties are deduced via asymptotic expansion of the effective wavenumber from the effective waves method, introduced in [41]. These formulas are validated against high-fidelity Monte Carlo simulations of acoustic wave transmission by a layer and scattering from a circle filled with particles, providing a close match for moderately low frequencies. We further demonstrate how these formulae can be applied to design both multiple and wide band gaps, within their range of validity.

Bibliography

[1] Paulo S Piva, Kevish K Napal, and Art L Gower. Acoustic waves in a halfspace material filled with random particulate. New Journal of Physics, 26(12):123033, 2024. doi: 10.1088/1367-2630/ad9ed0.

[2] Paulo S. Piva, Art L. Gower, and I. David Abrahams. Designing band gaps with randomly distributed sub-wavelength helmholtz resonators. npj Acoustics, 2:10, 2026. doi: 10.1038/s44384-026-00045-w.

[3] Aristeidis Karnezis, Paulo S Piva, and Art L Gower. The average transmitted wave in random particulate materials. New Journal of Physics, 26(6):063002, 2024. doi: 10.1088/1367-2630/ad49c2.

[4] K. K. Napal, P. S. Piva, and A. L. Gower. Effective T-matrix of a cylinder filled with a random two-dimensional particulate. Proceedings of the Royal Society A: Mathematical, Physical and Engineering Sciences, 480(2292):20230660, 2024. doi: 10.1098/rspa.2023.0660.

[5] David R. Dowling and Karim G. Sabra. Acoustic remote sensing. Annual Review of Fluid Mechanics, 47(Volume 47, 2015):221–243, 2015. ISSN 1545-4479. doi: 10.1146/annurev-fluid-010814-014747.

[6] F.T. Mackenzie, R.H. Byrne, and A.C. Duxbury. Seawater. Encyclopedia Britannica, 2025. URL https://www.britannica.com/science/seawater.

[7] Preston S. Wilson and Ronald A. Roy. An audible demonstration of the speed of sound in bubbly liquids. American Journal of Physics, 76(10):975–981, 10 2008. ISSN 0002-9505. doi: 10.1119/1.2907773.

[8] R. E. Challis, M. J. W. Povey, M. L. Mather, and A. K. Holmes. Ultrasound techniques for characterizing colloidal dispersions. Reports on Progress in Physics, 68(7):1541–1637, 2005. doi: 10.1088/0034-4885/68/7/R01.

[9] Malcolm J.W. Povey. Ultrasound particle sizing: A review. Particuology, 11(2):135–147, 2013. ISSN 1674-2001. doi: 10.1016/j.partic.2012.05.010.

[10] Leslie L. Foldy. The multiple scattering of waves. I. general theory of isotropic scattering by randomly distributed scatterers. Phys. Rev., 67:107–119, feb 1945. doi: 10.1103/PhysRev.67.107.

[11] J.W. Strutt. XV. on the light from the sky, its polarization and colour. The London,

Edinburgh, and Dublin Philosophical Magazine and Journal of Science, 41(271): 107–120, 1871. doi: 10.1080/14786447108640452.

[12] Gustav Mie. Beiträge zur optik trüber medien, speziell kolloidaler metallösungen. Annalen der Physik, 330(3):377–445, 1908. doi: 10.1002/andp.19083300302. Translation available at https://scattport.org/images/pdfs/SAND78-6018-Mie-1908-translation.pdf.

[13] Melvin Lax. Multiple scattering of waves. II. the effective field in dense systems. Phys. Rev., 85:621–629, 1952. doi: 10.1103/PhysRev.85.621.

[14] Peter Cary Waterman and Rohn Truell. Multiple scattering of waves. Journal of mathematical physics, 2(4):512–537, 1961. doi: 10.1063/1.1703737.

[15] P.C. Waterman. Matrix formulation of electromagnetic scattering. Proceedings of the IEEE, 53(8):805–812, 1965. doi: 10.1109/PROC.1965.4058.

[16] P. C. Waterman. New formulation of acoustic scattering. The Journal of the Acoustical Society of America, 45(6):1417–1429, 06 1969. ISSN 0001-4966. doi: 10.1121/1.1911619.

[17] M.I. Mishchenko and P.A. Martin. Peter Waterman and T-matrix methods. Journal of Quantitative Spectroscopy and Radiative Transfer, 123:2–7, 2013. ISSN 0022-4073. doi: https://doi.org/10.1016/j.jqsrt.2012.10.025.

[18] C. M. Linton and P. A. Martin. Multiple scattering by random configurations of circular cylinders: Second-order corrections for the effective wavenumber. The Journal of the Acoustical Society of America, 117(6):3413–3423, 2005. doi: 10.1121/1.1904270.

[19] C. Linton and Paul Martin. Multiple scattering by multiple spheres: A new proof of the Lloyd–Berry formula for the effective wavenumber. SIAM Journal on Applied Mathematics, 66, 2006. doi: 10.1137/050636401.

[20] L. Tsang and J. A. Kong. Effective propagation constants for coherent electromagnetic wave propagation in media embedded with dielectric scatters. Journal of Applied Physics, 53(11):7162–7173, 11 1982. ISSN 0021-8979. doi: 10.1063/1.331611.

[21] Enrique Sanchez-Palencia. Non-Homogeneous Media and Vibration Theory, volume 127 of Lecture Notes in Physics. Springer-Verlag, Berlin, Germany, 1980. ISBN 978-3-540-10000-3.

[22] N. Bakhvalov and G. Panasenko. Homogenisation: averaging processes in periodic

media: mathematical problems in the mechanics of composite materials. Mathematics and its applications (Soviet series) ; 36. Kluwer, 1989. ISBN 0792300491.

[23] Vladimir G. Maz'ya, Sergei Nazarov, and Boris Plamenevskii. Asymptotic Theory of Elliptic Boundary Value Problems in Singularly Perturbed Domains, volume 111 of Operator Theory: Advances and Applications. Birkhäuser, Basel, Switzerland, 2000. ISBN 978-3-0348-9572-9.

[24] Vladimir G. Maz'ya, Sergei Nazarov, and Boris Plamenevskii. Asymptotic Theory of Elliptic Boundary Value Problems in Singularly Perturbed Domains, Volume II, volume 112 of Operator Theory: Advances and Applications. Birkhäuser, Basel, Switzerland, 2000. ISBN 978-3-7643-6323-9.

[25] Vladimir A. Marchenko and Evgueni Ya. Khruslov. Homogenization of Partial Differential Equations, volume 46 of Progress in Mathematical Physics. Birkhäuser, Basel, Switzerland, 2006. ISBN 978-0-8176-4351-5. doi: 10.1007/978-0-8176-4479-6.

[26] C. Leal and J. Sanchez-Hubert. Perturbation of the eigenvalues of a membrane with a concentrated mass. Quarterly of Applied Mathematics, 47(1):93–103, 1989.

[27] Sergei A. Nazarov. Interaction of concentrated masses in a harmonically oscillating spatial body with Neumann boundary conditions. RAIRO - Modélisation Mathématique et Analyse Numérique, 27(7):777–799, 1993.

[28] Habib Ammari, Hyeonbae Kang, and Hyundae Lee. Asymptotic expansions for eigenvalues of the Lamé system in the presence of small inclusions. Communications in Partial Differential Equations, 32(11):1715–1736, 2007. doi: 10.1080/03605300601088711.

[29] D. Gomez, S. A. Nazarov, and M.-E. Perez. The formal asymptotics of eigenmodes for oscillating elastic spatial body with concentrated masses. Zapiski Nauchnykh Seminarov POMI, 342:31–76, 2007. English translation: (2008) J. Math. Sci. 148, 650–674.

[30] René Pernas-Salomón and Gal Shmuel. Dynamic homogenization of composite and locally resonant flexural systems. Journal of the Mechanics and Physics of Solids, 119:43–59, 2018. doi: 10.1016/j.jmps.2018.06.007.

[31] Michael J. Nieves and Alexander B. Movchan. Asymptotic theory of generalised Rayleigh beams and their dynamic response. In Michael J. Nieves, Gennady

Mishuris, and Andrea Piccolroaz, editors, Mechanics of High-Contrast Elastic Solids: Contributions from Euromech Colloquium 626, volume 284 of Springer Proceedings in Physics, pages 155–172. Springer, Cham, Switzerland, 2023. doi: 10.1007/978-3-031-23112-4_11.

[32] Daniel Torrent and José Sánchez-Dehesa. Effective parameters of clusters of cylinders embedded in a nonviscous fluid or gas. Phys. Rev. B, 74:224305, 2006. doi: 10.1103/PhysRevB.74.224305.

[33] Anton Krynkin, Olga Umnova, Alvin Y B Chong, Shahram Taherzadeh, and Keith Attenborough. Scattering by coupled resonating elements in air. Journal of Physics D: Applied Physics, 44(12):125501, mar 2011. doi: 10.1088/0022-3727/44/12/125501.

[34] Vladimir Maz'ya, Alexander Movchan, and Michael Nieves. Green's Kernels and Meso-scale Approximations in Perforated Domains, volume 2077 of Lecture Notes in Mathematics. Springer, Berlin, Germany, 2013. doi: 10.1007/978-3-319-00032-9.

[35] M. A. Nethercote, A. V. Kisil, and R. C. Assier. Diffraction of acoustic waves by a wedge of point scatterers. Proceedings of the Royal Society A, 477(2252):20210311, 2021. doi: 10.1098/rspa.2021.0311.

[36] Vladimir G. Maz'ya, Alexander B. Movchan, and Michael J. Nieves. Mesoscale asymptotic approximations in the dynamics of solids with defects. Journal of Mathematical Sciences, 268(4):443–457, 2022. doi: 10.1007/s10958-023-06240-5.

[37] Michael J. Nieves and Alexander B. Movchan. Asymptotic analysis of in-plane dynamic problems for elastic media with rigid clusters of small inclusions. Philosophical Transactions of the Royal Society A: Mathematical, Physical and Engineering Sciences, 380(2231):20210392, 2022. doi: 10.1098/rsta.2021.0392.

[38] Michael J. Nieves and Alexander B. Movchan. Meso-scale method of asymptotic analysis of elastic vibrations in periodic and non-periodic multi-structures. The Quarterly Journal of Mechanics and Applied Mathematics, 75(3):171–214, 2022. doi: 10.1093/qjmam/hbac009.

[39] Janna M. Dlugach, Michael I. Mishchenko, Li Liu, and Daniel W. Mackowski. Numerically exact computer simulations of light scattering by densely packed, random particulate media. Journal of Quantitative Spectroscopy and Radiative Transfer, 112 (13):2068–2078, 2011. ISSN 0022-4073. doi: 10.1016/j.jqsrt.2011.02.009.

[40] Adrien Rohfritsch, Jean-Marc Conoir, Régis Marchiano, and Tony Valier-Brasier. Numerical simulation of two-dimensional multiple scattering of sound by a large number of circular cylinders. The Journal of the Acoustical Society of America, 145(6): 3320–3329, 06 2019. doi: 10.1121/1.5110310.

[41] Artur L Gower and Gerhard Kristensson. Effective waves for random three-dimensional particulate materials. New Journal of Physics, 23(6):063083, 2021. doi: 10.1088/1367-2630/abdfee.

[42] Paul A. Martin. Multiple Scattering: Interaction of Time-Harmonic Waves with N Obstacles. Cambridge University Press, Cambridge, UK, 2006. ISBN 978-0521582392.

[43] P. S. Epstein and R. R. Carhart. The absorption of sound in suspensions and emulsions. I. Water fog in air. The Journal of the Acoustical Society of America, 25(3): 553–565, 1953. doi: 10.1121/1.1907107.

[44] J. R. Allegra and S. A. Hawley. Attenuation of sound in suspensions and emulsions: Theory and experiments. The Journal of the Acoustical Society of America, 51(5): 1545–1564, 1972. doi: 10.1121/1.1912999.

[45] Bassam Jameel, Tomasz Hornowski, Rafał Bielas, and Arkadiusz Jozefczak. Ultrasound study of magnetic and non-magnetic nanoparticle agglomeration in high viscous media. Materials, 15(10):3450, 2022. doi: 10.3390/ma15103450.

[46] M. A. Biot. Theory of propagation of elastic waves in a fluid-saturated porous solid. II. Higher frequency range. The Journal of the Acoustical Society of America, 28(2): 179–191, 1956. doi: 10.1121/1.1908241.

[47] Keith A. Wear, Andres Laib, Angela P. Stuber, and James C. Reynolds. Comparison of measurements of phase velocity in human calcaneus to biot theory. The Journal of the Acoustical Society of America, 117(5):3319–3324, 2005. doi: 10.1121/1.1886388.

[48] Ory Schnitzer and Richard V. Craster. Bloch waves in an arbitrary two-dimensional lattice of subwavelength Dirichlet scatterers. SIAM Journal on Applied Mathematics, 77(6):2119–2135, 2017. doi: 10.1137/17M112658X.

[49] Mario Lázaro, Vicent Romero-García, Richard Wiltshaw, and Richard V. Craster. Dispersion relations of generalized one-dimensional phononic crystals. Proceedings of the Royal Society A: Mathematical, Physical and Engineering Sciences, 481(2302): 20250210, 2025. doi: 10.1098/rspa.2025.0210.

[50] M. Lázaro, R. Wiltshaw, R. V. Craster, and L. M. García-Raffí. Analytical approximations for multiple scattering in one-dimensional waveguides with small inclusions. Mechanical Systems and Signal Processing, 224:112046, 2025. doi: 10.1016/j.ymssp.2024.112046.

[51] M. Lázaro, R. Wiltshaw, R. V. Craster, and V. Romero-García. Wave propagation in beams with multiple resonators: conditions for weak scattering and the Born approximation. Journal of Sound and Vibration, 618:119277, 2025. doi: 10.1016/j.jsv.2025.119277.

[52] Jari Kaipio and Erkki Somersalo. Statistical and Computational Inverse Problems, volume 160 of Applied Mathematical Sciences. Springer, New York, 2004. ISBN 0-387-22073-9.

[53] R C Asher. Ultrasonic sensors in the chemical and process industries. Journal of Physics E: Scientific Instruments, 16(10):959, 1983. doi: 10.1088/0022-3735/16/10/004.

[54] Amitosh Dash, Willian Hogendoorn, and Christian Poelma. Ultrasonic particle volume fraction profiling: an evaluation of empirical approaches. Experiments in Fluids, 62(4):85, 2021. doi: 10.1007/s00348-020-03132-0.

[55] Gerhard Kristensson and Niklas Wellander. Multiple scattering by a collection of randomly located obstacles distributed in a dielectric slab, chapter 25. Advances in Mathematical Methods for Electromagnetics, 2020. doi: 10.1049/SBEW528E_ch25.

[56] Alverède Simon, Régis Wunenburger, and Tony Valier-Brasier. Propagation of coherent shear waves in scattering elastic media. Physical Review E, 103(L051001), 2021. doi: 10.1103/PhysRevE.103.L051001.

[57] Alverède Simon, Quentin Baudis, Régis Wunenburger, and Tony Valier-Brasier. Propagation of elastic waves in correlated dispersions of resonant scatterers. The Journal of the Acoustical Society of America, 155(6):3627–3638, 2024. doi: 10.1121/10.0026233.

[58] Tony Valier-Brasier, Adrien Rohfritsch, Ludovic Alhaïtz, and Jean-Marc Conoir. Fabry–pérot resonances of acoustic waves in disordered slabs. Applied Physics Letters, 125(4):041704, 07 2024. doi: 10.1063/5.0220808.

[59] Hsiao Mun Lee, Yuting Hua, Zhaomeng Wang, Kian Meng Lim, and Heow Pueh Lee. A review of the application of active noise control technologies on windows: Chal-

lenges and limitations. Applied Acoustics, 174:107753, 2021. ISSN 0003-682X. doi: 10.1016/j.apacoust.2020.107753.

[60] Arun Arjunan, Ahmad Baroutaji, John Robinson, Aaron Vance, and Abul Arafat. Acoustic metamaterials for sound absorption and insulation in buildings. Building and Environment, 251:111250, 2024. ISSN 0360-1323. doi: 10.1016/j.buildenv.2024.111250.

[61] Fudong Fan. Band gap. Encyclopedia Britannica, 2025. URL https://www.britannica.com/science/band-gap.

[62] Junxiang Fan, Lei Zhang, Shuaishuai Wei, Zhi Zhang, Seung-Kyum Choi, Bo Song, and Yusheng Shi. A review of additive manufacturing of metamaterials and developing trends. Materials Today, 50:303–328, 2021.

[63] Smith M. J. A., Cotterill P. A., Nigro D., Parnell W. J., and Abrahams I. D. Asymptotics of the meta-atom: plane wave scattering by a single helmholtz resonator. Phil. Trans. R. Soc. A, 380, 2022. doi: 10.1098/rsta.2021.0383.

[64] Smith Michael J. A. and Abrahams I. David. Tailored acoustic metamaterials. Part I. Thin- and thick-walled helmholtz resonator arrays. Proc. R. Soc. A, 478, 2022. doi: 10.1098/rspa.2022.0124.

[65] Smith Michael J. A. and Abrahams I. David. Tailored acoustic metamaterials. Part II. Extremely thick-walled helmholtz resonator arrays. Proc. R. Soc. A, 478, 2022. doi: 10.1098/rspa.2022.0125.

[66] P. A. Martin, A. Maurel, and W. J. Parnell. Estimating the dynamic effective mass density of random composites. The Journal of the Acoustical Society of America, 128 (2):571–577, 08 2010. doi: 10.1121/1.3458849.

[67] Daniel Torrent and José Sánchez-Dehesa. Acoustic metamaterials for new two-dimensional sonic devices. New Journal of Physics, 9(9):323, 2007. doi: 10.1088/1367-2630/9/9/323.

Chapter 2

Acoustic waves in a halfspace material filled with random particulate

PAULO S. PIVA, KEVISH K. NAPAL, ART L. GOWER

Declaration of Authorship and Publication Status

This chapter is a substantially identical reproduction of a published article.

Publication Details:
Piva, P. S., Napal, K. K., & Gower, A. L. (2024). Acoustic waves in a halfspace material filled with random particulate. *New Journal of Physics*, *26*, 123033.

DOI: https://doi.org/10.1088/1367-2630/ad9ed0

Statement of Contribution:

As the primary author, my specific contributions to this published work were: conceptualization, formal analysis, investigation, methodology, project administration, writing code, producing all figures, writing the original draft, review and editing.

My co-authors contributed by providing primary supervision, support in the coceptualisation and investigation, and critical review/editing of the manuscript.

Abstract

Particulate materials include a wide range of materials, such as powders, emulsions, composites, and many others. Measuring these materials has become important for both industry and scientific applications. For industrial applications, the greatest need is to measure dense particulates, in situ, and non-destructively, to ensure production standards and quality control in processes without the need for dilution in a lab environment. In theory, this could be achieved with acoustics: the standard method is to send an acoustic wave through the particulate and then attempt to measure the effective wave speed and attenuation. This method has led to the famous results of ECAH theory, and the Lloyd-Berry formula; however, a major obstacle here is that it is not clear how to relate the effective wave speed and attenuation to the reflection and transmission coefficients for a broad frequency range. This is because it has been very difficult to mathematically account for different background media. In this paper, we resolve this obstacle. To help comprehension, we present how to account for different background media for a simple case: a halfspace filled with a random particulate, where the background of the halfspace is different from the exterior medium. The key to solving this problem was to derive a systematic extension of a widely used closure approximation: the quasi-crystalline approximation, which assumes a specific family of correlations between pairs of particles to simplify scattering equations. We present some numerical results to demonstrate that the reflection coefficient can be easily calculated for a broad range of frequencies and particle properties.

2.1 Introduction

Particulate materials are composed of small particles embedded in a continuous medium, like a powder in air, emulsions such as oil droplets in water, or air bubbles appearing in boiling water. Many applications, for example sensing, require a descriptive model of particulate materials. The positions of the particles are disordered and are either not known or cannot be completely controlled. Therefore, the most important features of particulate materials are statistical, such as the average particle size or inter-particle distance.

Sensing. Non-destructive measurements of particle size and properties can be achieved using wave scattering (acoustic, electromagnetic or elastic) [1–4]. Characterising, or mon-

itoring, the particles is needed to ensure quality, or can be used in feedback loops during production or manufacturing. As the particles can change position (or even properties) in time, to obtain a reliable measurement, experiments need to be repeated many times to then compute the average wave response. This average response depends only on the statistical properties, such as average concentration and particle size, which are usually the most important features for industrial applications. Mathematically, the result of averaging over measurements in time (or space) can be equivalent to a procedure called ensemble averaging, which we use in this work, see [5–7] for details.

Broad frequency range. To sense the size of particles, we need to consider a broad range of frequencies, so that the wavelengths are comparable to the particle size. It is not enough to develop a theory for only the low frequency limit, as in this limit, it is not possible to sense particle size distribution. For example, in the long wavelength limit (low frequency) for acoustics [8], the material is completely described by two numbers: the effective density and effective bulk modulus [9]. So, in terms of sensing, to learn more than just two numbers from a wave experiment, we need to consider shorter wavelengths.

Effective Waves Method. As we need a broad range of frequencies, we make use of a method called the *Effective Waves Method* [10–12], which can account for wave scattering in dense or sparse particulate materials for a broad range of frequencies (see [13] for phase diagrams). This method accounts for multiple scattering between all particles and provides a way to perform sensitivity studies on a wide range of parameters, such as particle size distribution and volume fraction.

Different background media. When using the Effective Waves Method to design ways to sense particles, we came across a significant barrier: it is not clear how to calculate the average scattering when the source comes from a medium which is different from the background medium of the particles. An example is shown in Figure 2.1, which depicts an emulsion (particles in a fluid) travelling along a metal pipe. The pipe material is different from the background fluid. There have been work and experiments in the literature that consider the case of different background media [15–17], but the expressions used do not come from first principles calculations. We discuss this further in the literature review below. To design robust sensing methods, we need to account for these different media, which is the main goal of this paper. After significant calculations from first principles, we arrive at a simple strategy which will lead to more robust sensing methods.

Quasi-crystalline approximation. To solve for all orders of multiple scattering between particles, on average, one needs to use a closure approximation [18, 19]. The most standard closure assumption to account for scattering between particles is called the Quasi-Crystalline Approximation (QCA) [20–22]. We derive a consistent extension to

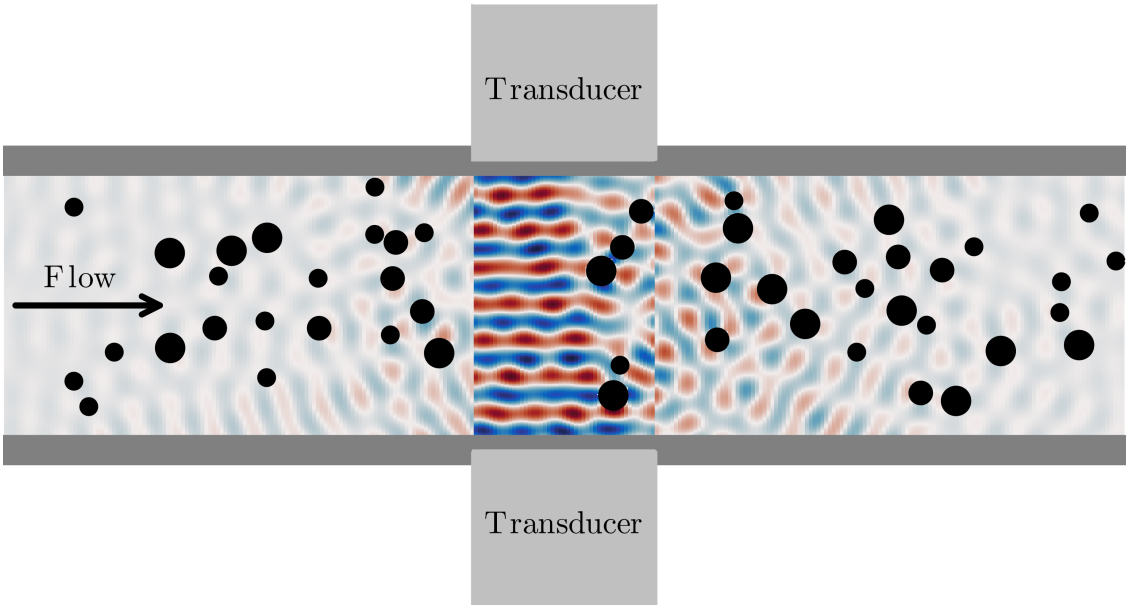

Figure 2.1: Shows the cross-section of a pipe, with a fluid flowing in the direction of the black arrow. Particles are suspended in the fluid, represented by black circles. A pair of transducers (acoustic sensors) is attached to the pipe walls. One transducer emits waves and measures their reflection, while the other measures the transmitted wave. This illustration is just a pictorial representation. For any real applications, particles would be much smaller and more numerous. The figure was generated in Julia with the MultipleScattering.jl library [14].

QCA (named X-QCA) to also account for scattering between particles and interfaces. To summarise, X-QCA accounts for the same scattering orders as QCA and leads to simpler calculations. For clarity, we consider only a simple case: plane wave incidence on a halfspace filled with random particles (see Figure 2.4), and only for acoustic wave scattering.

Further applications. Other than sensing, accounting for scattering between layers and particles can lead to improved design of: graded particulate materials [23] and disordered metamaterials with tailored frequency response. Disordered particulate materials can be far simpler to manufacture on a large scale, because the exact positioning of the particles does not need to be carefully controlled, as it does in most periodic metamaterials.

A brief literature review. Most of the work done in particulates and composites is focused on the low frequency limit, for example [24], or for broader frequencies but with only one background medium [8, 25–27].

Recent work on acoustic scattering by random composite media has been carried out by John R. Willis [28–30], in which a broad frequency response is considered. According to [28], the model framework is based on elasticity [31], and it describes wave scattering (acoustic or elastic) from a halfspace formed by three distinct phases. Compared to Fig-

ure 2.3 later in the text, one phase would be represented by the exterior medium (blue), the second could be thought of as the matrix (yellow), and the last as the particles (black circles). However, the distribution of each phase in the halfspace is given in terms of a two-point correlation function, and not by placing particles as shown in Figures 2.1 and 2.3. To solve the resulting equations, Willis assumed two of the phases have the same bulk modulus in [30]. In this paper, we do not impose any restrictions on the acoustic properties of the three phases.

In this work, we follow a first principles approach similar to [32], which accounts for all orders of multiple scattering. To solve for the average reflected and transmitted waves, Kristensson and Wellander [32] used the standard QCA (for scattering between particles) and specialised to either a low particle volume fraction or low frequency. In contrast, in this paper, we do not need to specialise to a low particle volume fraction or low frequency and reach solutions which are easier to compute and are, in principle, as accurate. To achieve this we deduce an extension of the quasi-crystalline approximation (X-QCA), which simplifies the scattering between particles and walls.

Summary of the paper. In Section 2.1.1, we introduce an overview of how to account for multiple scattering between particles and interfaces for the average wave in materials with random microstructure. In Section 2.2, we define the setup of a plane wave incident on a halfspace filled with particles. In Section 2.3 we explicitly write the system of equations of the problem for acoustic scattering of waves for one configuration of particles. In Section 2.4 we define the probability density of each realisation, and all the statistical assumptions used throughout the paper. In Section 2.5 we compute the average of the total pressure field and apply boundary conditions on the interface between the different media in the halfspace. In Section 2.6, we use X-QCA to determine the average of the backscattering operator to make a clear connection with the strategy introduced in Section 2.1.1. In Section 2.7, we derive X-QCA, which can be used in the presence of different background media. In Section 2.8, we apply the Effective Waves Method and present the numerical results achieved.

2.1.1 Overview of the strategy

In this section, we show how to intuitively deduce wave scattering from a random particulate in the presence of different background media. We do this for the simplest scenario: plane wave scattering. After this section, we deduce rigorously the results presented here.

Let $\boldsymbol{r} = (x, y, z)$ be a position in $\mathbb{R}^3$. Consider a homogeneous acoustic halfspace, which

we call the background matrix, occupying the region $z > 0$, in $\mathbb{R}^3$, which is filled with a random complex material.

Consider another homogeneous acoustic halfspace $z < 0$ which has different properties to the background matrix in $z > 0$. From the region $z < 0$, an incident plane wave propagates in the positive z direction, given by

$$u_{\text{in}}(\boldsymbol{r}) = G\mathrm{e}^{\mathrm{i}kz}$$

with $k > 0$ being the wavenumber of the $z < 0$ region.

Surprisingly, to describe the average transmitted and reflected waves due to the incident plane wave is not straightforward, and arguably unsolved when considering all the multiple scattering between the interface and the embedded random medium. During our work, we realised a simple, intuitive trick to arrive at the same results achieved by the first principles calculations. The idea is to use what is already known: the solution of an average reflected plane wave from a complex material that is embedded in just one homogeneous medium. To use this solution, we consider an artificial region $0 < z < \delta$ which is homogeneous and has the same properties as the background matrix. See Figure 2.2a for an illustration.

For just one realisation of the complex material, i.e. the deterministic case, the total acoustic field is given by

$$u_{\text{tot}}(\boldsymbol{r}) = \begin{cases} G\mathrm{e}^{\mathrm{i}kz} + R\mathrm{e}^{-\mathrm{i}kz} + \varepsilon_-(\boldsymbol{r}), & z < 0 \\ A\mathrm{e}^{\mathrm{i}k_0 z} + B\mathrm{e}^{-\mathrm{i}k_0 z} + \varepsilon_+(\boldsymbol{r}), & 0 < z < \delta \end{cases} \tag{2.1}$$

where k_0 is the wavenumber of the region $0 < z < \delta$, and $G, R, A, B \in \mathbb{C}$ are the amplitudes of the: incident plane wave, reflected plane wave, and two transmitted plane waves, respectively. The terms $\varepsilon_\pm(\boldsymbol{r})$ represent the non-planar contribution from the random material. This non-planar contribution will be zero later when taking an ensemble average over the random variables.

We can calculate the unknown amplitudes by applying standard transmission boundary conditions across $z = 0$, which require continuity of the pressure field and the normal component of the material velocity. These boundary conditions are given by

$$\begin{cases} u_{\text{tot}}(\boldsymbol{r}) \text{ is continuous at } z = 0, \\ \dfrac{1}{\rho(\boldsymbol{r})}\dfrac{\partial}{\partial z} u_{\text{tot}}(\boldsymbol{r}) \text{ is continuous at } z = 0, \end{cases} \tag{2.2}$$

where $\rho(\boldsymbol{r})$ represents the density of either the background medium or the random com-

posite material.

Let us attempt to use (2.2) to deduce the average reflection. To describe averages, we introduce the random variable σ to denote one realisation (or configuration) of this random material. For example, in a material composed of small particles σ represents one possible configuration of the particles and their acoustic properties, see Figure 2.2b. In this sense, the ensemble average $\langle\circ\rangle$ gives the average of $\circ$ over all possible realisations σ. Later, we will define this in detail.

Returning to (2.1), we know that on average $\langle\varepsilon_{\pm}(\boldsymbol{r})\rangle = 0$ due to planar symmetry. Performing the ensemble average of both sides of (2.1) then leads to

$$\langle u_{\text{tot}}(\boldsymbol{r})\rangle = \begin{cases} G\mathrm{e}^{\mathrm{i}kz} + \langle R\rangle \mathrm{e}^{-\mathrm{i}kz}, & z < 0, \\ \langle A\rangle \mathrm{e}^{\mathrm{i}k_0 z} + \langle B\rangle \mathrm{e}^{-\mathrm{i}k_0 z}, & 0 < z < \delta, \end{cases}$$

where $\langle G\rangle = G$ because the incident wave is the same for each realisation σ. Figure 2.2a shows how each plane wave contributes to the average field. The goal is to first solve the case shown in Figure 2.2a and then take the limit $\delta \to 0$ to reach the solution of the case shown in Figure 2.2b.

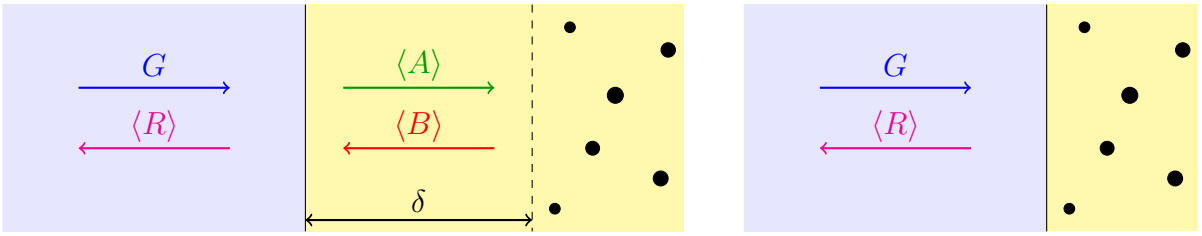

(a) Case $\delta > 0$ (b) Case $\delta \to 0$

Figure 2.2: An illustration of the amplitudes of different plane waves. The blue on the left is the homogeneous halfspace from where the source (G) originates, and the reflected wave ($\langle R\rangle$) heads into. The region on the right of both (a) and (b) with the particles is a homogeneous matrix with an embedded random complex material (shown as particles here). The middle of (a) is a yellow layer with thickness δ, which is homogeneous, and has the same properties as the background matrix of the halfspace filled with particles.

Taking an ensemble average on both sides of the boundary conditions (2.2), after some algebra, results in

$$\begin{cases} \langle R\rangle = \zeta_R\, G + \zeta_T\, \langle B\rangle, \\ \langle A\rangle = \gamma_0 \zeta_T\, G - \zeta_R\, \langle B\rangle, \end{cases} \tag{2.3}$$

with ζ_R, ζ_T and γ_0 being constants that depend on the material properties of the background media and are provided in Section 2.5.2.

With the system (2.3), we have 3 unknowns: $\langle R\rangle$, $\langle B\rangle$, $\langle A\rangle$, but only 2 equations. We

need another equation. We can obtain another equation by knowing how the particles themselves reflect a plane wave. The transmitted wave with amplitude A is reflected, in some sense, by the particulate material in the region $z > \delta$, and creates the reflected wave with amplitude B. This reflection is linear and can be represented by some scalar $\mathbb{T}_\sigma$ such that

$$\mathbb{T}_\sigma A := B. \tag{2.4}$$

We call $\mathbb{T}_\sigma$ the backscattering operator, and it depends on each realisation σ. See [10, 22] for examples of the average of this operator.

The main issue now is that taking an ensemble average on both sides of (2.4) results in

$$\langle B \rangle = \langle \mathbb{T}_\sigma A \rangle, \tag{2.5}$$

which does provide another equation, but also delivers another unknown $\langle \mathbb{T}_\sigma A \rangle$, which cannot be written directly in terms of $\langle A \rangle$. This is because the waves A and B have been reflected between the complex random material and the interface at $z = 0$, so both of these waves do depend on the realisation σ. If the background matrix medium (yellow) was the same as the exterior (blue) medium, both shown in Figure 2.2, then A would be the incident wave ($A = G$) and we would have $\langle \mathbb{T}_\sigma A \rangle = \langle \mathbb{T}_\sigma \rangle A$, as the incident wave does not depend on the realisation σ.

To resolve this, it is normal to assume a closure relation [18, 19]. The simplest and most commonly used is a naive mean field approximation [33], given by

$$\langle B \rangle = \langle \mathbb{T}_\sigma A \rangle \approx \langle \mathbb{T}_\sigma \rangle \langle A \rangle. \tag{2.6}$$

At first, this approximation may appear crude. However, we will show in this paper that (2.6) is equivalent to the Quasi-crystalline approximation (QCA). Therefore, when QCA is assumed, it would not be useful (or consistent) to use a more accurate approximation than (2.6).

The main goal of this work is to show that closure approximations of the form (2.6) can be deduced from first principles when using the same assumptions as QCA. Beyond just scattering by a halfspace, our approach leads to a general strategy to calculate (on average) multiple scattering between random particles and different background media.

2.2 Setting of the problem

Our aim is to describe wave scattering from a halfspace,

$$\mathcal{R} := \left\{ \boldsymbol{r} = (x, y, z) \in \mathbb{R}^3 \,|\, z \geq 0 \right\},$$

filled with particles. For simplicity, we restrict ourselves to spherical particles, however this approach can be easily extended for other particle shapes [34]. The region that all particles occupy is denoted by $\mathcal{P} \subset \mathcal{R}$, which is the union of non-overlapping homogeneous spheres with radius $a > 0$, sound speed $c_s \in \mathbb{C}$ and density $\varrho_s \in \mathbb{R}$[1].

We call the region in between all the particles, $\mathcal{R} \setminus \mathcal{P}$, the matrix, and the region $z < 0$ the exterior medium, from where the incident wave originates. See Figure 2.3 for an illustration. The exterior medium has a speed of sound $c \in \mathbb{R}$ and density $\varrho \in \mathbb{R}$, while the matrix has homogeneous acoustic properties, $c_0 \in \mathbb{R}$ and $\varrho_0 \in \mathbb{R}$.

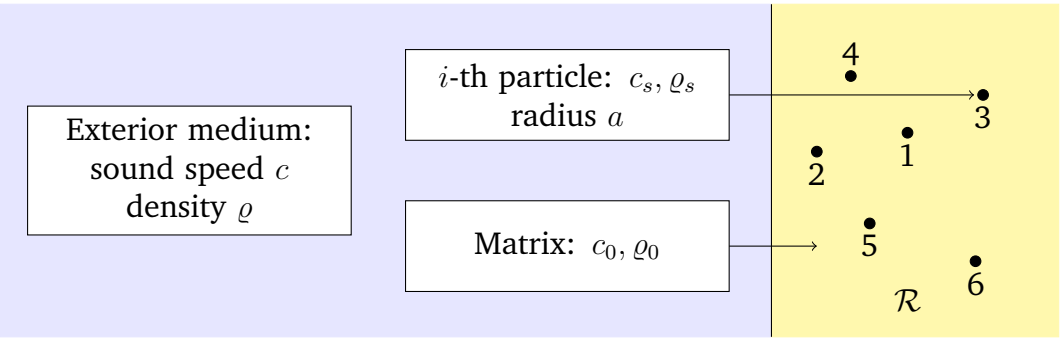

Figure 2.3: Cross-section of a homogeneous halfspace $\mathcal{R}$, filled with homogeneous spherical particles. The set of all points in particles is denoted by $\mathcal{P}$. The acoustic properties of each medium (sound speed and density) are specified, together with particle radius.

The pressure field in the frequency domain is denoted by u_{tot} and it satisfies the following Helmholtz equations:

$$\begin{aligned} \nabla^2 u_{\text{tot}}(\boldsymbol{r}) + k^2 u_{\text{tot}}(\boldsymbol{r}) &= 0, \quad \text{for} \quad \boldsymbol{r} \notin \mathcal{R}, \\ \nabla^2 u_{\text{tot}}(\boldsymbol{r}) + k_0^2 u_{\text{tot}}(\boldsymbol{r}) &= 0, \quad \text{for} \quad \boldsymbol{r} \in \mathcal{R} \setminus \mathcal{P}, \end{aligned}$$

where $\omega \in \mathbb{R}$ is the angular frequency, $k := \omega/c$ is the wavenumber for the exterior medium (blue region), $k_0 := \omega/c_0$ is the wavenumber for the matrix (yellow region). There are two types of boundaries for the Helmholtz equations above: the interface between the exterior medium and the matrix $\partial\mathcal{R}$, and the interface between the matrix and each particle $\partial\mathcal{P}$.

[1] It is not difficult to generalize all results presented here for the polydisperse case, where each particle can have a different radius, sound speed and density. The procedure is explained in Chapter 3.

As discussed in Section 4.1, we apply transmission boundary conditions on all interfaces, ensuring continuity of pressure and normal material velocity.

The total field in the exterior region equals the incident wave plus a reflected field,

$$u_{\text{tot}}(\boldsymbol{r}) = u_{\text{in}}(\boldsymbol{r}) + u_{\text{rf}}(\boldsymbol{r}) = G\mathrm{e}^{\mathrm{i}\boldsymbol{k}\cdot\boldsymbol{r}} + u_{\text{rf}}(\boldsymbol{r}), \quad \boldsymbol{r} \notin \mathcal{R}, \tag{2.7}$$

where $G \in \mathbb{C}$ is the incident plane wave amplitude, and $\boldsymbol{k} = (k_x, k_y, k_z)$ its wavevector, with $|\boldsymbol{k}| = k = \omega/c$ and $k_z > 0$. The reflected field u_{rf} is complicated and has no symmetry. We describe it in more detail in Section 2.3.

2.3 One configuration of particles

Solving any wave scattering from one configuration of spheres in the matrix is a difficult problem [32, 35], and as far as we know, there is no efficient semi-analytic solution for it. In this section, we formulate the basic equations for one configuration, which we use to study the ensemble average system.

We define the spherical solutions of the Helmholtz equation $\mathrm{u}_{\boldsymbol{n}}$ and $\mathrm{v}_{\boldsymbol{n}}$ (with $\boldsymbol{n} = (\ell, m)$, $\ell \in \mathbb{Z}_+$, $m = -\ell, \ldots, \ell$), defined as

$$\begin{aligned}
\mathrm{u}_{\boldsymbol{n}}(k\boldsymbol{r}) = \mathrm{u}_{(\ell,m)}(k\boldsymbol{r}) &:= \mathrm{h}_\ell(kr)\mathrm{Y}_{\boldsymbol{n}}(\hat{\boldsymbol{r}}),\\
\mathrm{v}_{\boldsymbol{n}}(k\boldsymbol{r}) = \mathrm{v}_{(\ell,m)}(k\boldsymbol{r}) &:= \mathrm{j}_\ell(kr)\mathrm{Y}_{\boldsymbol{n}}(\hat{\boldsymbol{r}}),
\end{aligned}$$

where (r, θ, ϕ) are the spherical coordinates of $\boldsymbol{r} \in \mathbb{R}^3$; $\hat{\boldsymbol{r}}$ is the unit vector in the direction of $\boldsymbol{r}$; $\mathrm{Y}_{\boldsymbol{n}}(\hat{\boldsymbol{r}})$ are the spherical harmonic functions defined in Appendix 2.B; j_ℓ are spherical Bessel functions and h_ℓ are spherical Hankel functions, both of the first kind.

Within the matrix, and outside the particles, the field can be written as a regular wave plus the waves scattered from each particle u^i_{sc} in the form

$$\begin{aligned}
u_{\text{tot}}(\boldsymbol{r}) &= u_{\text{reg}}(\boldsymbol{r}) + \sum_{i=1}^{J} u^i_{\text{sc}}(\boldsymbol{r})\\
&= \sum_{\boldsymbol{n}} g_{\boldsymbol{n}}\mathrm{v}_{\boldsymbol{n}}(k_0\boldsymbol{r}) + \sum_{i=1}^{J}\sum_{\boldsymbol{n}} f^i_{\boldsymbol{n}}\mathrm{u}_{\boldsymbol{n}}(k_0\boldsymbol{r} - k_0\boldsymbol{r}_i), \quad \text{for} \quad \boldsymbol{r} \in \mathcal{R} \setminus \mathcal{P},
\end{aligned} \tag{2.8}$$

where $\boldsymbol{r}_i$ is the position of the center of the i-th particle. The summations over the bold index $\boldsymbol{n}$ are performed as defined in Appendix 2.A. Figure 2.4 makes use of an arrow diagram to illustrate how waves scatter for one configuration of particles in the matrix.

Two types of waves contribute to the regular field $u_{\text{reg}}(\boldsymbol{r})$: 1) the waves scattered

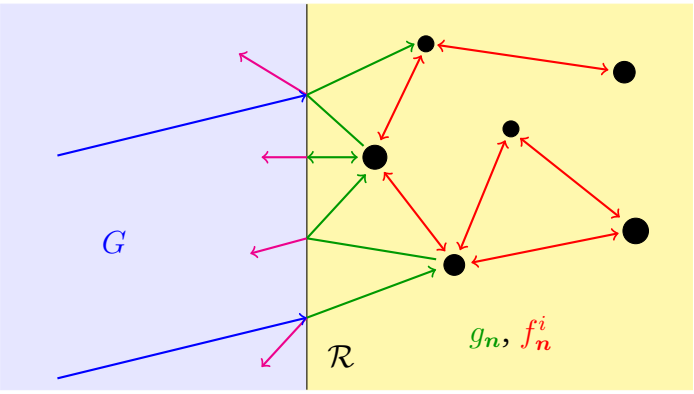

Figure 2.4: Shows the different waves that are scattered from, and arrive at, the particles and the boundary of $\mathcal{R}$. Each arrow identifies where the wave was generated and what it excites. The colour of each arrow indicates which term of equations (2.7) and (2.8) it is associated with. Magenta arrows represent the reflected field outside $\mathcal{R}$.

between the boundary $\partial\mathcal{R}$ and the particles, and 2) the transmission of the incident field into the matrix. As $u_{\text{reg}}(\boldsymbol{r})$ contains no sources, it is smooth in $\mathcal{R} \setminus \mathcal{P}$, and can therefore be expressed in terms of regular spherical waves.

We can use the boundary conditions on each of the particles to establish a relation between $g_{\boldsymbol{n}}$ and the $f_{\boldsymbol{n}}^i$. To achieve this, we define the field that excites the i-th particle $u_{\text{exc}}^i(\boldsymbol{r})$. This exciting wave is the sum of the waves scattered from all J particles different from the i-th particle and the background regular field:

$$\begin{aligned} u_{\text{exc}}^i(\boldsymbol{r}) &:= u_{\text{reg}}(\boldsymbol{r}) + \sum_{\substack{j=1 \\ j\neq i}}^{J} u_{\text{sc}}^j(\boldsymbol{r}) \\ &= \sum_{\boldsymbol{n}} g_{\boldsymbol{n}} \mathrm{v}_{\boldsymbol{n}}(k_0\boldsymbol{r}) + \sum_{\boldsymbol{n}} \sum_{j\neq i} f_{\boldsymbol{n}}^j \mathrm{u}_{\boldsymbol{n}}(k_0\boldsymbol{r} - k_0\boldsymbol{r}_j). \end{aligned} \tag{2.9}$$

To be consistent with (2.2), the boundary conditions on each particle require continuity of the pressure field, and the normal component of the material velocity across the surface of each particle.

To apply the boundary conditions for particle i, we write (2.9) in a basis of spherical waves centred at $\boldsymbol{r}_i$ by using (2.62) from Appendix 2.A, which leads to

$$u_{\text{exc}}^i(\boldsymbol{r}) = \sum_{\boldsymbol{n}\boldsymbol{n}'} \left[g_{\boldsymbol{n}} \mathcal{V}_{\boldsymbol{n}\boldsymbol{n}'}(k_0\boldsymbol{r}_i) + \sum_{j\neq i} f_{\boldsymbol{n}}^j \mathcal{U}_{\boldsymbol{n}\boldsymbol{n}'}(k_0\boldsymbol{r}_i - k_0\boldsymbol{r}_j) \right] \mathrm{v}_{\boldsymbol{n}'}(k_0\boldsymbol{r} - k_0\boldsymbol{r}_i), \tag{2.10}$$

for $|\boldsymbol{r} - \boldsymbol{r}_i| < |\boldsymbol{r}_j - \boldsymbol{r}_i|$. Solving the boundary condition for particle i is now equivalent to applying the T-matrix, $T_{\boldsymbol{n}}$ to the terms between square brackets in (2.10), as explained in

[10, 34, 36, 37]. This procedure, called the T-matrix method, leads to

$$f_{\boldsymbol{n}}^{i} = T_{\boldsymbol{n}} \sum_{\boldsymbol{n}'} g_{\boldsymbol{n}'} \mathcal{V}_{\boldsymbol{n}'\boldsymbol{n}}(k\boldsymbol{r}_i) + T_{\boldsymbol{n}} \sum_{j\neq i} \sum_{\boldsymbol{n}'} f_{\boldsymbol{n}'}^{j} \mathcal{U}_{\boldsymbol{n}'\boldsymbol{n}}(k_0\boldsymbol{r}_i - k_0\boldsymbol{r}_j), \tag{2.11}$$

where the expression of the T-matrix for a homogeneous spherical particle is given by

$$T_{\boldsymbol{n}} = T_{(\ell,m)} = -\frac{\gamma_s \mathrm{j}_\ell'(k_0 a)\mathrm{j}_\ell(k_s a) - \mathrm{j}_\ell(k_0 a)\mathrm{j}_\ell'(k_s a)}{\gamma_s \mathrm{h}_\ell'(k_0 a)\mathrm{j}_\ell(k_s a) - \mathrm{h}_\ell(k_0 a)\mathrm{j}_\ell'(k_s a)},$$

with $\gamma_s := (\varrho_s c_s)/(\varrho_0 c_0)$ and $k_s := \omega/c_s$.

The governing equation (2.11) is a straightforward generalisation of the case of particles in only one background medium. If the material properties of the matrix were the same as the exterior medium ($\varrho = \varrho_0$ and $c = c_0$), then $g_{\boldsymbol{n}}$ would represent the incident wave, as in [10, Equation (2.7)].

Next, we need to establish a relation between the waves inside and outside the matrix; (2.11) and (2.7) respectively. Instead of directly using the boundary conditions (2.2), it is simpler to ensemble average the fields first. The averaging process will result in planar symmetry and simplify the form of (2.7) and (2.8), so that we can then apply the boundary condition at $z = 0$.

2.4 Ensemble averaging

One clear lesson from Figure 2.4 is that $g_{\boldsymbol{n}}$ and $f_{\boldsymbol{n}}^{i}$ each depends on the positions of all the particles. Despite the rich number of interactions for one specific configuration, we show how the average field over all possible configurations can be simpler.

To reach the limit of an infinite number of particles, in a mathematically consistent way, we start with a cube $\mathcal{R}_\eta^L$ with a finite number of particles J. In set notation, we have

$$\mathcal{R}_\eta^L := \big\{\boldsymbol{r}_i \in \mathbb{R}^3 \mid x_i \in (-L/2, L/2),\ y_i \in (-L/2, L/2),\ z_i \in (\eta, L+\eta)\big\}, \tag{2.12}$$

where η is chosen later to create a space between the particles and the boundary, similar to Section 2.1.1.

Now we can consider an ensemble for particles within $\mathcal{R}_\eta^L$. The probability density for the particles occupying the positions $\boldsymbol{r}_1, \boldsymbol{r}_2, \ldots, \boldsymbol{r}_J$ is given by

$$p(\boldsymbol{r}_1, \boldsymbol{r}_2, \ldots, \boldsymbol{r}_J), \tag{2.13}$$

which describes the statistical likelihood of a specific spatial configuration of all particles

within the material. Physically, (2.13) can be interpreted as a map of the microscopic structure of the material. Since we cannot know the exact position of every particle at any given moment, we treat the material as a collection (an ensemble) of many possible realisations of these positions.

The primary application of (2.13) is to calculate the ensemble average. In a real setting, this represents the acoustic wave response after the incident wave (3.4) has been scattered by a large number of different particle arrangements. By averaging these possibilities, we can predict the macroscopic behavior of the wave without knowing the position of every single particle. We define the ensemble average of any function f, which implicitly depends on the position and properties of the particles, over the configuration space as

$$\langle \mathrm{f} \rangle := \int_{\left(\mathcal{R}_\eta^L\right)^J} \mathrm{f}\, p(\boldsymbol{r}_1, \boldsymbol{r}_2, \ldots, \boldsymbol{r}_J)\, \mathrm{d}\boldsymbol{r}_1 \mathrm{d}\boldsymbol{r}_2 \ldots \mathrm{d}\boldsymbol{r}_J, \tag{2.14}$$

where a set to the power J denotes the Cartesian product with itself J times.

Rather than averaging over every possible particle configuration, we can focus on a specific subset of arrangements. This is achieved through conditional probability densities, which describe the likelihood of finding J particles at various positions given that a few specific particles (such as particle 1, or the pair 1 and 2) are locked into fixed positions ($\mathbf{r}_1$, or $\mathbf{r}_1$ and $\mathbf{r}_2$). Imagine holding one particle in place and observing how the other particles spread out around it. In the context of wave scattering, this allows us to calculate how a wave interacts with a specific particle and its immediate neighbors, accounting for the fact that particles are not just independent dots, but occupy physical space, which prevents them from overlapping. This leads us to define conditional probabilities, which read

$$\begin{aligned} p(\boldsymbol{r}_2, \ldots, \boldsymbol{r}_J | \boldsymbol{r}_1) &:= \frac{p(\boldsymbol{r}_1, \ldots, \boldsymbol{r}_J)}{p(\boldsymbol{r}_1)}, \\ p(\boldsymbol{r}_3, \ldots, \boldsymbol{r}_J | \boldsymbol{r}_1, \boldsymbol{r}_2) &:= \frac{p(\boldsymbol{r}_1, \ldots, \boldsymbol{r}_J)}{p(\boldsymbol{r}_1, \boldsymbol{r}_2)}, \end{aligned} \tag{2.15}$$

where we have used the marginalised probability functions for one and two particles, given by

$$\begin{aligned} p(\boldsymbol{r}_1) &:= \int_{\left(\mathcal{R}_\eta^L\right)^{J-1}} p(\boldsymbol{r}_1, \ldots, \boldsymbol{r}_J)\, \mathrm{d}\boldsymbol{r}_2 \ldots \mathrm{d}\boldsymbol{r}_J, \\ p(\boldsymbol{r}_1, \boldsymbol{r}_2) &:= \int_{\left(\mathcal{R}_\eta^L\right)^{J-2}} p(\boldsymbol{r}_1, \ldots, \boldsymbol{r}_J)\, \mathrm{d}\boldsymbol{r}_3 \ldots \mathrm{d}\boldsymbol{r}_J. \end{aligned}$$

These conditional probabilities (2.16) motivate the definition of both first and second

conditional ensemble averages, given by

$$\begin{aligned}\langle \mathrm{f} \rangle(\boldsymbol{r}_1) &:= \int_{\left(\mathcal{R}_\eta^L\right)^{J-1}} \mathrm{f}\; p(\boldsymbol{r}_2, \ldots, \boldsymbol{r}_J | \boldsymbol{r}_1)\; \mathrm{d}\boldsymbol{r}_2 \ldots \mathrm{d}\boldsymbol{r}_J, \\ \langle \mathrm{f} \rangle(\boldsymbol{r}_1, \boldsymbol{r}_2) &:= \int_{\left(\mathcal{R}_\eta^L\right)^{J-2}} \mathrm{f}\; p(\boldsymbol{r}_3, \ldots, \boldsymbol{r}_J | \boldsymbol{r}_1, \boldsymbol{r}_2)\; \mathrm{d}\boldsymbol{r}_3 \ldots \mathrm{d}\boldsymbol{r}_J,\end{aligned} \tag{2.16}$$

which will be used to derive the average fields in Section 2.5.

As in Section 2.1.1, we assume particles are distributed homogeneously, which implies that

$$p(\boldsymbol{r}_i) = \frac{1}{L^3} = \frac{\mathfrak{n}}{J}, \quad \text{with} \quad \mathfrak{n} := \frac{J}{L^3}. \tag{2.17}$$

We call $\mathfrak{n}$ the particle number density.

For simplicity, we assume our particles are hard spheres (non-overlapping), and make use of the approximation known as hole correction:

$$p(\boldsymbol{r}_i | \boldsymbol{r}_j) = \begin{cases} p(\boldsymbol{r}_i) \dfrac{J}{J-1}, & \text{for } |\boldsymbol{r}_i - \boldsymbol{r}_j| > 2a, \\ 0 \qquad\qquad\;\; , & \text{for } |\boldsymbol{r}_i - \boldsymbol{r}_j| \leq 2a, \end{cases} \tag{2.18}$$

where the factor $J/(J-1)$ comes from the fact that there are J particles within the cube $\mathcal{R}_\eta^L$. The need to add this extra factor in the case of a finite number of particles is explained in [38, Equation (8.1.2)].

With our choice of pair correlation (2.18), and assuming the volume of $\mathcal{R}_\eta^L$ is much larger than the volume of the particles, we conclude that the position of just one of the particles does not significantly affect the probability distribution of the other particles. In other words, we assume

$$p(\boldsymbol{r}_2, \ldots, \boldsymbol{r}_J | \boldsymbol{r}_1) \approx p(\boldsymbol{r}_2, \ldots, \boldsymbol{r}_J), \tag{2.19}$$

$$p(\boldsymbol{r}_3, \ldots, \boldsymbol{r}_J | \boldsymbol{r}_2, \boldsymbol{r}_1) \approx p(\boldsymbol{r}_3, \ldots, \boldsymbol{r}_J | \boldsymbol{r}_2). \tag{2.20}$$

Another way to arrive at these approximations is by replacing conditional probabilities with their average over all possible values of $\boldsymbol{r}_1$, and then using the definition of conditional and marginal probability distributions in (2.15) and below, which reads

$$\begin{aligned} p(\boldsymbol{r}_2, \ldots, \boldsymbol{r}_J | \boldsymbol{r}_1) &\approx \int_{\mathcal{R}_\eta^L} p(\boldsymbol{r}_2, \ldots, \boldsymbol{r}_J | \boldsymbol{r}_1) p(\boldsymbol{r}_1) \mathrm{d}\boldsymbol{r}_1 = p(\boldsymbol{r}_2, \ldots, \boldsymbol{r}_J), \\ p(\boldsymbol{r}_3, \ldots, \boldsymbol{r}_J | \boldsymbol{r}_2, \boldsymbol{r}_1) &\approx \int_{\mathcal{R}_\eta^L} p(\boldsymbol{r}_3, \ldots, \boldsymbol{r}_J | \boldsymbol{r}_2, \boldsymbol{r}_1) p(\boldsymbol{r}_1 | \boldsymbol{r}_2) \mathrm{d}\boldsymbol{r}_1 = p(\boldsymbol{r}_3, \ldots, \boldsymbol{r}_J | \boldsymbol{r}_2). \end{aligned}$$

2.5 Average fields

Our goal in this section is to describe the average scattered field close to the interface $z = 0$, so we can apply boundary conditions for the average total field. To make sure the particles do not touch the boundary at $z = 0$, as done in Section 2.1.1, we take $\eta = a + \delta$ in (2.12), see Figure 2.2a. We remind the reader that a is the radius of the particles and $\delta/a \ll 1$ is a small parameter.

We start by computing the average of the total field. We multiply equation (2.7) by (2.13), use definition (2.14) for some fixed value of L, and then integrate over all possible particle positions to obtain

$$\langle u_{\text{tot}}(\boldsymbol{r})\rangle = G\mathrm{e}^{\mathrm{i}\boldsymbol{k}\cdot\boldsymbol{r}} + \langle u_{\text{rf}}(\boldsymbol{r})\rangle, \quad \text{for} \quad \boldsymbol{r} \notin \mathcal{R}, \tag{2.21}$$

Here we have $\langle G\rangle = G$ because the incident wave is the same for every configuration of particles. Computing the average of equation (2.8) results in

$$\langle u_{\text{tot}}(\boldsymbol{r})\rangle = \langle u_{\text{reg}}(\boldsymbol{r})\rangle + \sum_{j=1}^{J}\langle u_{\text{sc}}^{j}(\boldsymbol{r})\rangle,$$

where

$$\langle u_{\text{reg}}(\boldsymbol{r})\rangle = \sum_{\boldsymbol{n}}\langle g_{\boldsymbol{n}}\rangle \mathrm{v}_{\boldsymbol{n}}(k_0\boldsymbol{r}), \quad \text{for} \quad \boldsymbol{r} \in \mathcal{R}, \tag{2.22}$$

$$\sum_{j=1}^{J}\langle u_{\text{sc}}^{j}(\boldsymbol{r})\rangle = \sum_{i=1}^{J}\sum_{\boldsymbol{n}}\int_{\mathcal{R}_{a+\delta}^{L}} \langle f_{\boldsymbol{n}}^{i}\rangle(\boldsymbol{r}_i)\mathrm{u}_{\boldsymbol{n}}(k_0\boldsymbol{r} - k_0\boldsymbol{r}_i)p(\boldsymbol{r}_i)\mathrm{d}\boldsymbol{r}_i, \tag{2.23}$$

and (2.23) is valid for $0 \le z \le \delta$. This is because if $z > \delta$ then $\boldsymbol{r}$ could be inside a particle, in which case (2.8) would not be valid. In (2.23), $\langle f_{\boldsymbol{n}}^{i}\rangle(\boldsymbol{r}_i)$ is the average of $f_{\boldsymbol{n}}^{i}$ conditional to $\boldsymbol{r}_i$ as defined in $(2.16)_1$.

In our problem, particles are indistinguishable, which enables us to use the simpler notation:

$$\langle f_{\boldsymbol{n}}\rangle(\boldsymbol{r}_i) := \langle f_{\boldsymbol{n}}^{i}\rangle(\boldsymbol{r}_i), \tag{2.24}$$

for $i = 1, 2, \ldots, J$. This notation makes it clear how to simplify the sums over particle indices. For example, substituting (2.17) and (2.24) into (2.23), leads to

$$\sum_{i=1}^{J}\langle u_{\text{sc}}^{i}(\boldsymbol{r})\rangle = \mathfrak{n}\sum_{\boldsymbol{n}}\int_{\mathcal{R}_{a+\delta}^{L}} \langle f_{\boldsymbol{n}}\rangle(\boldsymbol{r}_1)\mathrm{u}_{\boldsymbol{n}}(k_0\boldsymbol{r} - k_0\boldsymbol{r}_1)\mathrm{d}\boldsymbol{r}_1. \tag{2.25}$$

2.5.1 The infinite volume limit

We now take the limit of $L \to \infty$ so that $\mathcal{R}^L_{a+\delta}$ becomes a halfspace, and compute the ensemble average for each term of the total average field, inside and outside the matrix.

Average regular field. Because we assume particles are uniformly distributed, see equation (2.17), and due to planar symmetry of the problem, the regular field evaluated in $z > 0$, shown in (2.22), can be represented as a plane wave after averaging:

$$\lim_{L\to\infty} \langle u_{\text{reg}}(\boldsymbol{r})\rangle = \langle A\rangle \mathrm{e}^{\mathrm{i}\boldsymbol{k}_0\cdot\boldsymbol{r}} + \langle A_-\rangle \mathrm{e}^{\mathrm{i}\boldsymbol{k}_0^-\cdot\boldsymbol{r}}, \quad \text{for} \quad z \geq 0,$$

where $\boldsymbol{k}_0 = (k_{0x}, k_{0y}, k_{0z}) := \left(k_x, k_y, \sqrt{k_0^2 - k_x^2 - k_y^2}\right)$ and $\boldsymbol{k}_0^- := (k_{0x}, k_{0y}, -k_{0z})$ are the wavevectors[2] of the plane waves. Without loss of generality, we choose $\mathrm{Im}[k_{0z}] \geq 0$, which implies that $\langle A_-\rangle = 0$ to avoid an unphysical wave. This choice also allows us to represent (2.22) in terms of a single plane wave, given by

$$\lim_{L\to\infty} \langle u_{\text{reg}}(\boldsymbol{r})\rangle = \langle A\rangle \mathrm{e}^{\mathrm{i}\boldsymbol{k}_0\cdot\boldsymbol{r}}. \tag{2.26}$$

The explicit expression for $\langle A\rangle$ in terms of $\langle g_{\boldsymbol{n}}\rangle$ is given in Appendix 2.B.

Average backscattered field. Taking the limit of $L \to \infty$ for the average backscattered field (2.25) leads to

$$\lim_{\substack{J\to\infty \\ L\to\infty}} \sum_{i=1}^{J} \langle u^i_{\text{sc}}(\boldsymbol{r})\rangle = \mathfrak{n} \sum_{\boldsymbol{n}} \int_{\mathcal{R}_{a+\delta}} \langle f_{\boldsymbol{n}}\rangle(\boldsymbol{r}_1)\mathrm{u}_{\boldsymbol{n}}(k_0\boldsymbol{r} - k_0\boldsymbol{r}_1)\mathrm{d}\boldsymbol{r}_1, \tag{2.27}$$

where $\mathcal{R}_{a+\delta} := \lim_{L\to\infty} \mathcal{R}^L_{a+\delta}$ is the halfspace $z \geq a + \delta$. When taking this limit, we need to keep the particle number density $\mathfrak{n}$ fixed, which requires that $J \to \infty$ as well. The relative rate that $J \to \infty$ when $L \to \infty$ is provided by expression $(2.17)_2$, which can be rearranged as $J = \mathfrak{n}L^3$.

Less obviously, (2.27) also has a plane wave representation due to symmetry. In Appendices 2.C and 2.D we show how to rewrite (2.27) as

$$\lim_{L\to\infty} \sum_{i=1}^{\infty} \langle u^i_{\text{sc}}(\boldsymbol{r})\rangle = \langle B\rangle \mathrm{e}^{\mathrm{i}\boldsymbol{k}_0^-\cdot\boldsymbol{r}}, \quad \text{for} \quad 0 \leq z \leq \delta, \tag{2.28}$$

[2] Here we have used Snell's law to determine the components of the wavevectors for simplicity of the equations. However, this can be deduced directly from the transmission boundary conditions (2.31) in Section 2.5.2 ahead.

where the average backscattering amplitude $\langle B\rangle$ is given by

$$\langle B\rangle := \frac{2\pi\mathfrak{n}}{k_0 k_{0z}} \sum_{\ell,m} \mathrm{i}^\ell \mathrm{Y}_{(\ell,m)}(\hat{\boldsymbol{k}}_0) \int_{a+\delta}^{\infty} \langle f_{\boldsymbol{n}}\rangle(0,0,z_1)\mathrm{e}^{\mathrm{i}k_{0z}z_1}\mathrm{d}z_1, \tag{2.29}$$

where we remind the reader that $\mathrm{Y}_{(\ell,m)}$ are the spherical harmonic functions, defined in Appendix 2.B.

Average external field. By the same symmetry arguments, we know that the waves outside $\mathcal{R}$ can also be represented in terms of plane waves[2]:

$$\langle u_{\text{tot}}(\boldsymbol{r})\rangle = G\mathrm{e}^{\mathrm{i}\boldsymbol{k}\cdot\boldsymbol{r}} + \langle R\rangle \mathrm{e}^{\mathrm{i}(k_x x + k_y y - k_z z)}, \quad \text{for} \quad z \le 0 \tag{2.30}$$

where $\langle R\rangle$ is the average reflection amplitude. In Section 2.5.2, we will derive a system of equations relating the amplitudes of the different fields. This will enable us to deduce $\langle R\rangle$, which is the quantity of main interest in this paper.

2.5.2 Boundary conditions at the interface

To write down relations between the average amplitudes $\langle A\rangle$, $\langle B\rangle$ and $\langle R\rangle$, we need to impose boundary conditions at $z = 0$. We are interested in the case of homogeneous background media, so we choose transmission boundary conditions, which read

$$\begin{cases} \langle u_{\text{tot}}(\boldsymbol{r})\rangle \text{ is continuous at } z = 0, \\ \dfrac{1}{\rho(\boldsymbol{r})} \dfrac{\partial \langle u_{\text{tot}}(\boldsymbol{r})\rangle}{\partial z} \text{ is continuous at } z = 0, \end{cases} \tag{2.31}$$

where $\rho(\boldsymbol{r})$ is the density, which is a function of $\boldsymbol{r} \in \mathbb{R}^3$.

We substitute (2.26), (2.28) and (2.30) into $(2.31)_1$ at the boundary $\overline{\boldsymbol{r}} = (x, y, 0)$:

$$G\mathrm{e}^{\mathrm{i}\boldsymbol{k}\cdot\overline{\boldsymbol{r}}} + \langle R\rangle \mathrm{e}^{\mathrm{i}\boldsymbol{k}\cdot\overline{\boldsymbol{r}}} = \langle A\rangle \mathrm{e}^{\mathrm{i}\boldsymbol{k}_0\cdot\overline{\boldsymbol{r}}} + \langle B\rangle\, \mathrm{e}^{\mathrm{i}\boldsymbol{k}_0\cdot\overline{\boldsymbol{r}}}$$

Because $\boldsymbol{k}\cdot\overline{\boldsymbol{r}} = \boldsymbol{k}_0\cdot\overline{\boldsymbol{r}} = k_x x + k_y y$, the above simplifies to

$$G + \langle R\rangle = \langle A\rangle + \langle B\rangle. \tag{2.32}$$

Similar computations can be done as above, starting from $(2.31)_2$ instead of $(2.31)_1$. These result in another relation,

$$\frac{k_z}{\varrho}\left(G - \langle R\rangle\right) = \frac{k_{0z}}{\varrho_0}\left(\langle A\rangle - \langle B\rangle\right). \tag{2.33}$$

The system of equations (2.32)-(2.33) can be rearranged into

$$\langle R\rangle = \zeta_R G + \zeta_T\langle B\rangle, \quad \langle A\rangle = \gamma_0\zeta_T G - \zeta_R\langle B\rangle, \tag{2.34}$$

where the newly introduced parameters ζ_R, ζ_T, γ_0 are given by

$$\zeta_R := \frac{\varrho_0\, k_z - \varrho\, k_{0z}}{\varrho_0\, k_z + \varrho\, k_{0z}}, \quad \zeta_T := \frac{2\varrho\, k_{0z}}{\varrho_0\, k_z + \varrho\, k_{0z}}, \quad \gamma_0 := \frac{\varrho_0\, k_z}{\varrho\, k_{0z}}.$$

At this point, we have three unknowns $\langle A\rangle$, $\langle B\rangle$, and $\langle R\rangle$ and two equations (2.34). The missing equation, which will be deduced in Section 2.6, is determined by how the particles reflect waves in the region $\mathcal{R}$.

2.5.3 Single medium limit

As a sanity check, we can see how the equations (2.29) and (2.34) recover the single background medium limit. Taking the acoustic properties of the exterior medium and the matrix as the same ($c_0 = c$ and $\varrho_0 = \varrho$), we have that $\boldsymbol{k}_0 = \boldsymbol{k}$, which means $\zeta_R = 0$ and $\zeta_T = \gamma_0 = 1$. Substituting these values in (2.34) provides us with

$$\langle A\rangle = G, \quad \langle R\rangle = \langle B\rangle = \frac{2\pi\mathfrak{n}}{kk_z}\sum_{\ell,m}\mathrm{i}^\ell \mathrm{Y}_{(\ell,m)}(\hat{\boldsymbol{k}})\int_a^\infty \langle f_{(\ell,m)}\rangle(z_1)\mathrm{e}^{\mathrm{i}kz_1}\mathrm{d}z_1,$$

where we used (2.29) and took the limit $\delta \to 0$ to recover the formulas for particles distributed in a halfspace region $\mathcal{R}$, see Figure 2.2b. The above is the same formula for reflection of a halfspace as [10, Eq. (7.6)]. This means the approach is consistent with the average response of random particulate materials in the case of particles embedded in only one homogeneous medium.

2.6 Average backscattering operator

To obtain the final equation needed to determine the average amplitudes in (2.34), we follow the notation introduced in Section 2.1.1. That is, we need to find an equation relating $\langle B\rangle$ and $\langle A\rangle$ through some backscattering operator $\langle \mathbb{T}_\sigma\rangle$. This final equation comes from the microstructure, which in our case is the ensemble-averaged version of the boundary conditions of the particles (2.11).

Following the strategy of [10], we take a conditional ensemble average of (2.11) with

respect to $\boldsymbol{r}_1$, and use assumptions (2.17), (2.18), (2.24) to obtain

$$\begin{aligned}\langle f_{\boldsymbol{n}}\rangle(\boldsymbol{r}_1) = & T_{\boldsymbol{n}} \sum_{\boldsymbol{n}'} \langle g_{\boldsymbol{n}'}\rangle(\boldsymbol{r}_1)\mathcal{V}_{\boldsymbol{n}'\boldsymbol{n}}(k_0\boldsymbol{r}_1) \\ & + \mathfrak{n}\, T_{\boldsymbol{n}} \sum_{\boldsymbol{n}'} \int_{\mathcal{R}_a\setminus\mathcal{B}(\boldsymbol{r}_1,2a)} \mathcal{U}_{\boldsymbol{n}'\boldsymbol{n}}(k_0\boldsymbol{r}_1 - k_0\boldsymbol{r}_2)\langle f_{\boldsymbol{n}'}\rangle(\boldsymbol{r}_2)\mathrm{d}\boldsymbol{r}_2.\end{aligned} \tag{2.35}$$

where we used the standard Quasi-Crystalline Approximation (QCA) to substitute $\langle f_{\boldsymbol{n}}\rangle(\boldsymbol{r}_2,\boldsymbol{r}_1) = \langle f_{\boldsymbol{n}}\rangle(\boldsymbol{r}_2)$ [10].

By assuming that (2.35) has a unique solution for $\langle f_{\boldsymbol{n}}\rangle(\boldsymbol{r}_1)$ given $\langle g_{\boldsymbol{n}'}\rangle(\boldsymbol{r}_1)$, then, formally, we can use (2.35) to represent $\langle f_{\boldsymbol{n}}\rangle(\boldsymbol{r}_1)$ as

$$\langle f_{\boldsymbol{n}}\rangle(\boldsymbol{r}_1) = \sum_{\boldsymbol{n}'} \mathcal{L}^f_{\boldsymbol{n}\boldsymbol{n}'}[\langle g_{\boldsymbol{n}'}\rangle(\boldsymbol{r}_1')], \tag{2.36}$$

for some linear operator $\mathcal{L}^f_{\boldsymbol{n}\boldsymbol{n}'}$ acting on $\langle g_{\boldsymbol{n}'}\rangle(\boldsymbol{r}_1')$. This operator notation $\mathcal{L}^f_{\boldsymbol{n}\boldsymbol{n}'}$ will help to compute $\langle \mathbb{T}_\sigma\rangle$. From (2.29) we see that $\langle B\rangle$ is a linear map acting on $\langle f_{\boldsymbol{n}}\rangle$. For convenience, let us also represent (2.29) in the form $\langle B\rangle = \sum_{\boldsymbol{n}} \mathcal{L}^B_{\boldsymbol{n}}[\langle f_{\boldsymbol{n}}\rangle(\boldsymbol{r}_1)]$. Substituting (2.36) into this representation leads to

$$\langle B\rangle = \sum_{\boldsymbol{n}\boldsymbol{n}'} \mathcal{L}^B_{\boldsymbol{n}}\left[\mathcal{L}^f_{\boldsymbol{n}\boldsymbol{n}'}[\langle g_{\boldsymbol{n}'}\rangle(\boldsymbol{r}_1')]\right]. \tag{2.37}$$

It is not obvious, but (2.37) is the same as (2.5). And, just like in Section 2.1.1, when combining (2.37) with the boundary conditions (2.34), we still have too many unknowns, and a closure assumption is required. The closure assumption, which is consistent with the standard QCA, is given by

$$\begin{aligned}&\langle f_{\boldsymbol{n}}\rangle(\boldsymbol{r}_2,\boldsymbol{r}_1) = \langle f_{\boldsymbol{n}}\rangle(\boldsymbol{r}_2), \\ &\langle g_{\boldsymbol{n}}\rangle(\boldsymbol{r}_1) = \langle g_{\boldsymbol{n}}\rangle,\end{aligned} \quad \text{(X-QCA)} \tag{2.38}$$

where X-QCA stands for the eXtended Quasi-Crystalline Approximation. Below, we show how this matches the closure assumption (2.6) in the introduction. In Section 2.7 we deduce X-QCA from first principles, show why it is the consistent way to extend QCA, and provide the physical interpretation behind this approximation.

Substituting $(2.38)_2$ into (2.37), and using (2.66) from Appendix 2.B, leads to

$$\langle B\rangle = \langle \mathbb{T}_\sigma\rangle\langle A\rangle, \quad \text{with} \quad \langle \mathbb{T}_\sigma\rangle \equiv \sum_{\boldsymbol{n}\boldsymbol{n}'} \mathcal{L}^B_{\boldsymbol{n}}\left[\mathcal{L}^f_{\boldsymbol{n}\boldsymbol{n}'}[\mathrm{C}_{\boldsymbol{n}'}]\right],$$

where the coefficients $\mathrm{C}_{\boldsymbol{n}'}$ are known quantities defined in Appendix 2.B. We clearly see now how the above is equivalent to approximation (2.6) in Section 2.1.1.

Given the above, together with (2.34), we can now calculate the solution with an efficient numerical scheme shown in Section 2.8, where we use the Effective Waves Method. To summarise, we can now achieve a governing equation for the unknowns by substituting (2.37) into (2.35), and using (2.66) from Appendix 2.B, to obtain:

$$\begin{aligned}\langle f_{\boldsymbol{n}}\rangle(\boldsymbol{r}_1) = \langle A\rangle T_{\boldsymbol{n}} \sum_{\boldsymbol{n}'} \mathrm{C}_{\boldsymbol{n}'} \mathcal{V}_{\boldsymbol{n}'\boldsymbol{n}}(k_0\boldsymbol{r}_1) \\ + \mathfrak{n}\, T_{\boldsymbol{n}} \sum_{\boldsymbol{n}'} \int_{\mathcal{R}_a\setminus\mathcal{B}(\boldsymbol{r}_1,2a)} \mathcal{U}_{\boldsymbol{n}'\boldsymbol{n}}(k_0\boldsymbol{r}_1 - k_0\boldsymbol{r}_2)\langle f_{\boldsymbol{n}'}\rangle(\boldsymbol{r}_2)\mathrm{d}\boldsymbol{r}_2.\end{aligned} \tag{2.39}$$

We could now, in theory, numerically solve for the four unknowns $\langle f_{\boldsymbol{n}}\rangle(\boldsymbol{r}_1)$, $\langle A\rangle$, $\langle B\rangle$, and $\langle R\rangle$. That would be done by combining (2.39) with the boundary conditions (2.34) and the definition of $\langle B\rangle$ in terms of the $\langle f_{\boldsymbol{n}}\rangle(\boldsymbol{r}_1)$ given by (2.29), which results in a system of four equations to be solved simultaneously. However, we present a far more efficient method to solve this in Section 2.8.

2.6.1 The average reflection coefficient

With all the computations so far, we have successfully deduced the contribution to sound wave scattering due to particles (2.39) and the halfspace interface (2.34) as two separate equations, as briefed in Section 2.1.1. Then, to achieve a single equation in terms of $\langle f_{\boldsymbol{n}}\rangle$ only, we substitute $(2.34)_{(2)}$ into (2.39) to compute a single integral equation in $\langle f_{\boldsymbol{n}}\rangle(\boldsymbol{r}_1)$, which reads

$$\langle f_{\boldsymbol{n}}\rangle(\boldsymbol{r}_1) = \gamma_0\zeta_T\, T_{\boldsymbol{n}} W_{\boldsymbol{n}}(\boldsymbol{r}_1)G + T_{\boldsymbol{n}} D_{\boldsymbol{n}}(\boldsymbol{r}_1)\,[\langle f_{\boldsymbol{n}'}\rangle] - \zeta_R\, T_{\boldsymbol{n}} W_{\boldsymbol{n}}(\boldsymbol{r}_1)\langle B\rangle[\langle f_{\boldsymbol{n}'}\rangle], \tag{2.40}$$

where we have defined the particle-rescattering operator

$$D_{\boldsymbol{n}}(\boldsymbol{r})[\langle f_{\boldsymbol{n}'}\rangle] := \mathfrak{n} \sum_{\boldsymbol{n}'} \int_{\mathcal{R}_a\setminus\mathcal{B}(\boldsymbol{r},2a)} \mathcal{U}_{\boldsymbol{n}'\boldsymbol{n}}(k_0\boldsymbol{r} - k_0\boldsymbol{r}')\langle f_{\boldsymbol{n}'}\rangle(\boldsymbol{r}')\mathrm{d}\boldsymbol{r}'.$$

together with the interface coupling function to simplify the notation in (2.40)

$$W_{\boldsymbol{n}}(\boldsymbol{r}_1) := \sum_{\boldsymbol{n}'} \mathrm{C}_{\boldsymbol{n}'} \mathcal{V}_{\boldsymbol{n}'\boldsymbol{n}}(k_0\boldsymbol{r}_1) = \mathrm{C}_{\boldsymbol{n}} \mathrm{e}^{\mathrm{i}\boldsymbol{k}_0\cdot\boldsymbol{r}_1}, \tag{2.41}$$

where we used [10, eqs. (A.2) and (B.12)] to write the second equality in (2.41).

If the geometry of the matrix containing the particles is changed, the same equation (2.40) can still be used; however, the terms involving the interface coupling factor (2.41) will change. Also, the explicit equation for the boundary conditions (2.34) will not be the same. For example, if the particles were embedded in a layer of finite thickness instead of a halfspace, then the boundary conditions would involve both reflection and transmission coefficients at each interface of the slab, and the interface coupling function (2.41) would also be modified, as shown in Chapter 3.

As we shall see further on, equation (2.40) is enough to determine $\langle f_{\boldsymbol{n}} \rangle(\boldsymbol{r}_1)$, making it possible to compute the expression of the total wave outside the halfspace $\mathcal{R}$. We recall the expression for the reflection coefficient $(2.34)_{(1)}$ below:

$$\langle R \rangle = \zeta_R \, G + \zeta_T \, \langle B \rangle .$$

The first term is the reflection coefficient from a homogeneous matrix without any particles inside. Only the second term $\zeta_T \, \langle B \rangle$ carries the effects of scattering from the particles. In other words, if we knew the background material and wanted to use a reflection experiment to characterise the particles, then we should use the term $\langle R \rangle - \zeta_R \, G$ to do so.

There have been many uses of reflection coefficients from particulates in the literature, see for example [16, 17, 39]. In [17], they used approximate formulas for the reflection coefficient $(2.34)_{(1)}$ and obtained a good qualitative agreement with experimental data [17]. Having the exact formula $(2.34)_{(1)}$, calculated from first principles, would likely lead to more accurate predictions, especially for a broad frequency range, which is less understood.

2.7 Extended quasi-crystalline approximation

In this section, we explain why the eXtended Quasi-Crystalline Approximation (X-QCA) (2.38) is accurate, for low and high volume fractions of particles, and show that it is the systematic extension of the standard Quasi-Crystalline Approximation (QCA) [20] to scenarios with different background media.

To justify X-QCA (2.38) it is best to start with just one configuration of particles, as this will help us understand the role of the different waves.

We recall from Figure 2.4 that the field (2.9) which excites particle i depends on the configuration of all particles, including its own position $\boldsymbol{r}_i$. Take, for example, any wave which is initially scattered from particle i and then returns to particle i due to multiple scattering. This type of dependence is called self-interaction, and it is known in the statistical mechanics literature that accounting for self-interactions can lead to unsolvable

equations, or even divergences, when ensemble averaging [40, 41]. This is the case for any particulate material, whether there are different background media or not.

For clarity, let us introduce the notation:

$$u^1_{\text{exc}}(\boldsymbol{r};\boldsymbol{r}_1,\boldsymbol{r}_2,\ldots,\boldsymbol{r}_J) := u^1_{\text{exc}}(\boldsymbol{r}),$$

to denote the exciting field u^1_{exc}, so that we can explicitly discuss how u^1_{exc} depends on the positions $\boldsymbol{r}_j$ of each particle.

A possible strategy to simplify the self-interactions is to approximate the field exciting particle 1, for example, by its own conditional average:

$$u^1_{\text{exc}}(\boldsymbol{r};\boldsymbol{r}_1,\boldsymbol{r}_2,\ldots,\boldsymbol{r}_J) \approx \langle u^1_{\text{exc}}\rangle_1(\boldsymbol{r};\boldsymbol{r}_2,\ldots,\boldsymbol{r}_J) \tag{2.42}$$

where we used the conditional average:

$$\langle u^1_{\text{exc}}\rangle_1(\boldsymbol{r};\boldsymbol{r}_2,\ldots,\boldsymbol{r}_J) := \int_{\mathcal{R}^L_{a+\delta}} u^1_{\text{exc}}(\boldsymbol{r};\boldsymbol{r}'_1,\boldsymbol{r}_2,\ldots,\boldsymbol{r}_J)p(\boldsymbol{r}'_1|\boldsymbol{r}_2,\ldots,\boldsymbol{r}_J)\mathrm{d}\boldsymbol{r}'_1. \tag{2.43}$$

We will show how (2.42) leads to the standard QCA [20] when there is just one background medium, and it also leads to X-QCA when there are different background media and interfaces. But first, let us consider whether it is a sensible approximation.

Is the approximation (2.42) accurate? Figure 2.5 illustrates some of the possible positions $\boldsymbol{r}'_1$ of the first particle, and how they contribute to the field exciting the particle positioned at $\boldsymbol{r}_1$. We will explain why (2.42) is highly accurate for large and small particle volume fractions. We note that similar arguments have been used in [21, 42, 43].

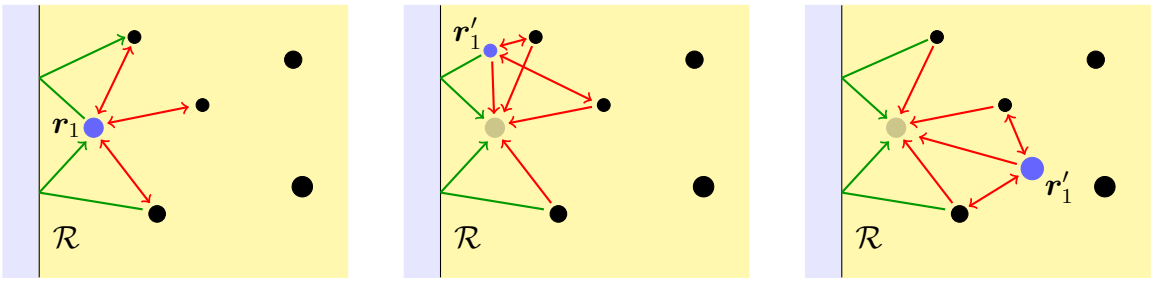

Figure 2.5: The image on the left shows how waves scattered from the particle at $\boldsymbol{r}_1$ (blue disk) contribute to the field $u^1_{\text{exc}}(\boldsymbol{r};\boldsymbol{r}_1;\ldots)$ evaluated for $\boldsymbol{r}$ close to $\boldsymbol{r}_1$. The image in the centre, and on the right, show how the exciting field $u^1_{\text{exc}}(\boldsymbol{r};\boldsymbol{r}'_1;\ldots)$, evaluated near $\boldsymbol{r}$, changes when moving particle 1 to the position $\boldsymbol{r}'_1$. Note that $\boldsymbol{r}'_1 = \boldsymbol{r}_1$ is always a feasible position, as there is no other particle at $\boldsymbol{r}_1$, and therefore the case $\boldsymbol{r}'_1 = \boldsymbol{r}_1$ always has a significant contribution in the integral (2.43) when calculating $\langle u^1_{\text{exc}}\rangle_1$.

For a small volume fraction of particles, the wave scattered from particle i will be weakly rescattered by the same particle i, as the average distances to the next particle, or interface, are large. In which case $u^1_{\text{exc}}(\boldsymbol{r};\boldsymbol{r}_1,\boldsymbol{r}_2,\ldots)$ weakly depends on the position of particle 1. From this we can deduce the approximation (2.42) by taking $u^1_{\text{exc}}(\boldsymbol{r};\boldsymbol{r}_1,\boldsymbol{r}_2,\ldots)$ out of the integral in (2.43) together with

$$\int_{\mathcal{R}^L_{a+\delta}} p(\boldsymbol{r}_1'|\boldsymbol{r}_2\ldots,\boldsymbol{r}_J)\mathrm{d}\boldsymbol{r}_1' \approx 1.$$

For a large volume fraction of particles, most of all particle positions $\boldsymbol{r}_1'$ in the integral (2.43) would be prohibitive, as the particles are densely packed together and particles cannot overlap. That is, the function $p(\boldsymbol{r}_1'|\boldsymbol{r}_2\ldots,\boldsymbol{r}_J)$ is zero when particles overlap. This is illustrated in Figure 2.5. The one region that most contributes to the integral in (2.43) is the region around the original particle position $\boldsymbol{r}_1$. An extreme example of this is a crystal, where the neighboring particles exactly determine the position of $\boldsymbol{r}_1'$ and

$$p(\boldsymbol{r}_1'|\boldsymbol{r}_2,\ldots,\boldsymbol{r}_J) = \delta(\boldsymbol{r}_1'-\boldsymbol{r}_1),$$

which substituted into (2.42) leads to $u^1_{\text{exc}}(\boldsymbol{r};\boldsymbol{r}_1,\boldsymbol{r}_2\ldots) = \langle u^1_{\text{exc}}\rangle_1(\boldsymbol{r};\boldsymbol{r}_2,\ldots)$ exactly.

The discussion above shows why (2.42) is a good approximation, which justifies why it is commonly used in the literature [12, 13, 21, 22, 26, 32, 44]. In Section 2.7.1 we show how approximation (2.42) leads to X-QCA (2.38), and therefore is equivalent to standard QCA when there is just one background medium.

2.7.1 The average exciting field

To reach X-QCA (2.38) (or the standard QCA) from the approximation (2.42), we start with the definition (2.9) for $i=1$, rename $\boldsymbol{r}_1$ to $\boldsymbol{r}_1'$, multiply both sides by $p(\boldsymbol{r}_1'|\boldsymbol{r}_2,\ldots,\boldsymbol{r}_J)$, integrate over $\boldsymbol{r}_1'$, and then use (2.43) together with the approximation (2.42) to arrive at

$$u^1_{\text{exc}}(\boldsymbol{r}) = \sum_{\boldsymbol{n}}\langle g_{\boldsymbol{n}}\rangle_1 \mathrm{v}_{\boldsymbol{n}}(k_0\boldsymbol{r}) + \sum_{\boldsymbol{n}}\sum_{j=2}^{J}\langle f^j_{\boldsymbol{n}}\rangle_1 \mathrm{u}_{\boldsymbol{n}}(k_0\boldsymbol{r}-k_0\boldsymbol{r}_j). \tag{2.44}$$

Note, in practice the only difference between (2.44) and (2.9) is that we have replaced $g_{\boldsymbol{n}}$ by $\langle g_{\boldsymbol{n}}\rangle_1$ and $f^j_{\boldsymbol{n}}$ by $\langle f^j_{\boldsymbol{n}}\rangle_1$ for $j\neq 1$.

Following the same steps as done in Sections 2.5 and 2.6, we would obtain the same

expression as in (2.35), except with the substitutions

$$\langle g_{\boldsymbol{n}}\rangle(\boldsymbol{r}_1) = \langle\langle g_{\boldsymbol{n}}\rangle_1\rangle(\boldsymbol{r}_1) \quad \text{and} \quad \langle f_{\boldsymbol{n}}\rangle(\boldsymbol{r}_2,\boldsymbol{r}_1) = \langle\langle f_{\boldsymbol{n}}\rangle_1\rangle(\boldsymbol{r}_2,\boldsymbol{r}_1),$$

we show below that these are equivalent to (2.38) for disordered particulates. Combining the definition (2.43) (with g_n in place of u^1_{exc}) with the definition (2.16) leads to

$$\begin{aligned}
\langle\langle g_{\boldsymbol{n}}\rangle_1\rangle(\boldsymbol{r}_1) &= \int g_{\boldsymbol{n}} p(\boldsymbol{r}_1'|\boldsymbol{r}_2,\ldots)p(\boldsymbol{r}_2,\ldots|\boldsymbol{r}_1)\mathrm{d}\boldsymbol{r}_1'\mathrm{d}\boldsymbol{r}_2\ldots\mathrm{d}\boldsymbol{r}_J \\
&= \int g_{\boldsymbol{n}} \frac{p(\boldsymbol{r}_1',\boldsymbol{r}_2,\ldots)}{p(\boldsymbol{r}_2,\boldsymbol{r}_3,\ldots)} p(\boldsymbol{r}_2,\boldsymbol{r}_3,\ldots|\boldsymbol{r}_1)\mathrm{d}\boldsymbol{r}_1'\mathrm{d}\boldsymbol{r}_2\ldots\mathrm{d}\boldsymbol{r}_J \\
&= \int g_{\boldsymbol{n}} p(\boldsymbol{r}_1',\boldsymbol{r}_2,\ldots)\mathrm{d}\boldsymbol{r}_1'\ldots\mathrm{d}\boldsymbol{r}_J = \langle g_{\boldsymbol{n}}\rangle,
\end{aligned} \tag{2.45}$$

where in the third line we used assumption (2.19), which is valid for a large number of disordered particles. Similarly, we have that

$$\begin{aligned}
\langle\langle f^2_{\boldsymbol{n}'}\rangle_1\rangle(\boldsymbol{r}_2,\boldsymbol{r}_1) &= \int f^2_{\boldsymbol{n}'} p(\boldsymbol{r}_1'|\boldsymbol{r}_2,\ldots)p(\boldsymbol{r}_3,\ldots|\boldsymbol{r}_2,\boldsymbol{r}_1)\mathrm{d}\boldsymbol{r}_1'\mathrm{d}\boldsymbol{r}_3\ldots\mathrm{d}\boldsymbol{r}_J \\
&= \int f^2_{\boldsymbol{n}'} \frac{p(\boldsymbol{r}_1',\ldots)}{p(\boldsymbol{r}_2,\ldots)} p(\boldsymbol{r}_3,\ldots|\boldsymbol{r}_2,\boldsymbol{r}_1)\mathrm{d}\boldsymbol{r}_1'\mathrm{d}\boldsymbol{r}_3\ldots\mathrm{d}\boldsymbol{r}_J \\
&= \int f^2_{\boldsymbol{n}'} \frac{p(\boldsymbol{r}_1',\boldsymbol{r}_3,\ldots|\boldsymbol{r}_2)}{p(\boldsymbol{r}_3.,\ldots|\boldsymbol{r}_2)} p(\boldsymbol{r}_3,\ldots|\boldsymbol{r}_2,\boldsymbol{r}_1)\mathrm{d}\boldsymbol{r}_1'\mathrm{d}\boldsymbol{r}_3\ldots\mathrm{d}\boldsymbol{r}_J \\
&= \int f^2_{\boldsymbol{n}'} p(\boldsymbol{r}_1',\boldsymbol{r}_3,\ldots|\boldsymbol{r}_2)\mathrm{d}\boldsymbol{r}_1'\mathrm{d}\boldsymbol{r}_3\ldots\mathrm{d}\boldsymbol{r}_J \\
&= \langle f^2_{\boldsymbol{n}'}\rangle(\boldsymbol{r}_2) = \langle f_{\boldsymbol{n}'}\rangle(\boldsymbol{r}_2),
\end{aligned} \tag{2.46}$$

where we repeatedly used the definition of conditional probability, and to reach the fourth line we used assumption (2.20).

The results in (2.45) and (2.46) demonstrate that approximation (2.38) is a consequence of approximation (2.42) for disordered particulates as defined in Section 2.4. Because the approximation holds for any number of particles and any size of $|\mathcal{R}^L_{a+\delta}|$, (2.38) is valid for the limit of infinite particles defined in Section 2.5.1.

An advantage of using approximations in terms of the exciting field (2.42), instead of quantities which are more directly related to the particles, such as (2.38), is that it is clear how to extend this approximation to more complex scenarios. In the presence of other geometries, layers, or multispecies [9], we can still define an exciting field, and then use (2.42) directly. It is also possible to account for more complex interactions between particles other than the pair correlation (2.18) assumed in this work. See [44, 45] for a broader discussion on how to account for different pair correlations for standard QCA.

In other words, approximation (2.42) leads to a systematic way to generalise the original QCA introduced in [20].

Beyond generalising QCA, we feel that approximation (2.42) provides more physical insight. We saw from the Section 2.7 that QCA, and its extension, only approximate the self-interaction by averaging it (conditioned on the position of the other particles). This has already been discussed for the classical QCA through a scattering series expansion [44]. As a consequence, QCA, and its extension, is only making an approximation about third-order and higher scattering[3]. This sheds light on the agreement between second-order weak scattering approximations and QCA, as discussed in [46].

Finally, we note that some work has been carried out in the literature [32], which was able to write down a closed system of equations by using the classical QCA, but without making an approximation on the regular field $\langle g_{\boldsymbol{n}} \rangle(\boldsymbol{r}_1)$. However, when using QCA, we would already be making an approximation about third-order scattering, so there is no reason to retain high-order scattering for some terms (from a wall) but not from others (particles). Further, X-QCA leads to systems which are far simpler to solve, as we demonstrate in Section 2.8.

2.8 Effective Waves Method

We use the Effective Waves Method, introduced in [10], to solve the governing equation (2.40). As shown in [10], assuming that $\langle f_{\boldsymbol{n}} \rangle$ satisfies the 3D Helmholtz equation with the effective wavenumber k_* provides a good approximation for the solution of (2.40), even for a broad range of frequencies and particle volume fractions[4]. This assumption can be written as

$$\nabla^2 \langle f_{\boldsymbol{n}} \rangle(\boldsymbol{r}_1) + k_*^2 \langle f_{\boldsymbol{n}} \rangle(\boldsymbol{r}_1) = 0 \quad \text{for} \quad \boldsymbol{r}_1 \in \mathcal{R}_a. \tag{2.47}$$

Then, by using plane wave symmetry (2.68) from Appendix 2.C, together with (2.47), we conclude that

$$\langle f_{\boldsymbol{n}} \rangle(\boldsymbol{r}_1) = F_{\boldsymbol{n}} \mathrm{e}^{\mathrm{i}\boldsymbol{k}_* \cdot \boldsymbol{r}_1}, \tag{2.48}$$

where $\boldsymbol{k}_* = (k_{*x}, k_{*y}, k_{*z}) := \left(k_x, k_y, \sqrt{k_*^2 - k_x^2 - k_z^2}\right)$. We also choose $\mathrm{Im}[k_{*z}] \geq 0$, similarly to (2.26) in Section 2.5.1.

Now, we take the limit $\delta \to 0$ to represent the case of a halfspace $\mathcal{R}$ filled with particles,

[3] An example of third-order self-interaction scattering would be: the incident wave scatters on the i-th particle, which then gets scattered by the j-th particle, and finally reaches the i-th particle again, scattering once more. See Fig. 3 in [44] for the Feynman diagrams.

[4] The general solution presented in [10] introduces multiple wavenumbers, although they show that there is usually only one dominant wavenumber k_* for most properties and frequencies. See [13] for phase diagrams that show when more than one wavenumber is needed.

as illustrated in Figure 2.2b. We also define the bulk region as done in [11]:

$$\mathcal{R}_{\text{Bulk}} := \{\boldsymbol{r}_1 \in \mathbb{R}^3 | z_1 > 2a\}. \tag{2.49}$$

Below we follow the steps shown in [11] to deduce an effective wave equation and ensemble boundary conditions. We need to redo the steps here, as having a different background medium for the matrix does lead to some important differences.

To start, we note that

$$\begin{aligned}(k_0^2 - k_*^2)\mathcal{U}_{\boldsymbol{n}'\boldsymbol{n}}(k\boldsymbol{r}_1 - k\boldsymbol{r}_2)\langle f_{\boldsymbol{n}'}\rangle(\boldsymbol{r}_2) = \\ = \mathcal{U}_{\boldsymbol{n}'\boldsymbol{n}}(k_0\boldsymbol{r}_1 - k_0\boldsymbol{r}_2)\nabla^2_{\boldsymbol{r}_2}\langle f_{\boldsymbol{n}'}\rangle(\boldsymbol{r}_2) - \langle f_{\boldsymbol{n}'}\rangle(\boldsymbol{r}_2)\nabla^2_{\boldsymbol{r}_2}\mathcal{U}_{\boldsymbol{n}'\boldsymbol{n}}(k_0\boldsymbol{r}_1 - k_0\boldsymbol{r}_2),\end{aligned} \tag{2.50}$$

for $\boldsymbol{r}_1 \in \mathcal{R}_{\text{Bulk}}$ and $\boldsymbol{r}_2 \in \mathcal{R}_a$, because $\mathcal{U}_{\boldsymbol{n}'\boldsymbol{n}}(k\boldsymbol{r}_1 - k\boldsymbol{r}_2)$ and $\langle f_{\boldsymbol{n}'}\rangle(\boldsymbol{r}_2)$ satisfy Helmholtz equations with wavenumbers k_0 and k_* respectively. Then, by integrating the right side of (2.50) over $\boldsymbol{r}_2 \in \mathcal{R}_a \backslash \mathcal{B}(\boldsymbol{r}_1, 2a)$ and using Green's second identity, we get

$$\int_{\mathcal{R}_a\backslash\mathcal{B}(\boldsymbol{r}_1,2a)} \mathcal{U}_{\boldsymbol{n}'\boldsymbol{n}}(k_0\boldsymbol{r}_1 - k_0\boldsymbol{r}_2)\langle f_{\boldsymbol{n}'}\rangle(\boldsymbol{r}_2)\mathrm{d}\boldsymbol{r}_2\mathrm{d}\lambda = \frac{\mathcal{I}_{\boldsymbol{n}'\boldsymbol{n}}(\boldsymbol{r}_1) - \mathcal{J}_{\boldsymbol{n}'\boldsymbol{n}}(\boldsymbol{r}_1)}{(k_0^2 - k_*^2)}, \tag{2.51}$$

where $\mathcal{I}_{\boldsymbol{n}'\boldsymbol{n}}(\boldsymbol{r})$ and $\mathcal{J}_{\boldsymbol{n}'\boldsymbol{n}}(\boldsymbol{r})$ are given by

$$\begin{aligned}\mathcal{I}_{\boldsymbol{n}'\boldsymbol{n}}(\boldsymbol{r}_1) &:= -F_{\boldsymbol{n}'}\int_{\partial\mathcal{R}_a} \mathcal{U}_{\boldsymbol{n}'\boldsymbol{n}}(k_0\boldsymbol{r}_1 - k_0\boldsymbol{r}_2)\frac{\partial \mathrm{e}^{\mathrm{i}\boldsymbol{k}_*\cdot\boldsymbol{r}_2}}{\partial z_2} - \frac{\partial \mathcal{U}_{\boldsymbol{n}'\boldsymbol{n}}(k_0\boldsymbol{r}_1 - k_0\boldsymbol{r}_2)}{\partial z_2}\mathrm{e}^{\mathrm{i}\boldsymbol{k}_*\cdot\boldsymbol{r}_2}\mathrm{d}S_2, \\ \mathcal{J}_{\boldsymbol{n}'\boldsymbol{n}}(\boldsymbol{r}_1) &:= F_{\boldsymbol{n}'}\int_{\partial\mathcal{B}(\boldsymbol{0},2a)} \mathcal{U}_{\boldsymbol{n}'\boldsymbol{n}}(-k_0\boldsymbol{r}')\frac{\partial \mathrm{e}^{\mathrm{i}\boldsymbol{k}_*\cdot(\boldsymbol{r}'+\boldsymbol{r}_1)}}{\partial z} - \frac{\partial \mathcal{U}_{\boldsymbol{n}'\boldsymbol{n}}(-k_0\boldsymbol{r}')}{\partial z}\mathrm{e}^{\mathrm{i}\boldsymbol{k}_*\cdot(\boldsymbol{r}'+\boldsymbol{r}_1)}\mathrm{d}S',\end{aligned}$$

with $\mathrm{d}S_2$ and $\mathrm{d}S'$ being the area elements. Also, in the second line of the above, we have performed the change of coordinates $\boldsymbol{r}_2 \to \boldsymbol{r}' + \boldsymbol{r}_1$.

We substitute expression (2.51) into (2.40) to reach

$$\langle f_{\boldsymbol{n}}\rangle(\boldsymbol{r}_1) = T_{\boldsymbol{n}}W_{\boldsymbol{n}}(\boldsymbol{r}_1)(\gamma_0\zeta_T G - \zeta_R\langle B\rangle) + \mathfrak{n}\frac{T_{\boldsymbol{n}}}{k_0^2 - k_*^2}\sum_{\boldsymbol{n}'}\left(\mathcal{I}_{\boldsymbol{n}'\boldsymbol{n}}(\boldsymbol{r}_1) - \mathcal{J}_{\boldsymbol{n}'\boldsymbol{n}}(\boldsymbol{r}_1)\right), \tag{2.52}$$

and we notice that $\langle f_{\boldsymbol{n}}\rangle(\boldsymbol{r}_1)$ and $\mathcal{J}_{\boldsymbol{n}'\boldsymbol{n}}(\boldsymbol{r}_1)$ satisfy the Helmholtz equation with wavenumber k_*, while $W_{\boldsymbol{n}}(\boldsymbol{r}_1)$ and $\mathcal{I}_{\boldsymbol{n}'\boldsymbol{n}}(\boldsymbol{r}_1)$ satisfy the Helmholtz equation with wavenumber k_0.

Because $k_0 \neq k_*$, see [10, Appendix C], we can split (2.52) into

$$\langle f_{\boldsymbol{n}} \rangle(\boldsymbol{r}_1) + \mathfrak{n} \sum_{\boldsymbol{n}'} \frac{T_{\boldsymbol{n}}}{k_0^2 - k_*^2} \mathcal{J}_{\boldsymbol{n}'\boldsymbol{n}}(\boldsymbol{r}_1) = 0, \tag{2.53}$$

$$W_{\boldsymbol{n}}(\boldsymbol{r}_1) \left(\gamma_0 \zeta_T G - \zeta_R \langle B \rangle\right) + \frac{\mathfrak{n}}{k_0^2 - k_*^2} \sum_{\boldsymbol{n}'} \mathcal{I}_{\boldsymbol{n}'\boldsymbol{n}}(\boldsymbol{r}_1) = 0. \tag{2.54}$$

Equation (2.53) is called the ensemble wave equation, and it is identical to [10, eq. (4.7)], which is expected because (2.53) is fully determined by the microstructure of the particulate material and not the exterior medium.

Equation (2.54) is similar to the ensemble boundary conditions in [10, eq. 4.8]. However, (2.54) has one extra term representing the interaction between particles and the interface of the halfspace at $z = 0$.

Following the same steps as in [10], one can use (2.53) to write down the following eigensystem for the eigenpair $(k_*, F_{\boldsymbol{n}})$:

$$F_{\boldsymbol{n}} + 8\pi a T_{\boldsymbol{n}} \sum_{\boldsymbol{n}', \boldsymbol{n}_1} \frac{c_{\boldsymbol{n}'\boldsymbol{n}\boldsymbol{n}_1}}{k_*^2 - k_0^2} \mathrm{i}^{-\ell_1} \mathrm{Y}_{\boldsymbol{n}_1}(\hat{\boldsymbol{k}}_*) \mathrm{N}_{\ell_1}(2k_0 a, 2k_* a) \mathfrak{n} F_{\boldsymbol{n}'} = 0, \tag{2.55}$$

with $\boldsymbol{n}_1 = (\ell_1, m_1)$ and $c_{\boldsymbol{n}\boldsymbol{n}'\boldsymbol{n}_1}$ defined in Appendix 2.A as (2.63). The expression for N_ℓ is given by

$$\mathrm{N}_\ell(x, y) := x \mathrm{h}_\ell'(x) \mathrm{j}_\ell(y) - y \mathrm{h}_\ell(x) \mathrm{j}_\ell'(y). \tag{2.56}$$

where we remind the reader that h_ℓ and j_ℓ are the spherical Hankel and Bessel functions of the first kind respectively.

2.8.1 Normalisation condition

The solution of (2.55) provides the effective wavenumber k_*; however, the eigenvectors $F_{\boldsymbol{n}}$ are determined only up to a multiplicative factor. The ensemble boundary condition (2.54) is needed to find a normalisation condition for $F_{\boldsymbol{n}}$, and fully determine the average field amplitude. To do so, we start by substituting (2.41) and [10, Eq. (7.10)] into (2.54), leading to

$$\mathrm{C}_{\boldsymbol{n}} \mathrm{e}^{\mathrm{i}\boldsymbol{k}_0 \cdot \boldsymbol{r}_1} \left(\gamma_0 \zeta_T G - \zeta_R \langle B \rangle\right) = \mathrm{C}_{\boldsymbol{n}} \mathrm{e}^{\mathrm{i}\boldsymbol{k}_0 \cdot \boldsymbol{r}_1} \frac{\mathfrak{n}}{k_0^2 - k_*^2} \sum_{\boldsymbol{n}'} \mathrm{K}_{\boldsymbol{n}'}(a) F_{\boldsymbol{n}'}, \tag{2.57}$$

where we defined

$$\mathrm{K}_{(\ell',m')}(a) := \frac{2\pi \mathrm{i}}{k_0 k_{0z}}(-\mathrm{i})^{\ell'}\mathrm{Y}_{(\ell',m')}(\hat{\boldsymbol{k}}_0)(k_{*z}+k_{0z})\mathrm{e}^{\mathrm{i}(k_{*z}-k_{0z})a}.$$

Then, we substitute (2.48) into (2.29) to write down

$$\langle B\rangle = -\frac{2\pi\mathfrak{n}}{k_0 k_{0z}}\frac{\mathrm{e}^{\mathrm{i}(k_{*z}+k_{0z})a}}{\mathrm{i}(k_{*z}+k_{0z})}\sum_{(\ell,m)}\mathrm{i}^{\ell}\mathrm{Y}_{(\ell,m)}(\hat{\boldsymbol{k}}_0)F_{(\ell,m)}, \tag{2.58}$$

and we remind the reader we have already taken the limit $\delta \to 0$ at the beginning of Section 2.8.

Then, we substitute (2.58) into (2.57) and divide both sides by $\mathrm{C}_{\boldsymbol{n}}\mathrm{e}^{\mathrm{i}\boldsymbol{k}_0\cdot\boldsymbol{r}_1}$ to obtain

$$\gamma_0\zeta_T G + \zeta_R\frac{2\pi\mathfrak{n}}{k_0 k_{0z}}\frac{\mathrm{e}^{\mathrm{i}(k_{*z}+k_{0z})a}}{\mathrm{i}(k_{*z}+k_{0z})}\sum_{\boldsymbol{n}'}\mathrm{i}^{\ell'}\mathrm{Y}_{\boldsymbol{n}'}(\hat{\boldsymbol{k}}_0)F_{\boldsymbol{n}'} = \frac{\mathfrak{n}}{k_0^2-k_*^2}\sum_{\boldsymbol{n}'}\mathrm{K}_{\boldsymbol{n}'}(a)F_{\boldsymbol{n}'},$$

where $\boldsymbol{n}' = (\ell', m')$.

Finally, we gather the terms which contain $F_{\boldsymbol{n}'}$ on the left-hand side to write down the following normalisation condition:

$$\sum_{\boldsymbol{n}'}\mathrm{M}_{\boldsymbol{n}'}F_{\boldsymbol{n}'} = \gamma_0\zeta_T G, \tag{2.59}$$

where

$$\mathrm{M}_{(\ell',m')} := \frac{\mathfrak{n}}{k_0^2-k_*^2}\mathrm{K}_{(\ell',m')}(a) - \zeta_R\frac{2\pi\mathfrak{n}}{k_0 k_{0z}}\frac{\mathrm{e}^{\mathrm{i}(k_{*z}+k_{0z})a}}{(k_{*z}+k_{0z})}\mathrm{i}^{\ell'-1}\mathrm{Y}_{(\ell',m')}(\hat{\boldsymbol{k}}_0).$$

This normalisation condition is the last equation needed to numerically calculate the eigenvectors $F_{\boldsymbol{n}}$, and together with k_*, they determine all the average amplitudes $\langle B\rangle$, $\langle R\rangle$ and $\langle A\rangle$ through equations (2.29) and (2.34) respectively.

2.8.2 High frequency limit

As a side quest, here we deduce that, in the high frequency limit, the average reflection coefficient $\langle R\rangle$ does not depend on the particle properties. In fact, $\langle R\rangle$ is just the reflection from the matrix itself without particles in this limit. Results for high frequency, such as this, are not very common or well understood in the literature.

We start by defining the volume fraction of particles as

$$\phi := \frac{|\mathcal{P}|}{|\mathcal{R}_a|} = \frac{4\pi a^3}{3}\mathfrak{n}. \tag{2.60}$$

Substituting (2.60) into (2.58), one can deduce that

$$\begin{aligned} |\langle B\rangle| =& \frac{3}{2}\frac{\phi\, \mathrm{e}^{-\mathrm{Im}[k_{*z}]a}}{(k_0a)(k_{0z}a)|k_{*z}+k_{0z}|a}\left|\sum_{(\ell,m)} \mathrm{i}^{\ell}\mathrm{Y}_{(\ell,m)}(\hat{\boldsymbol{k}}_0)F_{(\ell,m)}\right| \\ \leq& \frac{3}{2}\frac{\phi\, \mathrm{e}^{-\mathrm{Im}[k_{*z}]a}}{(k_0a)(k_{0z}a)|k_{*z}+k_{0z}|a}\sum_{\boldsymbol{n}}\left|\mathrm{Y}_{\boldsymbol{n}}(\hat{\boldsymbol{k}}_0)\right||F_{\boldsymbol{n}}|\,, \end{aligned} \tag{2.61}$$

which we will use to show that $|\langle B\rangle| \to 0$ when $ka \to \infty$.

Next, we write down the following relations between wavenumbers

$$k_0 = \frac{c}{c_0}k,\ k_{0z} = \sqrt{\left(\frac{c}{c_0}\right)^2 k^2 - k_x^2 - k_y^2},$$

from which we conclude that $k_0a \to \infty$ and $k_{0z}a \to \infty$ when $ka \to \infty$ for a fixed angle of incidence. Using these limits in (2.61), we conclude that $\langle B\rangle \to 0$ with one added assumption: the absolute value of the eigenvectors $|F_{\boldsymbol{n}}|$ does not increase indefinitely for higher frequencies. This is reasonable because the norm of $F_{\boldsymbol{n}}$ is linked to the amplitude of the incident wave through the boundary condition (2.54), though we have not been able to demonstrate this formally.

In other words, the response from the particles averages to zero due to incoherence for high frequency, and the reflected wave sees only an empty halfspace with just the background matrix:

$$\langle R\rangle \to \zeta_R G.$$

It is possible to use this result to help calibrate an experimental measurement. As mentioned in the previous section, if we wish to use $\langle B\rangle$ to characterise the particles, we need to subtract $\zeta_R G$ from the average reflection coefficient $\langle R\rangle$. If the background matrix properties are not known, one could perform scattering experiments while increasing the frequency until the reflected wave response stops changing. At this point, the reflection coefficient would equal $\zeta_R G$.

2.8.3 Numerical results

In this section, we present some examples of numerical computations of the eigensystem (2.55) and the normalisation condition (2.59), using the Julia library [47]. The main purpose of these numerical results is to show that the system is easily solvable for broad frequencies and volume fractions. We also demonstrate how sensitive reflection is to average particle size, which could be useful for designing characterisation experiments. All

infinite summations over double indices defined in Appendix 2.A were truncated at $\ell = 2$ for numerical computations. This truncation provides a finite eigenvalue problem, which is solved numerically. We not that the choice of truncation at $\ell = 2$ is enough to achieve convergence in the examples shown below; however, truncation at higher orders may be needed to achieve accurate results for different numerical examples.

These calculations performed in Julia provide the effective wavenumber k_* and the eigenvectors $F_{\boldsymbol{n}}$. We substitute the expressions for k_* and $F_{\boldsymbol{n}}$ into (2.58) to calculate the average backscattered amplitude $\langle B \rangle$, and then substitute $\langle B \rangle$ into $(2.34)_2$ to calculate the average reflection coefficient $\langle R \rangle$. To show how general the model is, and also provide some insight into the physics of the problem, we present three examples with very different material properties.

Case 1. We consider that the matrix is water, the exterior medium is a solid with acoustic properties $c = 3c_0$ and $\varrho = 3\varrho_0$, and particles are some gas with $c_s = c_0/100$ and $\varrho_s = \varrho_0/100$. The reflection coefficients $\langle R \rangle$ are presented in Figure 2.6 for the case of volume fraction $\phi = 10\%$.

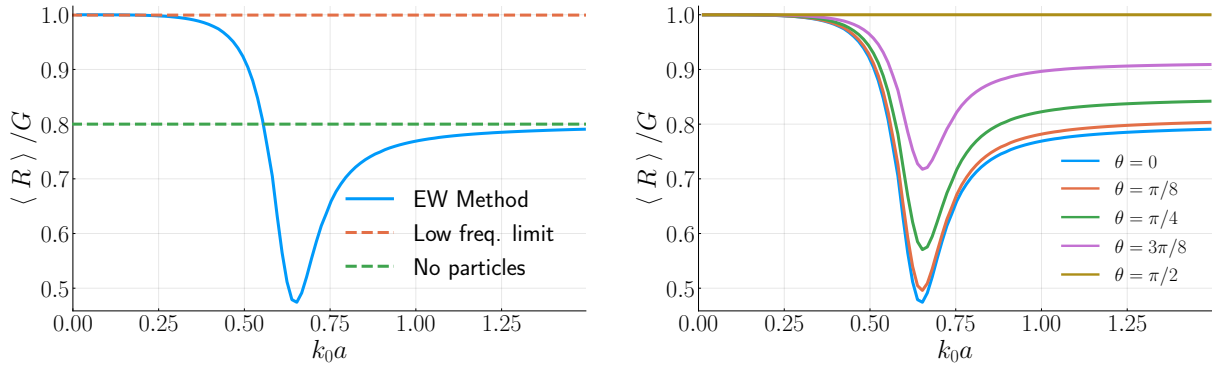

(a) Normal incidence

(b) Varying angle of incidence

Figure 2.6: Numerical computations of the average reflection coefficient $\langle R \rangle$ divided by the incident wave amplitude G by using the Effective Waves Method ("EW Method"). The particles are bubbles of gas in water ($c_s = c_0/100$, $\varrho_s = \varrho_0/100$) with volume fraction $\phi = 10\%$. The horizontal axis is the dimensionless frequency $k_0 a$, and θ is the angle of incidence. On the left, the plane wave incidence is normal ($k_x = k_y = 0$), while on the right the angle of incidence is varying ($k_x \geq 0$, $k_y = 0$). The dashed lines represent the low frequency limit response and the reflection without any particles in the matrix. The exterior medium is a solid ($c = 3c_0$, $\varrho = 3\varrho_0$).

In Figure 2.6, the low frequency limit is computed with the formulas provided in [10], and the reflection coefficient of a homogeneous halfspace with no particles is given by $R = \zeta_R G$. The agreement between low frequency limit and the Effective Waves Method for $ka \ll 1$ is a good sanity check for the formulas for the normalisation condition (2.59).

Three main results can be obtained from Figure 2.6: 1) The average reflection is sensitive to particle radius, with a drop of more than 50% in Figure 2.6a if varying radius a for a fixed frequency ω; 2) we have numerical evidence that the high frequency limit matches the case with no particles; and 3) changing the angle of incidence in Figure 2.6b only makes reflection less sensitive to particle radius. The last result suggests that normal incidence should be the optimal strategy to sense particle size if $\langle R \rangle$ can be measured with only one angle of incidence.

Case 2. We consider that the matrix is a solid medium ($c_0 = 3c$ and $\varrho_0 = 3\varrho$), and the exterior medium is water. In this case, we choose solid inclusions in the matrix such that $c_s = 10c$ and $\varrho_s = 10\varrho$, and we vary the angle of incidence by rotating the wavevector $\boldsymbol{k}$ of the incident plane wave in (2.7). Note that the wavenumber $k = |\boldsymbol{k}|$ does not change when the wavevector is rotated. The results are presented in Figure 2.7.

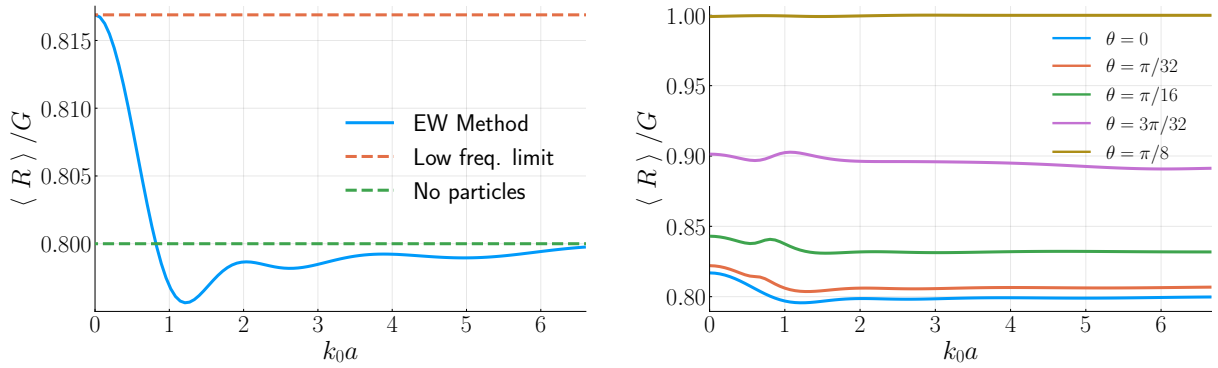

(a) Normal incidence

(b) Varying angle of incidence

Figure 2.7: Numerical computations for dimensionless average reflection using the Effective Waves Method ("EW Method"). The exterior medium is water, and the matrix is solid ($c_0 = 3c$, $\varrho_0 = 3\varrho$). The particles are solid inclusions ($c_s = 10c$, $\varrho_s = 10\varrho$) with volume fraction $\phi = 10\%$. The horizontal axis is the dimensionless frequency $k_0 a$, and θ is the angle of incidence. On the left, the plane wave incidence is normal ($k_x = k_y = 0$), while on the right, the angle of incidence varies ($k_x \geq 0$, $k_y = 0$). The dashed lines represent the low frequency limit response and the reflection without any particles in the matrix.

In this case 2, Figure 2.7 shows the same qualitative behaviour as in Figure 2.6. However, two observations must be made: 1) the average reflection is less sensitive to particle radius, with only a drop of about 3% in Figure 2.7a when varying radius a for a fixed frequency ω; and 2) in Figure 2.7b, total reflection happens for angle of incidence θ bigger than the critical angle for the homogeneous matrix without particles, given by

$$\theta_c = \arcsin\left(\frac{c}{c_0}\right),$$

which for case 2 is equal to $\theta_c \approx 0.34\text{rad} < \pi/8$.

Case 3. To study how reflection changes when varying the volume fraction of particles, defined in (2.60), we compute the average reflection coefficient for hard solid particles in water, $c_s = 100c$ and $\varrho_s = 100\varrho_0$. We take the exterior medium as a softer solid ($c = 3c_0$ and $\varrho = \varrho_0$). The results are presented in Figure 2.8.

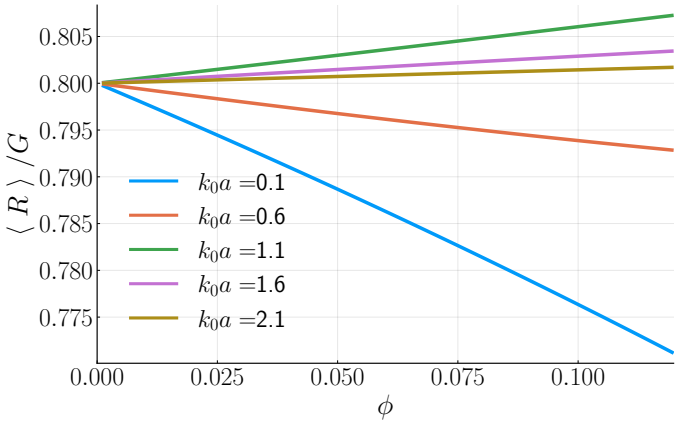

Figure 2.8: Numerical computations for dimensionless average reflection using the Effective Waves Method ("EW Method"). We have a hard powder in water ($c_s = 100c_0$, $\varrho_s = 100\varrho$) for some values of dimensionless frequent k_0a. The horizontal axis is the volume fraction ϕ. The plane wave incidence is normal ($k_x = k_y = 0$) and the exterior medium is a solid ($c = 3c_0$, $\varrho = 3\varrho_0$).

Figure 2.8 shows that the dependence of $\langle R \rangle$ on volume fraction is approximately linear, suggesting that a first-order expansion — as used in ECAH theory [48, 49] — is accurate for particle size measurements under these conditions. Combining this linear effective wavenumber expansion with our reflection coefficient formulas should provide a valid approach for particle sizing experiments across a broad frequency range. We also notice that the slope of the curves in Figure 2.8 is sensitive to radius a, which may be useful for sensing methods for the particle size distribution.

Conclusions

In this work, we solve an open challenge on how to calculate sound wave scattering from particles embedded in a matrix with different acoustic properties than the exterior medium. It seems we are the first to reach simple solvable equations, while retaining the same order of approximation as in the Quasi-Crystalline Approximation (QCA) [20]. The QCA is one of the most successful approximations that captures multiple scattering between particles [21, 22, 26].

The method we develop can be applied to any material geometry, but for simplicity, we

explore the simplest case in this paper: plane wave incidence on a halfspace.

Theoretical results. The key to solve for more than one background medium was to reformulate the QCA in terms of an approximation involving the field that excites each particle, as shown in (2.42). This reformulation shows that QCA is equivalent to averaging over self-interactions for all orders of multiple scattering. A similar interpretation has been noted before by [44] by comparing QCA with a diagrammatic approximation given by Twersky [45]. However, unlike the Twersky approximation, QCA does not discard any scattering contributions if defined as $(2.38)_{(1)}$ or (2.42). Instead, QCA averages over self-interactions. Our calculations confirm that, for a big class of ensembles presented in Section 2.4, QCA is exact up to second-order scattering, as demonstrated in [46].

Our reformulation of QCA enabled us to reach simple, solvable equations for the case of multiple background media. We call the extension of QCA to multiple media the eXtended Quasi-Crystalline Approximation (X-QCA). Using X-QCA leads to significant simplification in comparison to methods that use only QCA [32], and is applicable for a broad range of frequencies and particle properties.

Numerical results. To exemplify how the method works for a broad range of frequencies, volume fractions and material properties, we present explicit computations of the average reflection coefficient $\langle R \rangle$ in Section 2.8.3. We show numerically that the average reflection coefficient can be sensitive to particle radius, depending on the material properties. This result can contribute to the development of sensing methods for particle size distribution of powders, emulsions, porous materials or slurries.

We also give numerical evidence that, in the high-frequency limit, there is no coherent reflection due to particles. This means the high-frequency response can be used as calibration for equipment that uses the reflection coefficient to take measurements of particle scattering. If such measurements are not available, the simple measurement of reflected waves from the matrix with no particles can also be used as calibration, see discussion in Section 2.6.1.

Possible generalisations. The model presented makes use of the Effective Waves Method [10], which allows any geometry or acoustic properties. The same procedure in this work can be used to compute the average wave scattering by a compact material filled with particles. On top of that, our method can be easily applied to any linear wave, including electromagnetic and elastic waves.

Model restrictions. To simplify the equations and reach attainable numerical solutions, we have not considered any thermal-viscous effects, or elastic properties of solid particles in this work. On top of that, when the volume fraction gets higher, the particles may experience complex mechanical interactions between each other, leading to a differ-

ent pair correlation function than the hole correction (2.18). However, QCA (and X-QCA) can be extended to capture these effects [12, 26, 50], and the same procedure explored in this work can be used to study more complex scenarios.

Future work. The method introduced here is not a mere theoretical curiosity. It is a necessary step before reaching quantifiable methods to measure particles in many areas of science and engineering. It is needed because, in almost any sensor setup, there will be different background media. To account for these media, and calculate the average reflection and transmission, one would need our results. A simple example is illustrated in Figure 2.1, which involves a particulate flowing through a pipe past a sensor. In other words, a clear future avenue is to use the results here to develop sensors to predict the statistical properties of particulates from the measured reflection and transmission.

Other future avenues include extending our models to capture viscoelastic and thermal effects [48–50], or validating our method (X-QCA) against high-fidelity Monte Carlo simulations and experimental data. Another interesting step is to apply our results to design layered media containing particulates, as these can form functionally graded materials [23], which have applications in many areas like aerospace engineering, nuclear energy, optics, and others [51].

Acknowledgements

The authors would like to acknowledge Aristeidis Karnezis, Brandon O'Connell and Gerhard Kristensson for their insightful discussions. Paulo Piva gratefully acknowledges funding from an EPSRC Case studentship with Johnson Matthey. Kevish Napal and Art Gower gratefully acknowledge support from EPSRC (EP/V012436/1).

Appendices

2.A Addition translation matrices

Here, we provide the notation for addition translation matrices for spherical Bessel waves. For a translation $\boldsymbol{d}$ ($\boldsymbol{y} = \boldsymbol{x} + \boldsymbol{d}$), we have

$$\begin{aligned} \mathrm{v}_{\boldsymbol{n}}(\boldsymbol{y}) &= \sum_{\boldsymbol{n}'} \mathcal{V}_{\boldsymbol{n}\boldsymbol{n}'}(\boldsymbol{d})\mathrm{v}_{\boldsymbol{n}'}(\boldsymbol{x}) \quad \forall\, \boldsymbol{x}, \boldsymbol{d} \in \mathbb{R}^3, \\ \mathrm{u}_{\boldsymbol{n}}(\boldsymbol{y}) &= \sum_{\boldsymbol{n}'} \mathcal{V}_{\boldsymbol{n}\boldsymbol{n}'}(\boldsymbol{d})\mathrm{u}_{\boldsymbol{n}'}(\boldsymbol{x}) \quad \text{for } |\boldsymbol{x}| > |\boldsymbol{d}|, \\ \mathrm{u}_{\boldsymbol{n}}(\boldsymbol{y}) &= \sum_{\boldsymbol{n}'} \mathcal{U}_{\boldsymbol{n}\boldsymbol{n}'}(\boldsymbol{d})\mathrm{v}_{\boldsymbol{n}'}(\boldsymbol{x}) \quad \text{for } |\boldsymbol{x}| < |\boldsymbol{d}|, \end{aligned} \tag{2.62}$$

where the summations over double indices $\boldsymbol{n} = (\ell, m)$ represent double sums defined as

$$\sum_{\boldsymbol{n}} := \sum_{\ell=0}^{\infty} \sum_{m=-\ell}^{\ell}.$$

The addition translation matrices $\mathcal{V}_{\boldsymbol{n}\boldsymbol{n}'}(\boldsymbol{d})$ and $\mathcal{U}_{\boldsymbol{n}\boldsymbol{n}'}(\boldsymbol{d})$ are given by [10, eq. (B.3)]

$$\mathcal{V}_{\boldsymbol{n}\boldsymbol{n}'}(\boldsymbol{d}) = \sum_{\boldsymbol{n}_1} c_{\boldsymbol{n}\boldsymbol{n}'\boldsymbol{n}_1} \mathrm{v}_{\boldsymbol{n}_1}(\boldsymbol{d}) \quad \text{and} \quad \mathcal{U}_{\boldsymbol{n}\boldsymbol{n}'}(\boldsymbol{d}) = \sum_{\boldsymbol{n}_1} c_{\boldsymbol{n}\boldsymbol{n}'\boldsymbol{n}_1} \mathrm{u}_{\boldsymbol{n}_1}(\boldsymbol{d}),$$

where $\mathrm{u}_{\boldsymbol{n}_1}$ and $\mathrm{v}_{\boldsymbol{n}_1}$ are defined in the beginning of Section 2.3, and the coefficients $c_{\boldsymbol{n}\boldsymbol{n}'\boldsymbol{n}_1}$ are defined as

$$c_{\boldsymbol{n}\boldsymbol{n}'\boldsymbol{n}_1} := 4\pi \mathrm{i}^{\ell'-\ell+\ell_1} \int_{\Omega} \mathrm{Y}_{\boldsymbol{n}}(\hat{\boldsymbol{r}}) \mathrm{Y}^*_{\boldsymbol{n}'}(\hat{\boldsymbol{r}}) \mathrm{Y}^*_{\boldsymbol{n}_1}(\hat{\boldsymbol{r}}) \mathrm{d}\hat{\boldsymbol{r}}, \tag{2.63}$$

where Ω is the unit sphere, $\mathrm{Y}_{\boldsymbol{n}}(\hat{\boldsymbol{r}})$ are the spherical harmonic functions defined in Appendix 2.B, and $\mathrm{Y}^*_{\boldsymbol{n}}(\hat{\boldsymbol{r}})$ are their complex conjugates.

2.B Regular spherical to plane waves

In this section, we determine the expression that connects the spherical Bessel waves representation of the regular field (2.22) with its planar wave representation (2.26). These expressions are only valid after the $L \to \infty$ limit in Section 2.5.1. For that, we will use the following definition for the spherical harmonics

$$\mathrm{Y}_{(\ell,m)}(\hat{\boldsymbol{r}}) := (-1)^m \sqrt{\frac{2\ell+1}{4\pi}\frac{(\ell-m)!}{(\ell+m)!}}\mathrm{P}_\ell^m(\cos\theta)\mathrm{e}^{\mathrm{i}m\phi},$$

where P_ℓ^m are the usual associated Legendre polynomials.

We equate the averaged field expressed in both spherical Bessel (2.22) and planar representations (2.26), having in mind that we chose k_{0z} such that $\langle A_- \rangle = 0$. This results in

$$\langle A \rangle \mathrm{e}^{\mathrm{i}\boldsymbol{k}_0\cdot\boldsymbol{r}} = \sum_{\boldsymbol{n}} \langle g_{\boldsymbol{n}} \rangle \mathrm{v}_{\boldsymbol{n}}(k_0\boldsymbol{r}).$$

Then, we substitute the planar wave expansion in terms of spherical Bessel waves, given by

$$\mathrm{e}^{\mathrm{i}\boldsymbol{k}\cdot\boldsymbol{r}} = 4\pi \sum_{\ell=0}^{\infty}\sum_{m=-\ell}^{\ell} \mathrm{i}^\ell \overline{\mathrm{Y}_{(\ell,m)}}(\hat{\boldsymbol{k}})\mathrm{v}_{(\ell,m)}(k\boldsymbol{r}), \tag{2.64}$$

where the overline denotes complex conjugation. The final step is to use the orthogonality relations of the spherical harmonics, which leads to

$$\langle g_{\boldsymbol{n}} \rangle = \mathrm{C}_{\boldsymbol{n}} \langle A \rangle, \tag{2.65}$$

where we have defined

$$\mathrm{C}_{(\ell,m)} := 4\pi \mathrm{i}^\ell \, \overline{\mathrm{Y}_{(\ell,m)}}(\hat{\boldsymbol{k}}_0). \tag{2.66}$$

2.C Translation symmetry

In the limit of an infinite number of particles (see Section 2.5.1), the average regular field can be represented by a plane wave, given by (2.26). Then, its dependency on x and y is given only by a known complex phase. For a general translation in the $z = 0$ plane of

$\boldsymbol{b} = x_0\hat{\boldsymbol{x}} + y_0\hat{\boldsymbol{y}}$, we have

$$\langle u_{\text{reg}}(\boldsymbol{r}+\boldsymbol{b})\rangle = \langle u_{\text{reg}}(\boldsymbol{r})\rangle \mathrm{e}^{\mathrm{i}\boldsymbol{k}_0\cdot\boldsymbol{b}} = \sum_{\boldsymbol{n}'}\langle g_{\boldsymbol{n}'}\rangle \mathrm{v}_{\boldsymbol{n}'}(k_0\boldsymbol{r})\mathrm{e}^{\mathrm{i}\boldsymbol{k}_0\cdot\boldsymbol{b}},$$
$$\langle u_{\text{reg}}(\boldsymbol{r}+\boldsymbol{b})\rangle = \sum_{\boldsymbol{n}}\langle g_{\boldsymbol{n}}\rangle \mathrm{v}_{\boldsymbol{n}}(k_0\boldsymbol{r}+k_0\boldsymbol{b}) = \sum_{\boldsymbol{n}\boldsymbol{n}'}\langle g_{\boldsymbol{n}}\rangle \mathcal{V}_{\boldsymbol{n}\boldsymbol{n}'}(k_0\boldsymbol{b})\mathrm{v}_{\boldsymbol{n}'}(k_0\boldsymbol{r}),$$

where we have used (2.22) in both equations above, and translation matrices in Appendix 2.A in the second line. Equating both lines above and using the orthogonality relations of spherical harmonics, we conclude that

$$\langle g_{\boldsymbol{n}}\rangle \mathrm{e}^{\mathrm{i}\boldsymbol{k}_0\cdot\boldsymbol{b}} = \sum_{\boldsymbol{n}'}\langle g_{\boldsymbol{n}'}\rangle \mathcal{V}_{\boldsymbol{n}'\boldsymbol{n}}(k_0\boldsymbol{b}), \tag{2.67}$$

Then, we perform the same translation of $\boldsymbol{b}$ in (2.39) to get

$$\langle f_{\boldsymbol{n}}\rangle(\boldsymbol{r}_1+\boldsymbol{b}) = T_{\boldsymbol{n}}\sum_{\boldsymbol{n}'}\langle g_{\boldsymbol{n}'}\rangle \mathcal{V}_{\boldsymbol{n}'\boldsymbol{n}}(k_0\boldsymbol{r}_1+\boldsymbol{b}) + \\ + \mathfrak{n}\, T_{\boldsymbol{n}}\sum_{\boldsymbol{n}'}\int_{\mathcal{R}_a\setminus\mathcal{B}(\boldsymbol{r}_1+\boldsymbol{b},2a)} \mathcal{U}_{\boldsymbol{n}'\boldsymbol{n}}(k_0\boldsymbol{r}_1-k_0\boldsymbol{r}_2+k_0\boldsymbol{b})\langle f_{\boldsymbol{n}'}\rangle(\boldsymbol{r}_2)\mathrm{d}\boldsymbol{r}_2.$$

We decompose the regular translation matrix into two factors (see [10, eq. (B.3)]) and perform the change of variables $\boldsymbol{r}_2 \to \boldsymbol{r}_2' = \boldsymbol{r}_2 - \boldsymbol{b}$ into the above to reach

$$\langle f_{\boldsymbol{n}}\rangle(\boldsymbol{r}_1+\boldsymbol{b}) = T_{\boldsymbol{n}}\sum_{\boldsymbol{n}'\boldsymbol{n}''}\langle g_{\boldsymbol{n}'}\rangle \mathcal{V}_{\boldsymbol{n}'\boldsymbol{n}''}(k_0\boldsymbol{b})\mathcal{V}_{\boldsymbol{n}''\boldsymbol{n}}(k_0\boldsymbol{r}_1) + \\ + \mathfrak{n}\, T_{\boldsymbol{n}}\sum_{\boldsymbol{n}'}\int_{\mathcal{R}_a\setminus\mathcal{B}(\boldsymbol{r}_1,2a)} \mathcal{U}_{\boldsymbol{n}'\boldsymbol{n}}(k_0\boldsymbol{r}_1-k_0\boldsymbol{r}_2')\langle f_{\boldsymbol{n}'}\rangle(\boldsymbol{r}_2'+\boldsymbol{b})\mathrm{d}\boldsymbol{r}_2'.$$

Finally, we substitute (2.67) in the above, leading to

$$\langle f_{\boldsymbol{n}}\rangle(\boldsymbol{r}_1+\boldsymbol{b},\lambda) = T_{\boldsymbol{n}}\sum_{\boldsymbol{n}''}\langle g_{\boldsymbol{n}''}\rangle \mathcal{V}_{\boldsymbol{n}''\boldsymbol{n}}(k_0\boldsymbol{r}_1)\mathrm{e}^{\mathrm{i}\boldsymbol{k}_0\cdot\boldsymbol{b}} + \\ + \mathfrak{n}\, T_{\boldsymbol{n}}\sum_{\boldsymbol{n}'}\int_{\mathcal{R}_a\setminus\mathcal{B}(\boldsymbol{r}_1,2a)} \mathcal{U}_{\boldsymbol{n}'\boldsymbol{n}}(k_0\boldsymbol{r}_1-k_0\boldsymbol{r}_2')\langle f_{\boldsymbol{n}'}\rangle(\boldsymbol{r}_2'+\boldsymbol{b})\mathrm{d}\boldsymbol{r}_2',$$

which is the same equation as (2.39), but written in terms of $\langle f_{\boldsymbol{n}}\rangle(\boldsymbol{r}_1+\boldsymbol{b}) = \langle f_{\boldsymbol{n}}\rangle(\boldsymbol{r}_1)\mathrm{e}^{\mathrm{i}\boldsymbol{k}_0\cdot\boldsymbol{b}}$ instead of $\langle f_{\boldsymbol{n}}\rangle(\boldsymbol{r}_1)$. Assuming the uniqueness of the solution for (2.39), one can deduce that

$$\langle f_{\boldsymbol{n}}\rangle(\boldsymbol{r}_1) = \langle f_{\boldsymbol{n}}\rangle(0,0,z_1)\mathrm{e}^{\mathrm{i}(k_x x_1 + k_y y_1)}, \tag{2.68}$$

and we have reduced the dimension of our integral equation from three to one, due to

symmetry.

2.D Outgoing spherical to plane waves

To simplify (2.27), we use (2.68) from Appendix 2.C, which leads to

$$\lim_{\substack{J\to\infty\\L\to\infty}}\sum_i\langle u^i_{\mathrm{sc}}(\boldsymbol{r})\rangle=\mathfrak{n}\sum_{\boldsymbol{n}}\int_{a+\delta}^{\infty}\langle f_{\boldsymbol{n}}\rangle(0,0,z_1)I_{\boldsymbol{n}}(\boldsymbol{r},z_1)\mathrm{d}z_1, \tag{2.69}$$

where we have defined the following quantity that can be determined analytically:

$$I_{\boldsymbol{n}}(\boldsymbol{r},z_1):=\int_{\mathbb{R}^2}\mathrm{u}_{\boldsymbol{n}}(k_0\boldsymbol{r}-k_0\boldsymbol{r}_1)\mathrm{e}^{\mathrm{i}(k_xx_1+k_yy_1)}\mathrm{d}x_1\mathrm{d}y_1,\quad z\neq z_1, \tag{2.70}$$

and results in a plane wave in the z_1 direction. To simplify (2.70), we use the following transformation formula [10, 52–55]

$$\mathrm{u}_{\boldsymbol{n}}(k_0\boldsymbol{r})=\mathrm{u}_{(\ell,m)}(k_0\boldsymbol{r})=\frac{1}{2\pi\mathrm{i}^\ell}\int_{\mathbb{R}^2}\frac{\mathrm{Y}_{\boldsymbol{n}}(\hat{\boldsymbol{q}})}{k_0q_z}\mathrm{e}^{\mathrm{i}\boldsymbol{q}\cdot\boldsymbol{r}}\mathrm{d}q_x\mathrm{d}q_y,\quad z>0,$$

where $\boldsymbol{q}=(q_x,q_y,q_z)$ with $q_x^2+q_y^2+q_z^2=k_0^2$. We substitute the above into (2.70) and perform the following calculations for $z>z_1$ as follows:

$$\begin{aligned}
I_{\boldsymbol{n}}(\boldsymbol{r},z_1)&=\frac{1}{2\pi\mathrm{i}^\ell}\int_{\mathbb{R}^2}\left[\int_{\mathbb{R}^2}\frac{\mathrm{Y}_{\boldsymbol{n}}(\hat{\boldsymbol{q}})}{k_0q_z}e^{\mathrm{i}\boldsymbol{q}\cdot(\boldsymbol{r}-\boldsymbol{r}_1)+\mathrm{i}(k_xx_1+k_yy_1)}\mathrm{d}q_x\mathrm{d}q_y\right]\mathrm{d}x_1\mathrm{d}y_1\\
&=\frac{1}{2\pi\mathrm{i}^\ell}\int_{\mathbb{R}^2}\frac{\mathrm{Y}_{\boldsymbol{n}}(\hat{\boldsymbol{q}})}{k_0q_z}\mathrm{e}^{\mathrm{i}\boldsymbol{q}\cdot\boldsymbol{r}-\mathrm{i}q_zz_1}\left[\int_{-\infty}^{\infty}e^{\mathrm{i}(k_x-q_x)x_1}\mathrm{d}x_1\int_{-\infty}^{\infty}e^{\mathrm{i}(k_y-q_y)y_1}\mathrm{d}y_1\right]\mathrm{d}q_x\mathrm{d}q_y\\
&=\frac{2\pi}{\mathrm{i}^\ell k_0}\int_{\mathbb{R}^2}\frac{\mathrm{Y}_{\boldsymbol{n}}(\hat{\boldsymbol{q}})}{q_z}\mathrm{e}^{\mathrm{i}(\boldsymbol{q}\cdot\boldsymbol{r}-q_zz_1)}\delta(q_x-k_x)\delta(q_y-k_y)\mathrm{d}q_x\mathrm{d}q_y\\
&=\frac{2\pi\mathrm{i}^{-\ell}}{k_0k_{0z}}\mathrm{Y}_{\boldsymbol{n}}(\hat{\boldsymbol{k}})\mathrm{e}^{\mathrm{i}(k_xx+k_yy)+\mathrm{i}k_{0z}(z-z_1)},
\end{aligned} \tag{2.71}$$

where we have changed the order of integration, and used the Fourier expansion of the Dirac delta distribution:

$$\delta(q)=\frac{1}{2\pi}\int_{-\infty}^{\infty}\mathrm{e}^{-\mathrm{i}qx}\mathrm{d}x.$$

For the case $z<z_1$, we use the fact that

$$I_{\boldsymbol{n}}(\boldsymbol{r},z_1)=(-1)^\ell\int_{\mathbb{R}^2}\mathrm{u}_{\boldsymbol{n}}(k_0\boldsymbol{r}_1-k_0\boldsymbol{r})\mathrm{e}^{\mathrm{i}(k_xx_1+k_yy_1)}\mathrm{d}x_1\mathrm{d}y_1,\quad z\neq z_1,$$

and we repeat the same computations in (2.71) to reach

$$I_{\boldsymbol{n}}(\boldsymbol{r}, z_1) = \frac{2\pi \mathrm{i}^{\ell}}{k_0 k_{0z}} \mathrm{Y}_{\boldsymbol{n}}(\hat{\boldsymbol{k}}_0) \mathrm{e}^{\mathrm{i}(k_x x + k_y y) + \mathrm{i} k_{0z}(z_1 - z)}. \tag{2.72}$$

Substituting (2.72) into (2.69), we conclude that the sum of the average scattered waves by the particles (2.25) can also be represented as a plane wave in the region $0 < z < \delta$. The results of this appendix motivate the definition of the average backscattered amplitude $\langle B \rangle$ in (2.29).

Bibliography

[1] ISO 36BI 20998-3:2017. Measurement and Characterization of Particles by Acoustic Methods vol 3. London: British Standards Institution, 2017.

[2] R E Challis, M J W Povey, M L Mather, and A K Holmes. Ultrasound techniques for characterizing colloidal dispersions. Reports on Progress in Physics, 68(7):1541, 2005. doi: 10.1088/0034-4885/68/7/R01.

[3] Raied S. Al-Lashi and Richard E. Challis. Ultrasonic particle sizing in aqueous suspensions of solid particles of unknown density. The Journal of the Acoustical Society of America, 138(2):1023–1029, 2015. ISSN 0001-4966. doi: 10.1121/1.4927694.

[4] D.M. Forrester, J. Huang, and V.J. Pinfield. Characterisation of colloidal dispersions using ultrasound spectroscopy and multiple-scattering theory inclusive of shear-wave effects. Chemical Engineering Research and Design, 114:69–78, 2016. ISSN 0263-8762. doi: 10.1016/j.cherd.2016.08.008.

[5] Leslie L. Foldy. The multiple scattering of waves. I. general theory of isotropic scattering by randomly distributed scatterers. Phys. Rev., 67:107–119, 1945. doi: 10.1103/PhysRev.67.107.

[6] Michael I. Mishchenko, Janna M. Dlugach, Maxim A. Yurkin, Lei Bi, Brian Cairns, Li Liu, R. Lee Panetta, Larry D. Travis, Ping Yang, and Nadezhda T. Zakharova. First-principles modeling of electromagnetic scattering by discrete and discretely heterogeneous random media. Physics Reports, 632:1–75, 2016. ISSN 0370-1573. doi: 10.1016/j.physrep.2016.04.002.

[7] Kerson Huang. Statistical mechanics. Wiley,, New York:, 1963. ISBN 9780521432245.

[8] Mihai Caleap, Bruce W Drinkwater, and Paul D Wilcox. Effective dynamic constitutive parameters of acoustic metamaterials with random microstructure. New Journal of Physics, 14(3):033014, 2012. doi: 10.1088/1367-2630/14/3/033014.

[9] Artur L. Gower, M. J. A. Smith, W. J. Parnell, and I. D. Abrahams. Reflection from a multi-species material and its transmitted effective wavenumber. Proc. R. Soc. A, 474(2212):20170864, 2018. ISSN 1364-5021, 1471-2946. doi: 10.1098/rspa.2017.0864.

[10] Artur L Gower and Gerhard Kristensson. Effective waves for random three-dimensional particulate materials. New Journal of Physics, 23(6):063083, 2021. doi: 10.1088/1367-2630/abdfee.

[11] Artur L. Gower, Stuart C. Hawkins, and Gerhard Kristensson. A model to validate effective waves in random particulate media: spherical symmetry. Proc. R. Soc. A, 479:, 2023. doi: 10.1098/rspa.2023.0444.

[12] K. K. Napal, P. S. Piva, and A. L. Gower. Effective T-matrix of a cylinder filled with a random two-dimensional particulate. Proceedings of the Royal Society A: Mathematical, Physical and Engineering Sciences, 480(2292):20230660, 2024. doi: 10.1098/rspa.2023.0660.

[13] Aristeidis Karnezis, Paulo S Piva, and Art L Gower. The average transmitted wave in random particulate materials. New Journal of Physics, 26(6):063002, 2024. doi: 10.1088/1367-2630/ad49c2.

[14] Artur L Gower and J Deakin. Multiplescatering.jl: A julia library for simulating, processing, and plotting multiple scattering of waves. version 0.1.21. Github, 2024.

[15] John A Fawcett. The effective medium for a cylinder with cylindrical inclusions. The Journal of the Acoustical Society of America, 150(4):2600–2612, 2021.

[16] Augusto García-Valenzuela, Rubén G. Barrera, Celia Sánchez-Pérez, Alejandro Reyes-Coronado, and Eugenio R. Méndez. Coherent reflection of light from a turbid suspension of particles in an internal-reflection configuration: Theory versus experiment. Opt. Express, 13(18):6723–6737, 2005. doi: 10.1364/OPEX.13.006723.

[17] Alverède Simon, Quentin Baudis, Régis Wunenburger, and Tony Valier-Brasier. Propagation of elastic waves in correlated dispersions of resonant scatterers. The Journal of the Acoustical Society of America, 155(6):3627–3638, 2024. doi: 10.1121/10.0026233.

[18] G. Adomian. The closure approximation in the hierarchy equations. Journal of Statistical Physics, 3(2):127–133, 1971. doi: 10.1007/BF01019846.

[19] Christian Kuehn. Moment closure-a brief review. In Control of Self-Organizing Nonlinear Systems, chapter 13, pages 253–271. Springer International Publishing, 2016. doi: 10.1007/978-3-319-28028-8.

[20] Melvin Lax. Multiple scattering of waves. II. the effective field in dense systems. Phys. Rev., 85:621–629, 1952. doi: 10.1103/PhysRev.85.621.

[21] Y. Ma, V.V. Varadan, and V.K. Varadan. Multiple scattering theory for wave propagation in discrete random media. International Journal of Engineering Science, 22(8): 1139–1148, 1984. ISSN 0020-7225. doi: 10.1016/0020-7225(84)90115-0.

[22] Artur L. Gower, W. J. Parnell, and I. D. Abrahams. Multiple waves propagate in random particulate materials. SIAM J. Appl. Math., 79(6):2569–2592, 2019.

[23] Y Miyamoto, W A Kaysser, B H Rabin, A Kawasaki, and R G Ford. Functionally graded materials: Design, processing and applications, 1999.

[24] William Parnell and Ian Abrahams. Multiple point scattering to determine the effective wavenumber and effective material properties of an inhomogeneous slab. Waves in Random and Complex Media, 20:678–701, 2010. doi: 10.1080/17455030.2010.510858.

[25] Mihai Caleap and Bruce W Drinkwater. Metamaterials: supra-classical dynamic homogenization*. New Journal of Physics, 17(12):123022, 2015. doi: 10.1088/1367-2630/17/12/123022.

[26] C. M. Linton and P. A. Martin. Multiple scattering by random configurations of circular cylinders: Second-order corrections for the effective wavenumber. The Journal of the Acoustical Society of America, 117(6):3413–3423, 2005. doi: 10.1121/1.1904270.

[27] C. Linton and Paul Martin. Multiple scattering by multiple spheres: A new proof of the Lloyd–Berry formula for the effective wavenumber. SIAM Journal on Applied Mathematics, 66, 2006. doi: 10.1137/050636401.

[28] J. R. Willis. Transmission and reflection of waves at an interface between ordinary material and metamaterial. J. Mech. Phys. Solids, 136(103678), 2019. doi: 10.1016/j.jmps.2019.103678.

[29] J. R. Willis. Transmission and reflection at the boundary of a random two-component composite. Proc. R. Soc. A, 476(20190811), 2020. doi: 10.1098/rspa.2019.0811.

[30] J. R. Willis. Transmission and reflection of energy at the boundary of a random two-component composite. Proc. R. Soc. A, 479(20220730), 2023. doi: 10.1098/rspa.2022.0730.

[31] J.R. Willis. Variational principles for dynamic problems for inhomogeneous elastic media. Wave Motion, 3(1):1–11, 1981. doi: 10.1016/0165-2125(81)90008-1.

[32] Gerhard Kristensson and Niklas Wellander. Multiple scattering by a collection of randomly located obstacles distributed in a dielectric slab, chapter 25. Advances in Mathematical Methods for Electromagnetics, 2020. doi: 10.1049/SBEW528E_ch25.

[33] V.M. Kolomietz and S. Shlomo. Mean Field Theory. World Scientific Publishing Company, 2020. ISBN 9789811211799.

[34] Michael I. Mishchenko, Larry D. Travis, and Daniel W. Mackowski. T-matrix computations of light scattering by nonspherical particles: A review. Journal of Quantitative Spectroscopy and Radiative Transfer, 55(5):535–575, 1996. ISSN 0022-4073. doi: 10.1016/0022-4073(96)00002-7.

[35] P. A. Martin and A. T. Skvortsov. Scattering by a sphere in a tube, and related problems. The Journal of the Acoustical Society of America, 148(1):191–200, 2020. ISSN 0001-4966. doi: 10.1121/10.0001518.

[36] P. C. Waterman. Symmetry, unitarity, and geometry in electromagnetic scattering. Phys. Rev. D, 3:825–839, 1971. doi: 10.1103/PhysRevD.3.825.

[37] Vijay K. Varadan, Vasundara V. Varadan, and Yih-Hsing Pao. Multiple scattering of elastic waves by cylinders of arbitrary cross section. I. SH waves. The Journal of the Acoustical Society of America, 63(5):1310–1319, 1978. ISSN 0001-4966. doi: 10.1121/1.381883.

[38] Jin Au Kong, Leung Tsang, Kung-Hau Ding, and Chi On Ao. Scattering of electromagnetic waves: numerical simulations. John Wiley & Sons, 2004.

[39] Chul-Woo Chung, John S. Popovics, and Leslie J. Struble. Flocculation and sedimentation in suspensions using ultrasonic wave reflection. The Journal of the Acoustical Society of America, 129(5):2944–2951, 2011. ISSN 0001-4966. doi: 10.1121/1.3569730.

[40] F. Hynne, R. K. Bullough, and Samuel Frederick Edwards. The scattering of light. II.

The complex refractive index of a molecular fluid. Philosophical Transactions of the Royal Society of London. Series A, Mathematical and Physical Sciences, 321(1559): 305–360, 1987. doi: 10.1098/rsta.1987.0017.

[41] Adrian Doicu and Michael I. Mishchenko. Overview of methods for deriving the radiative transfer theory from the maxwell equations. I: Approach based on the far-field foldy equations. Journal of Quantitative Spectroscopy and Radiative Transfer, 220:123–139, 2018. ISSN 0022-4073. doi: 10.1016/j.jqsrt.2018.09.004.

[42] Peter Cary Waterman and Rohn Truell. Multiple scattering of waves. Journal of mathematical physics, 2(4):512–537, 1961. doi: 10.1063/1.1703737.

[43] JG Fikioris and PC Waterman. Multiple scattering of waves. II."Hole corrections" in the scalar case. Journal of Mathematical Physics, 5(10):1413–1420, 1964.

[44] Victor P. Tishkovets, Elena V. Petrova, and Michael I. Mishchenko. Scattering of electromagnetic waves by ensembles of particles and discrete random media. Journal of Quantitative Spectroscopy and Radiative Transfer, 112(13):2095–2127, 2011. ISSN 0022-4073. doi: 10.1016/j.jqsrt.2011.04.010. Polarimetric Detection, Characterization, and Remote Sensing.

[45] Victor Twersky. On propagation in random media of discrete scatterers. In Proc. Symp. Appl. Math, volume 16, pages 84–116, 1964.

[46] Paul Martin and Agnès Maurel. Multiple scattering by random configurations of circular cylinders: Weak scattering without closure assumptions. Wave Motion, 45: 865–880, 2008. doi: 10.1016/j.wavemoti.2008.03.004.

[47] Artur L. Gower and Paulo S. Piva. Effectivewaves.jl: A julia package to calculate ensemble averaged waves in heterogeneous materials. version 0.3.6. Github, 2024.

[48] P. S. Epstein and R. R. Carhart. The absorption of sound in suspensions and emulsions. I. Water fog in air. The Journal of the Acoustical Society of America, 25(3): 553–565, 1953. doi: 10.1121/1.1907107.

[49] J. R. Allegra and S. A. Hawley. Attenuation of sound in suspensions and emulsions: Theory and experiments. The Journal of the Acoustical Society of America, 51(5): 1545–1564, 1972. doi: 10.1121/1.1912999.

[50] P.A. Martin and V.J. Pinfield. Elastodynamic multiple scattering: Effective wavenumbers in three-dimensional elastic media. Wave Motion, 134:103478, 2025. ISSN 0165-2125. doi: 10.1016/j.wavemoti.2024.103478.

[51] Weikai Li and Baohong Han. Research and application of functionally gradient materials. IOP Conference Series: Materials Science and Engineering, 394(2):022065, 2018. doi: 10.1088/1757-899X/394/2/022065.

[52] M. Danos and L. C. Maximon. Multipole Matrix Elements of the Translation Operator. Journal of Mathematical Physics, 6(5):766–778, 1965. ISSN 0022-2488. doi: 10.1063/1.1704333.

[53] Anders Boström, Gerhard Kristensson, and Staffan Ström. Transformation properties of plane, spherical and cylindrical scalar and vector wave functions. In V. V. Varadan, A. Lakhtakia, and V. K. Varadan, editors, Field Representations and Introduction to Scattering, Acoustic, Electromagnetic and Elastic Wave Scattering, chapter 4, pages 165–210. 1991.

[54] Gerhard Kristensson. Scattering of Electromagnetic Waves by Obstacles. Mario Boella Series on Electromagnetism in Information and Communication. SciTech Publishing, Edison, NJ, USA, 2016.

[55] Gerhard Kristensson. Electromagnetic scattering from a buried three-dimensional inhomogeneity in a lossy ground. Number 79-29 in Technical Report, Institute of Theoterical Physics, Chalmers University of Technology. 1979.

Chapter 3

Acoustic waves in a layer filled with random polydisperse particulate

PAULO S. PIVA, ART L. GOWER

Abstract

Adding small particles to a material can dramatically change how it transmits sound. For example, mixing 10% metallic powder into water can increase sound transmission by 40%, while adding just 5% air bubbles can almost completely block sound. Although these effects seem very different, both are explained by the same theory: wave scattering by randomly placed particles. In this paper, we present a first principles model to calculate the average acoustic response of a layer containing particles of various sizes and material properties. Our approach covers a wide range of frequencies and particle concentrations, making it suitable for ultrasound-based applications such as material characterisation and particle size estimation. The model reproduces key experimental observations, including Fabry-Pérot resonances in particulate layers and cases where the effective mass density does not depend on particle properties. This work provides a general framework for predicting sound reflection and transmission in complex particulate materials.

3.1 Introduction

A collection of small particles suspended in a homogeneous background is called a particulate. Examples include solid particles in a slurry, bubbles in boiling water, or aerosols in air. Particulates are common in nature and industry, making it important to develop methods to monitor and characterise their properties in both laboratory and real-world

settings.

Ultrasound sensing. Ultrasound sensing is a widely used technique for characterising and monitoring particulates. It is fast, energy efficient, non-invasive, and can be performed non-intrusively from outside a container [1]. In this method, transducers send ultrasound waves into the material and measure the reflected and transmitted signals. These measurements provide information about the acoustic properties of the material, such as sound speed and attenuation.

The speed of sound and attenuation depend on both the matrix and the suspended particles. Changes in these measurements can indicate variations in chemical composition, particle concentration, size distribution, or phase behaviour. As a result, ultrasound sensing is a powerful tool for monitoring dynamic processes and detecting changes in complex multiphase systems. Applications include quality control in the food and agriculture industries [2, 3], monitoring sintered powder and additive manufacturing [4, 5], and estimating particle size distributions in suspensions and colloids [6–8].

Particle sizing and frequency ranges. To obtain accurate particle size distribution measurements, it is essential to use theoretical models that account for wavelengths comparable to the full range of particle sizes in the particulate material. Accordingly, the sizes of the particles in the particulate introduce the range of length scales that must be considered in the model. The model must be valid not only in the low-frequency regime (where wavelength is much larger than the largest particles), but also in the high-frequency regime (where wavelength is much shorter than the smallest particles). For simplicity, thermal and viscous effects are neglected in this work, as their inclusion would introduce additional length scales — the thickness of the thermal and viscous boundary layers around the particles — which would need to be compared with the wavelength as well [9, 10]. These additional length scales would introduce further notions of low and high frequency regimes that are not essential for particle sizing, although their effects must be considered if they significantly alter the acoustic response of the whole particulate [9, 10].

Effective medium. A lot of work in the literature focuses on deducing an effective medium for the particulate, which replaces the whole material with a homogeneous medium with effective-properties [11, 12]. These properties can be deduced by taking the low-frequency limit [13] where the wavelengths are much longer than any particle in the material (see Figure 3.1a), and the material responds like a homogeneous medium.

Effective reflection and transmission coefficients. For a particulate layer (see Figure 3.1), the quantities which are easier to measure in an experiment are the reflected and transmitted waves. If we assume that the layer has effective-properties, such as mass density ϱ_*, wavespeed c_* and attenuation α_*, then the effective reflection R_* and transmission

T_* coefficients are given by

$$R_* = \frac{\mathcal{Z}\left(1 - \mathrm{e}^{2\mathrm{i}k_* d}\right)}{1 - \mathcal{Z}^2 \mathrm{e}^{2\mathrm{i}k_* d}} \quad \text{and} \quad T_* = \frac{(1 - \mathcal{Z}^2)\,\mathrm{e}^{\mathrm{i}k_* d}}{1 - \mathcal{Z}^2 \mathrm{e}^{2\mathrm{i}k_* d}}, \quad \text{with} \quad \mathcal{Z} = \frac{Z_* - Z}{Z_* + Z}, \tag{3.1}$$

where $k_* = \omega/c_* + \mathrm{i}\alpha_*$ is the effective wavenumber, ω is the angular frequency, Z and Z_* are the acoustic impedances of the outer medium and the layer, respectively, and d is the thickness of the layer. The outer medium is homogeneous, shown by the blue region in Figure 3.1, with impedance $Z = c\varrho$, where c is the speed of sound and ϱ mass density. To account for k_* being complex valued, the effective impedance[1] of the layer is given by

$$Z_* = \frac{\omega \varrho_*}{k_*}. \tag{3.2}$$

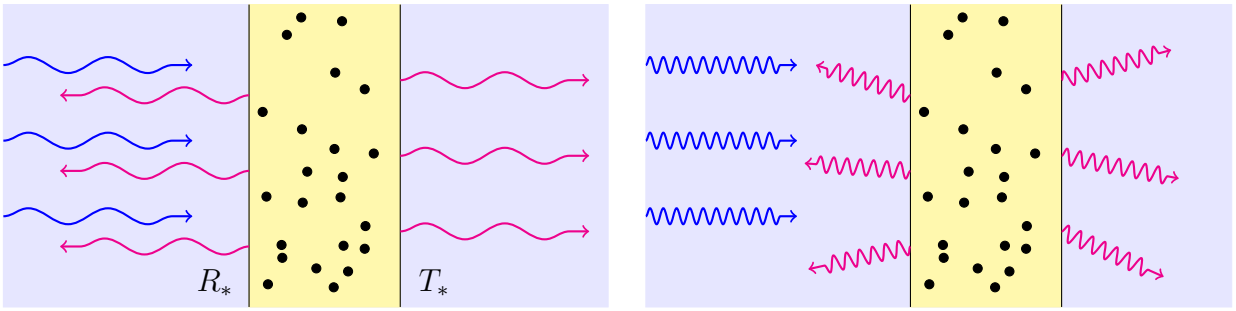

(a) Lower frequency incident wave

(b) Higher frequency incident wave

Figure 3.1: Illustrates acoustic waves which arrive at the particulate (blue arrows), and are reflected and transmitted (magenta arrows). In the low frequency limit (on the left), plane waves keep coherent after scattering, and effective medium theory with ϱ_* and c_* is accurate, represented by the effective reflection and transmission coefficients, R_* and T_* respectively. In the higher frequency case (on the right), plane waves do not keep their coherence, and both R_* and T_* from effective medium theory are no longer accurate.

Ensemble Averaging. At higher frequencies, when the wavelength is comparable to particle sizes, as shown in Figure 3.1b, effective medium theory is no longer an accurate description of wave propagation, reflection, or transmission. However, it is possible to accurately predict the average reflection and transmission coefficients for a broad range of frequencies by performing an ensemble average over particle configurations [13]. In practice, to obtain these average coefficients, $\langle R \rangle$ and $\langle T \rangle$, we need to measure the reflected and transmitted waves multiple times, and then take an average over these measurements.

[1]Here we call effective impedance Z_* the specific characteristic acoustic impedance of the entire layer, and not the surface impedance.

First principles model. In this paper, we obtain formulas for the average reflection and transmission coefficients for a broad range of frequencies and particle concentrations from first principles. We focus on the case where the matrix (yellow region in Figure 3.1) does not match the exterior medium (blue region in Figure 3.1), which is the typical case for non-intrusive acoustic sensing. We follow the method developed for reflection from a halfspace presented in Chapter 2, applied to a particulate layer illustrated in Figure 3.1. This strategy leads to a frequency dependent effective wavenumber $k_*(\omega)$, but does not result in any effective impedance or effective mass density. As motivation for the results of the paper, we show a comparison between our models for average reflection and transmission coefficients, $\langle R\rangle$ and $\langle T\rangle$ respectively, and the coefficients R_* and T_* from effective medium theory in Figure 3.2. We can see good agreement between both approaches only for lower frequencies ($ka < 0.25$), where the effective medium description is accurate.

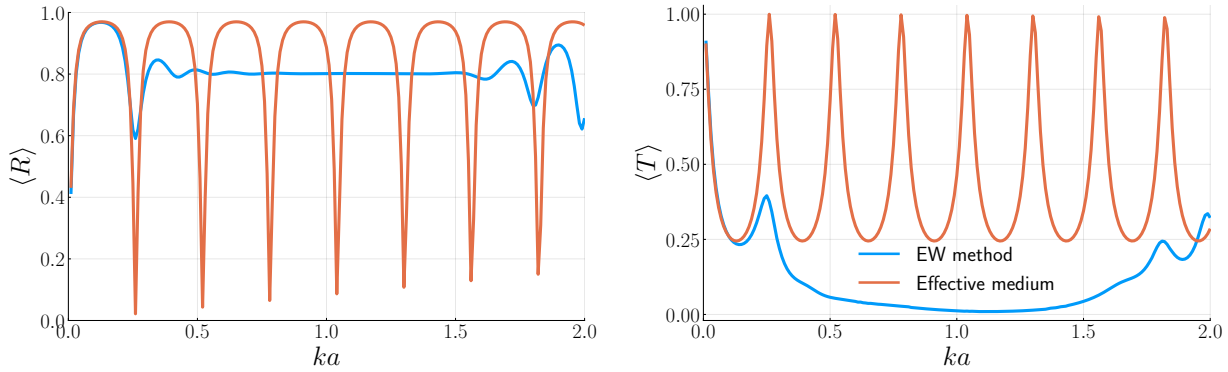

(a) Average reflection coefficient

(b) Average transmission coefficient

Figure 3.2: Graphs of the absolute values for the average reflection coefficient $\langle R\rangle$ (on the left) and the average transmission coefficients $\langle T\rangle$ (on the right) for a layer of particulate as illustrated in Figure 3.1. The matrix is a fluid layer of thickness $d = 100a$, where a is the radius of the solid particles, which constitute 10% of the volume of the layer. The incident wave is normal to the surface of the matrix and has unitary amplitude. In both graphs, we compare the effective waves method ("EW method"; orange curve) with the effective medium description (blue curve). The exterior medium is also solid, with wavenumber given by k.

This paper also extends the results in Chapter 2 to account for polydisperse particulates [13], that is, containing particles of different types and sizes. This paper is a necessary step towards advancing particle size distribution estimation from experiments, which is needed by many industries [6–8].

Extending effective medium. Although the formulas (3.1) are not strictly valid beyond the low-frequency regime (see discussion about effective medium in the paragraphs above), some authors developed strategies to extend their use to higher frequencies [14,

15]. To do this, they need some approximation, or model, for the effective mass density $\varrho_*(\omega)$, and then use $c_*(\omega)$ and $\alpha_*(\omega)$ from theoretical models valid beyond a low-frequency regime [13, 16]. For example in [14] the authors assume the effective density $\varrho_*(\omega)$ is the same as the background matrix density in (3.1)[2]. In this paper, we confirm that this assumption works remarkably well for specific cases (solid particles), but becomes inaccurate for other cases.

Another strategy to use the formulas (3.1) beyond a low frequency regime is to first assume they hold for any frequency and fit (3.1) to experimental data for reflection and transmission; and then obtain frequency-dependent effective-properties $c_*(\omega)$, $\varrho_*(\omega)$, and $\alpha_*(\omega)$ [14, 15] from this fitting. Then, from these parameters one can hope to obtain particle properties by again making use of theoretical models which relate $c_*(\omega)$ and $\alpha_*(\omega)$ to the particle properties.

We call both of these strategies the effective medium extension, which is not the approach we take in this paper. Instead, we can directly deduce reflection and transmission coefficients from the particle properties, valid for a broad frequency range.

Summary of the paper. In Section 3.2, we define the setup for the incidence of plane waves on a layer of particulate material. In Section 3.3, we define the statistics of all possible configurations of particles inside the layer, and present all statistical assumptions of the model. In Section 3.4, we calculate the total average wave outside the layer and apply boundary conditions at the interface of the layer. In Section 3.5, we present the governing equations derived in Chapter 2, and adapt them for polydisperse particles [13]. We then use the effective waves method to reach a dispersion equation and field normalisation conditions for a layer filled with polydispersed particles. In Section 3.6, we present the curves of average reflection and transmission for different examples of particulates, and discuss how they can reproduce phenomena observed in experiments in the literature.

3.2 Setting of the problem

This paper describes acoustic wave scattering from a layer of thickness d,

$$\mathcal{R} := \left\{(x, y, z) \in \mathbb{R}^3 \,|\, 0 < z < d\right\},$$

filled with randomly placed particles. Each particle is homogeneous and spherical, each one with a specific particle index $j \in 1, 2, \ldots$, radius $a_j \in \mathbb{R}$, speed of sound $c_j(\omega) \in \mathbb{C}$, and

[2]The expressions used in [14] for reflection and transmission coefficients are more complex than (3.1), because they acquire reflection and transmission data from a seven-layer setup. However, the formulas are just an extension of (3.1), because only one of the layers is composed of a particulate, as in Figure 3.1.

mass density $\varrho_j(\omega) \in \mathbb{R}$. The region in space that all particles occupy is denoted by $\mathcal{P} \subset \mathcal{R}$.

We refer to the region inside the layer and outside all particles ($\mathcal{R} \setminus \mathcal{P}$ in set notation) as the matrix. The matrix consists of a homogeneous acoustic medium with speed of sound c_0 and density ϱ_0. The exterior of the layer has speed of sound c and density ϱ. See Figure 3.3 for an illustration.

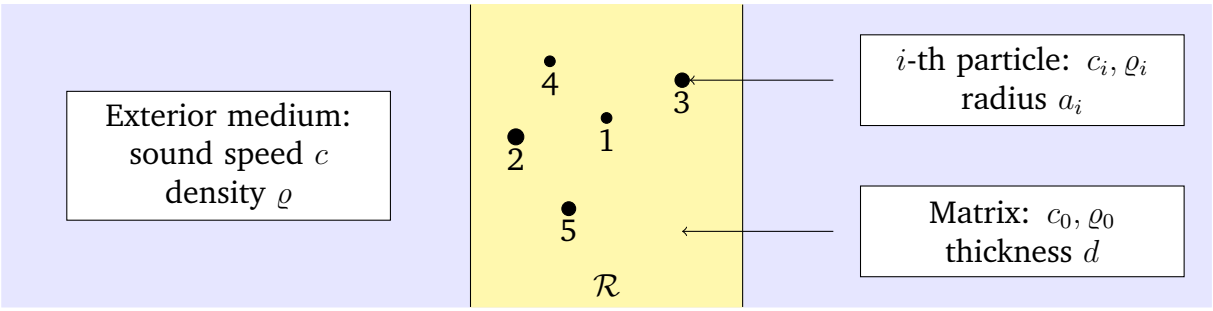

Figure 3.3: Cross-section of a layer $\mathcal{R}$, filled with homogeneous spherical particles. The acoustic properties of each medium (sound speed and density) are specified, together with the layer thickness and particle radius.

Let u_{tot} be the pressure field in the frequency domain, which satisfies the Helmholtz equations below

$$\begin{aligned} &\nabla^2 u_{\text{tot}}(\omega, x, y, z) + k^2 u_{\text{tot}}(\omega, x, y, z) = 0, \quad \text{for } z \leq 0 \text{ and } z \geq d. \\ &\nabla^2 u_{\text{tot}}(\omega, \boldsymbol{r}) + k_0^2 u_{\text{tot}}(\omega, \boldsymbol{r}) = 0, \quad \text{for } \boldsymbol{r} \in \mathcal{R} \setminus \mathcal{P}, \end{aligned} \tag{3.3}$$

where $\omega \in \mathbb{R}$ is the angular frequency, $\boldsymbol{r} = (x, y, z) \in \mathbb{R}^3$ is the position vector, $k = \omega/c$ and $k_0 = \omega/c_0$ are the wavenumbers on the exterior medium and matrix respectively. In what follows, we suppress the frequency dependence, ω, from the acoustic wave to simplify the notation. Similarly as in Section 2.2, we assume transmission boundary conditions at the surface of each particle, and at both interfaces of the layer $\mathcal{R}$ in Figure 3.3.

We focus on plane wave scattering in the frequency domain and, for simplicity, we assume normal incidence. The incident wave coming from the region $z < 0$ reads

$$u_{\text{in}}(x, y, z) = G\mathrm{e}^{\mathrm{i}kz}, \tag{3.4}$$

where $G \in \mathbb{C}$ is the amplitude, and i is the imaginary unit. We aim to derive both reflected and transmitted waves from the layer, so we write down the total acoustic field in both the

left and right-hand sides of the external medium as follows,

$$u_{\text{tot}}(x,y,z) = \begin{cases} G\mathrm{e}^{\mathrm{i}kz} + u_{\text{rf}}(x,y,z), & \text{for} \quad z \leq 0, \\ u_{\text{tr}}(x,y,z) & \text{for} \quad z \geq d. \end{cases} \tag{3.5}$$

To represent the waves in the matrix, we choose an expansion on spherical Bessel and Hankel modes, given by the following expression

$$\mathrm{v}_{\boldsymbol{n}}(\boldsymbol{x}) = \mathrm{v}_{(\ell,m)}(\boldsymbol{x}) = \mathrm{j}_\ell(x)\mathrm{Y}_{\boldsymbol{n}}(\hat{\boldsymbol{x}})$$
$$\mathrm{u}_{\boldsymbol{n}}(\boldsymbol{x}) = \mathrm{u}_{(\ell,m)}(\boldsymbol{x}) = \mathrm{h}_\ell(x)\mathrm{Y}_{\boldsymbol{n}}(\hat{\boldsymbol{x}})$$

where $\boldsymbol{n} = (\ell, m)$ is a double index with $\ell \in \mathbb{Z}_+$ and $m = -\ell, \ldots, \ell$, $\mathrm{Y}_{\boldsymbol{n}}$ are the spherical harmonic functions defined in Appendix 3.A, and j_ℓ and h_ℓ are the spherical Bessel and Hankel functions of first kind. The general expression for the total field in the matrix is given by a regular field, represented by the Bessel spherical waves, and the scattered field from each particle, represented by outgoing Hankel waves, as follows

$$u_{\text{tot}}(\boldsymbol{r}) = u_{\text{reg}}(\boldsymbol{r}) + \sum_{j=1}^{\infty} u_{\text{sc}}^{(j)}(\boldsymbol{r}) = \sum_{\boldsymbol{n}} g_{\boldsymbol{n}} \mathrm{v}_{\boldsymbol{n}}(k_0\boldsymbol{r}) + \sum_{j=1}^{\infty}\sum_{\boldsymbol{n}} f_{\boldsymbol{n}}^j \mathrm{u}_{\boldsymbol{n}}(k_0\boldsymbol{r} - k_0\boldsymbol{r}_j), \quad \text{for} \quad \boldsymbol{r} \in \mathcal{R}\setminus\mathcal{P}, \tag{3.6}$$

where $\boldsymbol{r}_j$ is the position of the centre of the j-th particle, $g_{\boldsymbol{n}} \in \mathbb{C}$ are the coefficients of the regular field, and $f_{\boldsymbol{n}}^j \in \mathbb{C}$ are the scattering coefficients of the $j-$th particle.

We point out that the sum over particle index j in (3.6) above runs from 1 to ∞ because we assume a fixed volume fraction of particles in the layer. The formal limit of infinite particles in a layer can be derived from the same procedure as done in Section 2.5.1 for a halfspace. We also do not discuss the waves inside the particles in this paper, *i. e.*, in the region $\mathcal{P}$.

As discussed in Chapter 2 and [13], the scattered field inside the layer (3.6) and, consequently, both reflected and transmitted waves (3.5) are complex because they depend on the configuration of each particle. See Figures 2.4 and 3.1 for an illustration. To render the calculations manageable, we consider the average reflection and transmission through the layer, which we introduce in Sections 3.3 and 3.4 that follow.

3.3 Particle configuration statistics

In this section, we present the mathematical definition of ensemble average and state all statistical assumptions underlying the approximations introduced in Chapter 2, which

will be used later in the text. We also detail additional assumptions to accommodate the case of a polydisperse particulate, following [13]. These definitions and assumptions are essential for deriving the average reflection and transmission of acoustic waves through a layer of particulate material.

3.3.1 Ensemble average definitions

At a fixed frequency of the incident wave (3.4), we denote the array of properties of the j-th particle by

$$\boldsymbol{\lambda}_j = (c_j, \varrho_j, a_j),$$

where we remind the reader that c_j is the speed of sound inside the particle, ϱ_j the mass density, and a_j the radius, as defined in Section 3.2. This array of properties $\boldsymbol{\lambda}_j$ is an element of $\mathcal{S}$, the set of acoustic and geometric properties. For example, $\mathcal{S}$ can be given by a parallelepiped in $\mathbb{R}^3$

$$\mathcal{S} := [c_{\text{min}}, c_{\text{max}}] \times [\varrho_{\text{min}}, \varrho_{\text{max}}] \times [a_{\text{min}}, a_{\text{max}}], \tag{3.7}$$

where the variables with index "max" are larger than the ones with index "min". We also define the set of all possible particle positions $\boldsymbol{r}_j$, given by

$$\mathcal{R}_j := \left\{ (x_j, y_j, z_j) \in \mathbb{R}^3 \,|\, z_j \in (a_j, d - a_j) \right\}, \tag{3.8}$$

where $d > 2a_{\text{max}}$, which guarantees that particles are not wider than the layer.

Both position $\boldsymbol{r}_j$ and properties $\boldsymbol{\lambda}_j$ of the j-th particle are random variables, so we define the following one-particle sample space as the Cartesian product of both (3.7) and (3.8),

$$\mathcal{Q}_j = \mathcal{R}_j \times \mathcal{S}, \tag{3.9}$$

whose elements are arrays of position and properties,

$$\boldsymbol{q}_j = (\boldsymbol{r}_j, \boldsymbol{\lambda}_j) = (x_j, y_j, z_j, c_j, \varrho_j, a_j).$$

The last component is the configuration space $\mathcal{C}$, which is the Cartesian product of the sample space of each particle (3.9),

$$\mathcal{C} = \mathcal{Q}_1 \times \mathcal{Q}_2 \times \ldots,$$

which accounts for all possible configurations of the particles. We note that we have an

infinite number of particles in the layer, because the volume of the layer is infinite, resulting on a fixed number of particles per unit volume.

Equipped with all previous definitions, we define the probability distribution of particle configuration as follows

$$p(\boldsymbol{q}_1, \boldsymbol{q}_2, \dots). \tag{3.10}$$

Analogously to (2.13) in Section 2.4, this probability density quantifies the chance of finding the whole collection of particles at specified locations $\boldsymbol{r}_i$, with specific properties $\boldsymbol{\lambda}_i$, which we use, once again, to calculate the mean wave scattered by all particles in the material; however, this time, particle radius or acoustic properties are also randomly distributed, because the particulate is polydisperse.

As discussed in Section 2.4, the probability distribution (3.10) leads to the following definition of ensemble average (and one particle conditional average) for polydisperse particulates

$$\langle \mathrm{f} \rangle = \int_{\mathcal{C}} \mathrm{f}\, p(\boldsymbol{q}_1, \boldsymbol{q}_2, \dots)\, \mathrm{d}\boldsymbol{q}_1 \mathrm{d}\boldsymbol{q}_2 \dots, \tag{3.11}$$

$$\langle \mathrm{f} \rangle(\boldsymbol{q}_1) = \langle \mathrm{f} \rangle(\boldsymbol{r}_1, \boldsymbol{\lambda}_1) = \int_{\mathcal{C}\setminus\mathcal{Q}_1} \mathrm{f}\, p(\boldsymbol{q}_2, \boldsymbol{q}_3, \dots)\, \mathrm{d}\boldsymbol{q}_2 \mathrm{d}\boldsymbol{q}_3 \dots, \tag{3.12}$$

where the marginal probability distributions we use in this section are the same as the ones introduced in Section 2.4, only exchanging the position vector $\boldsymbol{r}_i$ by the complete single particle configuration vector $\boldsymbol{q}_i = (\boldsymbol{r}_i, \boldsymbol{\lambda}_i)$ to account for polydispersed particles. The resulting marginal probability distributions are given by

$$\begin{aligned}
p(\boldsymbol{q}_1) &= \int_{\mathcal{C}\setminus\mathcal{Q}_1} p(\boldsymbol{q}_1, \boldsymbol{q}_2, \boldsymbol{q}_3, \dots)\, \mathrm{d}\boldsymbol{q}_2\, \mathrm{d}\boldsymbol{q}_3 \dots, \\
p(\boldsymbol{q}_1, \boldsymbol{q}_2) &= \int_{\mathcal{C}\setminus(\mathcal{Q}_1\times\mathcal{Q}_2)} p(\boldsymbol{q}_1, \boldsymbol{q}_2, \boldsymbol{q}_3, \boldsymbol{q}_4, \dots)\, \mathrm{d}\boldsymbol{q}_3\, \mathrm{d}\boldsymbol{q}_4 \dots, \\
p(\boldsymbol{q}_2, \boldsymbol{q}_3, \dots) &= \int_{\mathcal{Q}_1} p(\boldsymbol{q}_1, \boldsymbol{q}_2, \boldsymbol{q}_3, \dots)\, \mathrm{d}\boldsymbol{q}_1, \\
p(\boldsymbol{q}_3, \boldsymbol{q}_4, \dots) &= \int_{\mathcal{Q}_1\times\mathcal{Q}_2} p(\boldsymbol{q}_1, \boldsymbol{q}_2, \boldsymbol{q}_3, \boldsymbol{q}_4, \dots)\, \mathrm{d}\boldsymbol{q}_1\, \mathrm{d}\boldsymbol{q}_2.
\end{aligned}$$

We note that having infinite particles results in functions with an infinite number of arguments, and integrations over an infinite number of variables in the expressions above. The formal definitions of such functions and integrals are discussed in Section 2.5.1 for monodisperse particulates. The extension to polydisperse particulates is straightforward, once again only replacing the position vectors $\boldsymbol{r}_i$ by full particle configuration vectors $\boldsymbol{q}_i$,

and we omit the details to avoid repeating calculations already done in Chapter 2.

3.3.2 Statistical assumptions

The simplest case of random particulate material is when its particles are homogeneously distributed throughout the layer. Mathematically, this translates to the one-particle marginal distribution being independent of particle position. If we also know the number density of each type of particle inside the layer (average number of particles per volume of material), which we represent by $\mathfrak{n}(\boldsymbol{\lambda})$, we have

$$p(\boldsymbol{q}_j) = p(\boldsymbol{r}_j, \boldsymbol{\lambda}_j) = p(\boldsymbol{\lambda}_j) \propto \mathfrak{n}(\boldsymbol{\lambda}_j), \tag{3.13}$$

for the j-th particle.

Regarding particulate microstructure, one can consider different types of interparticle correlations, as discussed in [17, 18]. For simplicity, we assume the two-particle correlation function known as the hole correction, which does not allow overlapping between particles, and any non-overlapping configuration has the same probability of happening, given that the pairs share the same properties. This assumption reads

$$p(\boldsymbol{q}_i, \boldsymbol{q}_j) = p(\boldsymbol{r}_i, \boldsymbol{\lambda}_i, \boldsymbol{r}_j, \boldsymbol{\lambda}_j) = \begin{cases} p(\boldsymbol{\lambda}_i)p(\boldsymbol{\lambda}_j) & \text{if} \quad |\boldsymbol{r}_i - \boldsymbol{r}_j| > a_i + a_j, \\ 0 & \text{otherwise}, \end{cases} \tag{3.14}$$

for $i \neq j$. We note that (3.14) also imposes that geometric and acoustic particle properties are independent in any non-overlapping pair of particles in the particulate.

The last ingredient to calculate the average response of a particulate is a closure approximation [19, 20], which is a common strategy to reach closed-form integral equations when ensemble averaging. To deal with the case when the exterior medium in Figure 3.3 is different from the matrix, we choose the eXtended Quasi-Crystalline Approximation (X-QCA), introduced in Chapter 2, which requires the following approximations

$$p(\boldsymbol{q}_2, \boldsymbol{q}_3, \dots | \boldsymbol{q}_1) \approx p(\boldsymbol{q}_2, \boldsymbol{q}_3, \dots) \quad \text{and} \quad p(\boldsymbol{q}_3, \boldsymbol{q}_4, \dots | \boldsymbol{q}_1, \boldsymbol{q}_2) \approx p(\boldsymbol{q}_3, \boldsymbol{q}_4, \dots), \tag{3.15}$$

where the usual definition of conditional probability (2.15) holds. The interpretation of (3.15) is that: excluding only one single particle (or even one pair of particles) from the particulate with known position and property, can only slightly affect the statistics of the whole material.

3.4 Average reflection and transmission

In this section, we calculate the average acoustic field scattered by the particulate in the exterior medium, and also inside the layer but close to its interface. This is a necessary step to apply boundary conditions at the interface between the matrix and the exterior medium, which provides both average reflection and transmission coefficients.

To calculate an expression for the acoustic field inside the layer, we follow the procedure in Chapter 2, where we back off the particles by a short distance δ away from the interface ($\delta/a_j \ll 1,\ \forall j$). Then, we substitute the expression of the field inside the matrix (3.6) into (3.11), and due to the linearity of the wave equation (3.3) we reach

$$\langle u_{\text{reg}}(\boldsymbol{r})\rangle = \sum_{\boldsymbol{n}} \langle g_{\boldsymbol{n}}\rangle \mathrm{v}_{\boldsymbol{n}}(k_0\boldsymbol{r}), \quad \text{for} \quad \boldsymbol{r}\in\mathcal{R}, \quad \text{and} \tag{3.16}$$

$$\langle u^j_{\text{sc}}(x,y,z)\rangle = \sum_{j=1}^{\infty}\sum_{\boldsymbol{n}} \int_{\mathcal{S}} p(\boldsymbol{\lambda}_j) \int_{\mathcal{R}_j} \langle f_{\boldsymbol{n}}\rangle(\boldsymbol{r}_j,\boldsymbol{\lambda}_j)\mathrm{u}_{\boldsymbol{n}}(k_0(x,y,z)-k_0\boldsymbol{r}_j)\,\mathrm{d}\boldsymbol{r}_j\,\mathrm{d}\boldsymbol{\lambda}_j, \quad \text{for} \quad 0\le z\le\delta \text{ and } d-\delta<z<d, \tag{3.17}$$

where we have used the definition of one particle conditional average (3.12) together with the one particle probability distribution (3.13). We also drop the index j from the scattering coefficient $f^j_{\boldsymbol{n}}$ to simplify notation, which can be done without loss of generality because any particles with the same properties $\boldsymbol{\lambda}_j$ are indistinguishable from each other.

3.4.1 Plane wave representations

In what follows, we use the statistical homogeneity assumption (3.13). This assumption guarantees translation symmetry for the average fields (see Chapter 2 and [13]). These results lead to the following plane wave representations of the regular and scattered average fields, (3.16) and (3.17) respectively,

$$\langle u_{\text{reg}}(x,y,z)\rangle := \langle A_+\rangle \mathrm{e}^{\mathrm{i}k_0 z} + \langle A_-\rangle \mathrm{e}^{-\mathrm{i}k_0 z}, \quad \text{for} \quad 0\le z\le d, \tag{3.18}$$

$$\sum_{j=1}^{\infty}\langle u^j_{\text{sc}}(x,y,z)\rangle = \begin{cases} \langle B_-\rangle \mathrm{e}^{-\mathrm{i}k_0 z}, & \text{for} \quad 0\le z\le\delta, \\ \langle B_+\rangle \mathrm{e}^{\mathrm{i}k_0 z}, & \text{for} \quad d-\delta\le z\le d, \end{cases} \tag{3.19}$$

where the coefficients $\langle A_+\rangle$ and $\langle A_-\rangle$ relate to $\langle g_{\boldsymbol{n}}\rangle$ as described in Appendix 3.A. To compute $\langle B_+\rangle$ and $\langle B_-\rangle$, we use substitute both (2.69) and (2.70) into the right-hand side of (3.19), and use both (2.71) and (2.72) to reach the expressions on the right-hand side of (3.19). As a result, the expressions of both $\langle B_+\rangle$ and $\langle B_-\rangle$, with respect to the average

scattering coefficients $\langle f_{\boldsymbol{n}}\rangle$, are given by

$$\begin{aligned}\langle B_+\rangle &= \frac{2\pi}{k_0^2}\sum_{\boldsymbol{n}} \mathrm{i}^{-\ell}\mathrm{Y}_{\boldsymbol{n}}(\hat{\boldsymbol{z}})\int_{\mathcal{S}}\mathfrak{n}(\boldsymbol{\lambda}_1)\int_{a_1+\delta}^{d-a_1-\delta}\langle f_{\boldsymbol{n}}\rangle(0,0,z_1,\boldsymbol{\lambda_1})\mathrm{e}^{-\mathrm{i}k_0 z_1}\mathrm{d}z_1\mathrm{d}\boldsymbol{\lambda}_1,\\ \langle B_-\rangle &= \frac{2\pi}{k_0^2}\sum_{\boldsymbol{n}} \mathrm{i}^{\ell}\mathrm{Y}_{\boldsymbol{n}}(\hat{\boldsymbol{z}})\int_{\mathcal{S}}\mathfrak{n}(\boldsymbol{\lambda}_1)\int_{a_1+\delta}^{d-a_1-\delta}\langle f_{\boldsymbol{n}}\rangle(0,0,z_1,\boldsymbol{\lambda}_1)\mathrm{e}^{\mathrm{i}k_0 z_1}\mathrm{d}z_1\mathrm{d}\boldsymbol{\lambda}_1,\end{aligned} \tag{3.20}$$

where the average scattering coefficient $\langle f_{\boldsymbol{n}}\rangle$ does not depend on x_1 and y_1 due to the translation symmetry after average, and we remind the reader that $\mathfrak{n}(\boldsymbol{\lambda})$ is the number density of particles of type $\boldsymbol{\lambda}$.

We also compute the transmitted and reflected average waves, achieved by substituting the total field (3.5) into the definition of ensemble average (3.11). By the same symmetry arguments, we reach

$$\langle u_{\text{tot}}(x,y,z)\rangle = \begin{cases} G\mathrm{e}^{\mathrm{i}kz} + \langle R\rangle \mathrm{e}^{-\mathrm{i}kz}, & \text{for} \quad z\le 0,\\ \langle T\rangle \mathrm{e}^{\mathrm{i}k(z-d)}, & \text{for} \quad z\ge d,\end{cases} \tag{3.21}$$

where $\langle R\rangle$ and $\langle T\rangle$ are the average reflection and transmission coefficients respectively. We note that the amplitude of the incident wave G does not change because it is independent of particle configuration.

3.4.2 Boundary conditions at interfaces

The next step is to find a relation between the average macroscopic reflection and transmission of the layer, $\langle R\rangle$ and $\langle T\rangle$, and the scattering coefficients, $\langle f_{\boldsymbol{n}}\rangle(\boldsymbol{q}_1)$, which carry information from microscopic particle scattering pattern. This relation is indirectly given by forward and backward particle scattering amplitudes close to the boundary, given by (3.20).

We assume transmission boundary conditions, which read (after ensemble averaging)

$$\begin{cases} \langle u_{\text{tot}}(\boldsymbol{r})\rangle \text{ is continuous at } z=0 \text{ and } z=d,\\ \dfrac{1}{\varrho(\boldsymbol{r})}\dfrac{\partial\langle u_{\text{tot}}(\boldsymbol{r})\rangle}{\partial z} \text{ is continuous at } z=0 \text{ and } z=d,\end{cases} \tag{3.22}$$

where $\varrho(\boldsymbol{r})$ is the mass density at $\boldsymbol{r}$. Substituting (3.21), (3.18) and (3.19) into (3.22) for

both $z = 0$ and $z = d$ leads to

$$\begin{cases} G + \langle R\rangle = \langle A_+\rangle + \langle A_-\rangle + \langle B_-\rangle, \\ \dfrac{k}{\varrho}\left(G - \langle R\rangle\right) = \dfrac{k_0}{\varrho_0}\left(\langle A_+\rangle - \langle A_-\rangle - \langle B_-\rangle\right), \\ \langle T\rangle \mathrm{e}^{\mathrm{i}kd} = \langle A_+\rangle \mathrm{e}^{\mathrm{i}k_0 d} + \langle A_-\rangle \mathrm{e}^{-\mathrm{i}k_0 d} + \langle B_+\rangle \mathrm{e}^{\mathrm{i}k_0 d}, \\ \dfrac{k}{\varrho}\langle T\rangle \mathrm{e}^{\mathrm{i}kd} = \dfrac{k_0}{\varrho_0}\left[\left(\langle A_+\rangle + \langle B_+\rangle\right)\mathrm{e}^{\mathrm{i}k_0 d} - \langle A_-\rangle \mathrm{e}^{-\mathrm{i}k_0 d}\right]. \end{cases}$$

Rearranging the system above to solve for the unknowns $\langle R\rangle$, $\langle T\rangle$, $\langle A_+\rangle$ and $\langle A_-\rangle$, we achieve the expressions for average reflection and transmission coefficients

$$\begin{aligned} \langle R\rangle &= \mathrm{D}_+\langle B_-\rangle \mathrm{e}^{-\mathrm{i}k_0 d} + \mathrm{D}_-\langle B_+\rangle \mathrm{e}^{\mathrm{i}k_0 d} + 2\mathrm{i}\mathrm{D}_1 G \sin(k_0 d), \\ \langle T\rangle &= \mathrm{D}_-\langle B_-\rangle + \mathrm{D}_+\langle B_+\rangle + \mathrm{D}_0 G, \end{aligned} \tag{3.23}$$

and also the coefficients of the average regular field inside the layer

$$\begin{aligned} \langle A_+\rangle &= \mathrm{D}_1\langle B_-\rangle \mathrm{e}^{-\mathrm{i}k_0 d} + \mathrm{D}_2\langle B_+\rangle \mathrm{e}^{\mathrm{i}k_0 d} + \gamma_0 \mathrm{D}_+ G \mathrm{e}^{-\mathrm{i}k_0 d}, \\ \langle A_-\rangle &= \left(\mathrm{D}_2\langle B_-\rangle + \mathrm{D}_1\langle B_+\rangle + \gamma_0 \mathrm{D}_- G\right)\mathrm{e}^{\mathrm{i}k_0 d}, \end{aligned} \tag{3.24}$$

which are used in Section 3.5. The auxiliary coefficients $\mathrm{D}_{(\cdot)}$ depend only on the acoustic properties of the matrix and the exterior medium, and their expressions are given by

$$\begin{aligned} &\mathrm{D}_+ = \frac{k_0\varrho(k_0\varrho + k\varrho_0)}{\Delta}, \quad \mathrm{D}_- = \frac{k_0\varrho(k_0\varrho - k\varrho_0)}{\Delta}, \quad \gamma_0 = \frac{k\varrho_0}{k_0\varrho}, \\ &\mathrm{D}_0 = \frac{2kk_0\varrho\varrho_0}{\Delta}, \quad \mathrm{D}_1 = \frac{k_0^2\varrho^2 - k^2\varrho_0^2}{2\Delta}, \quad \mathrm{D}_2 = \frac{(k_0\varrho - k\varrho_0)^2}{2\Delta}, \\ &\Delta = 2kk_0\varrho\varrho_0\cos(k_0 d) - \mathrm{i}(k_0^2\varrho^2 + k^2\varrho_0^2)\sin(k_0 d). \end{aligned} \tag{3.25}$$

We point out that (3.23), (3.24) and (3.25) do not depend explicitly on the small distance δ that we introduce in Section 3.4.1. Following the steps in Chapter 2, we take the limit $\delta \to 0$ in the interval of integration of (3.20), which represents the case where particles are contained within the layer, and can be arbitrarily close to its interface, but never touching it.

We also note it is not difficult to account for oblique incidence in (3.23), which is when the incident wave (3.4) is replaced by

$$u_{\mathrm{in}}(\boldsymbol{r}) = G\mathrm{e}^{\mathrm{i}\boldsymbol{k}\cdot\boldsymbol{r}},$$

where the wavevector is given by $\boldsymbol{k} = (k_x, k_y, k_z)$, and $|\boldsymbol{k}| = k$ is the wavenumber of the exterior medium. In this case, we introduce the vector of matrix wavevector as $\boldsymbol{k}_0 = (k_{0x}, k_{0y}, k_{0z})$, equate the x and y components of $\boldsymbol{k}$ and $\boldsymbol{k}_0$, and calculate its missing component from Snell's law: $k_{0z} = (k_0^2 - k_{0x}^2 - k_{0y}^2)^{1/2}$. Finally, the values of k and k_0 in the auxiliary coefficients (3.25) are exchanged by k_z and k_{0z} respectively. However, in this chapter, we only consider normal incidence to avoid discussions about any critical angle of total reflection, as exemplified in case 2 of Section 2.8.3.

3.4.3 Single medium limit

In this section, we check the single background medium limit, when the acoustic properties of the matrix are the same as in the exterior medium, $c_0 = c$ and $\varrho_0 = \varrho$. Substituting these values of c_0 and ϱ_0 in (3.23), we get $\mathrm{D}_- = \mathrm{D}_1 = \mathrm{D}_2 = 0$, $\mathrm{D}_+ = \mathrm{D}_0 = \mathrm{e}^{\mathrm{i}kd}$, and $\gamma_0 = 1$ as auxiliary coefficients in (3.25), which feeds into (3.23) and leads to

$$\langle R \rangle = \langle B_- \rangle \quad \text{and} \quad \langle T \rangle = (G + \langle B_+ \rangle)\, \mathrm{e}^{\mathrm{i}kd}.$$

Both average reflection and transmission coefficients above are consistent with previous results in the literature for a layer of particles in a single background medium, see [13, eqs. 7.3 and 7.6].

The same can be said about the regular field inside the layer. Substituting $c_0 = c$ and $\varrho_0 = \varrho$ into (3.24), leads to the expression of the incident wave (3.4), which is the only contribution to the regular field in the case of a single background medium with no interfaces.

3.5 Average governing equation

The last step to calculate $\langle R \rangle$ and $\langle T \rangle$ in (3.23) is to determine the average scattering coefficient $\langle f_{\boldsymbol{n}} \rangle(\boldsymbol{q}_1)$ in (3.17). To account for all orders of multiple scattering between particles and interfaces, we consider the average governing equation for a poly-disperse particulate [13, eq. 3.7]. However, in this case, the matrix is different from the exterior medium, so we use the ensemble-averaged coefficients of the regular wave, $\langle g_{\boldsymbol{n}'} \rangle$, instead of $g_{\boldsymbol{n}'}$ in the original equation. This change is needed because the regular waves consist not only of the incident wave transmitted into the layer, but also of all reflections of scattered waves from particles at the layer's interface. The procedure results in the following

governing equation for a polydisperse particulate layer

$$\langle f_{\boldsymbol{n}}\rangle(\boldsymbol{r}_1,\boldsymbol{\lambda}_1) = T_{\boldsymbol{n}}(\boldsymbol{\lambda}_1)\sum_{\boldsymbol{n}'}\mathcal{V}_{\boldsymbol{n}'\boldsymbol{n}}(k_0\boldsymbol{r}_1)\langle g_{\boldsymbol{n}'}\rangle + T_{\boldsymbol{n}}(\boldsymbol{\lambda}_1)\sum_{\boldsymbol{n}'}\int_{\mathcal{S}}\mathfrak{n}(\boldsymbol{\lambda}_2)\int_{\mathcal{R}_2\setminus\mathcal{B}(\boldsymbol{r}_1;a_1+a_2)}\mathcal{U}_{\boldsymbol{n}'\boldsymbol{n}}(k_0\boldsymbol{r}_1-k_0\boldsymbol{r}_2)\langle f_{\boldsymbol{n}'}\rangle(\boldsymbol{r}_2,\boldsymbol{\lambda}_2)\mathrm{d}\boldsymbol{r}_2\mathrm{d}\boldsymbol{\lambda}_2, \quad (3.26)$$

where $T_{\boldsymbol{n}}(\boldsymbol{\lambda})$ is the T-matrix of the particle with properties $\boldsymbol{\lambda}$ [13, 21]; $\mathcal{B}(\boldsymbol{x},h)$ is a ball centered at $\boldsymbol{x}\in\mathbb{R}^3$ with radius $h\in\mathbb{R}$; $\mathcal{U}_{\boldsymbol{n}'\boldsymbol{n}}$ and $\mathcal{V}_{\boldsymbol{n}'\boldsymbol{n}}$ are, respectively, the outgoing and regular translation matrices for spherical waves, both defined in [13, eq. B.3].

To avoid repeating the extensive calculations done in Section 2.6, we do not present the full derivation of (3.26) here. Deriving (3.26) from first principles requires the eXtended Quasi-Crystalline Approximation (X-QCA), introduced in Chapter 2. X-QCA combines the statistical assumptions (3.15) with the approximation that the exciting field of any single particle can be replaced by its average over all possible configurations of that particle. A full derivation of (3.26) for monodisperse particulates is given in Sections 2.6 and 2.7.

An alternative way to reach (3.26) is to start from the average governing equation for a monodisperse particulate (2.35), and introduce the dependence on particle radius and properties $\boldsymbol{\lambda}_i=(c_i,\varrho_i,a_i)$ for $i=1,2$ a posteriori. To make this procedure consistent, we must also integrate the right-hand side of the resulting equation over all possible particle properties $\boldsymbol{\lambda}_2$ instead of only particle positions $\boldsymbol{r}_2$, which leads to (3.26).

3.5.1 Effective waves method

To solve the governing equation (3.26), we use the effective waves method, introduced in [13]. The method consists in assuming that the average scattering coefficient $\langle f_{\boldsymbol{n}}\rangle(\boldsymbol{r}_1,\boldsymbol{\lambda}_1)$ satisfies a Helmholtz equation with an effective wavenumber $k_*\in\mathbb{C}$, given by

$$\nabla^2\langle f_{\boldsymbol{n}}\rangle(\boldsymbol{r}_1,\boldsymbol{\lambda}_1)+k_*^2\langle f_{\boldsymbol{n}}\rangle(\boldsymbol{r}_1,\boldsymbol{\lambda}_1)=0 \quad \text{for} \quad \boldsymbol{r}_1\in\mathcal{R}_1.$$

This ansatz is shown to be accurate for a broad range of particle properties, frequencies, and concentrations in the literature [13, 17, 18]. Then, using the translation symmetry Appendix 2.C, we deduce the following plane wave modal expression for $\langle f_{\boldsymbol{n}}\rangle$

$$\langle f_{\boldsymbol{n}}\rangle(\boldsymbol{r}_1,\boldsymbol{\lambda}_1) = F_{\boldsymbol{n}}^{(+)}(\boldsymbol{\lambda}_1)\mathrm{e}^{\mathrm{i}k_*z_1}+F_{\boldsymbol{n}}^{(-)}(\boldsymbol{\lambda}_1)\mathrm{e}^{-\mathrm{i}k_*z_1} \quad \text{for} \quad \boldsymbol{r}_1\in\mathcal{R}_1, \quad (3.27)$$

where the amplitudes $F_{\boldsymbol{n}}^{(\pm)}(\boldsymbol{\lambda})$ depend only on particle properties.

As discussed in Section 2.8, the dispersion equation of the particulate, which deter-

mines $k_*(\omega)$, does not depend on the properties of the exterior medium, but only on the microstructure inside the layer. Then, the effective wavenumber is the solutions of the dispersion equation given by [13, eq. 5.11], which reads

$$F_{\boldsymbol{n}}^{(\pm)}(\boldsymbol{\lambda}_1) = \sum_{\boldsymbol{n}'\boldsymbol{n}_1} \frac{c_{\boldsymbol{n}'\boldsymbol{n}\boldsymbol{n}_1}}{k_0^2 - k_*^2} \mathrm{C}_{\boldsymbol{n}_1}^{\mp} T_{\boldsymbol{n}}(\boldsymbol{\lambda}_1) \int_{\mathcal{S}} a_{1\leftrightarrow 2} \mathrm{N}_{\ell_1}(k_0 a_{1\leftrightarrow 2}, k_* a_{1\leftrightarrow 2}) F_{\boldsymbol{n}'}^{(\pm)}(\boldsymbol{\lambda}_2) \mathfrak{n}(\boldsymbol{\lambda}_2) \mathrm{d}\boldsymbol{\lambda}_2, \tag{3.28}$$

where $a_{1\leftrightarrow 2} = a_1 + a_2$, $\mathrm{N}_{\ell 1}$ is given by (2.56), and $c_{\boldsymbol{n}\boldsymbol{n}'\boldsymbol{n}_1}$ is defined in Appendix 2.A as (2.63).

Beyond the dispersion equation (3.28), the plane wave modal representation (3.27) also simplifies the expression for both frontal and backscattering amplitudes (3.20). By substituting (3.27) into (3.20), and taking the limit $\delta \to 0$, we reach

$$\begin{aligned}
\langle B_+ \rangle &= \frac{1}{k_0^2} \sum_{\boldsymbol{n}} \mathrm{C}_{\boldsymbol{n}}^{-} \int_{\mathcal{S}} \left[\mathrm{Q}(k_*, -k_0, a_2) F_{\boldsymbol{n}}^{(+)}(\boldsymbol{\lambda}_2) + \mathrm{Q}(-k_*, -k_0, a_2) F_{\boldsymbol{n}}^{(-)}(\boldsymbol{\lambda}_2) \right] \mathfrak{n}(\boldsymbol{\lambda}_2) \mathrm{d}\boldsymbol{\lambda}_2, \\
\langle B_- \rangle &= \frac{1}{k_0^2} \sum_{\boldsymbol{n}} \mathrm{C}_{\boldsymbol{n}}^{+} \int_{\mathcal{S}} \left[\mathrm{Q}(k_*, k_0, a_2) F_{\boldsymbol{n}}^{(+)}(\boldsymbol{\lambda}_2) + \mathrm{Q}(-k_*, k_0, a_2) F_{\boldsymbol{n}}^{(-)}(\boldsymbol{\lambda}_2) \right] \mathfrak{n}(\boldsymbol{\lambda}_2) \mathrm{d}\boldsymbol{\lambda}_2,
\end{aligned} \tag{3.29}$$

where we have defined

$$\mathrm{Q}(x, y, r) = \frac{\mathrm{e}^{\mathrm{i}(x+y)d/2}}{x+y} \sin[(x+y)(d/2 - r)].$$

3.5.2 Normalisation conditions

Other than just the effective wavenumber, (3.28) also provides a solution for the amplitudes of the plane wave modes $F_{\boldsymbol{n}}^{(\pm)}(\boldsymbol{\lambda})$ in (3.27). However, this solution is not unique, and $F_{\boldsymbol{n}}^{(\pm)}(\boldsymbol{\lambda})$ is determined up to an arbitrary complex phase, which does not depend on the index $\boldsymbol{n}$ or material properties $\boldsymbol{\lambda}$. To achieve a unique solution, we need a pair of normalisation conditions, which are derived from the ensemble boundary conditions [13][sec. 4.1].

We substitute both (3.27) and (3.48), from Appendix 3.A, into the average governing equation (3.26). Then, we collect only the terms that satisfy the Helmholtz equation with wavenumber k_0, as done in Chapter 2, which leads to the following ensemble boundary conditions

$$\sum_{p\in\{+,-\}} \left[\sum_{\boldsymbol{n}'} \int_{\mathcal{S}} \frac{\mathcal{I}_{\boldsymbol{n}'\boldsymbol{n}}^{(p)}(z_1)}{k_0^2 - k_*^2} \mathfrak{n}(\boldsymbol{\lambda}_2) \mathrm{d}\boldsymbol{\lambda}_2 + \mathrm{E}_{\boldsymbol{n}}^{p}(z_1) \langle B_p \rangle \right] + \gamma_0 \mathrm{E}_{\boldsymbol{n}}^{0}(z_1) G = 0, \tag{3.30}$$

where the coefficients $\mathrm{E}_{\boldsymbol{n}}^{(\cdot)}(z_1)$ are given by

$$\begin{aligned}
\mathrm{E}_{\boldsymbol{n}}^{0}(z_1) &= \mathrm{C}_{\boldsymbol{n}}^{+}\mathrm{D}_{+}\mathrm{e}^{\mathrm{i}k_0(z_1-d)} + \mathrm{C}_{\boldsymbol{n}}^{-}\mathrm{D}_{-}\mathrm{e}^{-\mathrm{i}k_0(z_1-d)},\\
\mathrm{E}_{\boldsymbol{n}}^{-}(z_1) &= \mathrm{C}_{\boldsymbol{n}}^{+}\mathrm{D}_{1}\mathrm{e}^{\mathrm{i}k_0(z_1-d)} + \mathrm{C}_{\boldsymbol{n}}^{-}\mathrm{D}_{2}\mathrm{e}^{-\mathrm{i}k_0(z_1-d)},\\
\mathrm{E}_{\boldsymbol{n}}^{+}(z_1) &= \mathrm{C}_{\boldsymbol{n}}^{+}\mathrm{D}_{2}\mathrm{e}^{\mathrm{i}k_0(z_1+d)} + \mathrm{C}_{\boldsymbol{n}}^{-}\mathrm{D}_{1}\mathrm{e}^{-\mathrm{i}k_0(z_1-d)},
\end{aligned}$$

and the expression for $\mathcal{I}_{\boldsymbol{n}'\boldsymbol{n}}^{(\pm)}(z_1)$ is equivalent to [13, eq. 4.4] for the case of a layer, given by

$$\mathcal{I}_{\boldsymbol{n}'\boldsymbol{n}}^{(\pm)}(z_1) = F_{\boldsymbol{n}'}^{(\pm)}(\boldsymbol{\lambda}_2)\int_{\partial\mathcal{R}_2}\mathcal{U}_{\boldsymbol{n}'\boldsymbol{n}}(k_0\boldsymbol{r}_1-k_0\boldsymbol{r}_2)\frac{\partial \mathrm{e}^{\pm\mathrm{i}k_* z_2}}{\partial z_2} - \frac{\partial \mathcal{U}_{\boldsymbol{n}'\boldsymbol{n}}(k_0\boldsymbol{r}_1-k_0\boldsymbol{r}_2)}{\partial z_2}\mathrm{e}^{\pm\mathrm{i}k_* z_2}\mathrm{d}A_2, \quad (3.31)$$

where the sign of the area differential $\mathrm{d}A_2 = \pm\mathrm{d}x_2\mathrm{d}y_2$ is chosen to coincide with the outward normal convention for the surface integral on each interface of the layer.

The next step is to substitute (3.31) into (3.30), and separate the final expression into two independent normalisation conditions explicitly. This process involves multiple algebraic manipulations described in detail in Appendix 3.B, which leads to (3.52) that we substitute into (3.30) to obtain

$$\sum_{\boldsymbol{n}'}\left[\mathrm{M}_{\boldsymbol{n}'}^{(1)}\mathrm{C}_{\boldsymbol{n}}^{+}\mathrm{e}^{\mathrm{i}k_0 z_1} + \mathrm{M}_{\boldsymbol{n}'}^{(2)}\mathrm{C}_{\boldsymbol{n}}^{-}\mathrm{e}^{-\mathrm{i}k_0 z_1}\right] + \gamma_0\mathrm{E}_{\boldsymbol{n}}^{0}(z_1)G = 0, \quad (3.32)$$

where $\mathrm{M}_{\boldsymbol{n}'}^{(1)}$ and $\mathrm{M}_{\boldsymbol{n}'}^{(2)}$ are defined as follows

$$\begin{aligned}
\mathrm{M}_{\boldsymbol{n}'}^{(1)} &= \mathrm{D}_2\mathrm{e}^{\mathrm{i}k_0 d}\langle B_+\rangle + \mathrm{D}_1\mathrm{e}^{-\mathrm{i}k_0 d}\langle B_-\rangle\\
&\quad - \mathrm{i}\frac{\mathrm{C}_{\boldsymbol{n}'}^{-}}{2k_0^2}\int_{\mathcal{S}}\mathrm{e}^{-\mathrm{i}k_0 a_2}\left[\frac{\mathrm{e}^{\mathrm{i}k_* a_2}}{k_0-k_*}F_{\boldsymbol{n}'}^{(+)}(\boldsymbol{\lambda}_2) + \frac{\mathrm{e}^{-\mathrm{i}k_* a_2}}{k_0+k_*}F_{\boldsymbol{n}'}^{(-)}(\boldsymbol{\lambda}_2)\right]\mathfrak{n}(\boldsymbol{\lambda}_2)\mathrm{d}\boldsymbol{\lambda}_2,
\end{aligned}$$

$$\begin{aligned}
\mathrm{M}_{\boldsymbol{n}'}^{(2)} &= \left[\mathrm{D}_1\langle B_+\rangle + \mathrm{D}_2\langle B_-\rangle\right]\mathrm{e}^{\mathrm{i}k_0 d}\\
&\quad - \mathrm{i}\frac{\mathrm{C}_{\boldsymbol{n}'}^{+}}{2k_0^2}\int_{\mathcal{S}}\mathrm{e}^{\mathrm{i}k_0(d-a_2)}\left[\frac{\mathrm{e}^{\mathrm{i}k_*(d-a_2)}}{k_0+k_*}F_{\boldsymbol{n}'}^{(+)}(\boldsymbol{\lambda}_2) + \frac{\mathrm{e}^{-\mathrm{i}k_*(d-a_2)}}{k_0-k_*}F_{\boldsymbol{n}'}^{(-)}(\boldsymbol{\lambda}_2)\right]\mathfrak{n}(\boldsymbol{\lambda}_2)\mathrm{d}\boldsymbol{\lambda}_2.
\end{aligned}$$

Finally, we note that (3.32) can be rearranged as a system of two independent equations, one with a factor of $\mathrm{C}_{\boldsymbol{n}}^{+}\mathrm{e}^{\mathrm{i}k_0 z_1}$, and the other with a factor of $\mathrm{C}_{\boldsymbol{n}}^{-}\mathrm{e}^{-\mathrm{i}k_0 z_1}$. This pair of

equations, each one divided by its own common factor, is given by

$$\sum_{\boldsymbol{n}'} \mathrm{M}^{(1)}_{\boldsymbol{n}'} = -\gamma_0 \mathrm{D}_+ G \mathrm{e}^{-\mathrm{i}k_0 d}, \tag{3.33}$$

$$\sum_{\boldsymbol{n}'} \mathrm{M}^{(2)}_{\boldsymbol{n}'} = -\gamma_0 \mathrm{D}_- G \mathrm{e}^{\mathrm{i}k_0 d}, \tag{3.34}$$

which are the two normalisation condition equations required to fully determine $F^{(+)}_{\boldsymbol{n}}(\boldsymbol{\lambda})$ and $F^{(-)}_{\boldsymbol{n}}(\boldsymbol{\lambda})$, and consequently, the average reflection and transmission coefficients, $\langle R \rangle$ and $\langle T \rangle$ respectively.

3.5.3 Homogeneous layer limit and high frequency behaviour

To check if the expressions for average coefficients (3.23) are consistent with canonical scattering of a homogeneous layer, we take the limit of no particles in the material, which corresponds to a zero number density of particles in (3.20). We start by considering the absolute value of the coefficients in (3.29). The expression for $|\langle B_+ \rangle|$ reads

$$|\langle B_+ \rangle| = \left| \sum_{\boldsymbol{n}} \mathrm{C}^-_{\boldsymbol{n}} \int_{\mathcal{S}} \left[\frac{\mathrm{Q}(k_*, -k_0, a_2)}{k_0^2 a_2^3} F^{(+)}_{\boldsymbol{n}}(\boldsymbol{\lambda}_2) + \frac{\mathrm{Q}(-k_*, -k_0, a_2)}{k_0^2 a_2^3} F^{(-)}_{\boldsymbol{n}}(\boldsymbol{\lambda}_2) \right] \phi(\boldsymbol{\lambda}_2) \mathrm{d}\boldsymbol{\lambda}_2 \right|, \tag{3.35}$$

where we define the expressions of volume fraction as

$$\phi(\boldsymbol{\lambda}) = \frac{4\pi a_i^3}{3} \mathfrak{n}(\boldsymbol{\lambda}) \quad \text{and} \quad \varphi = \int_{\mathcal{S}} \phi(\boldsymbol{\lambda}) \mathrm{d}\boldsymbol{\lambda} \tag{3.36}$$

which represent the volume fraction of the layer occupied by each particle type individually, and by all particles collectively. Then, we write down the following bound for (3.35)

$$|\langle B_+ \rangle| \leq \varphi \sum_{\boldsymbol{n}} |\mathrm{C}^-_{\boldsymbol{n}}| \max_{\boldsymbol{\lambda} \in \mathcal{S}} \left[\frac{|Q(k_*, -k_0, a)|}{k_0^2 a^3} |F^{(+)}_{\boldsymbol{n}}(\boldsymbol{\lambda})| + \frac{|Q(-k_*, -k_0, a_2)|}{k_0^2 a_2^3} |F^{(-)}_{\boldsymbol{n}}(\boldsymbol{\lambda})| \right]. \tag{3.37}$$

If we assume the series in (3.35) converges, the limit of no particles in the layer, given by $\varphi \to 0$, leads to zero frontal scattering due to particles, $\langle B_+ \rangle \to 0$.

Analogously, we can repeat all the analysis above for the backwards scattering due to particles, $\langle B_- \rangle$ in (3.29), and reach the same conclusion that $\langle B_- \rangle \to 0$ as $\varphi \to 0$. Substituting both $\langle B_+ \rangle = \langle B_- \rangle = 0$ into the average reflection and transmission coefficients (3.23), we reach the exact formula of a homogeneous layer filled only by the matrix, given by (3.1) with $Z_0 = c_0 \varrho_0$ instead of Z_*.

In addition to just consistency checks, (3.35) also provides some insight into the high-frequency behaviour of the average reflection and transmission. To reach this insight, we also write down the following bounds for the absolute value of the following terms in (3.35)

$$|Q(k_*,-k_0,a)| \leq \frac{\mathrm{e}^{-\mathrm{Im}[k_*](d-a)}+\mathrm{e}^{-\mathrm{Im}[k_*]a}}{2|k_*-k_0|} \quad \text{and} \quad |Q(-k_*,-k_0,a)| \leq \frac{\mathrm{e}^{\mathrm{Im}[k_*](d-a)}+\mathrm{e}^{\mathrm{Im}[k_*]a}}{2|k_*+k_0|},$$

which grow exponentially for attenuating effective wavenumbers, $\mathrm{Im}[k_*] \neq 0$, that complicates the analysis for the formal high frequency limit. However, if we assume $|\mathrm{Im}[k_*]|$, $|F_{\boldsymbol{n}}^{(+)}(\boldsymbol{\lambda})|$ and $|F_{\boldsymbol{n}}^{(-)}(\boldsymbol{\lambda})|$ are bounded, and that the series in (3.35) converges, we conclude that $\langle B_+\rangle \to 0$ as $k_0 a_{\text{min}} \to 0$. Here we remind the reader that a_{min} is the minimum size of particle radius in the particulate.

Once again, we can repeat the analysis for $\langle B_-\rangle$, and reach the same conclusion that, for a fixed volume fraction φ, $\langle B_-\rangle \to 0$ as $k_0 a_{\text{min}} \to \infty$.

In short, under the strong assumptions outlined above, we find that the high-frequency behaviour of the average reflection and transmission approaches that of a homogeneous layer composed solely of the matrix, without particles, which is a remarkably simple outcome. However, it remains unclear to the authors under which conditions these assumptions hold. To address this, we present numerical simulations in Section 3.6.1, comparing the no-particle limit with the high-frequency behaviour.

3.6 Numerical results and discussion

In this section, we use the EffectiveWaves.jl package in Julia [22] to explore some examples of average reflection and transmission coefficients from a particulate layer, as shown in Figure 3.3. We solve (3.28) numerically to calculate the effective wavenumber $k_*(\omega)$, and also combine (3.28) with both normalisation conditions (3.33) and (3.34) to calculate $F_{\boldsymbol{n}}^{(\pm)}(\boldsymbol{\lambda})$, which feeds into (3.29) to reach both average reflection and transmission coefficients, $\langle R\rangle$ and $\langle T\rangle$ in (3.1). This procedure is the result of the effective waves method discussed in Section 3.5 (or "EW method" in the labels of the graphs).

Most analytic expressions so far are formulated in terms of the particle number density $\mathfrak{n}(\boldsymbol{\lambda})$, for both simplicity and consistency with the work from which our results are derived in Chapter 2. However, to provide a more intuitive interpretation of numerical calculations, in this section we express all results in terms of the dimensionless volume fractions, $\phi(\boldsymbol{\lambda})$ and φ, as defined in (3.36).

In what follows, we explore examples of particulates with two types of particles sus-

pended in water, bubbles (b) or solid powder (p). Then, we write down the following volume fraction distribution of particles

$$\phi(\boldsymbol{\lambda}) = \phi_b(a_b) + \phi_p(a_p), \tag{3.38}$$

where $\phi_{(.)}$ is the volume fraction, which depends on particle radius $a_{(.)}$ only, for either the bubbles (b) or powder (p). The acoustic properties of each type of particle are provided in Table 1.

	Material	Mass density	Speed of sound
Matrix medium	Water	ϱ_0	c_0
Exterior medium	Metal	$\varrho = 3\varrho_0$	$c = 3c_0$
Particles	Powder	$\varrho_p = 13\varrho_0$	$c_p = 2.5c_0$
	Bubbles	$\varrho_b = 0.01\varrho_0$	$c_b = 0.01c_0$

Table 1: Acoustic properties of each material used in the numerical examples in this section. All properties are defined relative to the mass density and speed of sound of "water", which is the medium of the matrix (see Figure 3.3).

We note that, in Table 1 above, we assume that no material in the particulate has frequency dependent properties. In practice, depending on the size of particles — and consequently on the wavelength range — both bubbles and powder have frequency dependent properties due to resonances or thermal and viscous effects [10, 23]. Although the model can accommodate frequency dependent properties for the particles (see Section 3.2), we leave this discussion to future work, and focus on multiple scattering effects in the context of ensemble averaging, which include frequency dependent behaviour and attenuation on its own.

Although the particles are sound penetrable, we refer to powder and bubbles as sound-hard like and sound-soft like scatterers in this chapter, due to the large contrast in acoustic impedance between these particles and the matrix ($\varrho_p c_p \gg \varrho_0 c_0$ and $\varrho_b c_b \ll \varrho_0 c_0$ in Table 1).

3.6.1 Limiting cases on a monodisperse particulate

We calculate the average reflection and transmission coefficients (3.23) for a layer of particles suspended in water, with exterior medium being metal (see Table 1). We assume a monodisperse distribution of powder, which is given by the volume fraction (3.38), where

$$\phi_b(a_b) = 0 \quad \text{and} \quad \phi_p(a_p) = \varphi\, \delta(a_p - a), \tag{3.39}$$

and δ is the Dirac delta distribution.

Figure 3.4 below shows the result of the numerical simulation of $\langle R \rangle$ and $\langle T \rangle$ for $\varphi = 20\%$ of powder in the matrix. The figure also shows the agreement between simulated values and limiting cases of both lower and higher frequencies. The low frequency limit (blue dashed curve) is given by an effective medium with constant properties, given by (3.1) and (3.2), while the high frequency behaviour is similar to the case of no particles in the layer, as discussed in Section 3.5.3. Both dashed curves are periodic, so we only represent their values in the region of interest for comparison against the solid black curve.

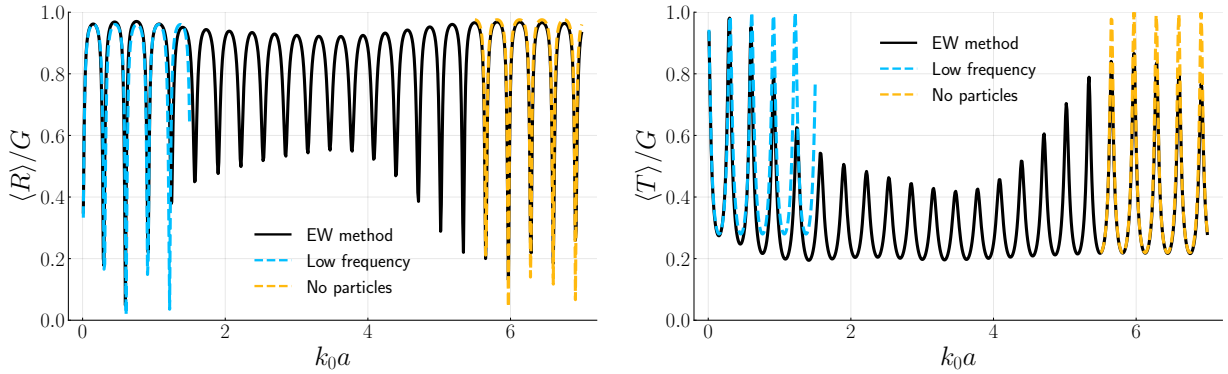

Figure 3.4: Absolute values of the average reflection coefficient $\langle R \rangle$ (on the left) and the average transmission coefficients $\langle T \rangle$ (on the right) for powder in water, see Table 1. The matrix has $\varphi = 20\%$ volume fraction of particles in a fluid layer of thickness $d = 10a$, where a is particle radius. The wavenumber of the matrix is k_0, and the incident wave has amplitude G. On both sides, we compare the results using the effective waves method ("EW method"; black curve), and the dashed curves, which represent the leading order contribution at low frequency (blue curve), and the case of no particles in the matrix (yellow curve).

We note that the curves for either $\langle R \rangle$ and $\langle T \rangle$ in Figure 3.4 have sharp valleys and peaks, respectively, usually referred to as Fabry-Pérot resonances in the literature [24]. However, Figure 3.4 does not have a sufficiently fine mesh to distinguish if these peaks and valleys reach full transmission ($\langle R \rangle = 0$ and $\langle T \rangle = 1$). To better resolve these resonances, and to illustrate the agreement between the lower and higher frequency cases, we plot these curves with a finer mesh in Figure 3.5 below.

From the curves in Figure 3.5, we reach three conclusions: 1) the low frequency effective medium description closely matches $\langle R \rangle$ and $\langle T \rangle$ for $k_0 a < 0.2$, and remains a reasonable approximation through the first few resonances; 2) only the first few Fabry-Pérot resonances achieve full transmission; and 3) at higher frequencies ($k_0 a \gg 1$), $\langle R \rangle$ and $\langle T \rangle$ converge to the reflection and transmission coefficients of a homogeneous layer for most

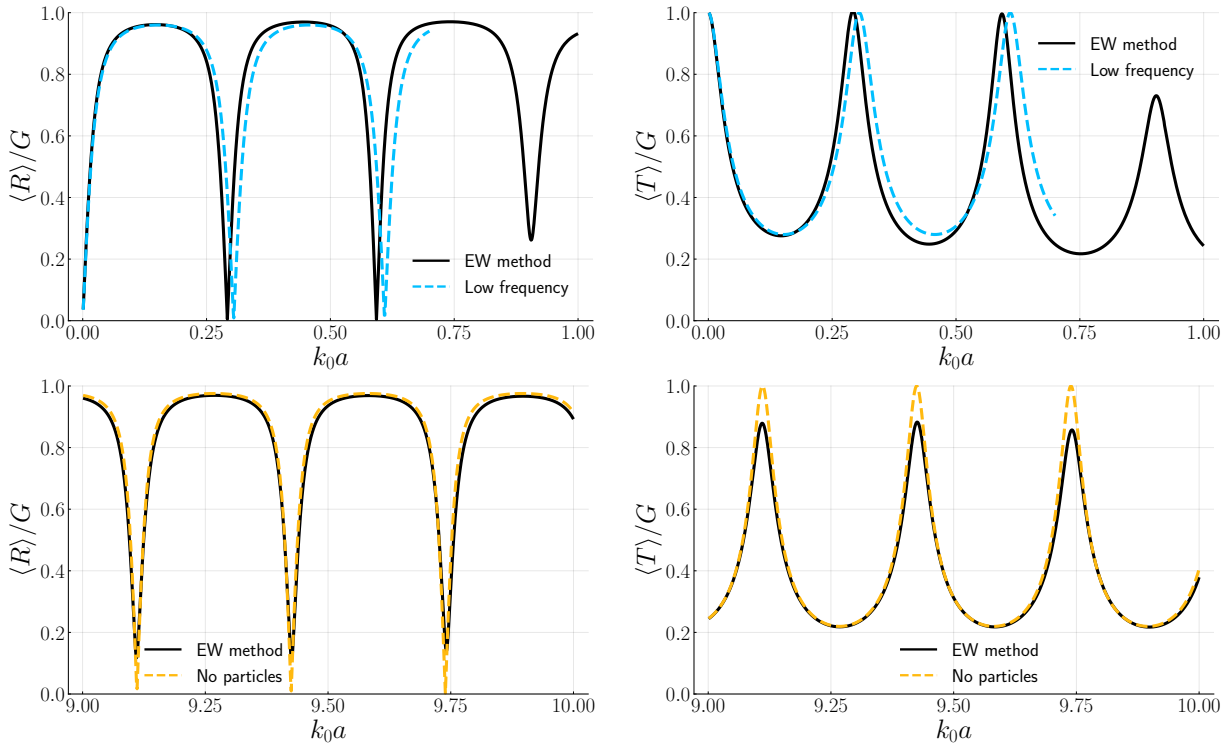

Figure 3.5: Finer mesh plot of the curves in Figure 3.4. The absolute values for the average reflection coefficient $\langle R\rangle$ (on the left) and the average transmission coefficients $\langle T\rangle$ (on the right) are represented for lower (on the top) and higher frequencies (on the bottom).

frequencies, diverging only near resonances due to amplitude attenuation. The first two of these conclusions are consistent with the experimental results reported in [24], while the third highlights an important feature of ensemble averaging of waves: the emergence of attenuation effects even in the absence of any physical energy dissipation mechanism.

To further investigate this attenuation, we begin with the definition of average intensity of the incident field (3.4), which is proportional to the energy density carried by the incident wave from the exterior medium

$$\frac{1}{4L^2}\int_{[-L,L]\times[-L,L]}\langle u_{\text{in}}(x,y,0)\overline{u_{\text{in}}}(x,y,0)\rangle \mathrm{d}x\mathrm{d}y = |G|^2, \tag{3.40}$$

where the overline represents complex conjugation. Because there is no dissipation or absorption, the energy that leaves the layer should match (3.40), which reads

$$\frac{1}{4L^2}\int_{[-L,L]\times[-L,L]}\Big[\langle u_{\text{rf}}(x,y,0)\overline{u_{\text{rf}}}(x,y,0)\rangle + \langle u_{\text{tr}}(x,y,d)\overline{u_{\text{tr}}}(x,y,d)\rangle\Big]\mathrm{d}x\mathrm{d}y = |G|^2, \tag{3.41}$$

Then, we apply the mean average square inequality, $\langle AA^*\rangle \geq |\langle A\rangle|^2$, to both reflected and

transmitted fields in (3.41), which leads to the following relation

$$|\langle R\rangle|^2 + |\langle T\rangle|^2 \leq |G|^2. \tag{3.42}$$

where the equality holds for a homogeneous layer, without particles.

The quantity on the left-hand side of (3.42) represents the intensity of the average wave, i.e., the energy density associated with coherent scattering by the particles. The remainder of the incident wave's energy density averages to zero due to phase cancellation among scattered waves from different particle configurations. This part of the field, which vanishes upon averaging, is referred to as an incoherently scattered wave. This energy loss due to incoherence leads to an imaginary part of the effective wavenumber $k_*(\omega)$, which introduces the apparent attenuation that broadens the peaks and valleys of Fabry-Pérot resonances in Figure 3.5. We illustrate this phenomenon in Figure 3.6, where the apparent energy loss for the layer is compared against an exponentially scaled curve of the effective attenuation.

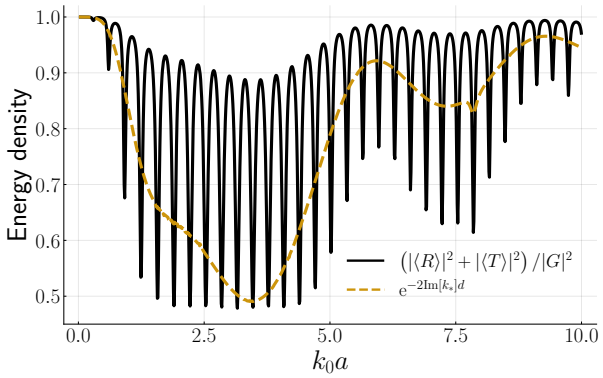

Figure 3.6: Apparent energy loss (solid line) due to incoherent scattering of particles in the layer described in the caption of Figure 3.4. The dashed line represents an exponentially scaled curve of attenuation.

The valleys of the solid black line in Figure 3.6 correspond to the Fabry-Pérot resonances, and the average reflection (and transmission) deviates from the pattern of a homogeneous layer with no particles, see bottom curves in Figure 3.5. This deviation at really short wavelengths, $k_0 a > 9$, is connected with the technical difficulties to reach an analytical closed-form expression for the high frequency limit in Section 3.5.3. However, away from Fabry-Pérot resonances (away from the valleys), the average reflection and transmission is well approximated by a homogeneous layer with no particles, as discussed in Section 3.5.3, and exemplified by the bottom graphs in Figure 3.5.

We also point out that the Fabry-Pérot resonance frequencies depend on the thickness

of the layer, $d = 10a$ in Figures 3.4 and 3.5. The thicker the layer, the low-frequency approximation is valid only around fewer first resonances. This dependence on thickness is illustrated by Figure 3.7 in Section 3.6.2, where the resonances for $k_0 a < 1$ occur twice more often for $d = 20a$ than in Figure 3.5 for $d = 10a$.

3.6.2 Comparison with effective-properties

As discussed in Section 4.1, one common approach to model $\langle R \rangle$ and $\langle T \rangle$ in the literature is to introduce frequency dependent effective-properties, which are wavespeed $c_*(\omega)$, attenuation $\alpha_*(\omega)$, and mass density $\varrho_*(\omega)$, and substitute these into the formulas for reflection and transmission for a homogeneous medium (3.1) and (3.2). We call this approach the effective medium extension, and compare it against the effective waves method in this section.

The first two of the effective-properties have a simple relation with the effective wavenumber, which we calculate numerically from (3.28), and are given by

$$c_*(\omega) = \frac{\omega}{\mathrm{Re}[k_*(\omega)]} \quad \text{and} \quad \alpha_*(\omega) = \mathrm{Im}[k_*(\omega)], \tag{3.43}$$

while the effective mass density is less understood for particulates in general, with different models tuned for specific particle properties, frequency and volume fraction ranges. Specifically, inspired by [14, 15], we consider the case where $\varrho_*(\omega)$ is constant and check three possible choices: $\varrho_*(\omega) = \varrho_0$ the matrix mass density, $\varrho_*(\omega) = \varrho_p$ the particle mass density, $\varrho_*(\omega) = \varrho_{\text{mix}}$ the mixture mass density defined below

$$\varrho_{\text{mix}} = \varrho_p \varphi + \varrho_0 (1 - \varphi). \tag{3.44}$$

Then, we substitute these effective-properties into (3.1). Each of the three resulting curves from the effective medium extension, together with $\langle R \rangle$ and $\langle T \rangle$ from the effective waves method, is shown in Figure 3.7 below.

Figure 3.7 shows a remarkable agreement between the solid black and dashed blue curves. This result suggests that only the effective wavenumber, $k_*(\omega)$, needs to be calculated from first principles models, and both $\langle R \rangle$ and $\langle T \rangle$ can be calculated simply from (3.1) with a constant effective mass density, same as the matrix $\varrho_* = \varrho_0$. The frequency dependent wavespeed and attenuation are given by (3.43) in this effective medium extension. In fact, we selected the acoustic properties of the powder in Table 1 to reproduce the exact contrasts in wavespeed and mass density between scatterers and matrix medium reported in [15].

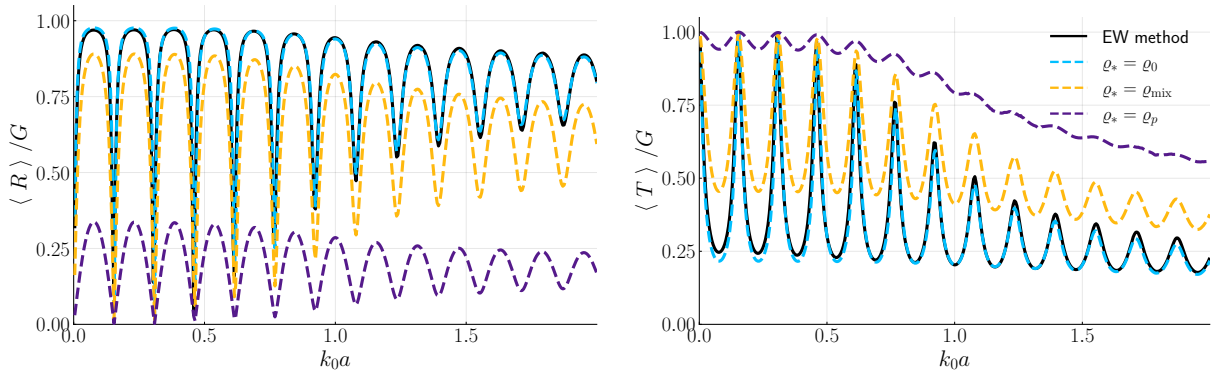

Figure 3.7: Absolute values of the average reflection coefficient $\langle R \rangle$ (on the left) and the average transmission coefficients $\langle T \rangle$ (on the right) for powder in water, see Table 1. The matrix has $\varphi = 10\%$ volume fraction of particles in a fluid layer of thickness $d = 20a$, where a is the particle radius. The wavenumber of the matrix is k_0, and the incident wave has amplitude G. On both sides, we plot the results using the effective waves method ("EW method"; black curve), and the dashed curves, which are given by the effective medium extension with different options for the effective mass density ϱ_*.

Although the effective waves method is in good qualitative agreement with the effective medium extension from [14, 15], two main observations should be noted: 1) in this paper, we focus exclusively on acoustic scattering. To account for reflection and transmission of both pressure and shear waves, our results would need to be generalised to elastic waves, as done in [25]; and 2) the procedure is not guaranteed to be accurate for cases beyond weak scatterers with sound-hard like boundaries. When dealing with stronger scatterers, which may be due to internal resonances of the particles or high contrast impedance of sound-soft like material, even multiple effective wavenumbers may arise (see [26]), and it is not clear how to calculate (3.1) in this case.

To provide an example of a particulate layer with strong scatterers, we repeat the calculations in Figure 3.7 for the case of bubbles in Table 1, which are sound-soft like, and the curves of $\langle R \rangle$ and $\langle T \rangle$ are shown in Figure 3.8 below. The curves in Figure 3.8 were generated in analogy to Figure 3.7, with the volume fraction distribution for the particulate given by

$$\phi_p(a_b) = \varphi\, \delta(a_b - a) \quad \text{and} \quad \phi_p(a_p) = 0, \tag{3.45}$$

and the formula for ϱ_{mix} given by (3.44), however exchanging ϱ_p by ϱ_b from Table 1. To generate Figure 3.8, we choose properties of the particles so that a single wavenumber provides a good approximation for reflection and transmission (see [26] for phase diagrams on multiple wavenumbers).

In Figure 3.8, we see no region of dimensionless wavenumber frequency, k_0a, with

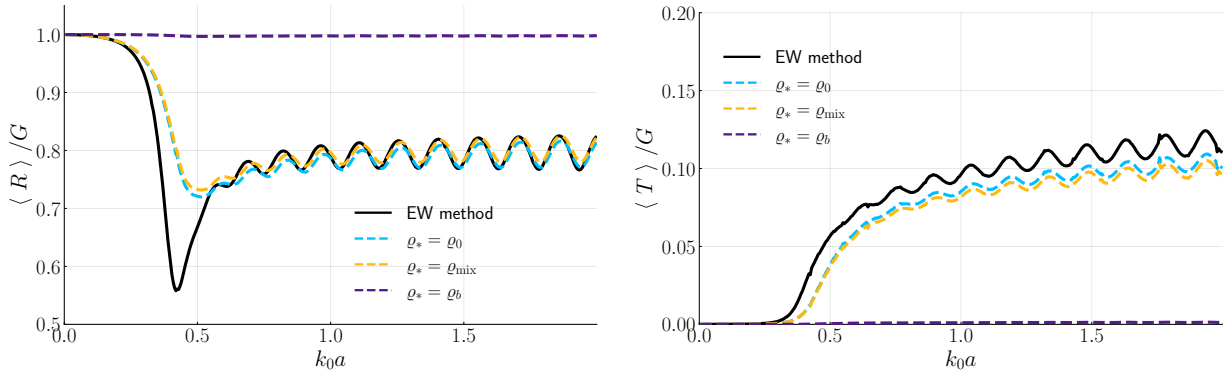

Figure 3.8: Absolute value of the average reflection coefficient $\langle R \rangle$ (on the left) and the average transmission coefficients $\langle T \rangle$ (on the right) for bubbles in water, see Table 1. The matrix has $\varphi = 5\%$ volume fraction of particles in a fluid layer of thickness $d = 20a$, where a is the particle radius. The wavenumber of the matrix is k_0, and the incident wave has amplitude G. On both sides, we plot the results using the effective waves method ("EW method"; black curve), and the dashed curves, which are given by the effective medium extension with different options for the effective mass density ϱ_*.

an agreement between the effective-properties approach (dashed lines), and the effective waves method (solid black line). For frequencies lower than $k_0 a = 0.4$, there is no transmission due to strong reflection; however, the reflection is consistently larger for the effective-properties approach compared to the effective waves method. The opposite happens for frequencies larger than $k_0 a = 0.6$, where the reflection coefficients are similar, while the transmission for the effective waves method is consistently lower. Within the mid-range frequency band, $0.4 \leq k_0 a \leq 0.6$, we have clear disagreement between both $\langle R \rangle$ and $\langle T \rangle$. We also point out that the contrast of the acoustic properties between bubbles and the background medium is high, which results in total reflection for the effective-properties approach when $\varrho_* = \varrho_b$ in Figure 3.8.

3.6.3 A mixture of bubbles and powder

To explore a polydisperse distribution of particles discussed in Sections 3.3 and 3.5, we present numerical simulations of a layer filled with a mixture of powder and bubbles with acoustic properties defined in Table 1. We start with both bubble and powder particles with the same radius, which leads to the following volume fraction distribution

$$\phi_b(a_b) = 0.05\,\delta(a_b - a) \quad \text{and} \quad \phi_p(a_p) = 0.1\,\delta(a_p - a), \tag{3.46}$$

where there is 5% of bubbles and 10% of powder, with a total particle volume fraction of $\varphi = 15\%$. Figure 3.9 shows the average reflection and transmission coefficients calculated

via the effective waves method for the polydisperse case in (3.46). Alongside, the figure also shows the curves for an isolated monodisperse particulate, containing either only 10% of powder, or 5% of bubbles.

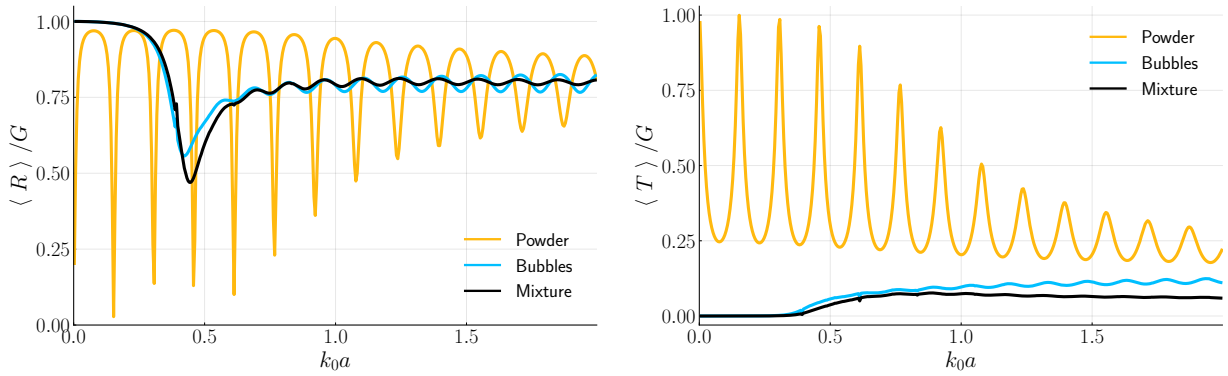

Figure 3.9: Absolute values of the average reflection coefficient $\langle R \rangle$ (on the left) and the average transmission coefficients $\langle T \rangle$ (on the right) for a mixture of bubbles and powder in water, see Table 1. The volume fraction of particles is given by (3.46), in a layer of thickness $d = 20a$, where a is the particle radius. The wavenumber of the matrix is k_0, and the incident wave has amplitude G. On both sides, we compare the results using the effective waves method (solid curves) for the complete mixture (black curve), and the case of a layer filled with each individual particle component: powder (yellow curve) and bubbles (blue curve).

In Figure 3.9, it is clear how the strong scattering behaviour of the bubbles dominate the reflection and transmission throughout the whole frequency range of the plot. For values of $k_0 a < 0.4$, the oscillatory behaviour due to Fabry-Pérot resonance for the case of monodisperse powder is completely wiped out by the strong reflection due to the bubbles. We also note that, although the Helmholtz equation is linear, the reflection and transmission coefficients for the mixture cannot be calculated by a superposition of both curves for the monodisperse particulates. That happens because the effective wavenumber comes from a non-linear dispersion equation (3.28). In other words, each of the three curves in the graphs of Figure 3.9 is an independent numerical simulation, which illustrates the difficulties in dealing with the polydisperse distribution of particles in particulate materials.

One interesting question is if this trend also holds when there is a separation of length scales for the particle radii in the mixture. To address this question, we compute one last numerical example, where we take the same particulate as in Figure 3.9, however with a larger radius for the bubbles. The volume fraction distribution is then given by

$$\phi_b(a_b) = 0.05\,\delta(a_b - 4a) \quad \text{and} \quad \phi_p(a_p) = 0.1\,\delta(a_p - a), \tag{3.47}$$

where the bubbles are four times larger than the particles of powder. The result is shown in Figure 3.10 below.

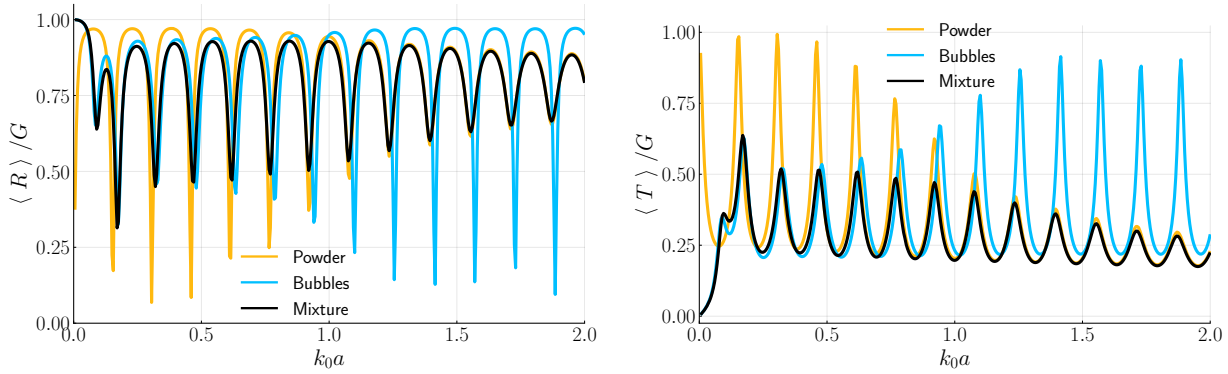

Figure 3.10: Absolute values of the average reflection coefficient $\langle R \rangle$ (on the left) and the average transmission coefficients $\langle T \rangle$ (on the right) for a mixture of bubbles and powder in water, see Table 1. The volume fraction of particles is given by (3.46), in a layer of thickness $d = 20a$, where a is the radius of powder particles. The wavenumber of the matrix is k_0, and the incident wave has amplitude G. On both sides, we compare the results using the effective waves method (solid curves) for the complete mixture (black curve), and the case of a layer filled with each individual particle component: powder (yellow curve) and bubbles (blue curve).

In Figure 3.10, there is a clear transition of the reflection and transmission curves when varying frequency. At lower frequencies ($k_0 a < 0.1$), the curves for the mixture (black curves) are close to the ones for bubbles only (blue curves). When the wavelength is much shorter than the radius of the bubbles, $4a$, but not too short compared to the powder, a, the curves of the mixture agree with the ones for the powder (yellow curves). In midrange frequencies ($0.1 < k_0 a < 1.2$), there is a transition region from the mixture behaving similarly to the monodisperse distribution of bubbles, into monodisperse powder. This behaviour is also seen in the effective wavespeed and attenuation, c_* and α_*, which are shown in Figure 3.11.

The left-hand side of Figure 3.11 illustrates the strong reflection of the mixture at low frequencies, due to a large contrast between effective wavespeed and speed of sound in the exterior medium (c). This frequency range is dominated by strong scattering from the bubbles, once again. As frequency increases, the wavespeed gets closer to the speed of sound in the matrix (c_0), and there is less contrast. The right-hand side of Figure 3.11 illustrates the transition of the incoherent scattering by the mixture, from attenuation similar to the case of monodisperse bubbles for lower frequencies, into attenuation similar to monodisperse powder for higher frequencies. We also point out that there is not much contrast in wavespeed for the case of monodisperse powder, compared to either the mixture or the

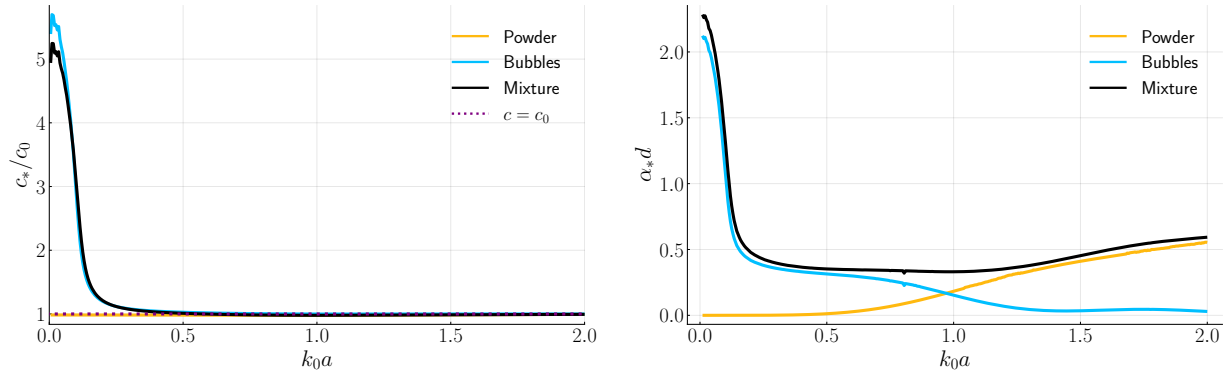

Figure 3.11: Non-dimentional plots of effective wavespeed (c_*/c_0 on the left), and effective attenuation ($\alpha_* d$ on the right), for the layer filled with particulate described in the caption of Figure 3.10. On both sides, we compare the results using the effective waves method (solid curves) for the complete mixture (black curve), and the case of a layer filled with each individual particle component: powder (yellow curve) and bubbles (blue curve). The dotted purple curve on the left highlights the value at which effective wavespeed is the same as the speed of sound in the matrix ($c_* = c_0$).

bubbles, for all frequency range in Figure 3.11.

The numerical results in both Figures 3.10 and 3.11 illustrate the high frequency behaviour of the particulate as discussed in Section 3.5.3. When the wavelength in the matrix is much shorter than the size of the bubbles, $4k_0a > 1$, but still comparable to powder particles, $k_0a \approx 1$, both average reflection and transmission coefficients are well approximated by a particulate with no bubbles, and only powder. This frequency separation of length scales is important for sensing applications. For example, if the goal is to sense powder in water, and bubbles are unavoidable in the mixture, the measurements of reflectance and transmittance can still be useful for a broad range of frequencies if the bubbles are much larger than the particles in the powder.

3.7 Conclusion

In this work, we solve the problem of acoustic wave scattering by a layer filled with randomly placed spherical particles, composed of any homogeneous material. Although the effective waves method used in this paper can be applied to any material geometry [13], we focus on the case of plane wave incidence in a layer without any dissipative effects or absorption. The assumptions we make in this paper are not just mere simplifications to obtain numerical computations; in fact, the case of a layer is broadly applicable to experimental investigation of particulates and their properties [14], or in characterisation settings for sensing applications [8]. On top of that, the attenuation of the average wave

due to incoherent scattering is an important concept to study in average scattering by random particulates, which could be masked by dissipative effects, if included.

Theoretical results. Our main theoretical contribution to random particulate materials is to show how to combine results from average wave scattering in the presence of interfaces, using the eXtended Quasi-Crystalline Approximation (X-QCA) derived in Chapter 2, together with the statistical description of polydisperse distribution of particles in a particulate, using the effective waves method from [13, 18].

From the expressions for the ensemble average reflection and transmission coefficients, we reach an approximate high frequency behaviour, which is equivalent to the response of the background matrix with no particles, together with some residual attenuation due to incoherent scattering. Our model is also consistent with both canonical scattering limits and the effective material properties in the low frequency limit [12, 13].

Numerical results. To investigate if our model predicts recent experimental findings for particulate layers, we calculate both average reflection and transmission coefficients numerically, given by $\langle R \rangle$ and $\langle T \rangle$ in (3.23). These simulations lead to two main results for sound-hard like (solid) particles: 1) both average $\langle R \rangle$ and $\langle T \rangle$ are well approximated by a constant effective density equal to the background matrix density ($\varrho_* = \varrho_0$), with only the need for frequency dependent effective wavespeed and attenuation; and 2) our simulations predict Fabry-Pérot resonances with almost full transmission for lower frequencies. These phenomena were observed experimentally in [14, 15] and [24], respectively.

Beyond asserted predictions, we also provide examples of simulations with sound-soft particles (bubbles), for which these phenomena are not present, and a first principles model is needed to describe a broad frequency response for both reflection and transmission coefficients. In other words, our models present evidence that constant effective density may not provide an accurate description for the average reflection and transmission of all types of material, especially for bubbles in a liquid background.

Non-intrusive transmission sensing. The extension of the results for average reflection from a halfspace in Chapter 2 provides a model which is sensitive to particle size for particles that are denser than the background matrix, as illustrated by the average transmission values in Figure 3.7. Reflection measurements are known to be much less sensitive in this case (see [14] and Section 2.8.3). On top of that, adding the effect of interfaces between exterior medium and matrix for polydisperse distributed particles allows to extend usual non-invasive and non-intrusive particle size distribution sensing strategies [1, 8].

Moreover, we show that in mixtures containing particles of different sizes or properties, the contribution of larger particles to the reflected and transmitted waves can reach the high-frequency regime at shorter wavelengths compared to smaller particles. Although this

result is expected from length scale separation arguments, our models can quantify this contribution for any type of homogeneous acoustic material, which is useful in designing optimal devices for particle size measurements.

Future avenues. Apart from experimental validation of the claims stated above, one clear path for future work is to extend these models to full linear elasticity, including both longitudinal and shear waves. Another important addition would be dissipation through viscosity and thermal effects, which would introduce absorption of energy by the background matrix and particles, allowing for direct quantitative comparison against experimental data, such as in [14, 15, 24] and others.

Acknowledgements

Paulo Piva gratefully acknowledges funding from an EPSRC Case studentship with Johnson Matthey. Art Gower gratefully acknowledges support from EPSRC (EP/V012436/1).

Appendices

3.A Regular spherical to plane wave

Based on the translation symmetry results discussed in Appendix 2.C, we equate both expressions for the average regular wave (3.16) and (3.18). Then, from the plane wave expansion in spherical harmonics (2.64), together with their standard orthogonality relations, we reach

$$\langle g_{\boldsymbol{n}} \rangle = \mathrm{C}^{+}_{\boldsymbol{n}} \langle A_{+} \rangle + \mathrm{C}^{-}_{\boldsymbol{n}} \langle A_{-} \rangle, \tag{3.48}$$

with the coefficients $C^{\pm}_{\boldsymbol{n}}$ given by

$$\mathrm{C}^{\pm}_{(\ell,m)} = 4\pi \mathrm{i}^{\ell} \mathrm{Y}_{(\ell,m)}(\pm\hat{\boldsymbol{z}}) = 4\pi \mathrm{i}^{\pm\ell} \mathrm{Y}_{(\ell,m)}(\hat{\boldsymbol{z}}) = 4\pi (\pm\mathrm{i})^{\ell} \mathrm{Y}_{(\ell,m)}(\hat{\boldsymbol{z}}),$$

where we choose the following convention for the spherical harmonic functions

$$\mathrm{Y}_{(\ell,m)}(\hat{\boldsymbol{r}}) = (-1)^{m} \sqrt{\frac{2\ell+1}{4\pi} \frac{(\ell-m)!}{(\ell+m)!}} \mathrm{P}^{m}_{\ell}(\cos\theta) \mathrm{e}^{\mathrm{i}m\phi},$$

with P^{m}_{ℓ} being the usual associated Legendre polynomials.

3.B Calculations for normalisation condition

In this appendix, we write the expression of (3.31) explicitly in terms of complex exponentials to simplify the ensemble boundary conditions (3.30), and reach a pair of normalisation conditions in Section 3.5.2. We start by rewriting (3.31) as follows

$$\mathrm{J}^{(\pm)}_{\boldsymbol{n}'\boldsymbol{n}} = \frac{\mathcal{I}^{(\pm)}_{\boldsymbol{n}'\boldsymbol{n}}(z_1)}{F^{(\pm)}_{\boldsymbol{n}'}(\boldsymbol{\lambda}_2)} = \int_{\partial\mathcal{R}_2} \mathcal{U}_{\boldsymbol{n}'\boldsymbol{n}}(k_0\boldsymbol{r}_1 - k_0\boldsymbol{r}_2) \frac{\partial \mathrm{e}^{\pm \mathrm{i}k_* z_2}}{\partial \boldsymbol{\nu}_2} - \frac{\partial \mathcal{U}_{\boldsymbol{n}'\boldsymbol{n}}(k_0\boldsymbol{r}_1 - k_0\boldsymbol{r}_2)}{\partial \boldsymbol{\nu}_2} \mathrm{e}^{\pm \mathrm{i}k_* z_2} \mathrm{d}A_2, \tag{3.49}$$

and we use the expressions of the addition translation matrices in [13, eq. B.3], together with the property of spherical waves that $\mathrm{u}_{\boldsymbol{n}}(-\boldsymbol{x}) = (-1)^{\ell} \mathrm{u}_{\boldsymbol{n}}(\boldsymbol{x})$, to write down the follow-

ing expression for the $(+)$ term in (3.49)

$$\mathrm{J}^{(+)}_{\boldsymbol{n}'\boldsymbol{n}} = \sum_{\boldsymbol{n}_1}(-1)^{\ell_1} c_{\boldsymbol{n}'\boldsymbol{n}\boldsymbol{n}_1}\Bigg[\int_{z_2=d-a_2} \mathrm{u}_{\boldsymbol{n}_1}(k_0\boldsymbol{r}_2-k_0\boldsymbol{r}_1)\frac{\partial \mathrm{e}^{\mathrm{i}k_* z_2}}{\partial z_2} - \frac{\partial \mathrm{u}_{\boldsymbol{n}_1}(k_0\boldsymbol{r}_2-k_0\boldsymbol{r}_1)}{\partial z_2}\mathrm{e}^{\mathrm{i}k_* z_2}\mathrm{d}A_2 \\ - \int_{z_2=a_2} \mathrm{u}_{\boldsymbol{n}_1}(k_0\boldsymbol{r}_2-k_0\boldsymbol{r}_1)\frac{\partial \mathrm{e}^{\mathrm{i}k_* z_2}}{\partial z_2} - \frac{\partial \mathrm{u}_{\boldsymbol{n}_1}(k_0\boldsymbol{r}_2-k_0\boldsymbol{r}_1)}{\partial z_2}\mathrm{e}^{\mathrm{i}k_* z_2}\mathrm{d}A_2\Bigg].$$

We perform the change of variables $\boldsymbol{r}_2 \to \boldsymbol{r} = \boldsymbol{r}_2 - \boldsymbol{r}_1$ in the equation above, which leads to

$$\mathrm{J}^{(+)}_{\boldsymbol{n}'\boldsymbol{n}} = \sum_{\boldsymbol{n}_1}(-1)^{\ell_1} c_{\boldsymbol{n}'\boldsymbol{n}\boldsymbol{n}_1}\Bigg[\int_{z=d-a_2-z_1} \mathrm{u}_{\boldsymbol{n}_1}(k_0\boldsymbol{r})\frac{\partial \mathrm{e}^{\mathrm{i}k_*(z+z_1)}}{\partial z} - \frac{\partial \mathrm{u}_{\boldsymbol{n}_1}(k_0\boldsymbol{r})}{\partial z}\mathrm{e}^{\mathrm{i}k_*(z+z_1)}\mathrm{d}A \\ - \int_{z=a_2-z_1} \mathrm{u}_{\boldsymbol{n}_1}(k_0\boldsymbol{r})\frac{\partial \mathrm{e}^{\mathrm{i}k_*(z+z_1)}}{\partial z} - \frac{\partial \mathrm{u}_{\boldsymbol{n}_1}(k_0\boldsymbol{r})}{\partial z}\mathrm{e}^{\mathrm{i}k_*(z+z_1)}\mathrm{d}A\Bigg].$$

Then, we use [13, eq. F.1] to obtain

$$\mathrm{J}^{(+)}_{\boldsymbol{n}'\boldsymbol{n}} = \frac{\mathcal{I}^{(+)}_{\boldsymbol{n}'\boldsymbol{n}}(z_1)}{F^{(+)}_{\boldsymbol{n}'}(\boldsymbol{\lambda}_2)} = \sum_{\boldsymbol{n}_1}(-1)^{\ell_1} c_{\boldsymbol{n}'\boldsymbol{n}\boldsymbol{n}_1}\left[L_{\boldsymbol{n}_1}(d-a_2-z_1) - L_{\boldsymbol{n}_1}(a_2-z_1)\right]\mathrm{e}^{\mathrm{i}k_* z_1},$$

which is valid in the bulk region of the particulate $\mathcal{R}_{\text{Bulk}}$, defined as $a_1+a_2 < z_1 < d-a_1-a_2$ in analogy with (2.49) in Chapter 2. Substituting [13, eq. F.6] into the above, we reach

$$\frac{\mathcal{I}^{(+)}_{\boldsymbol{n}'\boldsymbol{n}}(z_1)}{F^{(+)}_{\boldsymbol{n}'}(\boldsymbol{\lambda}_2)} = \frac{2\pi\mathrm{i}}{k_0^2}\sum_{\boldsymbol{n}_1}\mathrm{i}^{\ell_1} c_{\boldsymbol{n}'\boldsymbol{n}\boldsymbol{n}_1}\Big[\mathrm{Y}_{\boldsymbol{n}_1}(\hat{\boldsymbol{z}})(k_*-k_0)\mathrm{e}^{\mathrm{i}(k_*+k_0)(d-a_2)}\mathrm{e}^{-\mathrm{i}k_0 z_1} \\ - \mathrm{Y}_{\boldsymbol{n}_1}(-\hat{\boldsymbol{z}})(k_*+k_0)\mathrm{e}^{\mathrm{i}(k_*-k_0)a_2}\mathrm{e}^{\mathrm{i}k_0 z_1}\Big].$$

The last step for the $(+)$ term in (3.49) is to substitute [13, eqs. B.11 and B.12] and (3.48) into the above, which leads to

$$\frac{\mathcal{I}^{(+)}_{\boldsymbol{n}'\boldsymbol{n}}(z_1)}{F^{(+)}_{\boldsymbol{n}'}(\boldsymbol{\lambda}_2)} = \frac{\mathrm{i}}{2k_0^2}\Big[\mathrm{C}^{-}_{\boldsymbol{n}}\mathrm{C}^{+}_{\boldsymbol{n}'}(k_*-k_0)\mathrm{e}^{\mathrm{i}(k_*+k_0)(d-a_2)}\mathrm{e}^{-\mathrm{i}k_0 z_1} \\ - \mathrm{C}^{+}_{\boldsymbol{n}}\mathrm{C}^{-}_{\boldsymbol{n}'}(k_*+k_0)\mathrm{e}^{\mathrm{i}(k_*-k_0)a_2}\mathrm{e}^{\mathrm{i}k_0 z_1}\Big]. \quad (3.50)$$

For the $(-)$ term in (3.49), we substitute [13, eq. B.3] into (3.49) and perform the

change of coordinates $\boldsymbol{r}_2 \to \boldsymbol{r} = \boldsymbol{r}_1 - \boldsymbol{r}_2$ to obtain

$$\frac{\mathcal{I}^{(-)}_{\boldsymbol{n}'\boldsymbol{n}}(z_1)}{F^{(-)}_{\boldsymbol{n}'}(\boldsymbol{\lambda}_2)} = -\sum_{\boldsymbol{n}_1} c_{\boldsymbol{n}'\boldsymbol{n}\boldsymbol{n}_1}\left[\int_{z=z_1+a_2-d} \mathrm{u}_{\boldsymbol{n}_1}(k_0\boldsymbol{r})\frac{\partial \mathrm{e}^{\mathrm{i}k_*(z-z_1)}}{\partial z} - \frac{\partial \mathrm{u}_{\boldsymbol{n}_1}(k_0\boldsymbol{r})}{\partial z}\mathrm{e}^{\mathrm{i}k_*(z-z_1)}\mathrm{d}A \right.$$
$$\left. - \int_{z=z_1-a_2} \mathrm{u}_{\boldsymbol{n}_1}(k_0\boldsymbol{r})\frac{\partial \mathrm{e}^{\mathrm{i}k_*(z-z_1)}}{\partial z} - \frac{\partial \mathrm{u}_{\boldsymbol{n}_1}(k_0\boldsymbol{r})}{\partial z}\mathrm{e}^{\mathrm{i}k_*(z-z_1)}\mathrm{d}A\right].$$

Then, once again, we use [13, eq. F.1] to write down

$$\frac{\mathcal{I}^{(-)}_{\boldsymbol{n}'\boldsymbol{n}}(z_1)}{F^{(-)}_{\boldsymbol{n}'}(\boldsymbol{\lambda}_2)} = -\sum_{\boldsymbol{n}_1} c_{\boldsymbol{n}'\boldsymbol{n}\boldsymbol{n}_1}\left[L_{\boldsymbol{n}_1}(z_1+a_2-d) - L_{\boldsymbol{n}_1}(z_1-a_2)\right]\mathrm{e}^{-\mathrm{i}k_*z_1}.$$

Then, we restrict the values of z_1 to the region $a_1 + a_2 < z_1 < d - a_1 - a_2$, which makes it possible to use [13, eq. F.6] to express the above as

$$\frac{\mathcal{I}^{(-)}_{\boldsymbol{n}'\boldsymbol{n}}(z_1)}{F^{(-)}_{\boldsymbol{n}'}(\boldsymbol{\lambda}_2)} = -\frac{2\pi\mathrm{i}}{k_0^2}\sum_{\boldsymbol{n}_1}\mathrm{i}^{\ell_1}c_{\boldsymbol{n}'\boldsymbol{n}\boldsymbol{n}_1}\left[\mathrm{Y}_{\boldsymbol{n}_1}(\hat{\boldsymbol{z}})(k_*+k_0)\mathrm{e}^{\mathrm{i}(k_*-k_0)(a_2-d)}\mathrm{e}^{-\mathrm{i}k_0z_1}\right.$$
$$\left. - \mathrm{Y}_{\boldsymbol{n}_1}(-\hat{\boldsymbol{z}})(k_*-k_0)\mathrm{e}^{\mathrm{i}(k_*+k_0)(-a_2)}\mathrm{e}^{\mathrm{i}k_0z_1}\right]$$

The last step for the $(-)$ term in (3.49) is to substitute [13, eqs. B.11 and B.12] and (3.48) into the above, and we obtain

$$\frac{\mathcal{I}^{(-)}_{\boldsymbol{n}'\boldsymbol{n}}(z_1)}{F^{(-)}_{\boldsymbol{n}'}(\boldsymbol{\lambda}_2)} = \frac{-\mathrm{i}}{2k_0^2}\left[\mathrm{C}^-_{\boldsymbol{n}}\mathrm{C}^+_{\boldsymbol{n}'}(k_*+k_0)\mathrm{e}^{-\mathrm{i}(k_*-k_0)(d-a_2)}\mathrm{e}^{-\mathrm{i}k_0z_1}\right.$$
$$\left. - \mathrm{C}^+_{\boldsymbol{n}}\mathrm{C}^-_{\boldsymbol{n}'}(k_*-k_0)\mathrm{e}^{-\mathrm{i}(k_*+k_0)a_2}\mathrm{e}^{\mathrm{i}k_0z_1}\right]. \quad (3.51)$$

Joining both results (3.50) and (3.51) in one expression, we have

$$\frac{\mathcal{I}^{(\pm)}_{\boldsymbol{n}'\boldsymbol{n}}(z_1)}{F^{(\pm)}_{\boldsymbol{n}'}(\boldsymbol{\lambda}_2)} = \frac{-\mathrm{i}}{2k_0^2}\left[\mathrm{C}^-_{\boldsymbol{n}}\mathrm{C}^+_{\boldsymbol{n}'}(k_*\mp k_0)\mathrm{e}^{\pm\mathrm{i}(k_0\pm k_*)(d-a_2)}\mathrm{e}^{-\mathrm{i}k_0z_1}\right.$$
$$\left. + \mathrm{C}^+_{\boldsymbol{n}}\mathrm{C}^-_{\boldsymbol{n}'}(k_*\pm k_0)\mathrm{e}^{\pm\mathrm{i}(k_0\mp k_*)a_2}\mathrm{e}^{\mathrm{i}k_0z_1}\right]. \quad (3.52)$$

Bibliography

[1] R C Asher. Ultrasonic sensors in the chemical and process industries. Journal of Physics E: Scientific Instruments, 16(10):959, 1983. doi: 10.1088/0022-3735/16/10/004.

[2] Alexander Prosekov. The effect of ultrasound on the functionality and health-improving properties of dairy products (review). Food Production, Processing and Nutrition, 7(36), 2025. doi: 10.1186/s43014-025-00311-6.

[3] Muhammad Awais Sattar and Dina Shona Laila. A review of ultrasound monitoring applications in agriculture. Frontiers in Plant Science, 16:1620868, 2025. doi: 10.3389/fpls.2025.1620868.

[4] K. K. Phani. Prediction of ultrasonic wave velocities in sintered materials based on the ultrasonic properties of green or partially sintered compacts. Journal of materials science, 43(6):1811–1817, 2008. doi: 10.1007/s10853-007-2425-9.

[5] F. Honarvar and A. Varvani-Farahani. A review of ultrasonic testing applications in additive manufacturing: Defect evaluation, material characterization, and process control. Ultrasonics, 108:106227, 2020. ISSN 0041-624X. doi: 10.1016/j.ultras.2020.106227.

[6] R. E. Challis, M. J. W. Povey, M. L. Mather, and A. K. Holmes. Ultrasound techniques for characterizing colloidal dispersions. Reports on Progress in Physics, 68(7):1541–1637, 2005. doi: 10.1088/0034-4885/68/7/R01.

[7] Malcolm J.W. Povey. Ultrasound particle sizing: A review. Particuology, 11(2):135–147, 2013. ISSN 1674-2001. doi: 10.1016/j.partic.2012.05.010.

[8] Amitosh Dash, Willian Hogendoorn, and Christian Poelma. Ultrasonic particle volume fraction profiling: an evaluation of empirical approaches. Experiments in Fluids, 62(4):85, 2021. doi: 10.1007/s00348-020-03132-0.

[9] P. S. Epstein and R. R. Carhart. The absorption of sound in suspensions and emulsions. I. Water fog in air. The Journal of the Acoustical Society of America, 25(3):553–565, 1953. doi: 10.1121/1.1907107.

[10] J. R. Allegra and S. A. Hawley. Attenuation of sound in suspensions and emulsions: Theory and experiments. The Journal of the Acoustical Society of America, 51(5):1545–1564, 1972. doi: 10.1121/1.1912999.

[11] Daniel Torrent and José Sánchez-Dehesa. Effective parameters of clusters of cylinders embedded in a nonviscous fluid or gas. Phys. Rev. B, 74:224305, 2006. doi: 10.1103/PhysRevB.74.224305.

[12] P. A. Martin, A. Maurel, and W. J. Parnell. Estimating the dynamic effective mass

density of random composites. The Journal of the Acoustical Society of America, 128 (2):571–577, 08 2010. doi: 10.1121/1.3458849.

[13] Artur L Gower and Gerhard Kristensson. Effective waves for random three-dimensional particulate materials. New Journal of Physics, 23(6):063083, 2021. doi: 10.1088/1367-2630/abdfee.

[14] Alverède Simon, Régis Wunenburger, and Tony Valier-Brasier. Propagation of coherent shear waves in scattering elastic media. Physical Review E, 103(L051001), 2021. doi: 10.1103/PhysRevE.103.L051001.

[15] Alverède Simon, Quentin Baudis, Régis Wunenburger, and Tony Valier-Brasier. Propagation of elastic waves in correlated dispersions of resonant scatterers. The Journal of the Acoustical Society of America, 155(6):3627–3638, 2024. doi: 10.1121/10.0026233.

[16] C. M. Linton and P. A. Martin. Multiple scattering by random configurations of circular cylinders: Second-order corrections for the effective wavenumber. The Journal of the Acoustical Society of America, 117(6):3413–3423, 2005. doi: 10.1121/1.1904270.

[17] Artur L Gower, Stuart C Hawkins, and Gerhard Kristensson. A model to validate effective waves in random particulate media: spherical symmetry. Proceedings of the Royal Society A, 479(2279):20230444, 2023.

[18] K. K. Napal, P. S. Piva, and A. L. Gower. Effective T-matrix of a cylinder filled with a random two-dimensional particulate. Proceedings of the Royal Society A: Mathematical, Physical and Engineering Sciences, 480(2292):20230660, 2024. doi: 10.1098/rspa.2023.0660.

[19] Melvin Lax. Multiple scattering of waves. II. the effective field in dense systems. Phys. Rev., 85:621–629, 1952. doi: 10.1103/PhysRev.85.621.

[20] G. Adomian. The closure approximation in the hierarchy equations. Journal of Statistical Physics, 3(2):127–133, 1971. doi: 10.1007/BF01019846.

[21] Vijay K. Varadan, Vasundara V. Varadan, and Yih-Hsing Pao. Multiple scattering of elastic waves by cylinders of arbitrary cross section. I. SH waves. The Journal of the Acoustical Society of America, 63(5):1310–1319, 1978. ISSN 0001-4966. doi: 10.1121/1.381883.

[22] Artur L. Gower and Paulo S. Piva. Effectivewaves.jl: A julia package to calculate ensemble averaged waves in heterogeneous materials. version 0.3.6. Github, 2024.

[23] Kerry W. Commander and Andrea Prosperetti. Linear pressure waves in bubbly liquids: Comparison between theory and experiments. The Journal of the Acoustical Society of America, 85(2):732–746, 02 1989. ISSN 0001-4966. doi: 10.1121/1.397599. URL https://doi.org/10.1121/1.397599.

[24] Tony Valier-Brasier, Adrien Rohfritsch, Ludovic Alhaïtz, and Jean-Marc Conoir. Fabry–pérot resonances of acoustic waves in disordered slabs. Applied Physics Letters, 125(4):041704, 07 2024. doi: 10.1063/5.0220808.

[25] P.A. Martin and V.J. Pinfield. Elastodynamic multiple scattering: Effective wavenumbers in three-dimensional elastic media. Wave Motion, 134:103478, 2025. ISSN 0165-2125. doi: 10.1016/j.wavemoti.2024.103478.

[26] Aristeidis Karnezis, Paulo S Piva, and Art L Gower. The average transmitted wave in random particulate materials. New Journal of Physics, 26(6):063002, 2024. doi: 10.1088/1367-2630/ad49c2.

Chapter 4

Designing Band Gaps with Randomly Distributed Sub-Wavelength Helmholtz Resonators

PAULO S. PIVA, ART L. GOWER, I. DAVID ABRAHAMS

Declaration of Authorship and Publication Status

This chapter is a substantially identical reproduction of a published article.

Publication Details:
Piva, P. S., Gower, A. L., & Abrahams, I. D. (2026). Designing band gaps with randomly distributed sub-wavelength Helmholtz resonators. *npj Acoustics*, *2*, 10.

DOI: https://doi.org/10.1038/s44384-026-00045-w

Statement of Contribution:

As the primary author, my specific contributions to this published work were: conceptualization, formal analysis, investigation, methodology, writing code, producing all figures, writing the original draft, review and editing.

My co-authors contributed by providing primary supervision, support in the coceptualisation and investigation, support in code for visualisation, and critical review/editing of the manuscript.

Abstract

It is well-known that band gaps for wave propagation, in the frequency domain, can be achieved by using periodically arranged inclusions in a host material. However, it has been challenging to design materials with broad band gaps or that have multiple overlapping band gaps. For periodic composites, this difficulty arises because many different length scales would have to be repeated periodically within the same structure to have multiple overlapping band gaps. Here, we present an alternative: to design band gaps with disordered materials. We show how to tailor band gaps by choosing any combination of Helmholtz resonators that are positioned randomly within a host acoustic medium. One key result is that, via analytical (asymptotic) analysis, we are able to derive simple formulae for the effective material properties, which work over a broad frequency range. These can therefore be used to rapidly design tailored metamaterials. We show that these formulae are robust by comparing them with high-fidelity Monte Carlo simulations over randomly positioned resonant scatterers.

4.1 Introduction

Metamaterials are artificially fabricated materials, usually of composite constructing, which have properties not found in nature; they are designed for specific and targeted applications [1]. Wave motion control is an important application for electromagnetics, elastodynamics, and acoustics. There are many examples of fabricated materials that can distort or bend the path that waves propagate along, allow negative refraction [2], block specific frequencies [3], or cloak (i.e. render invisible) certain parts of space [4–7]. In recent years, the focus on elastic and acoustic metamaterial theory and design has broadened to include non-reciprocal wave propagation [8, 9], acoustic lenses [10], and optimal wave-absorbing layered media [11].

Sound absorption and reflection. Among the various applications of acoustic metamaterials, the one most relevant to this work is the control of transmission through one or multiple layers, commonly realized via structures designed for absorption and reflection. A widely used strategy for enhancing sound absorption involves tuned resonant elements. Helmholtz resonators, in particular, are highly tunable [12] and, when combined in dif-

ferent configurations, can give rise to a variety of absorption and reflection phenomena in metamaterials, such as perfectly absorbing systems [13]. This flexibility allows to design compact materials with both broadband and targeted absorption spectrum [14, 15].

Design and manufacture. In many applications, the design of metamaterials for wave control is often a heuristic process, which encourages heavy optimisation and machine learning techniques in the literature [16, 17]. However, even after long and extensive computations to find an optimal metamaterial arrangement, small manufacturing changes/defects can lead to errors that significantly alter the band structure. For this reason, these materials require elaborate manufacturing techniques [18, 19].

Disordered metamaterials. In this paper, we present a disordered (random) metamaterial, which can be designed to have broad as well as multiple localised (overlapping) low-frequency band gaps, that are robust to small changes in its microstructure. By low-frequency, we mean any frequency range for which the wavelength is larger than the characteristic size of the resonators, classifying them as sub-wavelength. We show how to design such metamaterials and, more importantly, derive simple explicit formulae for the band gaps which do not require heavy optimisation. One difficulty that has slowed progress in disordered materials is that the scattering response from any one configuration of resonators can be complicated; however, we show here how to completely overcome this difficulty by combining ensemble averaging techniques [20–22] together with asymptotic homogenisation.

Split-ring resonators. As an example, we develop our formulas for a mixture of split-ring resonators. A split-ring resonator, shown in Figure 4.1a, is a type of Helmholtz resonator, characterised by a cavity-neck system with a resonance peak located in the sub-wavelength range ($kb \leq 1$), shown in Figure 4.1b. We choose this specific type of resonator because its scattered wave has been deduced from first principles [23].

Band gaps. To achieve multiple band gaps, we combine different types of sub-wavelength split-ring resonators, each with a different resonance frequency. By a band gap, we mean a frequency range where the average wave cannot propagate, but incoherent speckle may still propagate [24]. To the best of the authors' knowledge, there has been no clear consistent strategy to derive a simple formula for effective-properties of a mix of different types of split-ring resonators. It has only been possible to derive effective-properties for a periodic array of identical sub-wavelength split-ring resonators [25–27]. To reach simple formulae, which are needed to easily design band gaps, asymptotic homogenisation is essential [25, 28–31]. It is common to enforce that the resonators are sub-wavelength, as we also do in this work. However, care must be taken to accurately capture the resonance beyond the quasi-static limit.

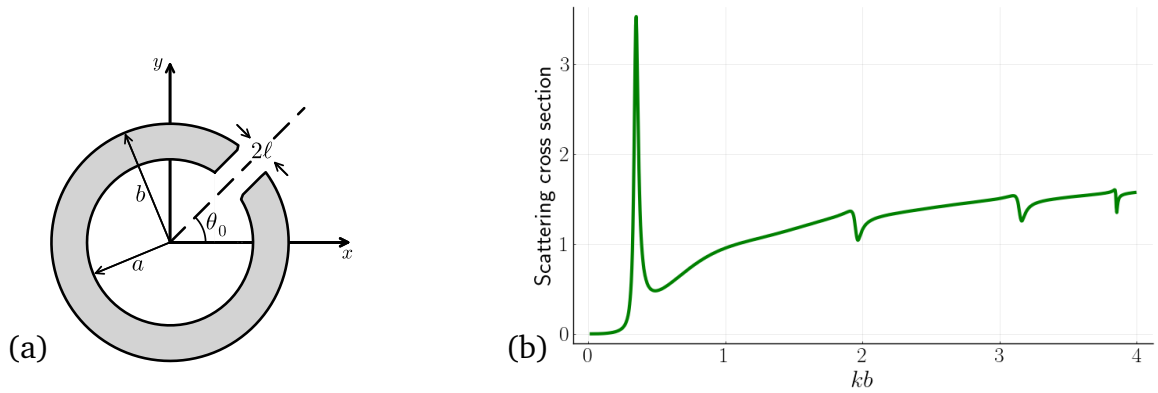

Figure 4.1: The left figure (a) shows an illustration of a typical split-ring resonator. The right figure (b) shows the scattering cross section of a sound-hard 2D split-ring resonator with an aperture size of $2\ell = 0.1b$, and k is the wavenumber of the background medium.

The literature. Effective material properties, for example mass density and speed of sound, have been deduced for a circular cluster of 2D particles (rods) [32–35]. To summarise, these papers consider a given particle configuration and, in the long-wavelength limit, determine the effective-properties of a single equivalent circle that would reproduce the same scattering as the entire cluster. This can lead to effective-properties which depend on frequency [34, 35] and on a specific particle configuration. Dependence on the particle configuration leads to extra degrees of freedom to tune the effective-properties, but also has drawbacks: it can be computationally difficult to calculate for a large number of particles, and then also requires fabricating material with exact particle positions. To remove the dependence on the particle configuration, it has been suggested to average over the effective-properties [33, 34]. However, this is not the same as averaging over the scattered wave from a disordered material, and can also have a high computation cost.

Beyond effective-properties. While effective-properties are useful for material design, they are not the only efficient means of determining metamaterial wave responses when wavelengths are longer than particle sizes. Semi-analytical models offer viable alternatives [36–39], which account for clusters of subwavelength resonators or inclusions. These methods are able to efficiently capture multiple scattering effects in a variety of scenarios, as in the weak scattering regime [40], or utilizing of meso-scale approximations to incorporate specific particle geometries and shapes [41]. However, unlike the explicit estimates provided by effective properties, these semi-analytical approaches require solving systems of equations that scale with particle count, becoming computationally intensive for large disordered systems.

Frequency dependent effective-properties. One concern raised in many papers [21, 42, 43] is that beyond the leading order low frequency limit, there is no unique way to

calculate effective-properties. That is, calculating the properties for an effective cylinder [32, 33] can lead to different results than calculating the properties for an effective slab [21], despite both having the same set of scatterers or microstructure. However, to include resonance effects, it is necessary to include terms beyond the low frequency approximation, so the question is how to do this correctly? Here we show how to deduce frequency dependent effective-properties directly from the dispersion equation for the effective wavenumber, which is valid for any material shape and frequency [21]. From this solid ground, we then use asymptotic expansions that capture the resonance of the scatterers. As a result, our method leads to effective-properties which provide the correct average wave scattering from a disordered material.

Motivating example. To showcase how simple it is to use our formulae to design a material, and motivate the reader for the rest of the paper, we present an acoustic version of a device that splits a signal into two different channels, or waveguides, dependent on its frequency components, shown in Figure 4.2. These devices are known as frequency demultiplexers. They are used in digital computing and telecommunication networks, and are often designed via tailored periodic structures, as in [44], or through black-box optimisation, as in [45]. In contrast, as illustrated in Figure 4.2, we are able to produce with little effort a low insertion loss ($\lesssim$ 5dB) and high contrast ($\sim 10-20$dB) demultiplexer using only randomly placed and oriented resonators, which has similar performance compared to the microchip in [45, Figure 4b]. Figure 4.2 also shows the amplitude of the transmitted waves for two wavelengths of high contrast in transmission through the top and bottom waveguides. We note that we used only one configuration of randomly placed particles for all the results shown in Figure 4.2.

Designing devices, such as the demultiplexer in Figure 4.2, with randomly oriented resonators makes them robust to manufacturing defects in terms of the positioning of each resonator. This is because the formulae for the effective-properties are agnostic to the position and orientation of the resonators. Alternatively, the performance could be further enhanced by optimising the position of the resonators.

4.2 Results

In this section, we present our main results: the effective-properties of the metamaterial. Later, in Section 4.3.3, we show how to derive these results. The focus below is on how to use the effective-properties, followed by examples, and to present high-fidelity Monte-Carlo validation.

The resonators in the material can have varied sizes, geometry, and properties, al-

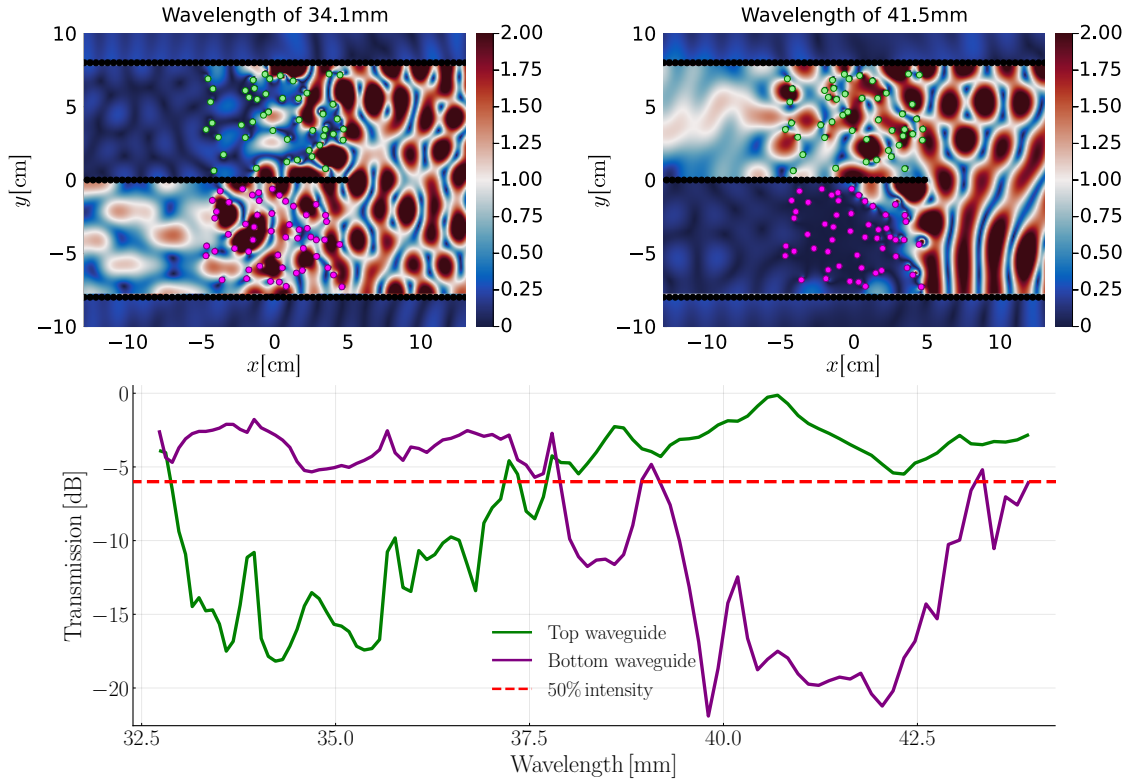

Figure 4.2: The top two images show a very simple frequency demultiplexer we designed using randomly placed Helmholtz resonators to illustrate our results. In the top two images, a harmonic plane source (of amplitude 1) travels from right to left inside a waveguide which then splits into two smaller waveguides at $x = 5$cm. The top waveguide filters out waves with wavelengths close to 34.1mm due to the scattering by resonators represented by green circles, with an aperture of $2\ell = 0.2$mm. In contrast, the bottom waveguide filters out waves with wavelengths close to 41.5mm with resonators represented by magenta circles, with an aperture of $2\ell = 0.04$mm. All resonators have rigid thin walls ($a = b = 2$mm in Figure 4.1a), (uniformly) randomly placed and oriented in air. The colour bar shows the amplitude of the total wave (incident plus scattered). The graph shows the transmitted intensity into each waveguide, calculated in dB. The values of transmission are calculated as the average intensity of the wave on the left-hand side of the region containing particles in each of the waveguides. Wavelengths from 33 to 38mm are mostly transmitted through the lower waveguide, while wavelengths from 38 to 43mm are mostly transmitted through the upper waveguide. All simulations to produce the figures above were performed using the MultipleScattering.jl library in Julia [46].

though for ease of exposition, we illustrate the case of circular sound-hard[1] split-ring resonators in 2D, as shown in Figure 4.3. Let us consider N different types of sound-hard Helmholtz resonators, which are randomly distributed in a homogeneous background

[1]By sound-hard in this chapter, we mean rigid, non-penetrable walls. In other words, the wave cannot access the regions shaded in gray in Figure 4.3. This is the result of applying Neumann boundary conditions to the resonator walls [23].

medium (see Figure 4.3). The properties of the resonators feed into the formulae for the effective bulk modulus ($\beta_\star$) and effective mass density ($\varrho_\star$), which are given by

$$\beta_\star(k) = \frac{\beta}{(1-\varphi) + \sum_{j=1}^{N} z(\boldsymbol{\lambda}_j)\phi_j} \quad \text{and} \quad \varrho_\star = \varrho\frac{1+\varphi}{1-\varphi}, \tag{4.1}$$

where β and ϱ are the bulk modulus and mass density of the background medium, ϕ_j is the volume fraction of the j-th type of resonator[2], with $\varphi = \sum_{j=1}^{N} \phi_j$ being the total volume fraction of the resonators (including their interiors). We call $z(\boldsymbol{\lambda}_j)$ the *resonance factor* of the j-th resonator type derived via careful matched asymptotic analysis [23, 26]. The resonance factor depends only on the geometrical properties of the resonator and the wavenumber k of the background medium. When hitting a resonance $z(\boldsymbol{\lambda}_j)$ increases in magnitude, and when there is no contribution from the resonator, then $z(\boldsymbol{\lambda}_j)$ is small. See Section 4.3.1 for more details and see Appendix 4.A for a derivation of a formula for $z(\boldsymbol{\lambda}_j)$ for split-ring resonators.

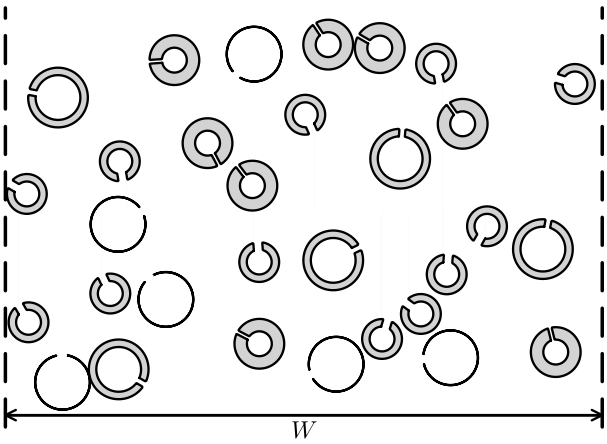

Figure 4.3: Representation of one possible configuration of split-ring resonators in a layer of width W. The resonators are randomly positioned and oriented in the layer, and have non-penetrable (sound-hard) rigid walls, which means the grey regions are inaccessible to acoustic waves.

The effective bulk modulus $\beta_\star$ is frequency dependent, and its behaviour depends on the geometry of each resonator in the mixture. $\beta_\star(k)$ is the most important parameter to design band gaps for metamaterials, since the effective mass density $\varrho_\star$ does not depend on frequency and only increases when adding more resonators to the mixture.

The formulae (4.1) can be used to calculate the transmission coefficient of acoustic

[2]For two dimensions, the volume fraction reduces to the ratio of the area occupied by a phase to the total area of the material.

waves through the layer in Figure 4.3, assuming continuity of the acoustic pressure and normal velocity across the interface of the layer (dashed lines in Figure 4.3). The formula for the transmission coefficient T through a layer of width W is given by[3]

$$T_\star = \frac{2ZZ_\star}{2ZZ_\star \cos(k_\star W) - \mathrm{i}(Z_\star^2 + Z^2)\sin(k_\star W)}, \tag{4.2}$$

where $Z = \varrho c$ and $Z_\star = \varrho_\star c_\star$ are the impedances of the background medium and the metamaterial respectively, with $c = \sqrt{\beta/\varrho}$ and $c_\star = \sqrt{\beta_\star/\varrho_\star}$ being the corresponding speeds of sound. The effective wavenumber in the metamaterial is given by $k_\star = \omega/c_\star$, where ω is the angular frequency of the incident wave.

Below we show three examples on designing band gaps by using the formulae above. After the examples, we show how high-fidelity Monte-Carlo simulations closely agree with our simple formulae for a broad frequency range.

4.2.1 Example band gap designs

In this section, we present three examples to show how to design band gaps using a layer of randomly placed and oriented resonators, as illustrated in Figure 4.3. For all the examples, we assume that the background medium is air (ϱ =1kg/m^3, β =117.6kPa).

Example 1 – changing volume fractions. Consider a material filled with a single species of thin-walled split-ring resonator ($a = b$ and one fixed value of the aperture 2ℓ in Figure 4.1a). To help illustrate the results, we consider a layer of width W (infinite length), shown in Figure 4.3, and calculate its effective transmission coefficient by assuming the material is homogeneous with the properties given by (4.1).

From the direct evaluation of (4.1) and (4.2), shown in Figure 4.4b, we see that only a small percentage of resonators are needed to completely stop transmission through this layer. As the volume fraction increases, the minimum grows wider and shifts towards higher frequencies. With only $\varphi = 6\%$ volume fraction, we reach a band gap around 140Hz, which shows that a thin layer of the proposed metamaterial is a good candidate for a sound-insulating material. To broaden the band gap, it is possible to either increase the width of the metamaterial layer W, or the volume fraction of resonators φ (see Figure 4.4b).

Another lesson to learn from Figure 4.4a is that the minimum of the curve $\varphi = 1\%$ is very close to the resonance frequency of a single thin-walled resonator, shown in (4.1)b. However, the minimum of the $\mathrm{Im}[\beta_\star]$ curve shifts to higher frequencies as φ increases

[3]This expression is equivalent to the effective transmission (3.1). In Chapter 3, we present this formula using the same notation as in experimental work we cite through the text for comparison.

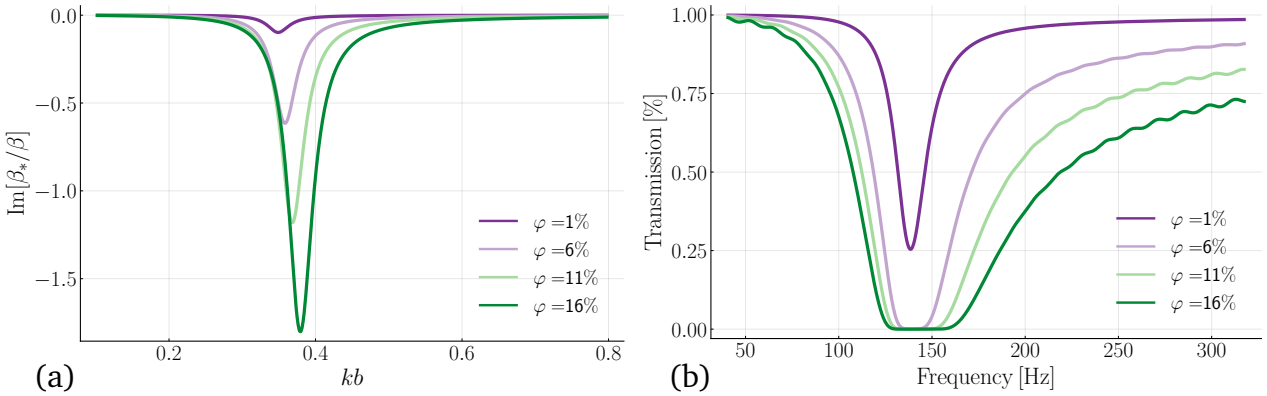

Figure 4.4: (a) shows the imaginary part of the effective bulk modulus $\beta_\star$ and (b) the magnitude of the transmission coefficient through a layer of width $W = 32$mm. The layer is composed of thin-walled randomly-positioned Helmholtz resonators with radius $b = 0.4$mm, and k is the background wavenumber. The aperture size of the resonators is $\ell = 0.05b$. Each curve has a different volume fraction of resonators.

because of multiple scattering effects between the resonators. Being able to predict this minimum with our formulae (4.1), rather than finding it through trial and error, can save time and resources in most applications.

Finally, because Figure 4.4a has non-dimensional axes, note that increasing the size of the resonators, while thickening the width of the layer W by the same ratio, would lead to the band gap shifting to a lower frequency range.

Example 2 – broadening band-gaps. To achieve a broader band gap, or separate band gaps, we could use layers of random resonators of the type discussed in Example 1. Instead, we show a case with two types of thin-walled resonators to the formulae (4.1) with multiple types of resonators. The two types have different radii, $b_1 \neq b_2$, and aperture sizes, $\ell_1 \neq \ell_2$. The results are presented in Figure 4.5.

In Figure 4.5(a), we notice that when the aperture ℓ_2 decreases, the graph of $\mathrm{Im}[\beta_\star]$ transitions from having one minimum to two distinct minima. The appearance of the second dip is due to the resonance frequencies of the two types of resonators moving further apart as we decrease ℓ_2. The overall result in the transmission (Figure 4.5b) is a wide band gap, which separates into two thinner band gaps as ℓ_2 decreases.

Example 3 – shifting band-gaps. Here we consider a mix of three types of resonators, each with a volume fraction of $\phi_j = 4\%$ for $j = 1, 2, 3$. We use three types just to showcase that we can. Each resonator has a different aperture size, but the three types have the same outer and inner radius b and a, for simplicity. Our goal is to show how the band gaps shift when the walls of the resonators become thicker. Increasing the thickness causes a non-intuitive change in the resonance, which can only be predicted with our effective-

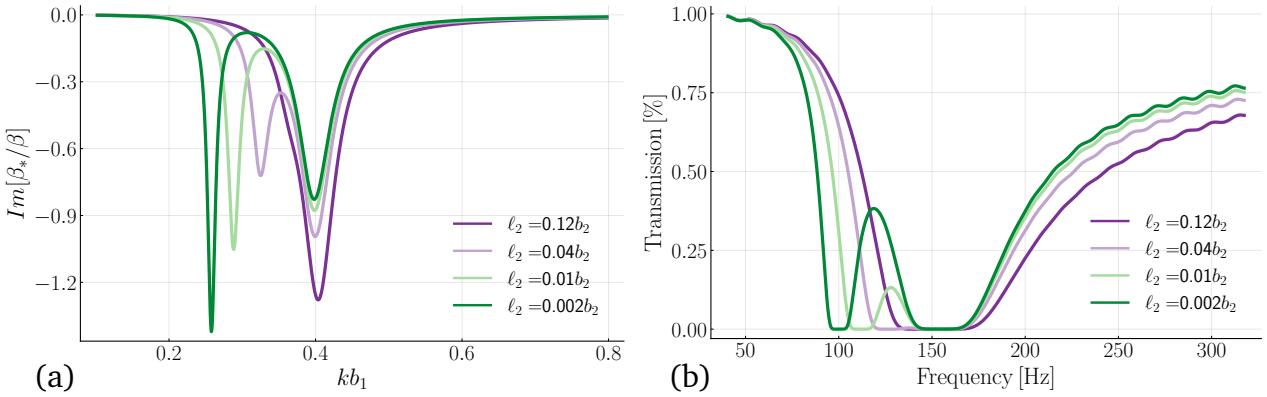

Figure 4.5: (a) shows the imaginary part of the effective bulk modulus and (b) shows the magnitude of the transmission coefficient through a layer of width $W = 32$mm. The layer is composed of thin-walled random Helmholtz resonators with radius $b_1 = 0.4$mm and $b_2 = 0.2$mm. The total volume fraction of resonators is $\varphi = 15\%$, and half of them ($\phi_1 = 7.5\%$) have an aperture size of $\ell_1 = 0.1b_1$. Only the aperture size ℓ_2 of the other half of the resonators changes between curves.

properties (4.1).

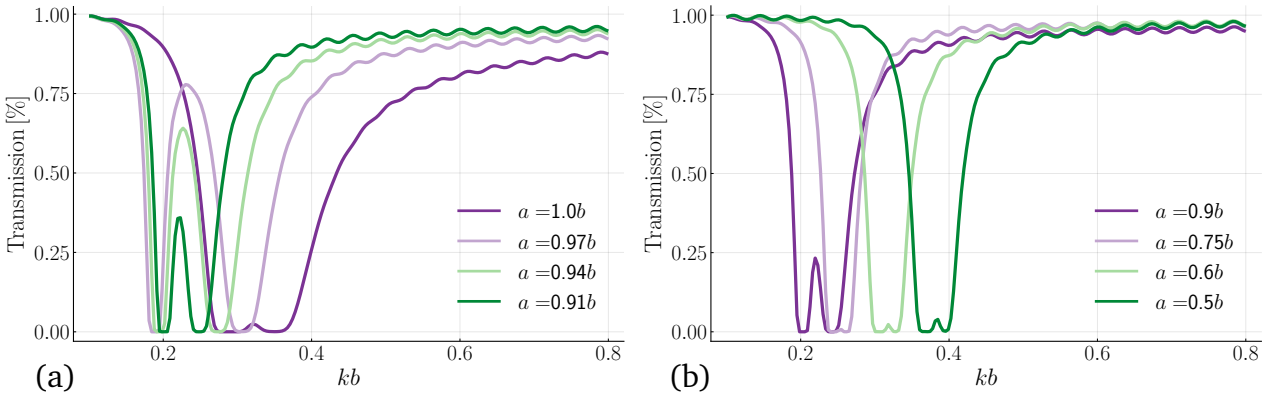

Figure 4.6: Both graphs show the transmission coefficient through a metamaterial of width $W = 32$mm filled with randomly positioned resonators, all with the same outer radius b. The total volume fraction of resonators is $\varphi = 12\%$, with a third of them having an aperture size of $\ell_1 = 0.05b$, another third with $\ell_2 = 0.01b$, and the final third with $\ell_3 = 0.005b$. For each curve, we use a different inner radius a for all the resonators.

The transmission results for different values of the inner radii a, which changes the wall thickness, are shown in Figure 4.6 below. In Figure 4.6a we see that as a gets smaller, and the wall thickness increases, the resonant frequency gets lower; however, there is a limit to this effect. In Figure 4.6b, we see that a further decrease in a makes the resonant frequency become higher again, as well as lessening the strength of the resonance. These effects illustrate the need for our formulae to guide the design process.

4.2.2 Monte-Carlo validation

When dealing with disordered materials, it is often impractical to predict the precise wave response of the material for each possible configuration of the microstructure. To reach our effective formulae (4.1) we used ensemble averaging techniques [47], which led to practical and explicit results. In this section, we validate these formulae by using high-fidelity Monte-Carlo simulations for both a layer and a circle filled with resonators. We also highlight some advantages and disadvantages of disordered metamaterials in general.

To get an exact match with a high-fidelity simulation, we need to perform simulations of wave scattering from one configuration at a time, performed using the MultipleScattering.jl Julia library [46]. In these simulations, the resonators do not overlap, and their positions are randomly chosen, see [48], and references within, for details on how to achieve this. Some noteworthy references include [49, 50]. The average wave is then calculated by taking the average total wave over all simulations. This is what we mean by a high-fidelity Monte-Carlo simulation. The mathematical details on ensemble averaging and the Monte-Carlo method are given in Section 4.3.2; here we focus mostly on showing the results.

A layer filled with resonators

We begin with the case of a layer filled with resonators and an incident plane wave. This is a case which is simpler to understand, though Monte-Carlo simulations can be challenging as the layer needs to be very tall, large H in Figure 4.7, as the effective theory assumes the layer is infinitely extent.

We perform a high-fidelity Monte-Carlo simulation for a plane incident wave, with wavenumber k, scattered by randomly distributed and randomly oriented thin-walled split-ring resonators ($b = a$ in Figure 4.1a) inside a long strip shown in Figure 4.7a. The transmitted field is measured one radius away from right-hand side of the layer as also illustrated in Figure 4.7a. This simulation is repeated many times, and the average transmission $\langle u \rangle$ is compared with the average intensity $\langle |u|^2 \rangle$, and the prediction from the effective-properties formulae (4.1) in Figure 4.7b below. The runtime of the MC simulation was over 24 hours, with parallelisation, and using all computational power available, while the effective formulas are computed in less than a second, using only a fraction of the computational power.

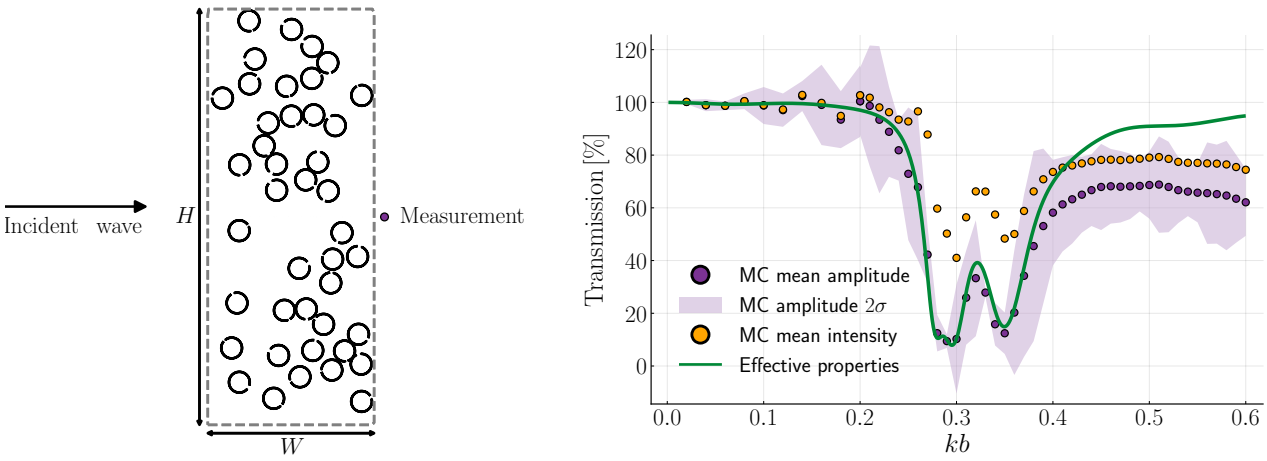

(a) (b)

Figure 4.7: (a) shows one realisation used for our Monte-Carlo (MC) simulations, where resonators are placed within a layer of width $W = 20b$, height $H = 200b$, and b is the resonator radius. An incident plane wave comes from the left, and the total field is then measured at a point at half height and one radius away from the layer. This simulation is repeated many times, each with a different configuration of resonators, and then the average MC field is compared with a transmission coefficient calculated by using the effective-properties (4.1), shown on the right (b). For the MC, we use three types of thin-walled resonators, each with 4% volume fraction, but with different aperture sizes $\ell_1 = 0.05b$, $\ell_2 = 0.01b$, and $\ell_3 = 0.005b$. In total 5,000 different configurations are calculated for the MC results in (b), and σ is the $2\times$ the standard deviation.

In Figure 4.7b we see that the average transmission calculated using the effective-properties (4.1) accurately matches the average from Monte-Carlo (MC) $\langle u \rangle$ in the frequency range $kb \lesssim 0.4$, which includes the resonant frequencies, and agrees with our derivations in Section 4.3.3. The MC mean intensity $\langle |u|^2 \rangle$ is higher than the MC mean amplitude, especially around resonance, due to phase cancellation when calculating $\langle u \rangle$; see discussion below (4.12) in Section 4.3.2 for more details. To qualitatively show the difference between mean amplitude and mean intensity, and better highlight the band gap as discussed in Section 4.1, we provide two examples with the same setup as Figure 4.7, except with two and three times more resonators respectively in the layer, shown in Figure 4.8 below.

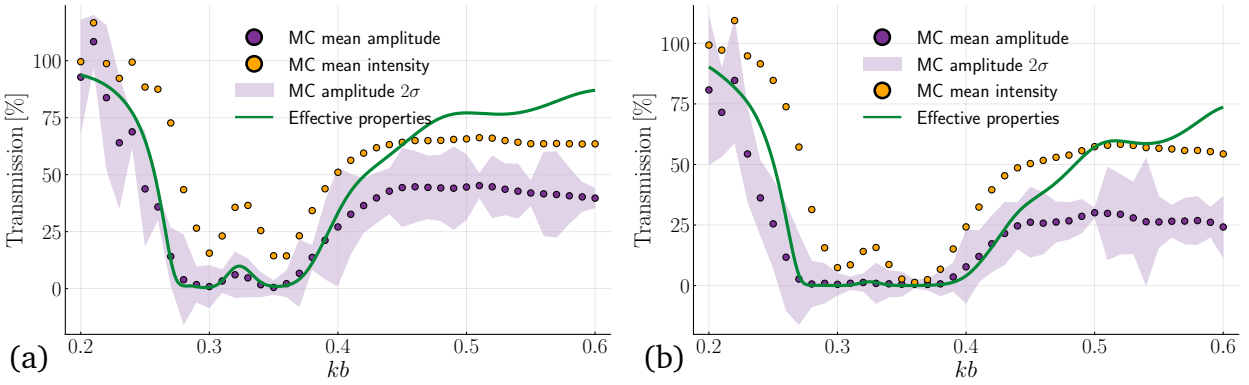

Figure 4.8: Results of 5000 different configurations of Monte-Carlo (MC) simulations for the same setup as in Figure 4.7, however with double (a), and triple (b), the volume fraction of each type of resonator in the mixture. In total, we have $\varphi = 24\%$ (a), and $\varphi = 36\%$ (b), volume fraction of resonators in the layer.

In Figure 4.8, even when the average wave is completely blocked by the layer (zero transmission), the average intensity is not zero as it is in a speckled or incoherent form [24]. This incoherent part is lost when taking the average of the field, due to phase cancellation, but not in the average intensity. This type of band gap, introduced in Section 4.1, is more general than the usual definition of band gap for periodic materials, as some part of the wave does get transmitted.

An important feature from Figure 4.7b and Figure 4.8 is that each realisation of the Monte-Carlo simulation is close to the MC mean amplitude for $kb \lessapprox 0.4$, especially in the band gap region. That is, the purple shaded area has a 95% statistical confidence (2σ). This suggests a powerful design strategy: 1) first use the effective formulae to decide on what types of resonators to use, given some target band diagram, then 2) produce one realisation with the resonators randomly placed, and finally 3) perform a local optimisation to adjust the position of the resonators to further refine the transmission or reflecting properties. This design strategy would be much less computationally intensive than pure optimisation strategies used in the literature [16, 17, 45], as we discussed in Section 4.1.

It is important to note that some MC points between $kb = 0.1$ and $kb = 0.22$ in Figure 4.7b and Figure 4.8 exceed 100%. If the height of the simulation domain H was infinite, and enough Monte-Carlo simulations (MC) were performed, then the average intensity must not exceed 100%. In our case, the transmission above 100% is due to the finite height H: the top and the bottom of the finite simulation domain lead to a diffracted wave which, for specific frequencies, tips the transmission over 100%. This has only a noticeable effect for one frequency in our results.

A circle filled with resonators

Our effective formulae (4.1) are valid for materials of any shape or size [21, 51]. In particular, a circle filled with resonators leads to finite size Monte Carlo (MC) simulations [51, 52] which makes validation far simpler. See Figure 4.9a for an illustration.

Our goal here is to compare three different methods to calculate the scattering cross-section of a circle filled with resonators: 1) MC simulations, 2) a circle with the effective-properties (4.1), and 3) the effective waves methods [21, 51], which works beyond low frequencies. The results are shown in Figure 4.9b. The runtime of the MC simulation was over 5 hours, with parallelisation, and using all computational power available. The effective waves method and effective formulas are computed in over 40 minutes and a few seconds, respectively, using only a fraction of the computational power.

When performing MC for a circle filled with resonators, we make use of the rotational symmetry to greatly reduce the computational cost of calculating the scattering cross-section, see [52] for details. For the circle with either effective-properties, or using the effective waves methods [21, 51], the average scattering cross-section becomes

$$\langle \Sigma_{\text{sc}} \rangle = \frac{2}{kR} \sum_{n=-\infty}^{\infty} |\langle \mathcal{F}_n \rangle|^2, \tag{4.3}$$

where R is the radius of the metamaterial, and $\langle \mathcal{F}_n \rangle$ are the average material coefficients defined in Section 4.3.2.

The results in Figure 4.9b again show that the mean of MC data is close to the results using the simple formulae for the effective-properties at lower frequencies $kb \lesssim 0.7$. The effective-properties are deduced as a low-frequency asymptotic approximation of the effective waves method, and it can be seen in Figure 4.9 that these two methods match for lower frequencies.

Figure 4.9 also shows that the effective waves method matches the Monte-Carlo results for all frequencies. This would not be expected for all resonators and volume fractions, because the effective waves method may lose accuracy when strong scattering is present. This is because strong scattering can trigger multiple effective wavenumbers [53], and the effective wave method shown here only considers one effective wavenumber. Despite being more accurate, the effective waves method has a significant drawback: it requires a much more elaborate calculation [51] than the formulae (4.1), which makes it less useful than the effective formulae for designing metamaterials.

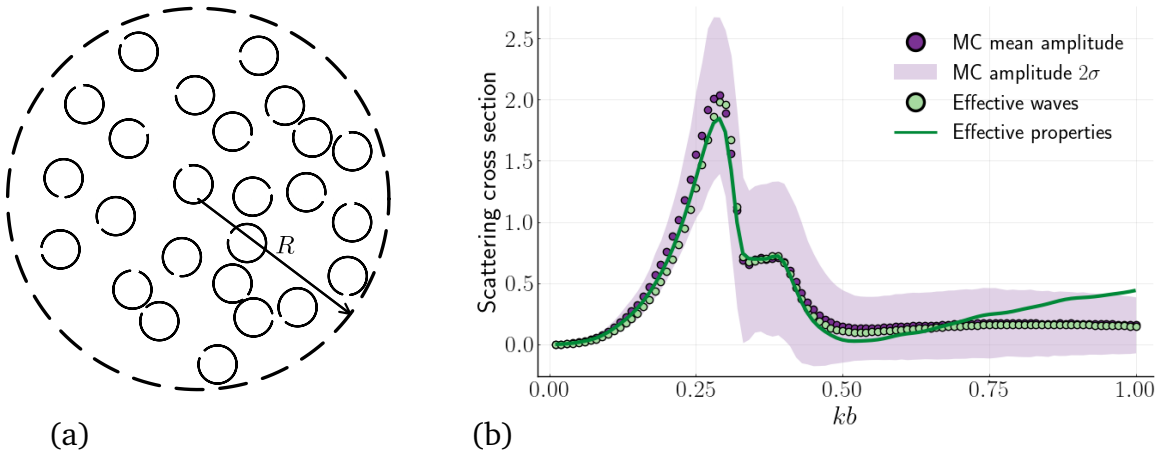

(a) (b)

Figure 4.9: (a) shows one configuration of resonators used for our Monte-Carlo (MC) simulations. The resonators are placed randomly within a circle of radius $R = 20b$. An incident plane wave comes from the left, and the resulting scattering cross-section is shown in (b) on the right for three different methods: MC simulations, the effective waves method [21], and by using the effective-properties formulae (4.1). The aperture size of all resonators is $\ell = 0.05b$, the volume fraction is $\varphi = 10\%$ in all 40,000 configurations of the MC simulations, and σ is the standard deviation. The scattering cross-section was calculated with the first nine scattering coefficients $\langle \mathcal{F}_n \rangle$ in (4.3).

4.3 Multiple scattering and ensemble average

Here we derive the effective-properties (4.1) in three steps: scattering by a single resonator in Section 4.3.1, scattering of the whole metamaterial in Section 4.3.2, and then an asymptotic low-frequency expansion in Section 4.3.3.

4.3.1 Scattering by a single resonator

Before calculating the acoustic response of the whole metamaterial, we need to describe how each resonator scatters waves. This is best done with the T-matrix method [54–56], which we describe below, as it facilitates calculations for multiple scattering.

Let the centre of the resonator be the origin of $\mathbb{R}^2$. We assume the incident wave is a regular function, which allows us to expand the incident wave in terms of a series of regular radial waves

$$u_{\text{inc}}(\boldsymbol{r}) = \sum_{n=-\infty}^{\infty} g_n \mathrm{V}_n(k\boldsymbol{r}) \quad \text{with} \quad \mathrm{V}_n(k\boldsymbol{r}) = \mathrm{J}_n(kr)\,\mathrm{e}^{\mathrm{i}n\theta}, \tag{4.4}$$

where $\boldsymbol{r} \in \mathbb{R}^2$, k is the wavenumber, J_n being the Bessel function of the first kind, and

(r, θ) polar coordinates of $\mathbb{R}^2$. Note that the time-harmonic dependence $\mathrm{e}^{-\mathrm{i}\omega t}$ is assumed throughout the paper for both incident and scattered waves, where ω is the angular frequency, and $k = \omega/c$, where c is the speed of sound in the background medium.

Due to the linearity of the Helmholtz equation, the total field is given by the superposition of the incident wave and the scattered field from our resonator

$$u_{\text{tot}}(\boldsymbol{r}) = u_{\text{inc}}(\boldsymbol{r}) + u_{\text{sc}}(\boldsymbol{r}),$$

and, outside the resonator, the scattered field can be represented as a series of outgoing radial modes

$$u_{\text{sc}}(\boldsymbol{r}) = \sum_{n=-\infty}^{\infty} f_n \mathrm{U}_n(k\boldsymbol{r}), \quad \text{for} \quad r = |\boldsymbol{r}| > b, \tag{4.5}$$

where b is the outer radius of the resonator, f_n are the scattering coefficients, and the outgoing radial modes are given by

$$\mathrm{U}_n(k\boldsymbol{r}) = \mathrm{H}_n(kr)\,\mathrm{e}^{\mathrm{i}n\theta},$$

with H_n being the Hankel function of the first kind[4].

To determine the scattered field, we need to apply boundary conditions at the walls of the resonator. The result of solving the boundary conditions can be expressed in terms of the T-matrix, which relates the incident wave to the scattered waves through

$$f_n = \sum_{m=-\infty}^{\infty} T_{nm} g_m, \tag{4.6}$$

where T_{nm} are the elements of the T-matrix. For a circular Helmholtz resonator with sound-hard walls (Neumann boundary conditions) and outer radius b, we deduce in Appendix 4.A the T-matrix

$$T_{np} = -\frac{\mathrm{J}'_p(kb)}{\mathrm{H}'_p(kb)}\delta_{np} - \frac{\mathrm{i}\mathrm{e}^{-\mathrm{i}(n-p)\theta_0}}{\pi \mathrm{H}'_n(kb)\mathrm{H}'_p(kb)} z(\boldsymbol{\lambda}), \tag{4.7}$$

where θ_0 is the orientation of the aperture (anticlockwise angle with the x-axis), prime denotes differentiation with respect to the argument, and $\boldsymbol{\lambda}$ is a set of properties that identifies one type of resonator.

In Appendix 4.A we use a closed form for $z(\boldsymbol{\lambda})$ for the split-ring resonator in Figure 4.1 which is fully characterised by $\boldsymbol{\lambda} = \{kb, ka, k\ell\}$, with outer radius b, inner radius a, and aperture of ℓ. However, the formula (4.7) is the same for any circular resonant structure,

[4]The usual superscript (1) on the Hankel function is suppressed here and henceforth for clarity.

with only $z(\boldsymbol{\lambda})$ changing, with some examples illustrated in Figure 4.10.

To determine the resonance factor $z(\boldsymbol{\lambda})$ for a different resonator (as in examples in Figure 4.10), one should redo the asymptotic calculations in [23] for its specific internal geometry, and then repeat the deduction in Section 4.A to arrive at (4.7). Similarly, we could easily adapt (4.7) to incorporate the case of multiple apertures in the same resonator.

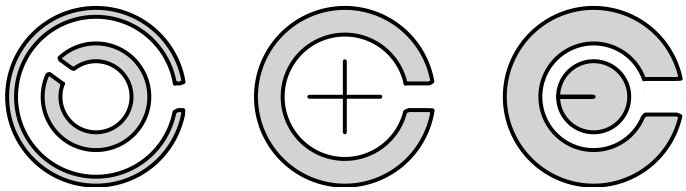

Figure 4.10: Three examples of Helmholtz resonators with different resonance factors $z(\boldsymbol{\lambda})$. The gray shaded areas represent the internal structure, and here are modeled as rigid (sound-hard) walls [23]. However, this can be generalized to penetrable, or even full elastic structures, and a new expression for the T-matrix (4.7) would be required.

4.3.2 Ensemble average and multiple scattering

To account for different types of resonators in the metamaterial, we need to first calculate the exact multiple scattering between the resonators, after which we will perform ensemble averaging as shown in [21, 52, 56]. We also borrow the notation from these references.

Let us number each resonator in the material. We denote the centre of the j-th resonator by $\boldsymbol{r}_j$, and the set of its properties by $\boldsymbol{\lambda}_j$. As an example, if the j-th resonator is a split-ring resonator, shown in Figure 4.1, we have the following set of properties

$$\boldsymbol{\lambda}_j = \{kb_j, ka_j, k\ell_j\}$$

where b_j is the outer radius, a_j the inner radius, and ℓ_j the aperture size.

The scattered field from all resonators is a sum of the waves scattered from each resonator

$$u_{\text{sc}}(\boldsymbol{r}) = \sum_{j=1}^{J} \sum_{n=-\infty}^{\infty} f_n^j \mathrm{U}_n(k\boldsymbol{r} - k\boldsymbol{r}_j), \tag{4.8}$$

where $\boldsymbol{r}$ cannot be within any resonator, J is the total number of resonators, and f_n^j are the scattering coefficient of the j-th resonator as introduced in Section 4.3.1.

For numerical validation, and to help explain the ensemble averaging, it helps to specialise to the case of all resonators within a large circular region. To achieve this, we use

Graf's addition theorem to rewrite (4.8) in terms of outgoing waves centred at the origin

$$u_{\text{sc}}(\boldsymbol{r}) = \sum_{j=1}^{J} \sum_{n,n'=-\infty}^{\infty} \mathrm{V}_{n-n'}(-k\boldsymbol{r}_j) f_n^j(\boldsymbol{\lambda}) \mathrm{U}_{n'}(k\boldsymbol{r}). \tag{4.9}$$

The coefficients f_n^j depend on all properties and positions of all resonators [21, 56]. To make this explicit, and simplify notation, we denote one configuration by $\boldsymbol{\lambda}$, which represents all possible positions and types (properties) for each resonator. We also define the material scattering coefficients of the whole region containing all resonators as:

$$\mathcal{F}_n(\boldsymbol{\lambda}) = \sum_{j=1}^{J} \sum_{n'=-\infty}^{\infty} \mathrm{V}_{n'-n}(-k\boldsymbol{r}_j)\, f_{n'}^j(\boldsymbol{\lambda}),$$

which simplifies (4.9) into

$$u_{\text{sc}}(\boldsymbol{r}) = \sum_{n'=-\infty}^{\infty} \mathcal{F}_n(\boldsymbol{\lambda}) \mathrm{U}_n(k\boldsymbol{r}). \tag{4.10}$$

To calculate the average response of the metamaterial, we ensemble average over all possible positions, orientations and properties [21, 22, 47], while assuming that resonators do not overlap, and that any possible configuration $\boldsymbol{\lambda}_i$ has the same probability (micro-canonical ensemble), which results in

$$\langle u_{\text{sc}}(\boldsymbol{r}) \rangle = \frac{1}{M} \sum_{i=1}^{M} \sum_{n=-\infty}^{\infty} \mathcal{F}_n(\boldsymbol{\lambda}_i) \mathrm{U}_n(k\boldsymbol{r}) = \sum_{n=-\infty}^{\infty} \langle \mathcal{F}_n \rangle \mathrm{U}_n(k\boldsymbol{r}), \tag{4.11}$$

where the bracket notation $\langle \circ \rangle$ denotes the ensemble average of $\circ$, and M is the number of possible configurations $\boldsymbol{\lambda}_i$ which tends to infinite.

The average material coefficients $\langle \mathcal{F}_n \rangle$ can be calculated either by the effective waves method [21, 52], or by brute force Monte-Carlo simulations using the Julia library MultipleScattering.jl [46].

The effective waves method calculates the average amplitude (4.11) directly, avoiding the explicit computation of the scattering from each configuration (4.10). Further, this method provides a semi-analytic formula for the dispersion equation of the meta-material, which we use to obtain a low-frequency expansion in Section 4.3.3, resulting in explicit formulae for the effective-properties.

On the other hand, Monte-Carlo simulations estimate the average response by explicitly calculating the scattering from each configuration $\boldsymbol{\lambda}_i$, repeating this for a very large

number of possible configurations, and then calculating the average (4.11). This strategy also allows the computation of higher statistical moments of the scattered field, such as the mean scattered intensity

$$\langle |u_{\text{sc}}(\boldsymbol{r})|^2 \rangle = \sum_{n,m=-\infty}^{\infty} \langle \mathcal{F}_n^* \mathcal{F}_m \rangle \mathrm{U}_n^*(k\boldsymbol{r}) \mathrm{U}_m(k\boldsymbol{r}), \tag{4.12}$$

where $*$ means complex conjugation. In Section 4.2.2 we used both the mean amplitude (4.11) and mean intensity (4.12) calculated from Monte-Carlo simulations for our disordered metamaterial, and compare them against the average response from the effective-properties (4.1) deduced in Section 4.3.3.

It is interesting to compare the average intensity against the intensity of the average to illustrate attenuation due to phase cancellation. The Jensen's inequality applied to (4.11) and (4.12) leads to

$$\langle |u_{\text{sc}}(\boldsymbol{r})|^2 \rangle \geq |\langle u_{\text{sc}}(\boldsymbol{r}) \rangle|^2. \tag{4.13}$$

In other words the "energy" of the average field $|\langle u_{\text{sc}}(\boldsymbol{r}) \rangle|^2$ is less than, or equal to, the average energy $\langle |u_{\text{sc}}(\boldsymbol{r})|^2 \rangle$. This apparent energy loss in the average field is due to phase cancellation. This effect is illustrated in Figure 4.7, where the mean intensity is consistently higher than the mean amplitude for moderate to high frequencies ($ka > 0.2$).

A simple way to see why (4.13) holds is to consider the average of the squared deviation from the mean amplitude of the scattered wave

$$\langle |u_{\text{sc}}(\boldsymbol{r}) - \langle u_{\text{sc}}(\boldsymbol{r}) \rangle|^2 \rangle = \langle [u_{\text{sc}}(\boldsymbol{r}) - \langle u_{\text{sc}}(\boldsymbol{r}) \rangle]^* [u_{\text{sc}}(\boldsymbol{r}) - \langle u_{\text{sc}}(\boldsymbol{r}) \rangle] \rangle = \langle |u_{\text{sc}}(\boldsymbol{r})|^2 \rangle - |\langle u_{\text{sc}}(\boldsymbol{r}) \rangle|^2 \geq 0,$$

which is always non-negative, as it is the average of a squared modulus.

4.3.3 low-frequency expansion

In this section, we use the dispersion equation for a 2D random particulate material from the effective waves method in [57, equation 4.10] to derive effective-properties of the metamaterial with resonators. The single species (one type of particle) version of this dispersion relation is the same as found in [22, 58]. As we are interested in the long wavelength regime, we assume that the resonators' positions, orientations, and properties are uncorrelated, except that the resonators cannot overlap[5]. For these assumptions, the

[5]To reach a dispersion equation, we also need a closure assumption. We use the Quasi-Crystalline Approximation discussed in [22, 59].

dispersion equation [52, equation 4.10] simplifies into

$$F_m(\boldsymbol{\lambda}_1) + \sum_{n'=-\infty}^{\infty} \frac{2\pi \overline{T}_n(\boldsymbol{\lambda}_1)}{k_\star^2 - k^2} \int_{\mathcal{S}} \mathrm{N}_{n'-m}[k(b_1+b_2), k_\star(b_1+b_2)] F_{n'}(\boldsymbol{\lambda}_2)\mathfrak{n}(\boldsymbol{\lambda}_2)\mathrm{d}\boldsymbol{\lambda}_2 = 0, \quad (4.14)$$

where $\mathrm{N}_n[x,y] = x\mathrm{H}_n'(x)\mathrm{J}_n(y) - y\mathrm{J}_n'(y)\mathrm{H}_n(x)$, $\mathfrak{n}(\boldsymbol{\lambda})$ is the number density of resonators of type $\boldsymbol{\lambda}$, $k_\star$ is the effective wavenumber, $\overline{T}_n(\boldsymbol{\lambda})$ is the isotropic T-matrix (4.29) derived in Appendix 4.A. The definition of the amplitude of the effective wave $F_n(\boldsymbol{\lambda})$ is given in [52], while the set of all possible resonator properties $\mathcal{S}$ is defined in Section 3.3.1.

We define the effective speed of sound as follows

$$c_\star = ck/k_\star. \quad (4.15)$$

To do an asymptotic expansion, we assume there is a maximum outer radius for the resonators $b_{\max}$, such that $b_j \leq b_{\max}$ for all j. We also recall that all resonators are subwavelength, so the dimensionless wavenumber $\epsilon = kb_{\max}$ is small. Then, we expand the effective wavenumber as a power series of ϵ

$$k_\star b_j = \chi\alpha_j\epsilon + \mathcal{O}(\epsilon^2), \quad (4.16)$$

where we have defined $\alpha_j = b_j/b_{\max}$, $b_{\max}$ is the larger outer radius of the resonators in the mixture, and we assume there is no wave propagation at arbitrarily long wavelength (no zero order term in (4.16)). We denote the leading order correction of the effective wavenumber as χ, which has yet to be determined. Then, substituting (2.47) into (4.15) leads to the following expansion for the effective speed

$$\frac{c}{c_\star} = \chi + \mathcal{O}(\epsilon). \quad (4.17)$$

To determine χ, we need to perform an asymptotic expansion of the terms in (4.14), including $\overline{T}_n(\boldsymbol{\lambda}_1)$ which depends on the resonance factor. The trick to do this elegantly is to make no assumptions about the asymptotic order of $z(\boldsymbol{\lambda})$ [26, 27]. This is because $z(\boldsymbol{\lambda})$ depends on the frequency in a non-trivial way, involving all parameters of the resonator's internal geometry (see (4.30) and (4.31) in Appendices 4.A and 4.B). Fortunately we can reach simple formulae without making any assumption about $z(\boldsymbol{\lambda})$. Instead, the resulting error of our method will be relative to $z(\boldsymbol{\lambda})$.

Performing an asymptotic expansion on the terms in (4.14) results in

$$\begin{aligned}
&\frac{1}{k_\star^2 - k^2} = \frac{b_{\max}^2}{\chi^2 - 1}\frac{1}{\epsilon^2} + \mathcal{O}(\epsilon^{-1}),\\
&\mathrm{N}_{n'-m}(kb_{1,2}, k_\star b_{1,2}) = \mathrm{N}^{(0)}_{n'-m}(\chi) + \mathcal{O}(\epsilon), \quad \text{with } \mathrm{N}^{(0)}_n(\chi) = \frac{2\mathrm{i}}{\pi}\sum_{m=-\infty}^{\infty}\chi^{|m|}\delta_{n,m},\\
&\overline{T}_n(\boldsymbol{\lambda}_1) = \overline{T}^{(2)}_n(\boldsymbol{\lambda}_1)\alpha_1^2\epsilon^2 + \mathcal{O}(\epsilon^3(1+z(\boldsymbol{\lambda}))), \quad \text{with}\\
&\overline{T}^{(2)}_n(\boldsymbol{\lambda}_1) = \frac{\mathrm{i}\pi}{4}\left[\delta_{n,1} + \delta_{n,-1} - \delta_{n,0} + z(\boldsymbol{\lambda}_1)\delta_{n,0}\right].
\end{aligned} \tag{4.18}$$

where $\delta_{n,m}$ is the delta Kronecker symbol. We have included $z(\boldsymbol{\lambda})$ in the error so that we do not need to make assumptions about the size of $z(\boldsymbol{\lambda})$, which can be large. Fortunately, this works well, as the maximum relative error of the leading order term for $\overline{T}_n$ is ϵ. We see this trend in the numerical validation.

Substituting (4.18) into (4.14), and retaining only the leading order terms we reach

$$F_n(\boldsymbol{\lambda}_1) - \frac{2\pi b_{\max}^2}{1-\chi^2}\overline{T}^{(2)}_n(\boldsymbol{\lambda}_1)\alpha_1^2\sum_{n'=-1}^{1}\mathrm{N}^{(0)}_{n'-n}(\chi)\int_{\mathcal{S}}F_{n'}(\boldsymbol{\lambda}_2)\mathfrak{n}(\boldsymbol{\lambda}_2)\mathrm{d}\boldsymbol{\lambda}_2 = 0, \tag{4.19}$$

where the sum is truncated, as the other terms are of higher order in ϵ. To determine χ we multiply both sides of (4.19) by $\mathfrak{n}(\boldsymbol{\lambda}_1)$ and integrate over $\boldsymbol{\lambda}_1$, leading to the following eigenvalue problem

$$\begin{aligned}
&\sum_{n'=-1}^{1}\mathrm{M}_{nn'}\tilde{F}_{n'} = 0, \quad \text{with} \quad \tilde{F}_n = \int_{\mathcal{S}}F_n(\boldsymbol{\lambda}_1)\mathfrak{n}(\boldsymbol{\lambda}_1)\mathrm{d}\boldsymbol{\lambda}_1 \quad \text{and}\\
&\mathrm{M}_{nn'} = \delta_{n,n'} - \frac{2\pi b_{\max}^2}{1-\chi^2}\mathrm{N}^{(0)}_{n'-n}(\chi)\int_{\mathcal{S}}\overline{T}^{(2)}_n(\boldsymbol{\lambda}_1)\alpha_1^2\mathfrak{n}(\boldsymbol{\lambda}_1)\mathrm{d}\boldsymbol{\lambda}_1.
\end{aligned} \tag{4.20}$$

We note that, due to the low-frequency expansion, the eigenvalue problem (4.20) only involves three modes $n = -1, 0, 1$, and hence M is a 3×3 matrix. By solving the dispersion relation $\det \mathrm{M} = 0$, we can obtain an exact expression for χ, which substituted into (4.17) leads to (at leading order)

$$c_\star^2 = \frac{\beta}{\varrho}\frac{(1-\varphi)}{\left(1-\varphi+\sum_{j=1}^{N}z(\boldsymbol{\lambda}_j)\phi_j\right)(1+\varphi)}, \tag{4.21}$$

where, to simplify the exposition, we have specialised the above to a mixture of N types

of resonators, which led us to substitute

$$\mathfrak{n}(\boldsymbol{\lambda}) = \sum_{j=1}^{N} \frac{\phi_j}{\pi b_j^2} \delta(\boldsymbol{\lambda} - \boldsymbol{\lambda}_j), \tag{4.22}$$

where ϕ_j is the volume fraction of the resonator of type j, $\varphi = \sum_{j=1}^{N} \phi_j$ is the total volume fraction of resonators, and δ is the Dirac delta distribution.

Finally, we want an effective density $\varrho_\star$ and bulk modulus $\beta_\star$ such that $c_\star^2 = \beta_\star/\varrho_\star$. Analogous to [20, 21], there is only one way to factor out $\beta_\star$ and $\varrho_\star$ such that the limits $\phi_j \to 0$ are consistent, and they lead to (4.1) presented in Section 4.2. Then, to calculate the average response of any metamaterial, one can replace it with an effective homogeneous medium with properties given by (4.1). We validate these results against Monte-Carlo simulations in Figures 4.7 to 4.9.

We note that it is expected that Helmholtz resonators, with only one gap such as the examples shown in Figure 4.10, only significantly alter the effective bulk modulus, as we deduced in (4.1). This is because one gap leads to a dominant monopole term, and the monopole terms from the resonators contribute to the effective bulk modulus while the dipole terms contribute to the effective density. Therefore, a dipole-dominant resonator would lead to a significant change in the effective density.

4.4 Concluding remarks and further avenues

Summary. We have introduced a disordered composite metamaterial, consisting of sub-wavelength Helmholtz resonators. Having small resonators compared to the wavelength ($kb < 1$) allowed us to deduce, from first principles, formulae for both effective bulk modulus and effective mass density (4.1). These formulae were validated against high-fidelity Monte-Carlo simulations for both a layer and a circle filled with resonators. Using our effective formulae, we are able to quickly design broad frequency band gaps without using multiple layers, periodicity, or heavy optimisation methods. In future work, we plan to expand our results to higher orders in kb and hence produce formulae that hold at higher frequencies. This would allow us to consider the effects of particle positioning, through the pair correlation, and allow us to quantify the difference between, say, random, periodic and hyperuniform materials. At higher frequencies, when the wavelength is similar to the diameter of resonators, the effects of viscous dissipation are likely to become important. Similarly, when resonators are thick-walled, the viscous-thermal boundary layers may have comparable thickness to the size of the aperture of the resonators and increase absorption in the narrow channel where air passes through. In such

cases viscous-thermal effects can be incorporated in the manner discussed in [23], or by more sophisticated asymptotic analysis.

Ensemble average properties. Contrary to the standard approach with periodic media, the formulae we deduce are based on ensemble averaging over the possible positions and orientations of the resonators, which introduces both advantages and disadvantages. The key advantages are that: 1) we were able to easily deduce effective-properties for any mix of different types of resonators, and 2) the effective-properties are robust with respect to changes in position and orientation of the resonators, as shown by the motivation example in Figure 4.2. However, the effective-properties in (4.1) do not give exactly the same results as any one specific configuration, and they also do not capture the average intensity of the scattered waves.

Applications. Despite using ensemble averaging in deriving (4.21), there are many applications for a single configuration of resonators. For example, the frequency demultiplexer in Figure 4.2 with only one configuration of resonator generated randomly had a similar performance compared with the one achieved via heavy optimisation in [45]. In part, this is due to the response of a single configuration being close to the mean response for low frequencies, as illustrated by the purple shaded region in Figures 4.7 to 4.9 which represents two standard deviations of the mean.

More general resonators. Throughout the whole paper, we only showed examples of split-ring resonators from [23, 26, 27]. However, the formulae for the T-matrix (4.7) has the same form for any sub-wavelength circular Helmholtz resonator (which has one aperture), like the ones depicted in Figure 4.10, and the derived effective-properties (4.1) would have the same formula, although the resonance factor $z(\boldsymbol{\lambda})$ would change. Resonators with different internal structures should result in richer effective-properties for the metamaterial, as illustrated in Figure 4.6 for thick-walled split-ring resonators.

Optimising band gaps. One interesting direction to explore as future work is to implement the enhanced design strategy described in Section 4.2.2. This strategy consists of finding one specific configuration for the particles via optimisation while being guided by the overall band structure from the effective-properties (4.1).

Future generalisations. Another future avenue would be to investigate possible generalisations of the metamaterial presented. The simplest example is the three-dimensional case, where the Helmholtz resonators are spherical shells with a small aperture. Different from the case of long cylinders, small spheres could be used to produce compact versions of the metamaterial presented in three dimensions. Other than just acoustics, the case of sub-wavelength resonating structures in electromagnetism or elasticity could lead to interesting applications. For example, one could study how to embed sub-wavelength res-

onators in the building blocks of low-frequency operating machinery or other structures, to prevent harmful vibrations from propagating.

Acknowledgement

The author(s) would like to thank the Isaac Newton Institute for Mathematical Sciences, Cambridge, for support and hospitality during the programme Mathematical Theory and Applications of Multiple Wave Scattering, where work on this paper was undertaken. This work was supported by EPSRC grant EP/R014604/1. Paulo Piva gratefully acknowledges funding from an EPSRC Case studentship with Johnson Matthey. Art Gower gratefully acknowledges support from EPSRC (EP/V012436/1). David Abrahams gratefully acknowledges funding from the Royal Society for an Industry Fellowship with Thales UK.

Appendices

4.A Expression for the T-matrix

In this section, we deduce the T-matrix for a split-ring resonator in (4.7) and use an expression for $z(\boldsymbol{\lambda})$ in (4.30) combined with (4.31) for a split-ring resonator.

Consider a resonator with outer radius b, inner radius a, aperture size 2ℓ, and orientation θ_0, as shown in Figure 4.1. Let us obtain the scattered field for the incident plane wave

$$v_{\text{inc}}(\boldsymbol{r}) = \mathrm{e}^{\mathrm{i}kr\cos(\theta-\theta_{\text{inc}})},$$

Using [23, Equation (3.1)] we can calculate the scattered field for $\theta_0 = 0$ which in our notation becomes

$$v_{\text{sc}}(\boldsymbol{r}) = A\mathrm{U}_0(k\tilde{\boldsymbol{r}}) + \sum_{n=-\infty}^{\infty} c_n \mathrm{U}_n(k\boldsymbol{r}), \tag{4.23}$$

where $\tilde{\boldsymbol{r}} = \boldsymbol{r} - b(\cos(\theta_0), \sin(\theta_0))$ is the aperture location, c_n and A are coefficients given by [23, Eqs. (3.4) and (3.6) respectively]. To obtain the scattered field for $\theta_0 \neq 0$, we rotate the coordinate system $\theta \to \theta - \theta_0$, followed by the rotation of the incident wave $\theta_{\text{inc}} \to \theta_{\text{inc}} - \theta_0$. These rotations leave the incident wave unaltered while rotating the resonator by an angle of θ_0 which together with [23, Equation (3.1)] results in

$$\begin{aligned} A &= -z(\boldsymbol{\lambda}) \sum_{p=-\infty}^{\infty} \frac{\mathrm{i}^p kb}{\mathrm{H}_p'(kb)} \mathrm{e}^{\mathrm{i}p(\theta_0-\theta_{\text{inc}})}, \\ c_n &= -\mathrm{i}^n \frac{\mathrm{J}_n'(kb)}{\mathrm{H}_n'(kb)} \mathrm{e}^{-\mathrm{i}n\theta_{\text{inc}}} - \frac{A}{2} \frac{\mathrm{Q}_n(kb)}{\mathrm{H}_n'(kb)} \mathrm{e}^{-\mathrm{i}n\theta_0}, \end{aligned} \tag{4.24}$$

where $\mathrm{Q}_n(x) = \mathrm{J}_n(x)\mathrm{H}_n'(x) + \mathrm{J}_n'(x)\mathrm{H}_n(x)$, the prime notation denotes the derivative with respect to the argument. We call the function $z(\boldsymbol{\lambda})$ the resonance factor, and it is defined by (4.30) in Appendix 4.B.

To rewrite (4.23) in terms of a T-matrix, shown in (4.6), we need to express all the terms centred at the origin, which leads us to use Graf's addition theorem to rewrite the

monopole term evaluated at $k\tilde{\boldsymbol{r}}$ in the form

$$\mathrm{U}_0(k\tilde{\boldsymbol{r}}) = \sum_{n=-\infty}^{\infty} \mathrm{J}_{-n}(kb)\mathrm{e}^{\mathrm{i}n(\pi-\theta_0)}\mathrm{U}_n(k\boldsymbol{r}),$$

which substituted into (4.23) leads to

$$v_{\mathrm{sc}}(\boldsymbol{r}) = \sum_{n=-\infty}^{\infty} d_n \mathrm{U}_n(k\boldsymbol{r}), \quad \text{with} \quad d_n = c_n + A\mathrm{J}_n(kb)\mathrm{e}^{-\mathrm{i}n\theta_0}. \tag{4.25}$$

Next, the T-matrix (4.6) relates any incident wave to the scattered wave, so we need to rewrite any incident wave $u_{\mathrm{inc}}(\boldsymbol{r})$ in terms of plane waves to use the results above. To achieve this, we use the Jacobi-Anger expansion of the plane wave:

$$v_{\mathrm{inc}}(\boldsymbol{r}) = \mathrm{e}^{\mathrm{i}kr\cos(\theta-\theta_{\mathrm{inc}})} = \sum_{n=-\infty}^{\infty} \mathrm{i}^n \mathrm{J}_n(kr)\mathrm{e}^{\mathrm{i}n(\theta-\theta_{\mathrm{inc}})},$$

followed by a superposition of plane waves

$$\begin{aligned} u_{\mathrm{inc}}(\boldsymbol{r}) &= \int_0^{2\pi} v_{\mathrm{inc}}(\boldsymbol{r})\mathrm{g}(\theta_{\mathrm{inc}})\mathrm{d}\theta_{\mathrm{inc}} = \int_0^{2\pi} \sum_n \mathrm{g}(\theta_{\mathrm{inc}})\mathrm{i}^n \mathrm{J}_n(kr)\mathrm{e}^{\mathrm{i}n(\theta-\theta_{\mathrm{inc}})}\mathrm{d}\theta_{\mathrm{inc}} \\ &= \sum_n \left[\mathrm{i}^n \int_0^{2\pi} \mathrm{g}(\theta_{\mathrm{inc}})\mathrm{e}^{-\mathrm{i}n\theta_{\mathrm{inc}}}\mathrm{d}\theta_{\mathrm{inc}}\right] \mathrm{V}_n(k\boldsymbol{r}). \end{aligned} \tag{4.26}$$

Without loss of generality, we choose the amplitude of the packet of plane waves $\mathrm{g}(\theta_{\mathrm{inc}})$ in (4.26) such that

$$\mathrm{i}^n \int_0^{2\pi} \mathrm{g}(\theta_{\mathrm{inc}})\mathrm{e}^{-\mathrm{i}n\theta_{\mathrm{inc}}}\mathrm{d}\theta_{\mathrm{inc}} = g_n,$$

which implies that (4.26) now matches the form of any regular incident wave (4.4).

Now we need to perform the same operations on the scattered field v_{sc} (4.25) from a plane wave to obtain the total scattered field from any incident wave u_{sc}, which is possible due to the linearity of the Helmholtz equation and results in

$$\begin{aligned} u_{\mathrm{sc}}(\boldsymbol{r}) &= \int_0^{2\pi} v_{\mathrm{sc}}(\boldsymbol{r})\mathrm{g}(\theta_{\mathrm{inc}})\mathrm{d}\theta_{\mathrm{inc}} = \sum_n \left[\int_0^{2\pi} d_n \mathrm{g}(\theta_{\mathrm{inc}})\mathrm{d}\theta_{\mathrm{inc}}\right] \mathrm{U}_n(k\boldsymbol{r}), \\ &= \sum_{n,p} \left[-\delta_{np}\frac{\mathrm{J}_p'(kb)}{\mathrm{H}_p'(kb)} + \frac{2\mathrm{e}^{-\mathrm{i}(n-p)\theta_0}}{(\pi kb)^2 h(\boldsymbol{\lambda})\mathrm{H}_n'(kb)\mathrm{H}_p'(kb)}\right] g_p \mathrm{U}_n(k\boldsymbol{r}), \end{aligned} \tag{4.27}$$

where we have used the Wronskian of Bessel-Hankel functions in the second line

$$\mathrm{J}_n(x)\mathrm{H}'_n(x) - \mathrm{J}'_n(x)\mathrm{H}_n(x) = \frac{2\mathrm{i}}{\pi x}.$$

Finally by comparing (4.6), (4.7) and (4.27) we conclude that

$$T_{np} = -\frac{\mathrm{J}'_p(kb)}{\mathrm{H}'_p(kb)}\delta_{np} + \frac{\mathrm{i}\mathrm{e}^{\mathrm{i}(n-p)\theta_0}}{\pi \mathrm{H}'_n(kb)\mathrm{H}'_p(kb)} z(\boldsymbol{\lambda}), \tag{4.28}$$

which is the general T-matrix for a Helmholtz resonator using formulae in [23].

In Section 4.3.3, the T-matrix (4.7) is used to calculate the dispersion equation. However, as discussed in [21, 52], only the average T-matrix over all orientations of the aperture θ_0 contributes to the dispersion equation. We call this orientation averaged version of (4.7) the isotropic T-matrix, which is given by terms in the diagonal of (4.7), as follows

$$\overline{T}_n(\boldsymbol{\lambda}) = -\frac{\mathrm{J}'_n(kb)}{\mathrm{H}'_n(kb)} - \frac{\mathrm{i}z(\boldsymbol{\lambda})}{\pi[\mathrm{H}'_n(kb)]^2}. \tag{4.29}$$

4.B Low-frequency behaviour of the resonance factor

In this section we show $z(\boldsymbol{\lambda})$ for a 2D thin walled-split resonator. Other expressions for $z(\boldsymbol{\lambda})$ for other Helmholtz resonators can be deduced from [25, 60, 61]

We use the results from [23], where $z(\boldsymbol{\lambda})$ is related to the function $h(\boldsymbol{\lambda})$ through

$$z(\boldsymbol{\lambda}) = \frac{2\mathrm{i}}{\pi(kb)^2 h(\boldsymbol{\lambda})}. \tag{4.30}$$

For a thin-walled Helmholtz resonator ($b = a$ in Figure 4.1) $h(\boldsymbol{\lambda})$ is given by [23, equation (3.7)]

$$h(kb, k\ell) = 2 + \frac{4\mathrm{i}}{\pi}\left(\gamma_e + \log\frac{k\ell}{4}\right) - \frac{1}{2}\sum_{m=-\infty}^{\infty}\frac{\mathrm{Q}_m^2(kb)}{\mathrm{H}'(kb)\mathrm{J}'(kb)}, \tag{4.31}$$

where $\mathrm{Q}_m(x) = \mathrm{J}_m(x)\mathrm{H}'_m(x) + \mathrm{J}'_m(x)\mathrm{H}_m(x)$ and γ_e is the Euler-Mascheroni constant. For the expression for $h(kb, ka, k\ell)$ for a thick-walled resonator ($a < b$) see [23, equation (3.7)], which we use to produce the results in Figure 4.6.

Performing the asymptotic expansion of $\epsilon = kb \ll 1$ in (4.31) we obtain

$$h(kb, k\ell) = 2 + \frac{4\mathrm{i}}{\pi}\left(\gamma_e + \log\frac{k\ell}{4}\right) + \frac{2\mathrm{i}}{\pi}\frac{1}{\epsilon^2} + \mathcal{O}\left(\frac{1}{\epsilon}\right), \tag{4.32}$$

where we do not expand the logarithmic term. From the above, and noting that $k\ell < kb$, we can conclude that $|h| \in \mathcal{O}(\epsilon^{-2})$ for frequencies away from resonance, which implies that $|z| \in \mathcal{O}(1)$. At resonance we have that $h(\boldsymbol{\lambda})$ is purely real, which occurs when $h(kb, k\ell) = 2$, and then $|z| \in \mathcal{O}(\epsilon^{-2})$. In other words, $z(\boldsymbol{\lambda})$ changes its order in ϵ when passing through resonance, which complicates an asymptotic analysis. Luckily, we do not need to perform an asymptotic expansion on $z(\boldsymbol{\lambda})$ to deduce simple effective formulae for the leading order term.

Bibliography

[1] Giuseppe Failla, Alessandro Marzani, Antonio Palermo, Andrea Francesco Russillo, and Daniel Colquitt. Current developments in elastic and acoustic metamaterials science. Philosophical Transactions of the Royal Society A: Mathematical, Physical and Engineering Sciences, 382(2278):20230369, 2024. doi: 10.1098/rsta.2023.0369.

[2] R. A. Shelby, D. R. Smith, and S. Schultz. Experimental verification of a negative index of refraction. Science, 292(5514):77–79, 2001. doi: 10.1126/science.1058847.

[3] Biswajit Banerjee. An introduction to metamaterials and waves in composites. Taylor & Francis, 2011.

[4] Steven A Cummer and David Schurig. One path to acoustic cloaking. New Journal of Physics, 9(3):45, mar 2007. doi: 10.1088/1367-2630/9/3/045.

[5] William J. Parnell and Tom Shearer. Antiplane elastic wave cloaking using metamaterials, homogenization and hyperelasticity. Wave Motion, 50(7):1140–1152, 2013. ISSN 0165-2125.

[6] J. B. Pendry, D. Schurig, and D. R. Smith. Controlling electromagnetic fields. Science, 312(5781):1780–1782, 2006. doi: 10.1126/science.1125907.

[7] A.N. Norris and A.L. Shuvalov. Elastic cloaking theory. Wave Motion, 48(6):525–538, 2011. ISSN 0165-2125. Special Issue on Cloaking of Wave Motion.

[8] H. Nassar, B. Yousefzadeh, R. Fleury, M. Ruzzene, A. Alù, C. Daraio, A. N. Norris, G. Huang, and M. R. Haberman. Nonreciprocal acoustic and elastic materials. Nature Reviews Materials, 5:667–685, 2020. doi: 10.1038/s41578-020-0206-0.

[9] G. Carta, M. J. Nieves, and M. Brun. Forcing the silence of the Lamb waves: Unidirectional propagation in structured gyro-elastic strips and networks. European

Journal of Mechanics - A/Solids, 101:105070, 2023. ISSN 0997-7538. doi: 10.1016/j.euromechsol.2023.105070.

[10] A. J. Lawrence, Benjamin M. Goldsberry, Samuel P. Wallen, and Michael R. Haberman. Numerical study of acoustic focusing using a bianisotropic acoustic lens. The Journal of the Acoustical Society of America, 148(4):EL365–EL369, 10 2020. ISSN 0001-4966. doi: 10.1121/10.0002137.

[11] Min Yang, Shuyu Chen, Caixing Fu, and Ping Sheng. Optimal sound-absorbing structures. Mater. Horiz., 4:673–680, 2017. doi: 10.1039/C7MH00129K.

[12] J.-P. Groby, C. Lagarrigue, B. Brouard, O. Dazel, V. Tournat, and B. Nennig. Enhancing the absorption properties of acoustic porous plates by periodically embedding helmholtz resonators. The Journal of the Acoustical Society of America, 137(1): 273–280, 2015. ISSN 0001-4966. doi: 10.1121/1.4904534.

[13] Jean Boulvert, Gwénaël Gabard, Vicente Romero-Garcia, and Jean-Philippe Groby. Compact resonant systems for perfect and broadband sound absorption in wide waveguides in transmission problems. Scientific Reports, 12, 2022. doi: 10.1038/s41598-022-13944-1.

[14] N. Jiménez, W. Huang, V. Romero-García, V. Pagneux, and J.-P. Groby. Ultra-thin metamaterial for perfect and quasi-omnidirectional sound absorption. Applied Physics Letters, 109(12):121902, 2016. ISSN 0003-6951. doi: 10.1063/1.4962328.

[15] Yang Meng, Hao Dong, Eric Ballestero, Simon Félix, Gwénaël Gabard, and Jean-Philippe Groby. Minimum-phase reflection for a passive acoustic absorber with target absorption spectrum and minimum volume. Phys. Rev. Appl., 22:064074, 2024. doi: 10.1103/PhysRevApplied.22.064074.

[16] S. Kumar, S. Tan, L. Zheng, and D. M. Kochmann. Inverse-designed spinodoid metamaterials. Npj Computational Materials, 6(1):1–10, 2020.

[17] Simei Mao, Lirong Cheng, Houyu Chen, Xuanyi Liu, Zihan Geng, Qian Li, and Hongyan Fu. Multi-task topology optimization of photonic devices in low-dimensional fourier domain via deep learning. Nanophotonics, 12(5):1007–1018, 2023. doi: 10.1515/nanoph-2022-0361.

[18] Meisam Askari et al. Additive manufacturing of metamaterials: A review. Additive Manufacturing, 36:101562, 2020. ISSN 2214-8604. doi: 10.1016/j.addma.2020.101562.

[19] Junxiang Fan, Lei Zhang, Shuaishuai Wei, Zhi Zhang, Seung-Kyum Choi, Bo Song, and Yusheng Shi. A review of additive manufacturing of metamaterials and developing trends. Materials Today, 50:303–328, 2021.

[20] P. A. Martin, A. Maurel, and W. J. Parnell. Estimating the dynamic effective mass density of random composites. The Journal of the Acoustical Society of America, 128 (2):571–577, 08 2010. doi: 10.1121/1.3458849.

[21] Artur L Gower and Gerhard Kristensson. Effective waves for random three-dimensional particulate materials. New Journal of Physics, 23(6):063083, 2021. doi: 10.1088/1367-2630/abdfee.

[22] Artur L. Gower, Michael J. A. Smith, William J. Parnell, and I. David Abrahams. Reflection from a multi-species material and its transmitted effective wavenumber. Proceedings of the Royal Society A: Mathematical, Physical and Engineering Sciences, 474(2212):20170864, 2018. doi: 10.1098/rspa.2017.0864.

[23] Smith M. J. A., Cotterill P. A., Nigro D., Parnell W. J., and Abrahams I. D. Asymptotics of the meta-atom: plane wave scattering by a single helmholtz resonator. Phil. Trans. R. Soc. A, 380, 2022. doi: 10.1098/rsta.2021.0383.

[24] Ping Sheng and Bart van Tiggelen. Introduction to wave scattering, localization and mesoscopic phenomena. Taylor & Francis, 2007.

[25] Anton Krynkin, Olga Umnova, Alvin Y B Chong, Shahram Taherzadeh, and Keith Attenborough. Scattering by coupled resonating elements in air. Journal of Physics D: Applied Physics, 44(12):125501, mar 2011. doi: 10.1088/0022-3727/44/12/125501.

[26] Smith Michael J. A. and Abrahams I. David. Tailored acoustic metamaterials. Part I. Thin- and thick-walled helmholtz resonator arrays. Proc. R. Soc. A, 478, 2022. doi: 10.1098/rspa.2022.0124.

[27] Smith Michael J. A. and Abrahams I. David. Tailored acoustic metamaterials. Part II. Extremely thick-walled helmholtz resonator arrays. Proc. R. Soc. A, 478, 2022. doi: 10.1098/rspa.2022.0125.

[28] N.S. Bakhvalov and G.P. Panasenko. Homogenisation: Averaging Processes in Periodic Media: Mathematical Problems in the Mechanics of Composite Materials. Kluwer Academic Publishers, Dordrecht, 1989.

[29] W.J. Parnell and I.D. Abrahams. Homogenization for wave propagation in peri-

odic fibre-reinforced media with complex microstructure. i—theory. Journal of the Mechanics and Physics of Solids, 56(7):2521–2540, 2008. ISSN 0022-5096. doi: 10.1016/j.jmps.2008.02.003.

[30] Carlo Vanoni, Jaeuk Kim, Paul J. Steinhardt, and Salvatore Torquato. Dynamical properties of particulate composites derived from ultradense stealthy hyperuniform sphere packings. Phys. Rev. E, 112:015406, 2025. doi: 10.1103/7bm7-yxjk.

[31] Asma Sellami, Hervé Franklin, Anouar Njeh, and Pierre Maréchal. Effective bulk and mass densities of randomly distributed coated cylinders in fluid. The Journal of the Acoustical Society of America, 157(1):409–419, 01 2025. ISSN 0001-4966. doi: 10.1121/10.0034840.

[32] Daniel Torrent, Andreas Håkansson, Francisco Cervera, and José Sánchez-Dehesa. Homogenization of two-dimensional clusters of rigid rods in air. Phys. Rev. Lett., 96: 204302, 2006. doi: 10.1103/PhysRevLett.96.204302.

[33] Daniel Torrent and José Sánchez-Dehesa. Effective parameters of clusters of cylinders embedded in a nonviscous fluid or gas. Phys. Rev. B, 74:224305, 2006. doi: 10.1103/PhysRevB.74.224305.

[34] Daniel Torrent and José Sánchez-Dehesa. Acoustic metamaterials for new two-dimensional sonic devices. New Journal of Physics, 9(9):323, 2007. doi: 10.1088/1367-2630/9/9/323.

[35] Daniel Torrent and José Sánchez-Dehesa. Multiple scattering formulation of two-dimensional acoustic and electromagnetic metamaterials. New Journal of Physics, 13(9):093018, 2011. doi: 10.1088/1367-2630/13/9/093018.

[36] Ory Schnitzer and Richard V. Craster. Bloch waves in an arbitrary two-dimensional lattice of subwavelength Dirichlet scatterers. SIAM Journal on Applied Mathematics, 77(6):2119–2135, 2017. doi: 10.1137/17M112658X.

[37] Michael J. Nieves and Alexander B. Movchan. Asymptotic theory of generalised Rayleigh beams and their dynamic response. In Michael J. Nieves, Gennady Mishuris, and Andrea Piccolroaz, editors, Mechanics of High-Contrast Elastic Solids: Contributions from Euromech Colloquium 626, volume 284 of Springer Proceedings in Physics, pages 155–172. Springer, Cham, Switzerland, 2023. doi: 10.1007/978-3-031-23112-4_11.

[38] Mario Lázaro, Vicent Romero-García, Richard Wiltshaw, and Richard V. Craster. Dis-

persion relations of generalized one-dimensional phononic crystals. Proceedings of the Royal Society A: Mathematical, Physical and Engineering Sciences, 481(2302): 20250210, 2025. doi: 10.1098/rspa.2025.0210.

[39] M. Lázaro, R. Wiltshaw, R. V. Craster, and L. M. García-Raffí. Analytical approximations for multiple scattering in one-dimensional waveguides with small inclusions. Mechanical Systems and Signal Processing, 224:112046, 2025. doi: 10.1016/j.ymssp.2024.112046.

[40] M. Lázaro, R. Wiltshaw, R. V. Craster, and V. Romero-García. Wave propagation in beams with multiple resonators: conditions for weak scattering and the Born approximation. Journal of Sound and Vibration, 618:119277, 2025. doi: 10.1016/j.jsv.2025.119277.

[41] Vladimir G. Maz'ya, Alexander B. Movchan, and Michael J. Nieves. Mesoscale asymptotic approximations in the dynamics of solids with defects. Journal of Mathematical Sciences, 268(4):443–457, 2022. doi: 10.1007/s10958-023-06240-5.

[42] Charles-Antoine Guérin, Pierre Mallet, and Anne Sentenac. Effective-medium theory for finite-size aggregates. J. Opt. Soc. Am. A, 23(2):349–358, 2006. doi: 10.1364/JOSAA.23.000349.

[43] Vadim A. Markel and Igor Tsukerman. Current-driven homogenization and effective medium parameters for finite samples. Phys. Rev. B, 88:125131, Sep 2013. doi: 10.1103/PhysRevB.88.125131.

[44] Rachel Sun, Jet Lem, Yun Kai, Washington DeLima, and Carlos M. Portela. Tailored ultrasound propagation in microscale metamaterials via inertia design. Science Advances, 10(45):eadq6425, 2024. doi: 10.1126/sciadv.adq6425.

[45] Alexander Y. Piggott, Jesse Lu, Konstantinos G. Lagoudakis, Jan Petykiewicz, Thomas M. Babinec, and Jelena Vučković. Inverse design and demonstration of a compact and broadband on-chip wavelength demultiplexer. Nature Photonics, 9(6): 374–377, 2015.

[46] Artur L Gower and J Deakin. Multiplescatering.jl: A julia library for simulating, processing, and plotting multiple scattering of waves. version 0.1.21. Github, 2024.

[47] Leslie L. Foldy. The multiple scattering of waves. I. general theory of isotropic scattering by randomly distributed scatterers. Phys. Rev., 67:107–119, feb 1945. doi: 10.1103/PhysRev.67.107.

[48] Aris Karnezis and Art L Gower. Calculating pair-correlations from random particle configurations. arXiv preprint arXiv:2401.09236, 2024.

[49] Valerie J Pinfield and Tony Valier-Brasier. Multimode multiple wave scattering in suspensions of solid particles in viscous liquids: part 2: numerical validation. Proceedings of the Royal Society A, 480(2292):20240106, 2024.

[50] Adrien Rohfritsch, Jean-Marc Conoir, Régis Marchiano, and Tony Valier-Brasier. Numerical simulation of two-dimensional multiple scattering of sound by a large number of circular cylinders. The Journal of the Acoustical Society of America, 145(6): 3320–3329, 2019.

[51] Artur L Gower, Stuart C Hawkins, and Gerhard Kristensson. A model to validate effective waves in random particulate media: spherical symmetry. Proceedings of the Royal Society A, 479(2279):20230444, 2023.

[52] K. K. Napal, P. S. Piva, and A. L. Gower. Effective t-matrix of a cylinder filled with a random two-dimensional particulate. Proceedings of the Royal Society A: Mathematical, Physical and Engineering Sciences, 480(2292):20230660, 2024. doi: 10.1098/rspa.2023.0660.

[53] Aristeidis Karnezis, Paulo S Piva, and Art L Gower. The average transmitted wave in random particulate materials. New Journal of Physics, 26(6):063002, 2024. doi: 10.1088/1367-2630/ad49c2.

[54] P.C. Waterman. Matrix formulation of electromagnetic scattering. Proceedings of the IEEE, 53(8):805–812, 1965. doi: 10.1109/PROC.1965.4058.

[55] P. C. Waterman. Symmetry, unitarity, and geometry in electromagnetic scattering. Phys. Rev. D, 3:825–839, 1971. doi: 10.1103/PhysRevD.3.825.

[56] Paul A. Martin. Multiple Scattering: Interaction of Time-Harmonic Waves with N Obstacles. Cambridge University Press, Cambridge, UK, 2006. ISBN 978-0521582392.

[57] K. K. Napal, P. S. Piva, and A. L. Gower. Effective T-matrix of a cylinder filled with a random two-dimensional particulate. Proceedings of the Royal Society A: Mathematical, Physical and Engineering Sciences, 480(2292):20230660, 2024. doi: 10.1098/rspa.2023.0660.

[58] C. M. Linton and P. A. Martin. Multiple scattering by random configurations of circular cylinders: Second-order corrections for the effective wavenumber. The

Journal of the Acoustical Society of America, 117(6):3413–3423, 2005. doi: 10.1121/1.1904270.

[59] Paulo S Piva, Kevish K Napal, and Art L Gower. Acoustic waves in a halfspace material filled with random particulate. New Journal of Physics, 26(12):123033, 2024. doi: 10.1088/1367-2630/ad9ed0.

[60] Alexei T. Skvortsov, Ian R. MacGillivray, and Oleg A. Godin. Acoustic waves in a perforated cylinder. The Journal of the Acoustical Society of America, 157(3):1880–1888, 03 2025. ISSN 0001-4966. doi: 10.1121/10.0036131.

[61] Tenneti C. Rao and Richard Barakat. Plane wave scattering from a cylindrical helmholtz resonator: Dirichlet case. Optics Communications, 164(4):223–232, 1999. ISSN 0030-4018. doi: 10.1016/S0030-4018(99)00178-9.

Chapter 5

Conclusions

The collection of chapters presented in this thesis focuses on theoretical advances in the study of the average wave propagation and scattering in particulate media, particularly when multiple scattering is relevant. All results are obtained using the effective waves method [1, 2], and contribute to efficient numerical calculation of broad frequency wave response in particulate media. These results serve as stepping stones to engineering ultrasound sensors that account for rescattering between particles and walls (or interfaces), and also for designing disordered metamaterials operating in the low frequency range. Below, we summarise the main insights, recommendations and future research directions.

Summary of Insights

The primary contribution of this research is the development of the eXtended Quasi-Crystalline Approximation (X-QCA) in Chapters 2 and 3. By deriving this framework from first principles, and with the same underlying assumptions as the usual Lax's Quasi-Crystalline Approximation (QCA) [3], we have successfully integrated multiple scattering effects between particles and boundaries. The resulting model applied to acoustic waves accounts for rescattering from walls of a vessel containing particulate material, or the interface of a probe and the surrounding medium. This addresses a significant limitation in classical models, allowing for the calculation of reflection and transmission coefficients in both half-space [4], and layered media experimental setups [5]. These results are applicable across a wide range of wavelengths compared to particle sizes, and accommodate both monodisperse and polydisperse particle distributions.

Furthermore, this framework provides a critical evaluation of existing effective medium models used to interpret experimental data [5–7]. Our simulations verified the validity of the assumption of constant effective mass density assumptions used in recent literature

(solid particles or weak scatterers) [5, 6], while simultaneously identifying the specific physical setups where these models lose accuracy (bubbles or strong scatterers). This predictive capability is essential for researchers to determine when more complex scattering models are required to interpret data of average wave response from particulates.

All numerical methods developed in both Chapters 2 and 3 have been implemented in an open-source Julia library, EffectiveWaves.jl [8], which is available on GitHub.

Another significant portion of the content in this thesis (Chapter 4) was dedicated to the calculation of effective-properties of disordered metamaterials composed of sub-wavelength Helmholtz resonators. By operating in the regime where the resonator size is small relative to the wavelength ($kb < 1$), this work has successfully deduced simple analytical formulae for both effective bulk modulus and effective mass density of such metamaterials. These formulae depend only on the volume fraction of each type of resonators in the material and the internal structure of each type (encoded in their resonance factor $z(\lambda)$). A key finding was that these effective-properties are robust against perturbations in the position and orientation of individual resonators. This suggests that, depending on application, disordered configurations can achieve performance levels comparable to highly optimized or periodic structures, such as frequency demultiplexrs, without the need for strict manufacturing tolerances or heavy computational optimization.

Recommendations for application

Below are key recommendations for researchers and engineers based on the findings of this thesis. These recommendations focus on the two primary applications addressed by our theoretical advancements: ultrasonic sensing of particulate media, and the design of disordered acoustic metamaterials.

Sensor design for particle sizing. Engineers designing particle size distribution sensors for slurries or emulsions should avoid direct contact of ultrasound transducers with the sample. When possible, a delay line should be implemented, not only to protect the probe, but also to avoid rescattering between particles and the surface of the transducer. Then, the X-QCA framework, presented in Chapters 2 and 3, can be used to model the average wave response, accounting for multiple scattering effects on the interface between particles and the delay line.

Callibration standards. When dealing with ultrasound particle size measurements in particulates, we recommend measuring the average reflection coefficien at high-frequencies (wavelengths much longer than any particle or inhomogeneity in the material). The high-frequency limit of the average reflection coefficient allows for the isolation of the matrix

response, even if the particles cannot be isolated from their homogeneous embedding medium (matrix), as discussed in Chapter 2. This measurement can then be used as a calibration standard to remove the matrix contribution from lower frequency measurements, where particle scattering is relevant.

Prioritize transmission for solid particle slurries. Based on our simulations for the average reflection and transmission coefficients in Chapters 2 and 3, we recommend that researchers characterizing solid particle slurries prioritize transmission-based sensing over reflection. Our results suggest that reflection measurements in this type of particulates may lack the sensitivity in the response when varying particle sizes.

Refinement of effective models. While a constant effective density may be a sufficient approximation for solid (sound-hard like) particles [5, 6], we explicitly recommend against this simplification for bubbly liquids or sound-soft like inclusions. Our numerical simulations in Chapter 3 suggest that, in these cases, a first-principles model as X-QCA must be used to capture the frequency-dependent impedance.

Disordered vs. periodic metamaterial design. Our Monte-Carlo simulations in Chapter 4 demonstrate that disordered composites remain stable under positional perturbations, unlike periodic metamaterials (as purpose built crystalline structures), where manufacturing imperfections can collapse material response. This resilience makes disordered metamaterials ideal for applications where manufacturing tolerances are a concern. However, for applications requiring extreme precision and zero variability in the wave response, periodic designs may remain the preferred choice.

Wide frequency range band gap design. To broaden band gaps without increasing material thickness, we recommend using polydisperse mixtures of Helmholtz resonators with varying aperture-to-diameter ratios for material design. Our effective-property formulae in Chapter 4 indicate that combining resonators with distinct resonance factors leads to multiple band gaps. By strategically selecting resonator types to produce overlapping resonances, the frequency range of inhibited wave propagation can be widened.

Further avenues

Beyond integrating our models in practical applications, as outlined in the conclusions here and at the end of each chapter, there are common directions for further research that apply to all the chapters. In this thesis, we have not considered any dissipation from thermal-viscous effects, which are relevant for micron-sized particles in liquids (Chapters 2 and 3), or thick-walled split ring resonators (Chapter 4). Although we expect only an additional overall attenuation of the average wave in such scenarios, it remains important

to quantify this effect for both sensing particle properties and designing metamaterials. Another clear future avenue is to generalise the models and formulas presented here for acoustics to accommodate full linear elastic multiple scattering of waves [9], or even to the electromagnetic case with dielectric background matrix [10].

Bibliography

[1] Artur L Gower and Gerhard Kristensson. Effective waves for random three-dimensional particulate materials. New Journal of Physics, 23(6):063083, 2021. doi: 10.1088/1367-2630/abdfee.

[2] K. K. Napal, P. S. Piva, and A. L. Gower. Effective T-matrix of a cylinder filled with a random two-dimensional particulate. Proceedings of the Royal Society A: Mathematical, Physical and Engineering Sciences, 480(2292):20230660, 2024. doi: 10.1098/rspa.2023.0660.

[3] Melvin Lax. Multiple scattering of waves. II. the effective field in dense systems. Phys. Rev., 85:621–629, 1952. doi: 10.1103/PhysRev.85.621.

[4] Amitosh Dash, Willian Hogendoorn, and Christian Poelma. Ultrasonic particle volume fraction profiling: an evaluation of empirical approaches. Experiments in Fluids, 62(4):85, 2021. doi: 10.1007/s00348-020-03132-0.

[5] Alverède Simon, Régis Wunenburger, and Tony Valier-Brasier. Propagation of coherent shear waves in scattering elastic media. Physical Review E, 103(L051001), 2021. doi: 10.1103/PhysRevE.103.L051001.

[6] Alverède Simon, Quentin Baudis, Régis Wunenburger, and Tony Valier-Brasier. Propagation of elastic waves in correlated dispersions of resonant scatterers. The Journal of the Acoustical Society of America, 155(6):3627–3638, 2024. doi: 10.1121/10.0026233.

[7] Tony Valier-Brasier, Adrien Rohfritsch, Ludovic Alhaïtz, and Jean-Marc Conoir. Fabry–pérot resonances of acoustic waves in disordered slabs. Applied Physics Letters, 125(4):041704, 07 2024. doi: 10.1063/5.0220808.

[8] Artur L. Gower and Paulo S. Piva. Effectivewaves.jl: A julia package to calculate ensemble averaged waves in heterogeneous materials. version 0.3.6. Github, 2024.

[9] P.A. Martin and V.J. Pinfield. Elastodynamic multiple scattering: Effective wavenum-

bers in three-dimensional elastic media. Wave Motion, 134:103478, 2025. ISSN 0165-2125. doi: 10.1016/j.wavemoti.2024.103478.

[10] Gerhard Kristensson and Niklas Wellander. Multiple scattering by a collection of randomly located obstacles distributed in a dielectric slab, chapter 25. Advances in Mathematical Methods for Electromagnetics, 2020. doi: 10.1049/SBEW528E_ch25.